NANYANG TECHNOLOGICAL UNIVERSITY

Design and Growth of High-Power Gallium Nitride Light-Emitting Diodes

ZHANG ZIHUI

SCHOOL OF ELECTRICAL AND ELECTRONIC ENGINEERING

2014

Design and Growth of High-Power Gallium Nitride Light-Emitting Diodes

ZHANG ZIHUI

School of Electrical and Electronic Engineering

A thesis submitted to the Nanyang Technological University

in partial fulfilment of the requirement for the degree of

Doctor of Philosophy

2014

ABSTRACT

In this dissertation, the InGaN/GaN multiple quantum well (MQW) light-emitting diodes (LEDs) have been studied from multiple aspects including improvement of material quality, suppression of quantum confined Stark effect (QCSE), promotion of carrier transport, enhancement of current spreading, reduction of electron overflow as well as increase in hole concentration of p-GaN through the generation of three-dimensional hole gas by dopant-free methods, with the aim to improve the optical performance of the devices. The InGaN/GaN LED epitaxial wafers are grown by metal-organic chemical vapor deposition (MOCVD) system on c-plane sapphire substrates. As it is well-known that the crystalline quality is crucial for high-efficiency InGaN/GaN LEDs, we have discussed and demonstrated the epitaxial films with optimized crystalline quality in this thesis. Besides, InGaN/GaN LEDs grown along polar-orientations (i.e., c^+/c^- orientations) suffer from the QCSE in the MQWs, which significantly reduces the spatial overlap of the electron-hole wave functions, and thus decreases the radiative recombination rates in the device active region. We have designed and demonstrated that the QCSE can be effectively suppressed by Si step-doping the quantum barriers, which enhances the optical output power and external quantum efficiency (EQE). In addition, by further Mg doping the Si step-doped quantum barriers with a proper Mg doping level and doing position, we have obtained the InGaN/GaN LEDs with PN-type quantum barriers. With this quantum barrier architecture, on one hand, the QCSE has been effectively screened, and on the other hand, the hole transport has also been promoted significantly. Hence, an even more enhancement in the optical output power and EQE has been obtained. The current crowding in the InGaN/GaN LEDs due to the low p-type conductivity is another challenge for achieving high-efficiency LEDs. In this dissertation, we have

proposed a solution for current spreading enhancement by embedding a thin weakly doped n-GaN layer into the p-GaN layer. Such that, the p-GaN/n-GaN/p-GaN (PNP-GaN) current spreading layer is formed. The advantage of this design is to achieve the current spreading layer directly in the MOCVD growth, which saves the post-growth treatment in the fabrication process for modulating the current distribution. Besides incorporating a resistive layer (i.e., weakly doped n-GaN) in the p-GaN layer to improve the current spreading, another way for a better current spreading is to increase the electrical conductivity of the top contact layer, i.e., p^+-GaN layer for the conventional InGaN/GaN LEDs. Therefore, we have grown the heavily doped n^+-GaN layer on top of the p^+-GaN layer to form a tunnel junction as the top contact layer. It is proved that the p^+-GaN/n^+-GaN tunnel junction has significantly improved the current spreading and thus the device performance. The additional voltage drop on the p^+-GaN/n^+-GaN tunnel junction can be relieved by inserting an InGaN layer between the p^+-GaN and n^+-GaN, i.e., a polarization tunnel junction which can also further improve the optical performance of the devices. We have also suggested InGaN/GaN LED devices with the electron overflow reduction through incorporating n-type InGaN layer and n-type AlGaN layer into the n-GaN layer, respectively, accompanied with which a mean-free-path model has been proposed and demonstrated to explain the mechanism of the electron overflow reduction through decreasing the electron mean free path. Lastly, as it has been mentioned previously, the low p-type conductivity in the InGaN/GaN LEDs has substantially limited the LED performance. The Mg dopants in the p-type GaN layers are only ionized by less than 1% at room temperature due to the large binding energy of Mg acceptors. In this dissertation, we have increased the hole concentration by inducing the three-dimensional (3D) hole gas without additional Mg doping. Our experiment shows that

the generation of the 3D hole gas has nothing to do with any external dopants. More importantly, the 3D hole gas can be injected into the MQWs for the radiative recombination. Hence, the 3D hole gas can be another hole source besides the one donated by the ionized Mg dopants.

ACKNOWLEDGEMENT

I feel very proud to have a chance studying in Nanyang Technological University (NTU) of Singapore, not only because of her beautiful campus and the friendly people there, but also her intensive scientific research of excellence and her opening to the world. Meanwhile, in the past few years, it was indeed my opportunity to work with those people worth mentioning here.

Firstly, I would like to show my sincere gratitude and respect to my PHD supervisor, Prof. Hilmi Volkan Demir. My interest to the scientific and engineering world will not be inspired if without his patience in supervising me. Furthermore, the completion of my research work in NTU will not happen if without his extensive and professional knowledge in the scientific field. I have also received significant encouragements from him whenever I met any challenges in my PHD career here.

Secondly, many thanks are also owing to my PHD co-supervisor, Prof. Sun Xiao Wei. If without his kind and unreserved supervisions, my PHD work can never happen. Whenever something interesting takes place in my experiments, he always shows me the correct directions. Besides, the encouragements from him cannot be forgotten. The scientific and technical discussions with him have refreshed my creativities.

Thirdly, I also feel grateful to Dr. Tan Swee Tiam for his kind support and being self-giving to my research work and even the article revising. His excellent leadership in the whole team guarantees the supply and growth of the samples for my research purpose. Besides, it is worthy of thanking Dr. Liu Wei for his expertise in the sample growth. His knowledge and kind assistance has tremendously helped me in my

research experiment. Whenever I met with any technical issues in my experiments, he was always the first one that I had in my mind for technical discussions and assistance.

Fourthly, I was lucky that I had the chance to work in a strong and collaborative team in NTU. Therefore, I have to thank Dr. Ju Zhengang for his kind support when I was growing my research samples. Moreover, his dedication to the metal-organic chemical vapor deposition (MOCVD) system including the maintenance and reparations cannot also be forgotten. Otherwise, the completion to my research wouldn't have been smoothly possible. Many thanks should be given to my other team members, Mr. Zhang Xueliang, Mr. Ji Yun, Mr. Zabu Kayw, Mr. Namig Hasanov, Mr. Zhang Yiping, Mr. Lu Shunpeng and Mr. Zhu Binbin for their contribution and assistance in the trouble solving and technology optimization in the device fabrication. My light-emitting diode (LED) chips would not have properly worked if without their brilliant work in photolithography, reactive ion etch (RIE), inductively coupled plasma etch (ICP), e-beam, rapid thermal annealing (RTA), electroluminescence (EL) measurement, photoluminescence (PL) and device current measurement.

Special thanks have to be given to my father (Mr. Zhang Qingzheng) and my mother (Ms. Feng Zunfang). Even more thanks should be given to my wife (Ms. Liu Qingqing). None achievements would have been made without the support and love from them.

Finally, I appreciate the financial support from NTU. I would not have concentrated myself on my research work if without their generous financial offer.

TABLE OF CONTENTS

LIST OF TABELS

LIST OF FIGURES

Chapter 1 Introduction

Considerable efforts have been paid to develop GaN and the related compound semiconductors for over the past thirty years. The first GaN thin film was grown by Dr. Paul Maruska through reacting liquid gallium metal with ammonia in 1968 [1]. However, since Maruska misunderstood the GaN-related literature by previous researchers, this first GaN thin film was formed at the temperature of 600 ^{o}C, resulting in a polycrystalline. In 1969, Maruska realized that the growth temperature is very critical, and he thus increased the growth temperature to 850 ^{o}C. The resultant epitaxial wafer was still transparent, as he characterized it in the analytical centre of Radio Corporation of America (RCA). It was revealed that this was indeed the first single-crystalline film of GaN [2]. After the achievement of the first single-crystalline GaN, his work inspired Dr. Jacques Pankove who was at RCA Laboratories in 1970. Later, the first demonstration of electroluminescence from GaN with emission wavelength centering at 475 nm was accomplished at RCA Laboratories by Pankove et al. in 1971 [3]. Soon later, Panknove et al. made the first current-injected green and blue GaN light-emitting diodes, which were named metal-insulator-semiconductor (MIS) diodes [4, 5]. In this epitaxial structure, there was an undoped n-type region, an insulating Zn-doped layer and an indium surface contact.

Pankove and his team attempted at making a PN-junction light emitter by obtaining the p-doped GaN layer. However, the GaN films at the early stage were unintentionally n-type doped with an electron concentration ranging from 10^{18} to 10^{20} cm^{-3}. Such a high n-type background doping level made it difficult to achieve GaN films with p-type conductivity. Nevertheless, they tried

magnesium rather than zinc by using metal organic vapor phase epitaxy (MOVPE) technology. In 1972, they succeeded in obtaining such a structure with the centre emission at 430 nm [4]. Note that this Mg-doped layer did not exhibit p-conductivity. The injected minority carriers and the impact ionization under high electric field were responsible for the radiative emission. Although Pankove et al. failed in achieving GaN film with p-conductivity, their effort inspired the future researchers after then. In 1989, the first p-type GaN film by low-energy electron-beam irradiation (LEEBI) treatment was successfully fabricated by Akasaki et al. [6], which produced a hole concentration of 2×10^{16} cm^{-3} with a sheet resistivity of 35 Ω-cm. Soon thereafter, Nakamura et al. also announced that p-type GaN can be made more conductive by rapid thermal annealing (RTA) in N_2 ambient [7], by means of which the hydrogen-magnesium bonds can be broken and a hole concentration of 3×10^{17} cm^{-3} with a sheet resistivity of 2 Ω-cm yielded.

In addition to the p-type GaN film, there was another obstacle, which prevented further development of GaN thin films in the early research. There were few lattice-matched substrates for the epitaxial growth of high-quality GaN films. The resulting hetero-epitaxial films had defects and dislocations of very high density, and in the meanwhile, the film surface morphology was very poor. These problems were solved in the mid-1980s by Akasaki et al. at Nagoya and Meijo Universities and Dr. Shuji Nakamura at Nichia Chemical Company in Japan, respectively. They used low-temperature AlN [8] and GaN [9] as the nucleation layer before the single crystalline GaN layer was deposited on sapphire by metal organic chemical vapor deposition (MOCVD) system, respectively, and GaN films with significantly improved quality have been

achieved. By then, most of the obstacles which hinder the further development of state-of-art solid-state lighting emitters have been solved. As a result, those efforts have opened the door to efficient nitride-based solid-state light emitters, such as the first PN-junction light-emitting diode (LED) in 1989 [10] and the first nitride-based laser diode with continuous-wave emission wavelength of 417 nm at room temperature [11]. Nowadays, even more tremendous progress has been made in the field of nitride-based LED and laser diodes (LDs), which are comprised of InGaN ternary alloyed quantum region as the active layer. The wavelength covers the range from UV to infrared emissions.

Although nitride-based solid state lighting source has currently been a fierce competitor to those conventional fluorescent and incandescent lighting sources, great success has been made, the device performance is still limited by a great number of factors including the strong polarization induced electric field, current crowding, electron overflow, insufficient hole transport across the active region and low hole concentration in the p-type layers [12-14], etc. Thus, the interest of this thesis is to propose ways to enhance the LED performance through further improving the crystal quality of the epitaxial films, designing and optimizing the LEDs with novel device architectures to address some of the key factors which affect the device performance.

The thesis is organized as follows: the radiation mechanism and current challenges for LEDs are presented in Chapter II; then, a brief introduction to MOCVD system is given in Chapter III, in which the growth procedure and the material optimization are also discussed; the standard chip-fabrication process for InGaN/GaN LED wafers has also been covered in this chapter. Chapter IV demonstrates two novel InGaN/GaN LED architectures to reduce the charge

separation and improve the hole transport within the InGaN/GaN multiple quantum wells (MQWs). As mentioned, the current crowding significantly limits the device performance, we have also proposed and demonstrated novel designs to increase the current spreading length and enhance the optical output power in Chapter V. Furthermore, the theoretical models to address the physical mechanism have also been presented. Manipulating the carrier injection is another research topic of this work. Chapter VI depicts the electron overflow reduction through electron cooler, along with which also shows the proposed physical model. Besides, with the proposed physical model, we have demonstrated the origin of reduced electron overflow by n-type electron blocking layer in Chapter VI. A novel InGaN/GaN LED completely lacking Mg-doped GaN layer is described in Chapter VII. Last, a conclusion for this thesis is presented in Chapter VIII.

Chapter 2 Optical radiation principles of InGaN/GaN light-emitting diodes

As energy-saving light sources, InGaN/GaN LEDs find applications in the back-lighting of liquid crystal displays, in signaling of traffic lights, in indoor/outdoor lighting and even possible for future visible light communication [12-17]. In this chapter, the physical principles of the light generation (i.e., radiative recombination) from InGaN/GaN LEDs are discussed. Meanwhile, the radiative recombination accompanied with those nonradiative recombination processes, including Auger recombination [18, 19] and Shockley-Read-Hall (SRH) recombination [19], are also discussed. InGaN/GaN LED epitaxial films grown along [0001]-orientation are strongly affected by the polarization induced electric fields [20]. The polarization induced electric fields in turn have a strong impact in the device optical and electrical performances. In this chapter, the details of polarization effects on InGaN/GaN LEDs are also explained. Finally, the technology issues which are challenging InGaN/GaN LEDs and the methods to solve them will be discussed.

2.1 Recombination in InGaN/GaN light-emitting diodes

Electrons and holes in the MQWs recombine either radiatively by emitting photons or nonradiatively by transferring the energy to phonons. In addition, carriers also tend to escape from the recombination region leading to a carrier overflow. The radiative recombination within the MQWs is preferable for a LED.

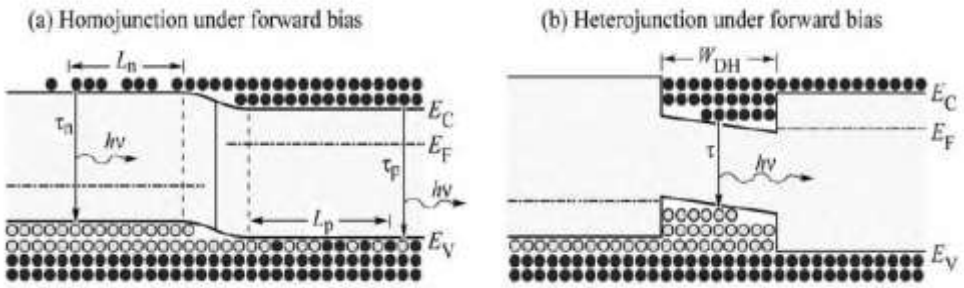

FIG. 2.1.1 Carrier distribution in a LED with (a) homojunction and (b) heterojunction under forward bias. After [1].

As depicted in Fig. 2.1.1(a), the electrons and holes are distributed within the diffusion length which is several hundred nanometers in a homojunction LED for III-nitride compounds [21, 22], thus yielding a low carrier concentration. As a result, the radiative efficiency of the homojunction LEDs is low. Improved carrier confinement can be achieved by employing the heterojunction structure as indicated in Fig. 2.1.1(b). The conduction and valence band offsets between the two semiconductor materials of a heterojunction are higher than the carrier thermal energy, and hence most of the carriers are confined within the material with the smaller energy band gap. Moreover, the heterojunction has been further developed to MQWs, such that the quantum well region is surrounded by thin quantum barriers as demonstrated in Fig. 2.1.2, in which energy states are quantized within each quantum well.

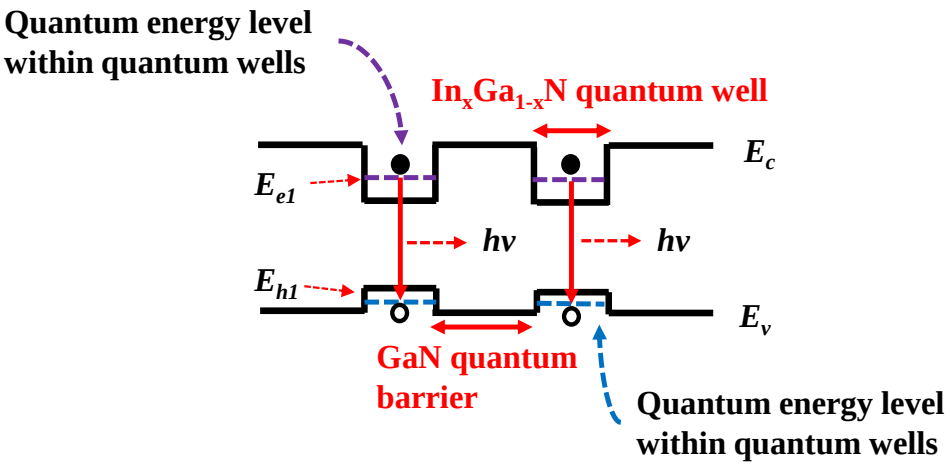

FIG. 2.1.2 Schematic diagram for InGaN/GaN MQWs, along with which is shown the example of quantized energy levels within the quantum wells. E_c and E_v denote the conduction and valence bands, respectively. E_{e1} and E_{h1} are the first quantized energy levels for electrons and holes, respectively. The energy of emission photons is given as hv.

Once the LED is no longer in an equilibrium state, i.e., under external biasing or light excitation, the electrons and holes will be excited to those discrete energy levels in the conduction band and valence band, respectively [23]. The energy of the excited electrons and holes can be depicted in Eqs. (2.1.1) and (2.1.2), respectively [1].

$$E_e = E_c + \frac{\hbar^2 k^2}{2m_e^*} \tag{2.1.1}$$

$$E_h = E_v - \frac{\hbar^2 k^2}{2m_h^*} \tag{2.1.2}$$

where m_e^* and m_h^* represent the effective mass for electrons and holes, respectively. $\hbar$ is Plank's constant, k is the wave number. Meanwhile, the conduction and valence band edges are denoted as E_c and E_v, respectively.

According to Eqs. (2.1.1) and (2.1.2), we can see that the energy distribution in *k*-space for electrons and holes follow the parabolic profiles. However, the excited electrons and holes recombine radiatively (i.e., emitting photons) provided that electrons and holes meet the momentum conservation (i.e., *k*-selection rule). The photon energy equals to the energy difference between the electrons and holes, such that $h\nu = E_e - E_h \approx E_g$, in which ν is the light frequency. Thus, the photon energy approximately equals the band gap energy of the quantum wells, i.e., E_g. For LEDs based on III-nitride material system, we use InGaN as the emitting layer. Furthermore, the energy band gap of the InGaN material is a function of the InN fraction (i.e., *x*), which can be expressed as a weighted sum of the energy band gaps of its relevant compound components. We also have to consider the bowing parameters, and thus $E_g(In_xGa_{1-x}N) = x \cdot E_g(InN) + (1-x) \cdot E_g(GaN) - 1.4 \cdot x \cdot (1-x)$.

It can be seen that smaller photon energy can be obtained as the InN fraction (i.e., *x*) of the InGaN layer is increased. Here, the emission energy/wavelength as a function of the crystalline lattice constant for III-nitride compounds is shown in Fig. 2.1.3.

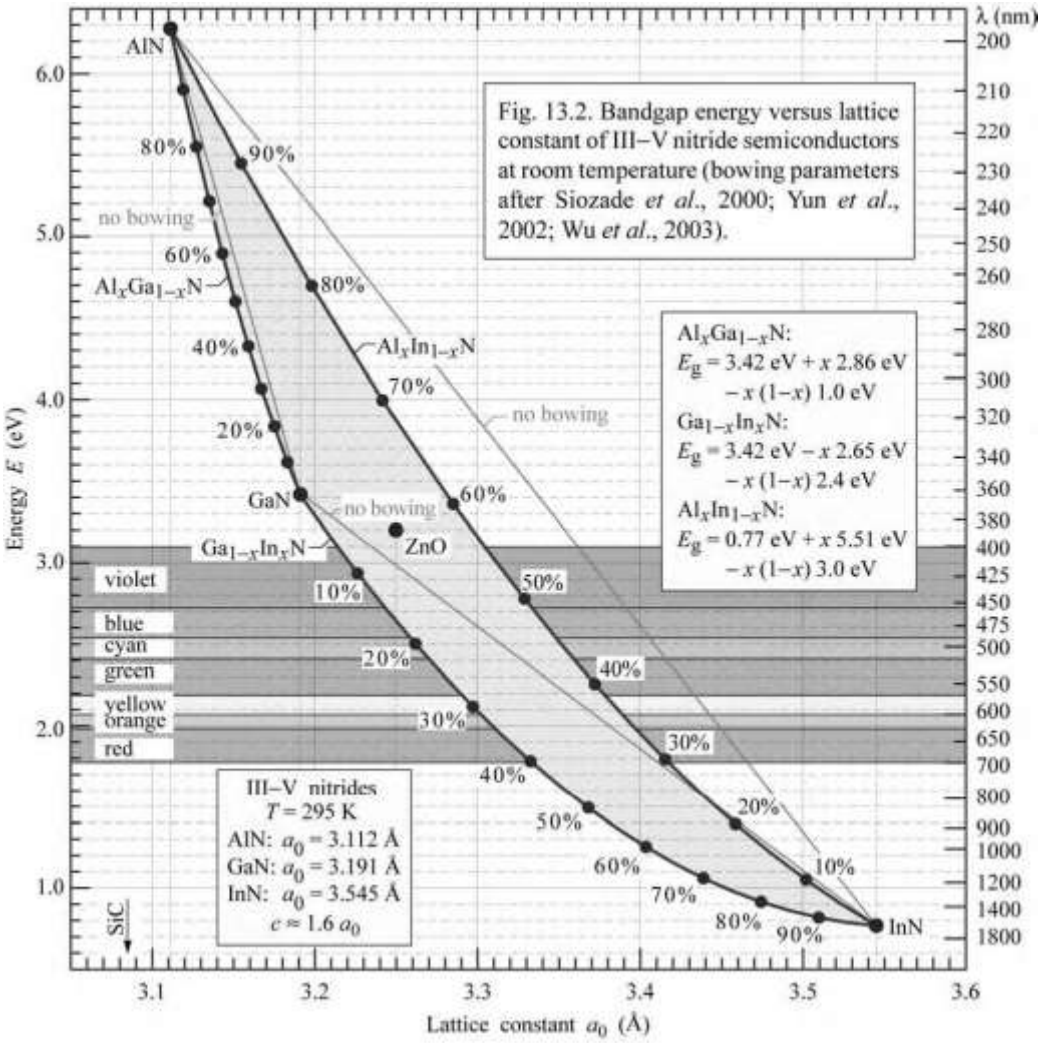

FIG. 2.1.3 Band gap energy/wavelength versus lattice constant for III-nitride semiconductors at room temperature. After [1].

In fact, the emission photon energy is not exactly the energy band gap of the emissive layer, since electrons and holes have a distribution in different energy states as shown in Eqs. (2.1.1) and (2.1.2). The line shape of the emission can be described by Eq. (2.1.3) [1].

$$I(E) \propto \sqrt{E - E_g} \cdot e^{-E/kT} \tag{2.1.3}$$

As has been shown in Fig. 2.1.2, the energy levels within the quantum wells are quantized, thus electrons and holes in the sub-bands (e.g., E_{e1} and E_{h1}) make

the radiative recombination. The sub-bands for electrons and holes can be obtained by solving the Schrödinger equation. A parabolic-band model is considered to calculate conduction sub-bands [24]. The valence sub-band structures for holes can be calculated by using the 6×6 $k \cdot p$ model [25-28].

The interband transition rate between conduction sub-bands and valence sub-bands for spontaneous emission follows the Fermi's Golden Rule [1], in which the spatial overlap between the electron wave function and the hole wave function determines the oscillation strength and thus the radiative recombination rate. In other words, those electrons and holes with spatially separated wave functions will contribute less to the radiative recombination. Thus, tremendous efforts have been devoted to improving the carrier distribution within the quantum wells [12-14, 29-34]. The details of those approaches are discussed subsequently.

Along with the radiative recombination within the multiple quantum wells, InGaN/GaN LEDs suffer from nonradiative recombinations, such as those related to Auger recombination [18] and SRH recombination [18, 19]. Thus, a significant carrier loss has been caused. The influences of Auger recombination and SRH recombination on InGaN/GaN LEDs have been extensively studied [35-37].

Auger recombination occurs when the electron-hole interband recombination transfers the excess energy to other electrons or holes rather than emitting photons, and as a result, those electrons or holes are excited to a higher energy level once obtaining the energy. Auger recombination rate can be expressed as $R_{Auger} = C \cdot n^3$, where C is Auger recombination coefficient while n represents

the carrier concentration. It is worth mentioning that Auger recombination coefficient decreases with increased energy band gap, and thus, it is negligible in GaN materials. However, Auger recombination cannot be neglected under high current injection level, since Auger recombination rate is proportional to n^3. So far, there are still discrepancies of the Auger recombination coefficient for nitrides. Meneghini et al. reported 1×10^{-30} cm^6/s [19], which was extracted by optical power and impedance measurement for a 450 nm packaged LED. Zhang et al. determined the Auger recombination coefficient to be 1.5×10^{-30} cm^6/s for $In_{0.10}Ga_{0.90}N/GaN$ quantum well [38], while a value of 3.5×10^{-31} cm^6/s was reported by Laubsch et al. for a 525 nm single quantum well InGaN/GaN light-emitting diode [39]. Meanwhile, a much smaller Auger recombination coefficient of 3.5×10^{-34} cm^6/s has been reported theoretically by Hader et al. [40], which implied Auger recombination can be negligible in InGaN/GaN MQWs LEDs. In this work, to reproduce the experimental results by correlating the relationship between the efficiency droop and the Auger recombination, we have performed all the numerical calculations by assuming an Auger recombination coefficient of 1×10^{-30} cm^6/s.

The carrier loss due to the recombination at crystal-defects is modelled by SRH recombination process, i.e., $R_{SRH} = A \cdot n$, where A is the SRH recombination coefficient. However, arguments whether SRH recombination takes accounts for efficiency droop for InGaN/GaN LEDs have never ended [35, 37, 41]. It is reported by Schubert et al. that the dislocation-induced carrier loss only affects the maximum quantum efficiency while not influencing the efficiency droop [37]. Nevertheless, SRH recombination may possibly lead to the efficiency droop provided that the SRH recombination lifetime reduces with

increasing current. Furthermore, the SRH recombination coefficient is likely to vary among samples with different dislocation density. Yet, in this work, we have assumed a constant SRH recombination lifetime of 43 ns for InGaN/GaN quantum wells according to the report of Meneghini et al. [19].

2.2 Polarization induced electric fields in InGaN/GaN light-emitting diodes

InGaN/GaN LEDs that are grown along *polar*-orientations (i.e., c^+/c^- orientations) exhibit very strong polarization effect [20, 42]. As a result, the polarization charges will be induced at the interface of the two materials, which generate very strong polarization-induced electric fields in the III-nitrides of *polar*-orientations. Thus, the polarization effect has a strong impact on the III-nitride LEDs both optically and electrically.

On one hand, there exists spontaneous polarization (P_{sp}) that occurs due to the asymmetry of the wurtzite crystal structure. The crystal structure of a III-nitride compound is shown in Figs. 2.2.1(a), 2.2.1(b) and 2.2.1(c) [43]. Fig. 2.1.1(a) shows the prime unit cell of the hexagonal III-nitride crystal structure. The ***a*** lattice constants for AlN, GaN and InN are 0.3112, 0.31892 and 0.353 nm, respectively, while the ***c*** lattice constants for AlN, GaN and InN are 0.4982, 0.5185 and 0.554 nm, respectively [24]. The lattice constants for AlGaN and InGaN ternary compounds can be obtained by linearly combining the lattice constants of AlN and GaN; and InN and GaN, respectively. Figs. 2.2.1(b) and 2.2.1(c) depict the atom layout for both c^+ and c^- orientations, respectively, which show the asymmetric atom arrangement along the *polar*-orientations. Such that, the bonds connecting the most neighboring atoms are not equivalent,

and some of the bonds show more/less ionic nature if compared to others. More specifically, there is no coincidence between the geometric center of the negative charged atoms and the positive charged atoms, and therefore the spontaneous polarization effect is seen from such low-symmetry hexagonal III-nitrides.

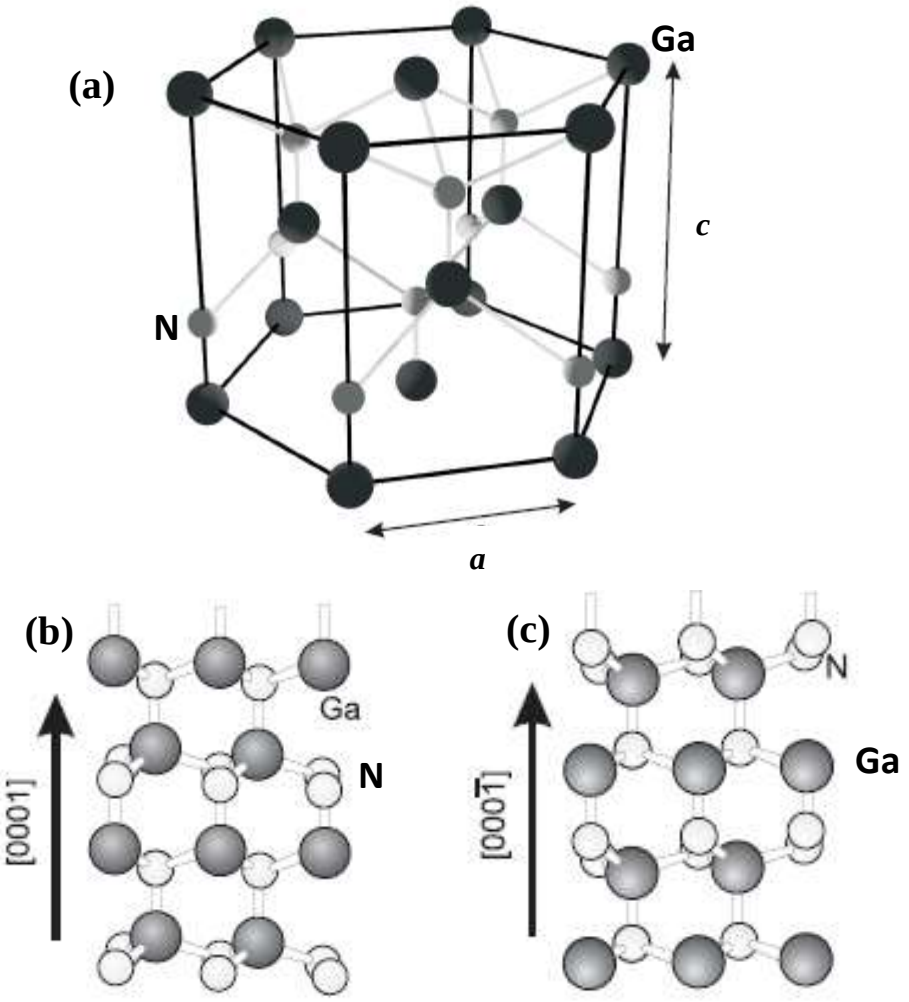

FIG. 2.2.1 (a) Crystal structure of one unit cell for hexagonal III-nitrides, e.g., GaN, (b) atom arrangement for c^+ oriented III-nitrides and (c) atom arrangement for c^- oriented III-nitrides. After [43].

Besides the spontaneous polarization, III-nitrides grown along *polar*-orientations also have a piezoelectric polarization (P_{pz}), which is induced by the

strain within the epitaxial films grown on a lattice mismatched substrate. The strain in the epitaxial films can be either in-plane compressive or tensile depending on the relative lattice constants of the two materials. The schematic diagram of spontaneous and piezoelectric polarization generation is presented in Figs. 2.2.2(a), 2.2.2(b), 2.2.2(c) and 2.2.2(d), respectively. Fig. 2.2.2(a) shows in-plane compressive strain for $In_xGa_{1-x}N$ layer on GaN substrate of c^+ orientation. The in-plane compressive strain in $In_xGa_{1-x}N$ layer is attributed to its larger lattice constant than that of GaN. Meanwhile, the polarization charges are generated in the $In_xGa_{1-x}N$/GaN interface as indicated in Fig. 2.2.2(a). According to Fig. 2.2.2(a), the direction of P_{sp} is oriented from the top surface to the substrate while P_{pz} is directed from the substrate to the top surface. However, if the epitaxial film is along c^- orientation, then P_{pz} is oriented from the top surface to the substrate while P_{sp} is directed from the substrate to the top surface, as suggested in Fig. 2.2.2(b). As has been mentioned previously, the in-plane tensile strain will be generated when the lattice constant of the top material is smaller than that of the substrate material, e.g., $Al_xGa_{1-x}N$ layer grown on GaN substrate [see Figs. 2.2.2(c) and 2.2.2(d)]. For a c^+ oriented film, such as those in Fig. 2.2.2(c), both P_{sp} and P_{pz} are directed from the top surface to the substrate. However, the directions of P_{sp} and P_{pz} will be aligned oppositely for c^- oriented films [e.g., Fig. 2.2.2(d)]. Nevertheless, the net polarization charge density is expressed as $div\ \vec{P}^{total} = div\ (\vec{P}_{sp} + \vec{P}_{pz}) = -\sigma_{polarization}$ [24]. As a result, the sheet charge density is accordingly calculated by $n_s = \frac{\sigma_{polarization}}{e}$, where e is the unit electronic charge.

According to the work by Fiorentini *et al.* [20], the spontaneous polarization for $Al_xGa_{1-x}N$ and $In_xGa_{1-x}N$ ternary compounds can be depicted in Eqs. (2.2.1) and (2.2.2), respectively, in C/cm^2.

$$P^{sp}_{Al_xGa_{1-x}N} = -0.090 \cdot x - 0.034 \cdot (1-x) + 0.019 \cdot x \cdot (1-x) \quad (2.2.1)$$

$$P^{sp}_{In_xGa_{1-x}N} = -0.042 \cdot x - 0.034 \cdot (1-x) + 0.038 \cdot x \cdot (1-x) \quad (2.2.2)$$

where, the first two numerical terms in Eqs. (2.2.1) and (2.2.2) represent the linear interpolation of the spontaneous polarization between the corresponding binary nitride compounds, while the third terms show the bowing factors. In addition, the piezoelectric polarization follows Vegard's law, such that the $P^{pz}_{X_xY_{1-x}N} = x \cdot P^{pz}_{XN} \cdot [\varepsilon(x)] + (1-x) \cdot P^{pz}_{YN} \cdot [\varepsilon(x)]$ for $X_xY_{1-x}N$ ternary compounds. Thus, we have to obtain the piezoelectric polarizations for AlN, GaN and InN, respectively, which are shown in Eq. (2.2.3).

$$\begin{aligned} P^{pz}_{AlN} &= -1.808 \cdot [\varepsilon(x)] + 5.624 \cdot [\varepsilon(x)]^2 \quad \text{for } \varepsilon(x) < 0 \\ P^{pz}_{AlN} &= -1.808 \cdot [\varepsilon(x)] - 7.888 \cdot [\varepsilon(x)]^2 \quad \text{for } \varepsilon(x) > 0 \\ P^{pz}_{GaN} &= -0.918 \cdot [\varepsilon(x)] + 9.541 \cdot [\varepsilon(x)]^2 \\ P^{pz}_{InN} &= -1.373 \cdot [\varepsilon(x)] + 7.559 \cdot [\varepsilon(x)]^2 \end{aligned} \quad (2.2.3)$$

where $\varepsilon(x)$ denotes the in-plane basal strain as shown in Eq. (2.2.4).

$$\varepsilon(x) = [a_{sub} - a(x)] / a(x) \quad (2.2.4)$$

in which, a_{sub} and $a(x)$ are the lattice constants for the substrate and the unstrained ternary compounds with the alloy composition of x. $a(x)$ for $Al_xGa_{1-x}N$ and $In_xGa_{1-x}N$ alloys can be demonstrated by Eq. (2.2.5).

$$\begin{aligned} a_{Al_xGa_{1-x}N}(x) &= 0.31986 - 0.00891 \cdot x \\ a_{In_xGa_{1-x}N}(x) &= 0.31986 + 0.03862 \cdot x \end{aligned} \quad (2.2.5)$$

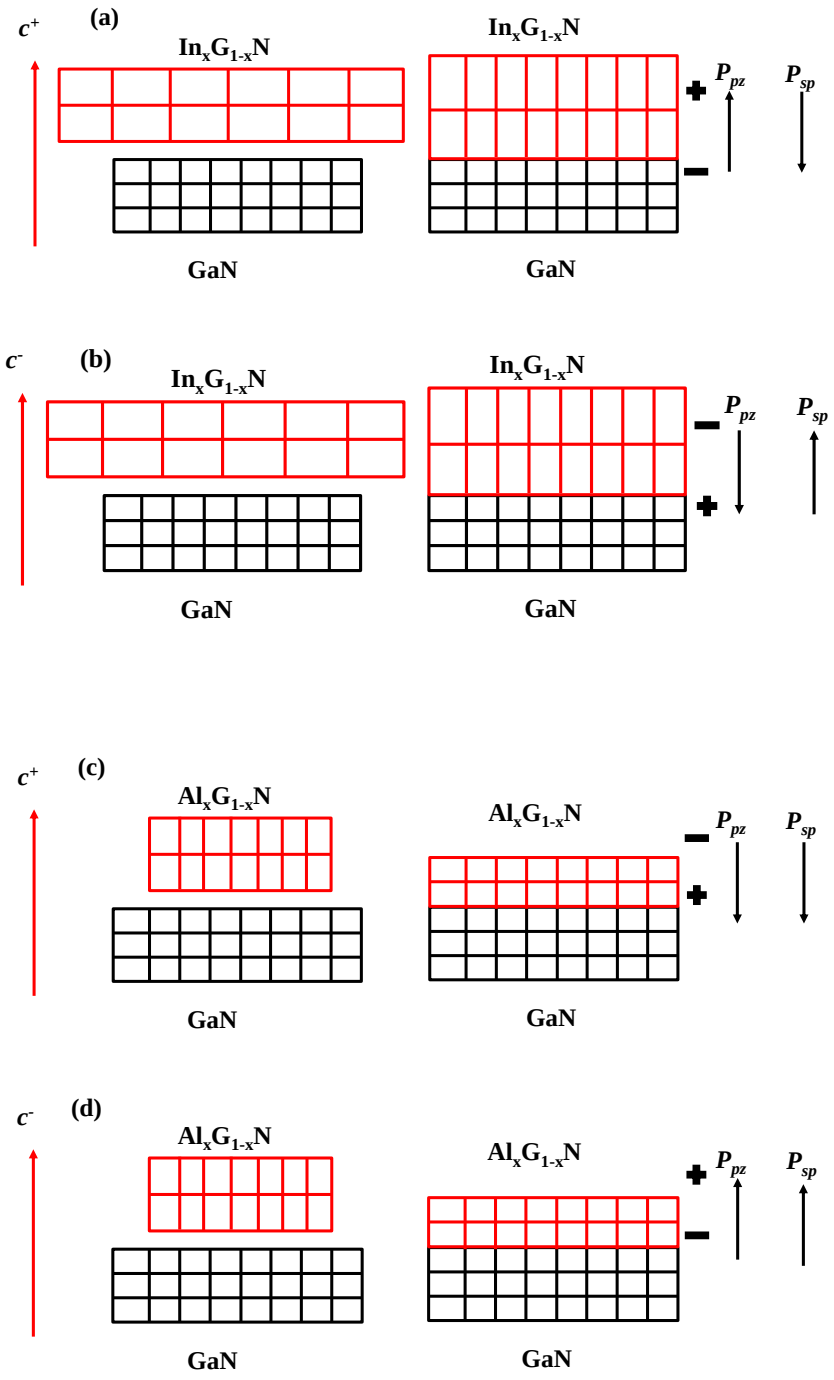

FIG. 2.2.2 Surface charges and directions of spontaneous and piezoelectric polarizations for (a) compressive strained $In_xGa_{1-x}N$ layer on GaN template of c^+ orientation, (b) compressive strained $In_xGa_{1-x}N$ layer on GaN template of c^- orientation, (c) tensile strained $Al_xGa_{1-x}N$ layer on GaN template of c^+ orientation, and (d) tensile strained $Al_xGa_{1-x}N$ layer on GaN template of c^- orientation.

As has been discussed previously, the spatial overlapping between the electron and hole wave functions determines the radiative recombination rates in InGaN/GaN MQWs. However, the spatial distribution of carrier wave functions is very sensitive to the polarization induced electric field for *polar*-oriented InGaN/GaN MQWs [28, 30, 31]. The schematic diagrams for carrier wave functions for InGaN/GaN MQWs with and without polarization effects are shown in Figs. 2.2.3(a) and 2.2.3(b), respectively [30]. As suggested in Fig. 2.2.3(a), the electron wave functions completely spatially overlap the hole wave function for a polarization effect free InGaN/GaN quantum well. However, we can see a spatial separation for carrier wave functions in Fig. 2.2.3(b) and this causes a reduced radiative recombination efficiency, i.e., quantum confined Stark effect (QCSE), which is due to the strong polarization-induced internal electric fields within the quantum well. The consequence of such spatial separation of carrier wave functions is the reduced radiative recombination rate, increased carrier lifetime and a significant blue shift of the emission wavelength with increasing excitation power. The blue shift of the wavelength is attributed to the screening effect to the QCSE by those injected carriers [30]. On the other hand, the band bending effect results in an effective band gap narrowing. Thus, for InGaN/GaN LEDs grown along c^+ orientation, it is necessary to reduce the quantum well thickness so as to increase the spatial overlapping of electron-hole wave functions. Meanwhile, the conduction band barrier height is reduced owing to the polarization field induced band bending, and as a result, the carrier injection efficiency has been substantially reduced [44-46].

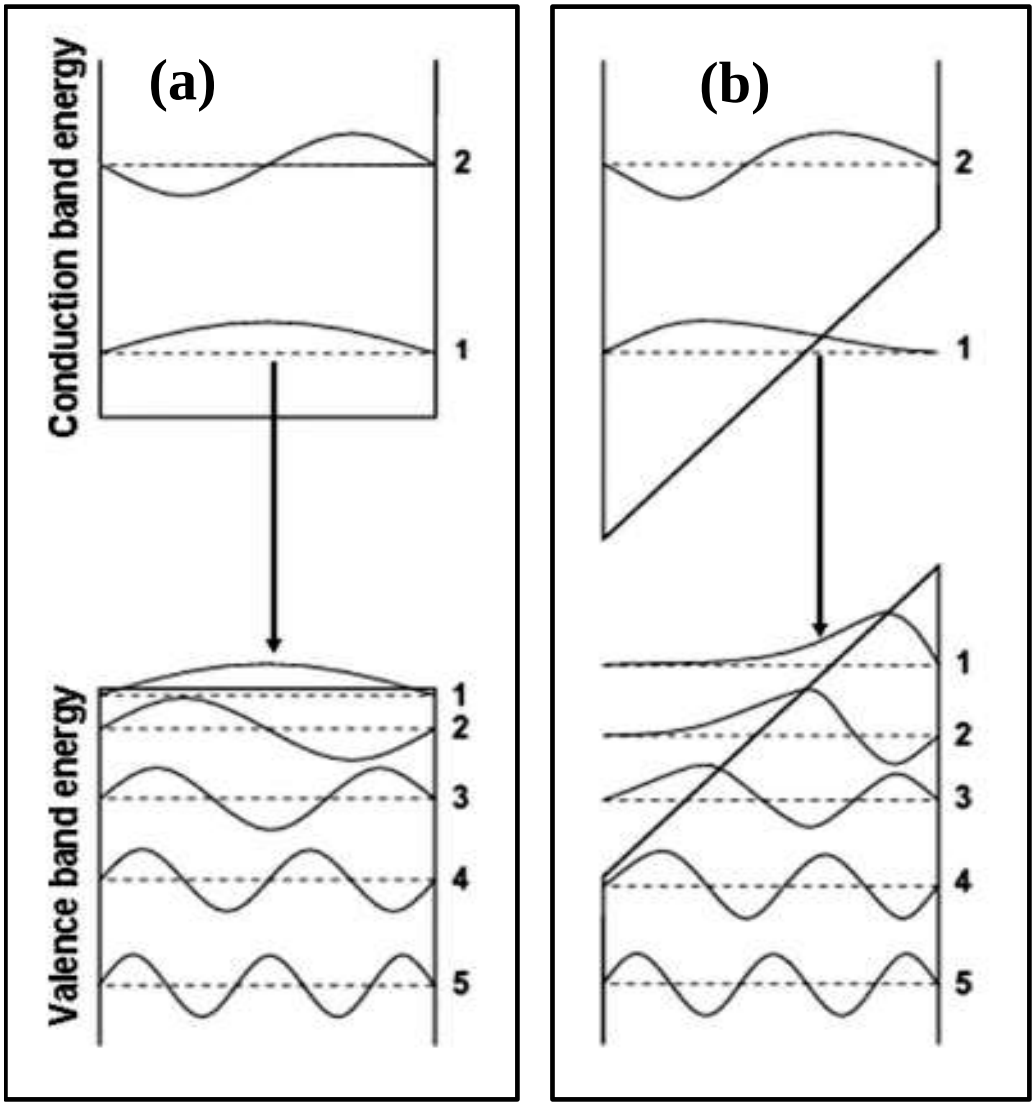

FIG. 2.2.3 Energy bands and carrier wave functions for (a) InGaN/GaN quantum well with no polarization effect, and (b) InGaN/GaN quantum well with polarization effect. After [30].

Nevertheless, the polarization level and the interband transition probability of carriers, as suggested in Figs. 2.2.4(a), 2.2.4(b) and 2.2.4(c), strongly depend on the growth orientations according to the work of Takeuchi et al. [47]. From Figs. 2.2.4(a), 2.2.4(b) and 2.2.4(c), we can see the polarization field is reduced to zero when $\theta = 90^{o}$. It is also zero when $\theta \sim 40^{o}$, and correspondingly, the highest interband transition probability is obtained. Note that the epi-layers of

$(10\bar{1}0)$ and $(11\bar{2}0)$ are not affected by the polarization fields due to the fact that the polarizations are within the growth basal planes, while some semi-polar epi-layers such as those grown on $(11\bar{2}4)$ crystal planes are also polarization-free, and this is attributed to the geometrical coincidence of the ionic centers for the positive charged atoms (e.g., Ga, Al or In) and the negative charged atoms (e.g., N). Meanwhile, the interband transition energy is also larger than that for (0001) plane quantum wells. However, the strongest polarization field, the lowest interband transition probability and the smallest interband transition energy occur at $\theta = 0^{o}$, i.e., a (0001) plane. The reduced interband transition energy is due to the band gap narrowing effect caused by the polarization electric field induced band bending [30]. As depicted in Figs. 2.2.4(a), 2.2.4(b) and 2.2.4(c), epitaxial films completely/partially lacking polarization effect can be obtained from *non-polar/semi-polar* basal planes, and thus significant efforts have been made to investigate InGaN/GaN light-emitting diodes of *m*-plane with Miller index of $(10\bar{1}0)$, of *a*-plane with Miller index of $(11\bar{2}0)$ and of r-planes with Miller indexes of $(10\bar{1}2)$ and $(11\bar{2}4)$ [33, 34, 48-53]. However, more details regarding the dependence of the polarization induced electric field on the inclination angles between different growth orientations and [0001] orientation can be found elsewhere [54].

(a)

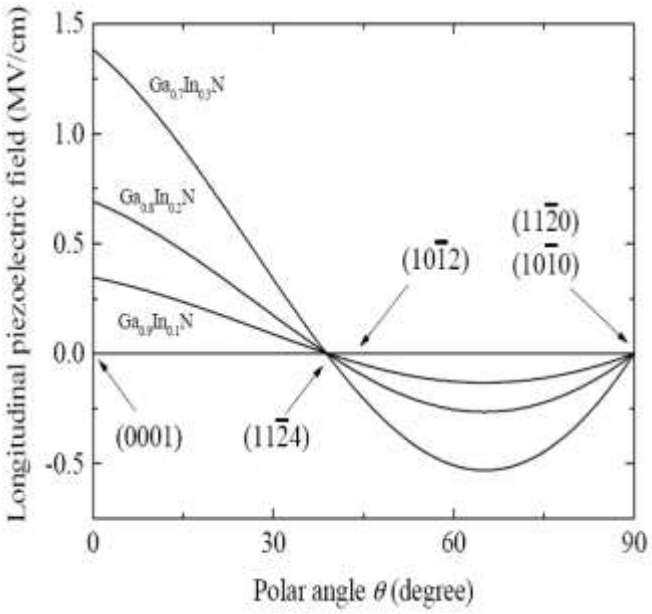
Longitudinal piezoelectric field (MV/cm)
1.5
1.0
0.5
0.0
-0.5
0
30
60
90
Polar angle θ (degree)
Ga0.7In0.3N
Ga0.8In0.2N
Ga0.9In0.1N
(0001)
(11$\bar{2}$4)
(10$\bar{1}$2)
(11$\bar{2}$0)
(10$\bar{1}$0)

(b)

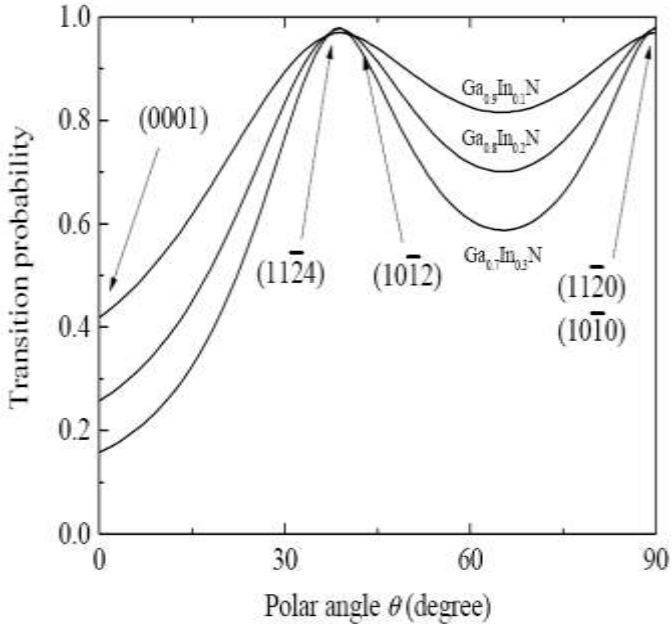
Transition probability
1.0
0.8
0.6
0.4
0.2
0.0
0
30
60
90
Polar angle θ (degree)
(0001)
(11$\bar{2}$4)
(10$\bar{1}$2)
(11$\bar{2}$0)
(10$\bar{1}$0)
Ga0.5In0.5N
Ga0.8In0.2N
Ga0.7In0.3N

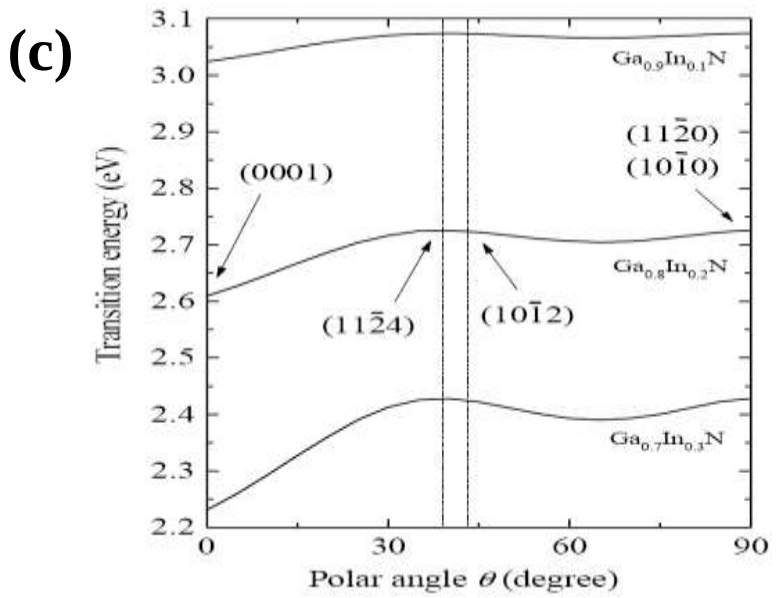

FIG. 2.2.4 Polar angle (θ) dependence of (a) piezoelectric field, (b) interband transition probability and (c) interband transition energy. The polar angle θ is referenced to (0001) plane (i.e., $\theta = 0^{o}$). After [47].

2.3 Challenges for InGaN/GaN light-emitting diodes along c^{+} orientation and objectives of this work

Although *non-polar/semi-polar* InGaN/GaN LEDs have shown quite promising material performances, yet to date, most of the market share of the LED based lighting, display back lighting and other LED applications are still based on InGaN/GaN multiple-quantum-well LEDs grown along [0001] orientation due to the mature epi-technology and the low-cost substrates [12-14]. Thus, there have been significant studies on c^{+} InGaN/GaN LEDs to improve the device performance both electrically and optically. So far, the quantum efficiency of the InGaN/GaN LEDs along c^{+} orientation is limited by charge separation [28-30, 55, 56], significant current crowding effect underneath the p-contact [21, 28, 57-61], low hole concentration in the p-GaN

layer [62, 63], hole retardation in transport into the multiple quantum wells [28, 56, 64, 65] and electron overflow from the active region [44, 46, 66-68].

Hence, the objective of this work is to address the above mentioned issues through optimizing the epitaxial film quality by metal-organic chemical vapor deposition (MOCVD) system and designing novel InGaN/GaN LED architectures. It is well-known that an improved crystal quality reduces the dislocation density of the epitaxial films, thus suppressing the defect-related SRH recombination rates. Meanwhile, by designing novel epitaxial InGaN/GaN LED devices, Auger recombination, charge separation within the InGaN/GaN MQWs, current crowding and electron overflow can be suppressed. In addition, the hole injection efficiency and the enhanced hole concentration in the p-type materials can also be obtained. Hence, the epitaxial growth and the novel device design are closely correlated with each other for high-performance solid-state lighting applications.

Chapter 3 Introduction to epitaxial growth and device fabrication of InGaN/GaN light-emitting diodes

III-nitride compound semiconductors have been an important member in the family of optoelectronic devices. The emission wavelength of III-nitride semiconductors covers from the violet to the infra-red spectrum. Nowadays, InGaN/GaN light-emitting diodes (LEDs) have occupied a big market share in lighting, and therefore, tremendous efforts have been devoted to the high-brightness white light-emitting diodes based on InGaN/GaN multiple quantum well (MQW) structures. On one hand, the InGaN/GaN LEDs are environmentally friendly due to their high device efficiency. Compared to those conventional fluorescent and incandescent light bulbs, less heat is generated. On the other hand, the long lifetime of the LED chip makes it an excellent candidate in those applications such as aviation, communication, flat-panel displays, *etc.* So far, most of the InGaN/GaN LED wafers are grown by advanced metal-organic chemical vapor deposition (MOCVD) systems, by means of which the crystal quality can be controlled and the layer information can be precisely monitored. More importantly, the LED architectures with custom designs can be excellently achieved by doing MOCVD growth.

In this chapter, a brief introduction to the MOCVD system will be given. Subsequently, the crystal growth procedure and the layer information of typical InGaN/GaN LEDs for the nucleation layer, the n-type GaN layer and so on are discussed. The LED devices are fabricated from the epitaxial wafers grown by MOCVD. The details the fabrication process will also be presented in this chapter.

3.1 Introduction to AIXTRON MOCVD system

III-nitride based LEDs for this work were grown by the advanced close-coupled showerhead (CCS) metal-organic chemical vapor deposition (MOCVD) system, as shown in Fig. 3.1.1. The growth of epitaxial III-nitride wafers is achieved through Group III and Group V sources. Group V sources (NH_3) and n-type dopant source (SiH_4) are carried through the hydride line while Group III sources (TMGa, TEGa, TMIn, TMAl and Cp_2Mg) are carried through the alkyl line. Those precursors are either carried into the reactor chamber through the run lines or to the exhaust through the vent lines. The carrier gas used is H_2 and N_2. The chart that depicts the gas lines are elucidated in Fig. 3.1.2 [69], where A is the N_2 purifier, B is the H_2 purifier, C is the NH_3 purifier, D is the hygrometer, E is the hydride source channel, F is the MO source channel, G is the MO bubbler, H is the gas supply for hydride sources, I is the gas supply for run lines. J is the hydride run line, K is the hydride vent line, L is the gas supply for auxiliary gas pipes, M is the purging-reactor sight glass, N is the MO1 run line, O is the MO1 vent line, P is the MO2 run bypass, Q is the MO2 run line, R is the MO2 run bypass, S is the gas supply for venting, T is the gas supply for MO2 sources, U is the gas supply for MO1 sources and V is the MO vacuum (for changing the MO bubbler).

FIG. 3.1.1 Image of our 3 × 2″ AIXTRON CCS MOCVD system.

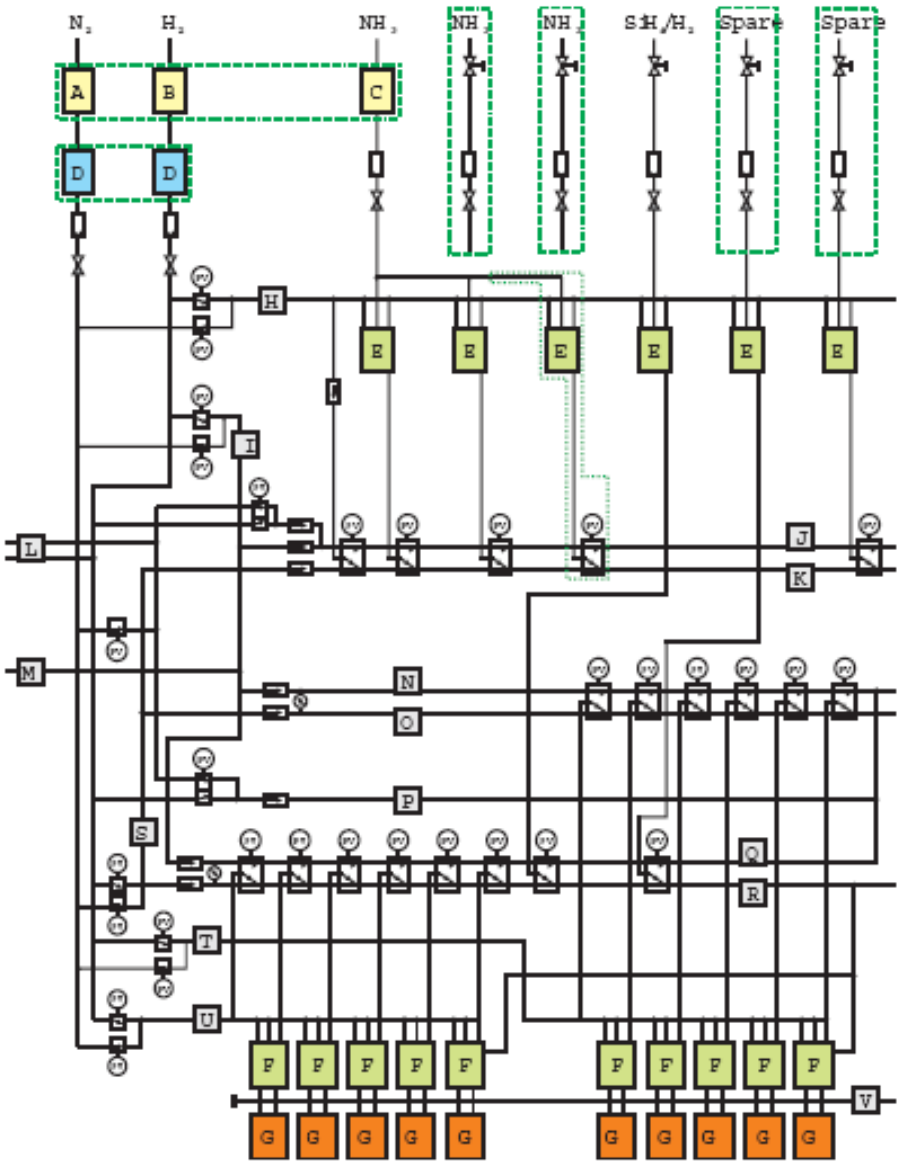

FIG. 3.1.2 Chart of gas lines in the 3 × 2″ AIXTRON CCS MOCVD system. After [69].

The MO sources are kept in the MO bubblers. The gas layouts for MO bubblers are shown in Figs. 3.1.3(a) and 3.1.3(b) [69]. We have two types of gas layouts for our MOCVD system. A standard MO source, e.g. TMGa, TMIn and Cp_2Mg, is depicted in Fig. 3.1.3(a), which consists of two mass flow controllers (MFCs, D and E) and one pressure controller (C). D is the input MFC and E is the push MFC. C controls the bubbler pressure. The carrier gas (either N_2 or H_2) is injected into the MO bubbler through A lines, while 4/2

pneumatic valve (G) manipulates if the carrier gas goes through the MO bubbler to carry out the MO source or bypass the MO bubbler. However, if the MO flow rate is to be precisely controlled, e.g., TEGa, then one has to use the MO bubbler with double dilution, as is shown in Fig. 3.1.3(b). The majority layout of Fig. 3.1.3(b) is identical to that of Fig. 3.1.3(a) except the additional inject MFC (F). Thus, the effective MO flow rate can be calculated by Eq. (3.1.1) provided that all MFCs are within the control range.

(a)

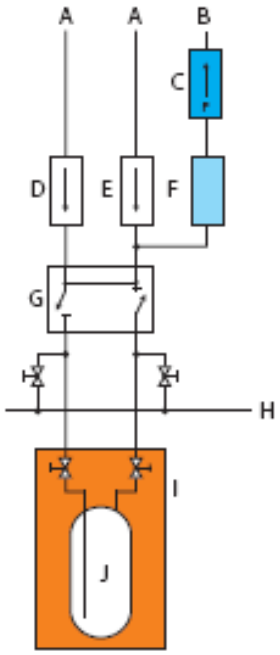

A is the carrier gas supply, B is the run/vent line, C is the pressure controller, D is the source mass flow controller (MFC) with the flow rate of F_{source}, E is the push MFC with the flow rate of F_{push}, F is used to measure gas concentrations (optional in our MOCVD system), G is a 4/2 pneumatic valve (controlled by 24V power controlling), H is the MO vacuum, I is the thermal heat bath to hold MO bubblers while J is the MO bubbler.

(b)

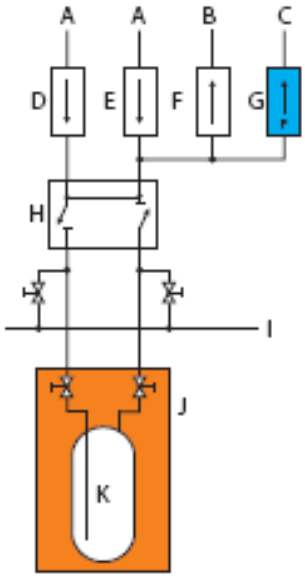

A is the carrier gas supply, B is the run/vent line, C is the pressure controller, D is the source input MFC with the flow rate of F_{source}, E is the dilution MFC with the flow rate of F_{dilute}, F is the inject (output) MFC with the flow rate of F_{inject}, G is the pressure controller, H is a 4/2 pneumatic valve (controlled by 24V power controlling), I is the MO vacuum, J is the thermal heat bath to hold MO bubblers while K is the MO bubbler.

FIG. 3.1.3 Gas lines for (a) a standard MO source and (b) for an MO source with double dilution. After [69].

$$F = F_{inject} \times \frac{F_{source}}{F_{source} + F_{dilute}} \tag{3.1.1}$$

Here, F is effective flow rate of the precursors, F_{source} denotes the flow rate through the source MFC, F_{dilute} is the flow rate through the dilute MFC and F_{inject} is the flow rate through the inject MFC. Thus, one can precisely tune the MO flow rate for the reaction process through the combination of F_{source}, F_{dilute} and F_{inject}.

Figures 3.1.4(a) and 3.1.4(b) show the gas lines for a hydride source [69]. The standard gas line for the hydride is shown in Fig. 3.1.4(a), i.e., for NH_3 in our MOCVD system, in which A is the gas supply, B is the hydride gas supply, C is a 3/2-way pneumatic valve to control whether the hydride gas will be supplied (i.e., carrier gas off/hydride gas on, and carrier gas on/hydride gas off), D is the source MFC, E is the pusher MFC, and F controls the hydride gas/carrier gas to the reactor or to the vent. Fig. 3.1.4(b) shows the gas lines for

the hydride (SiH_4 in our MOCVD system) with double dilution. All the configurations in Fig. 3.1.4(b) are identical to those in Fig. 3.1.4(a) except the additional two MFCs, i.e., the dilute MFC (E) and inject MFC (F). G is the 700 mbar check valve. The actual source flow rate into the reactor can be calculated by Eq. (3.1.1).

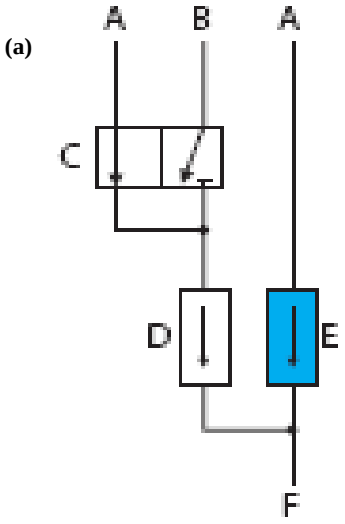

A is carrier gas supply, B is hydride gas supply, C is 3/2-way pneumatic valve (controlled by 24V power controlling), D is source MFC, E is pusher MFC, F is the hydride control to vent or run line.

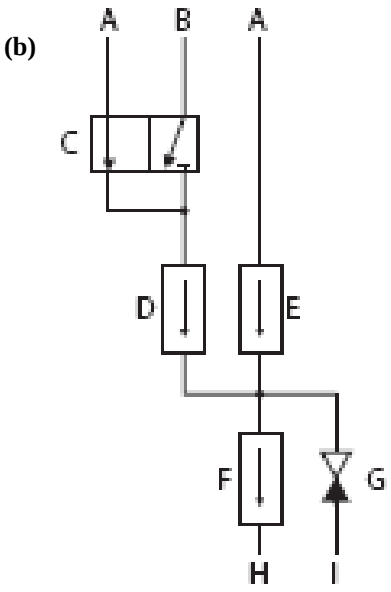

A is the carrier gas supply, B is the hydride gas supply, C is a 3/2-way pneumatic valve (controlled by 24V power controlling), D is the source MFC, E is the dilution MFC, F is the inject MFC, G is a 700 mbar check valve, H is the hydride control to vent/run line and I is to vent line.

FIG. 3.1.4 Gas lines for (a) a standard hydride source and (b) for hydride source with double dilution. After [69].

All the MO and hydride sources have to be injected into the MOCVD CCS-reactor for film growth. The MOCVD reactor is shown in Fig. 3.1.5 [69]. The temperature of the MOCVD reactor chamber is controlled by a thermocouple below the susceptor. The distance between the thermocouple and the susceptor is 1 mm. The susceptor is supported by a susceptor support, and the susceptor is a graphite disk coated with ~ 100 μm SiC layer, on which the processed wafers are placed. The processed wafers (GaN based) are heated by a tungsten heater, and the maximum temperature is 1200 ^{o}C. There are three heating zones in the heater as demonstrated in Fig. 3.1.6 [69], i.e., zone A, zone B and zone C. The temperature settings for the three heating zones are adjustable to achieve a uniform epitaxial film. As mentioned, MO and hydride sources are injected into the reactor through the showerhead. The detailed information of the showerhead is shown in Figs. 3.1.7(a) and 3.1.7(b) [69]. Our showerhead has many tiny tubes with a density of 100 tubes/inch^2 and a tube diameter of 0.6 mm, as can be shown in Fig. 3.1.7(a). Besides, it is noteworthy that the spacing between the showerhead and the susceptor for GaN system is 11 mm. In general, there are two plenums in the showerhead for hydride and MO sources, respectively as shown in Fig. 3.1.7(b). The showerhead is cooled down by a showerhead water cooling system (50 ^{o}C). The showerhead is sealed by double O-rings. The epitaxial wafers are *in-situ* monitored through the interferometer mounted on the reactor lid.

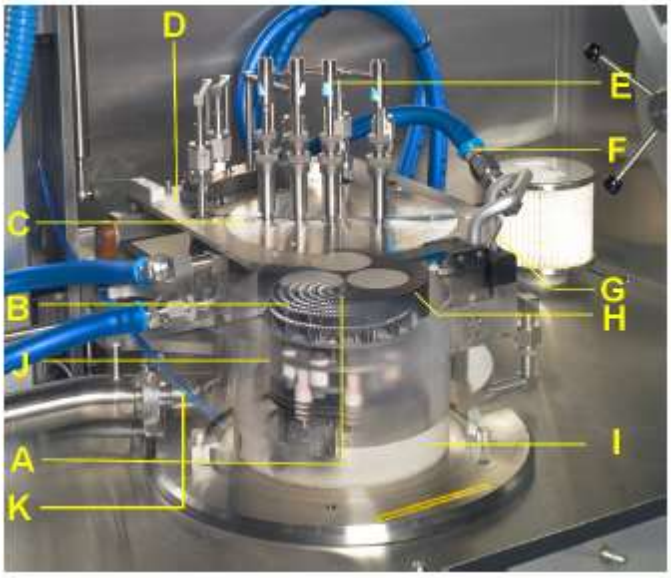

FIG. 3.1.5 Image of MOCVD reactor. A is the thermocouple, B is the tungsten heater, C is the showerhead, D is the reactor lid, E is the optical probe, F is the showerhead water cooling, G is the double O-ring seal, H is the susceptor, I is the susceptor support, J is the quart liner (also called J liner) and K is the exhaust. After [69].

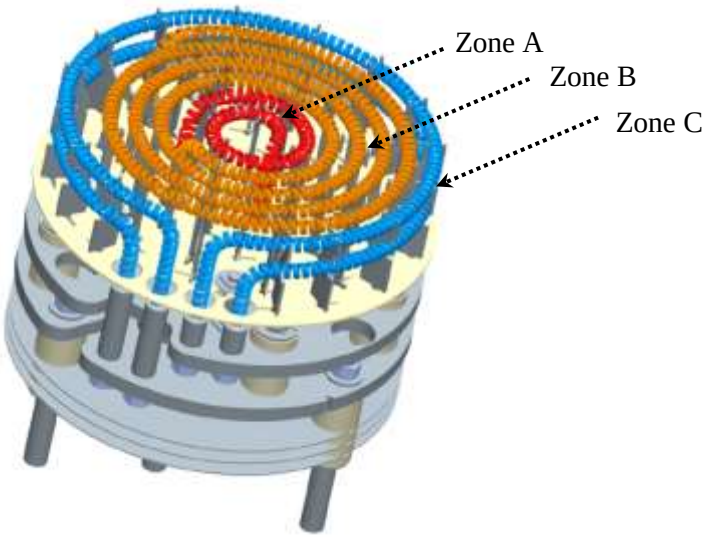

FIG. 3.1.6 Schematic diagram of the heater, in which zone A is in the center (red), zone B is in the middle (orange) and zone C in outside (blue). After [69].

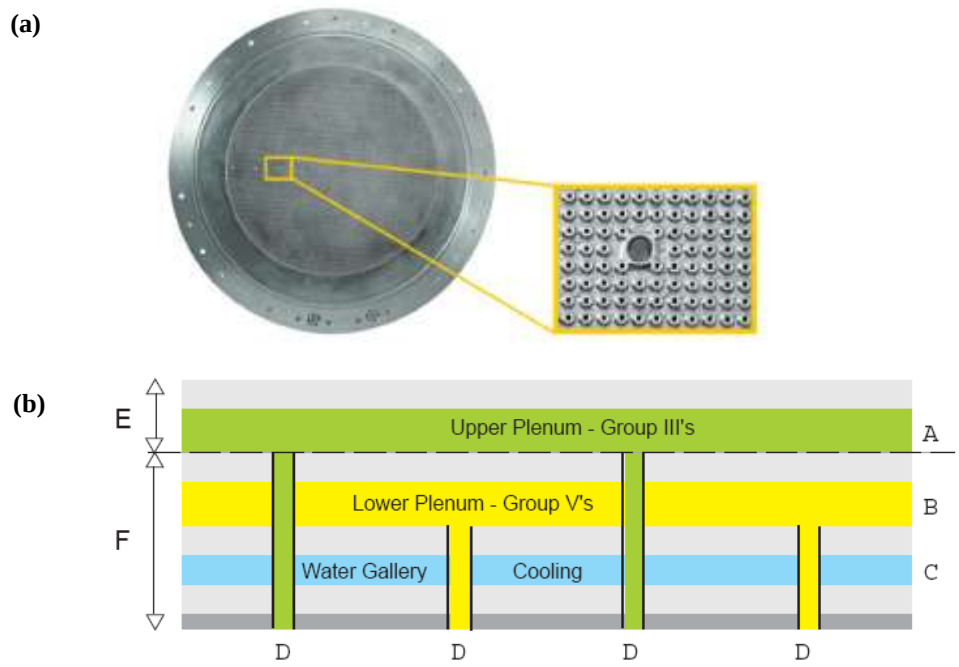

FIG. 3.1.7 (a) Images for CCS-showerhead, and (b) schematic diagram of the two plenums in showerhead. A is the upper plenum for MO sources, B is the lower plenum for hydride sources, C is the water cooling and Ds are the tubes. After [69].

Once the MO and hydride sources have been carried into the reactor, they are transported to the substrate surfaces, which is shown in Fig. 3.1.8 [43, 70]. During the transport, the MO and hydride sources are decomposed into different pyrolysis products under the high chamber temperature. And then the MO sources, hydride sources and the pyrolysis products are adsorbed onto the substrate surface and migrate to the growth sites to form epitaxial films by producing byproducts. The byproducts are carried out of the reactor through an exhaust line. The reaction process taking places for growing the III-nitride films in MOCVD growths is given in Eq. (3.1.2).

$$III-(CH)_x + V-H_x \rightarrow III-V + byproducts \qquad (3.1.2)$$

in which *III* represents the group-III elements (Ga, Al and In) and *V* denotes group-V element (N).

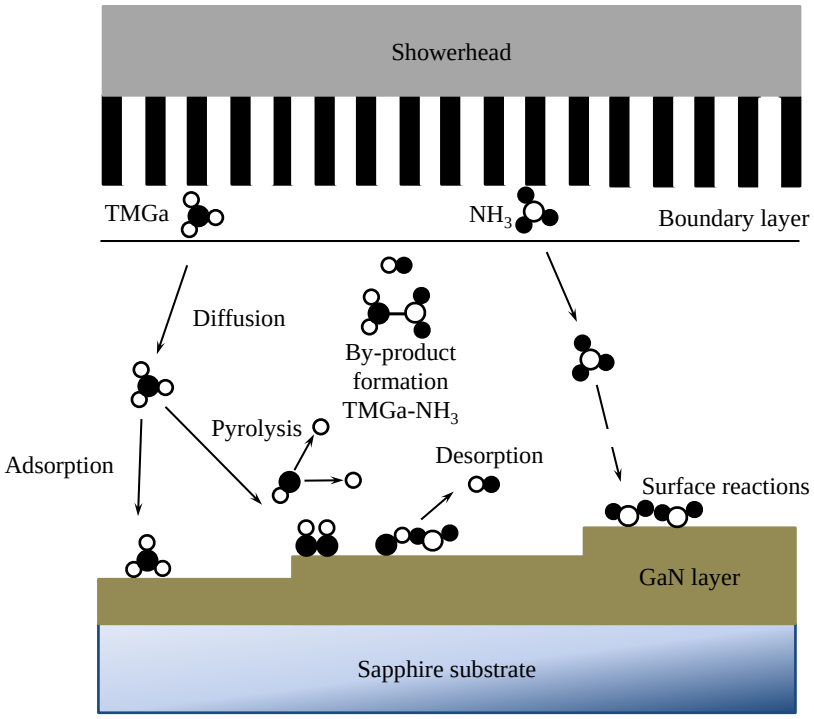

FIG. 3.1.8 Reaction process in MOCVD growth for III-V nitrides. After [43, 70].

The growth rate of the epitaxial layers is monitored by the *in-situ* interferometer (see Fig. 3.1.9). Furthermore, the interferometer can also provide the information of surface roughness and growth transition from layer to layer. The physical principle of the interference is depicted in Fig. 3.1.10 [71]. Once the light shines on the film, the light reflection takes places on both the air/film and film/substrate interfaces. Interference occurs between the two reflected beams. The light intensity after interference is expressed in Eq. (3.1.2).

$$R = \frac{r_1^2 + r_2^2 e^{-\alpha d} + 2 r_1 r_2 \cos\Delta e^{-\alpha d}}{1 + r_1^2 r_2^2 e^{-\alpha d} + 2 r_1 r_2 \cos\Delta e^{-\alpha d}} \tag{3.1.2}$$

$$r_1 = \frac{n_f - 1}{n_f + 1} \tag{3.1.3}$$

$$r_2 = \frac{n_s - n_f}{n_s + n_f} \tag{3.1.4}$$

Δ means periodicity (i.e., peak to peak) in the interference pattern, which will be shown and explained in section 3.3.1. r_1 and r_2 represent the Fresnel reflection coefficients for air/film and film/substrate, respectively, which are shown in Eq. (3.1.3) and (3.1.4). n_f and n_s are the film and substrate refractive indices, respectively. Thus, in order to have a constructive interference, the relationship between the optical path length and the wavelength is demonstrated in Eq. (3.1.5).

$$\frac{2n_f d}{\lambda} = N \tag{3.1.5}$$

Here, N is an integer. If we consider one periodicity (i.e., one peak to the next adjacent peak) in the interference pattern, then N is equal to one, and Eq. (3.1.5) can be changed to Eq. (3.1.6).

$$\frac{4\pi n_f d}{\lambda} = 2\pi = \Delta \tag{3.1.6}$$

in which d is the film thickness, and λ is the wavelength (635 nm used in our MOCVD system for measuring the growth rate and surface roughness).

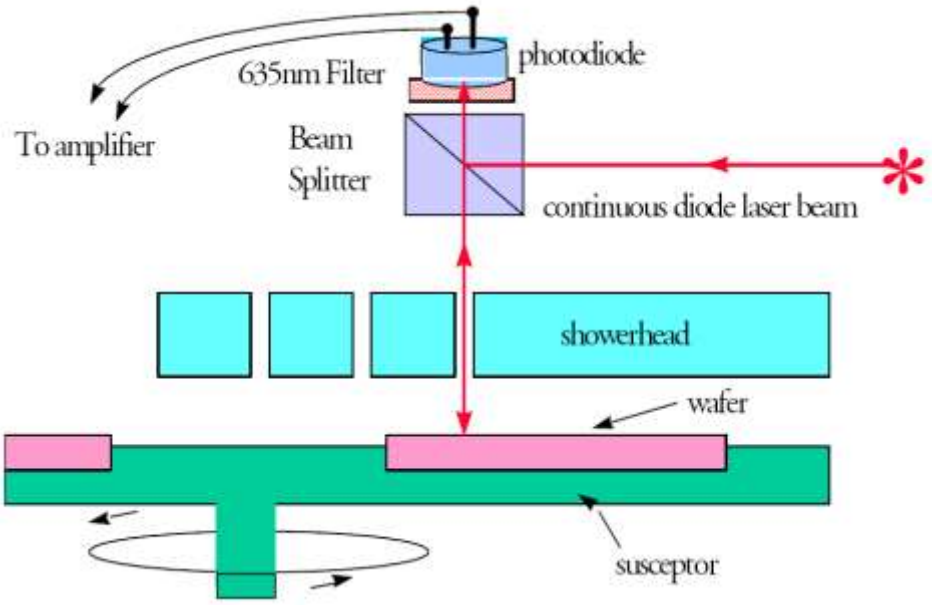

FIG. 3.1.9 Schematic diagram for the interferometer setup in AIXTRON MOCVD system. After [71].

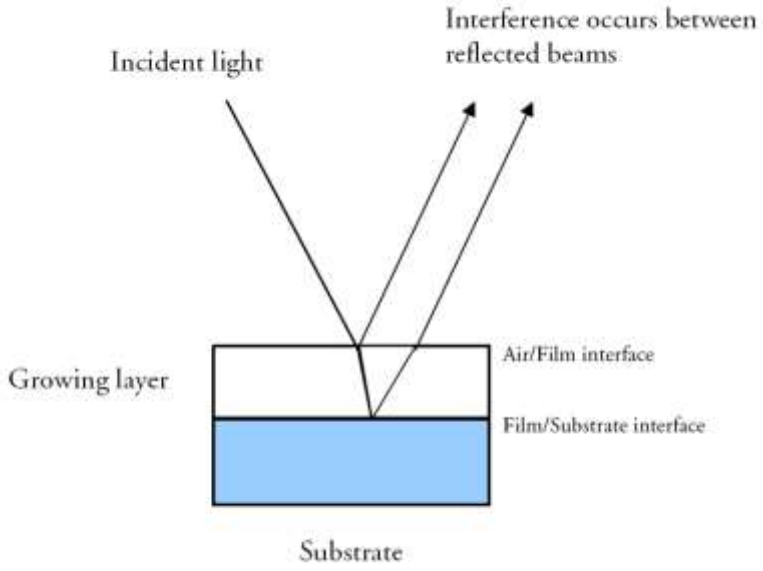

FIG. 3.1.10 Multiple reflection scheme for GaN films with air/film and film/substrate interferences. After [71].

3.2 Layer structure of the InGaN/GaN light-emitting diodes

To date, most of the InGaN/GaN LEDs available in the markets are grown on *c*-sapphire substrates along the [0001]-orientation. Fig. 3.2.1 shows the

typical layer structure of an InGaN/GaN LED. Normally, the epitaxial growth starts from a GaN nucleation layer. Then, a layer of unintentionally doped GaN (u-GaN) layer is grown on the nucleation layer for better crystal coalescence. The Si doped n-type GaN (n-GaN) layer is grown. This layer enables the electron injection during the device operation. After growing the n-GaN, the InGaN/GaN MQWs are grown, which is known as the light emission region, so-called the active region of the device. A p-type AlGaN electron blocking layer is then grown to prevent the electron overflow from the active region of the device. However, most of the holes are provided by the p-type GaN layer, which is grown on the top of the p-AlGaN electron blocking layer. The last layer is a heavily doped p-type GaN layer (p^+-GaN), and this layer is grown for making an Ohmic contact of the device.

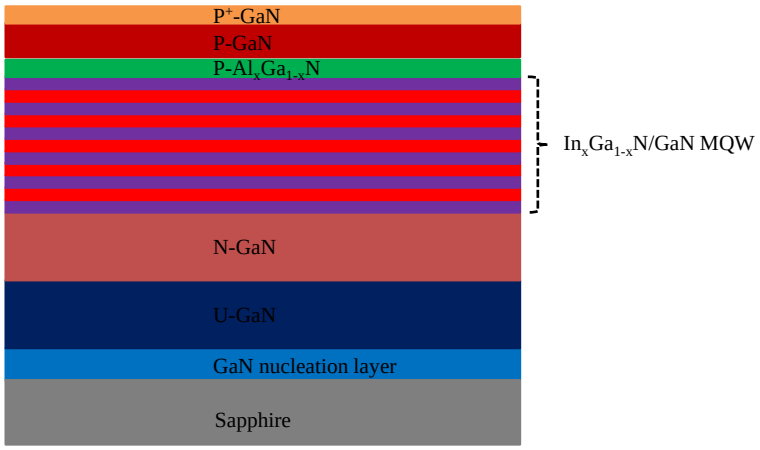

FIG. 3.2.1 Schematic diagram of a typical InGaN/GaN light-emitting diode layer structure.

3.3 Growth of InGaN/GaN light-emitting diode wafers in MOCVD

As mentioned previously, the growth of InGaN/GaN LEDs is initiated on *c*-sapphire substrates. First, the thermal annealing of the sapphire substrate is conducted in H_2 ambient at a high temperature, after which the substrate

nitridation is performed by the flowing NH_3. The resulting AlN or AlO_xN_{1-x} is formed as the strain relaxation layer [72, 73], hence facilitating the formation of the following nucleation layer (e.g., GaN). It is reported that the crystal quality of GaN is significantly affected by the substrate nitridation, and a properly shorter nitridation time (i.e., 60s) is beneficial for reducing the edge threading dislocation and increasing the electron mobility [74].

After the nitridation process, a GaN nucleation layer is grown at a low temperature, typically from 550 to 600 ^oC, while the optimized nucleation layer thickness is between 20 to 25 nm [9, 75]. The as-deposited GaN nucleation layer on the sapphire substrate is amorphous. Thus the thermal annealing of the sample at an elevated temperature (e.g., 1050 ^oC) is normally conducted for the purpose of recrystallization [75]. During the recrystallization, the supply of TMGa source will be terminated, some of the amorphous GaN nucleation layer will be evaporated from the substrate because of the high temperature. Correspondingly, islands will be formed in the remaining GaN material. It is worth mentioning that, for GaN grown on sapphire substrates, there is a 30-degree angle of the hexagonal crystalline lattice between GaN and the underneath sapphire substrate. This is achieved by the crystal rotation of GaN during such recrystallization process. At this stage, GaN islands are formed on the sapphire substrates [76]. Those GaN islands provide the epitaxial growth sites for the subsequent GaN film, during which the three-dimension (3D) growth mode transits into the two-dimensional (2D) growth mode and the GaN film is formed. This is called the unintentionally doped n-type GaN (u-GaN). After the u-GaN, an n-type GaN layer is grown by injecting the diluted SiH_4 source. Then, the InGaN/GaN MQWs are grown with the TEGa and TMIn

serving as the precursors for the Ga and In sources, respectively. In order to facilitate the InN incorporation efficiency into the InGaN quantum wells, a lower growth temperature is desired (e.g., 746 ^{o}C). Meanwhile, the cracking efficiency of the NH_3 is low at the temperature below 1000 ^{o}C, and thus a higher V/III ratio is necessary [77].

A typical InGaN/GaN LED device needs the p-type AlGaN as the electron blocking layer. The growth of AlGaN is challenging because of the parasitic reaction between the TMAl and NH_3 in the vapor phase before they reach the surface of the sapphire substrates [78, 79]. In order to suppress the parasitic reaction, a low growth pressure (e.g., 100 mbar) and a low V/III ratio is preferable [78, 79]. Besides, a higher growth temperature typically of 1200 ^{o}C is helpful in obtaining the high-quality crystal. However, we grow the p-type AlGaN electron blocking layer after the InGaN/GaN MQWs at the growth temperature not be higher than 1000 ^{o}C in order to reduce the out-diffusion of the InN from the InGaN quantum wells,. To form a pn-junction, the p-type GaN layer has also to be grown after growing p-AlGaN layer. The growth temperature of the p-GaN is kept lower (e.g., 1000 ^{o}C). The last layer for the InGaN/GaN LED is the heavily p-type doped GaN layer working as the contact layer for the Ohmic p-electrode. Details of the growth and optimization procedures are to be demonstrated and discussed subsequently.

3.3.1 Different layer information from in-situ reflectance

The *in-situ* reflectance and temperature variation of the growth of the InGaN/GaN LED wafer is shown in Fig. 3.3.1. The atomic force microscopy (AFM) images for GaN film in different growth stages are shown in Fig. 3.3.2 [71]. As mentioned previously, the growth process of InGaN/GaN LED wafers

consists of the stages of low-temperature (low-T) GaN nucleation layer [9], the high-temperature (high-T) unintentionally doped GaN (u-GaN) layer, the n-GaN layer, the InGaN/GaN MQW region, the p-AlGaN and p-GaN layers. The low-T GaN nucleation layer [Fig. 3.3.2(a)] is deposited on the sapphire substrate after substrate nitridation, and hence the reflectance is increased as shown in Fig. 3.3.1. The thermal annealing is later conducted for recrystallization, which promotes the decomposition of the pre-deposited GaN nucleation layer, and the rough surface is correspondingly generated, therefore reducing the surface reflectivity. However, the thermal annealing is terminated when sapphire substrate is locally exposed and the discrete GaN islands are simultaneously formed as shown in Fig. 3.3.2(b). Once the TMGa precursor is supplied, the GaN islands grow larger as shown in Fig. 3.3.2(c), and meanwhile, the island coalescence takes place such that the growth mode transits from 3D to 2D mode as shown in Figs. 3.3.2(d) and 3.3.2(e), respectively. The surface reflectivity is also increased because of the reduced roughness. A completely flat GaN epitaxial film is achieved as shown in Fig. 3.3.2(f) indicating that the 3D growth mode has been completed and the 2D growth mode dominates [76]. As mentioned previously, in order to prevent the out-diffusion of the InN from the InGaN/GaN multiple quantum wells region, the p-AlGaN and p-GaN layers are grown at a reduced temperature as indicated in Fig. 3.3.1.

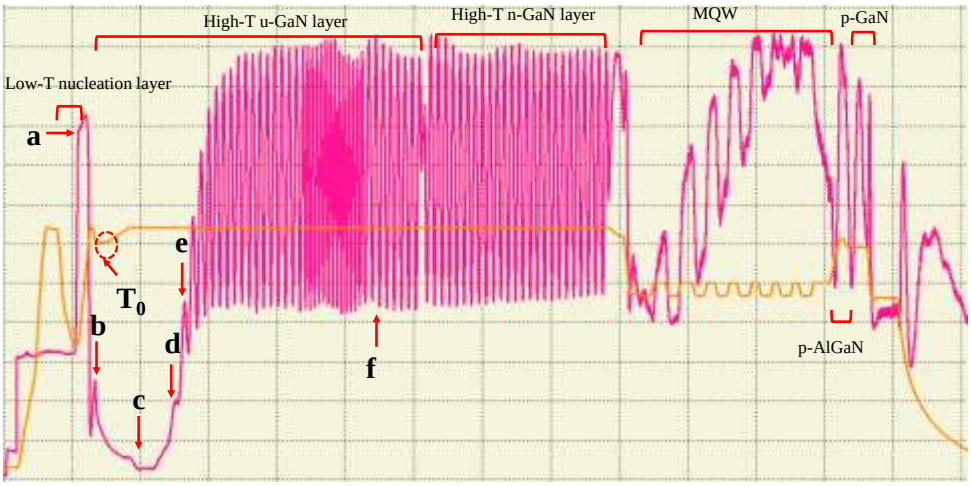

FIG. 3.3.1 *In-situ* reflectance and temperature variation of the InGaN/GaN LED growth process. Reflectance at stages of a. b. c. d, e and f correspond to the AFM images of Figs. 3.3.2(a), 3.3.2(b), 3.3.2(c), 3.3.2(d), 3.3.2(e) and 3.3.2(f), respectively.

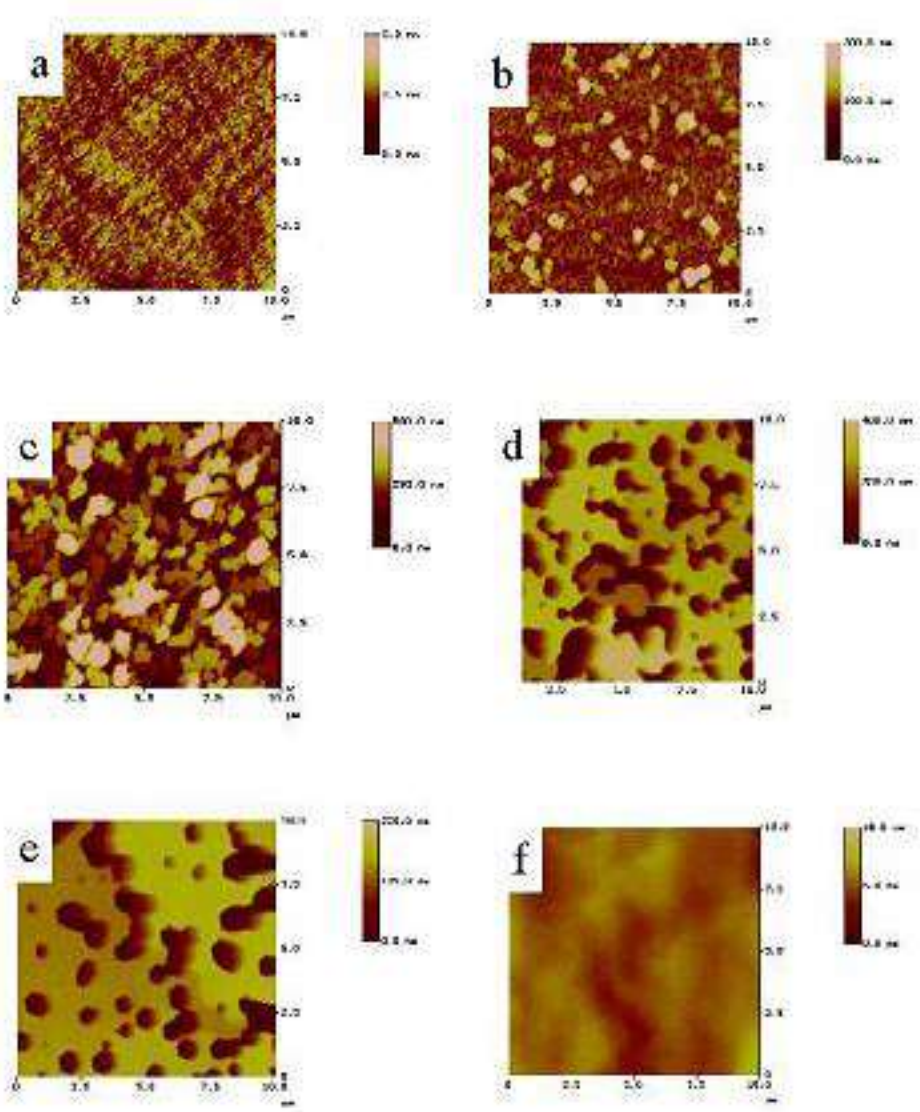

FIG. 3.3.2 AFM images of GaN film at different growth stages. After [71].

3.3.2 Optimization of u-GaN quality

It is found that the growth temperature (i.e., T_0 in Fig. 3.3.1) during the crystal coalescence is crucial in determining the crystal quality [80]. Therefore, the effect of the coalescence temperature on the crystal quality has been investigated by XRD. As shown in Fig. 3.3.3, both (102) and (002) rocking X-ray spectra of the samples were recorded and analyzed. It is found that the full-width-at-half-maximum (FWHM) of both the (002) and (102) rocking curves is

reduced with increasing T_0. Fig. 3.3.3 also reveals that the edge dislocation is more sensitive to T_0 than the screw dislocation. When T_0 is increased from 930 to 990 ^oC, the FWHM values of the (102) spectra are significantly reduced when compared to those of (002) spectra. We attribute the reduced dislocation density under the elevated coalescence temperature to the bigger and sparse GaN islands and formation [81].

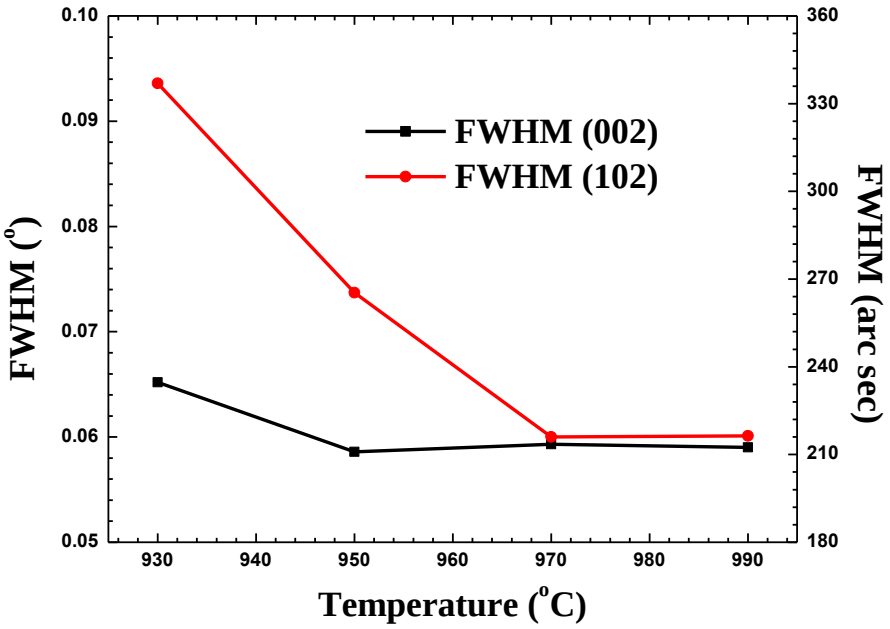

FIG. 3.3.3 FWHM of the (002) and (102) XRD rocking curves of GaN in terms of the coalescence temperature (T_0).

3.3.3 Emission wavelength for InGaN/GaN light-emitting diodes

It is worth discussing that the light is generated in the active region, i.e., the emission wavelength of the InGaN/GaN MQW region is tuned by varying the InN fraction in the InGaN quantum wells. The energy band gap of the unstrained InGaN and AlGaN is depicted in Eqs. (3.3.1) and (3.3.2), respectively [82].

$$E_g(In_xGa_{1-x}N) = x \cdot E_g(InN) + (1-x) \cdot E_g(GaN) - 1.4 \cdot x \cdot (1-x) \qquad (3.3.1)$$

$$E_g(Al_xGa_{1-x}N) = x \cdot E_g(AlN) + (1-x) \cdot E_g(GaN) - 0.7 \cdot x \cdot (1-x) \qquad (3.3.2)$$

where $E_g(InN)$, $E_g(GaN)$ and $E_g(AlN)$ denote the energy band gaps for the unstrained InN, GaN and AlN materials, which have the values of 0.78 eV, 3.51 eV and 6.25 eV at room temperature [83], respectively. 1.4 eV and 0.7 eV are the bowing parameters for InGaN and AlGaN compounds, respectively. The details on the relationship between the emission regimes, lattice constants and the alloy compositions can be found in Fig. 2.1.3.

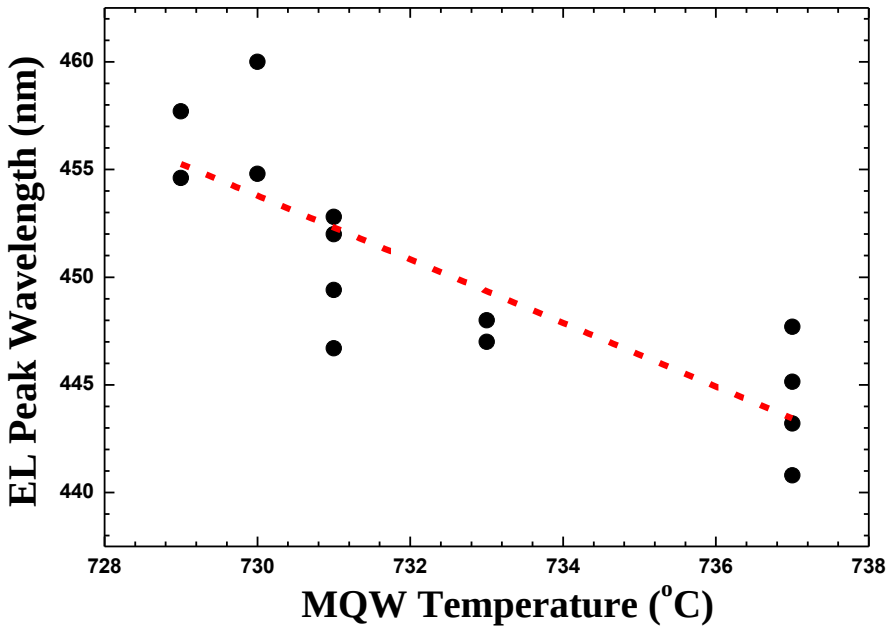

FIG. 3.3.4 Quantum well peak emission wavelength obtained from electroluminescence (EL) spectra as a function of the quantum well growth temperature.

As has been explained above, the emission wavelength of the InGaN/GaN MQWs strongly depends on the InN fraction according to Eq. (3.3.1). The InN incorporation can be adjusted and controlled by the quantum well growth temperature. The emission wavelength in terms of the quantum well growth

temperature is shown in Fig. 3.3.4, in which the TMIn/TEGa molar ratio is kept to be 16.10. We have found that a higher quantum well growth temperature reduces the peak emission wavelength. The shorter emission wavelength results from the low InN incorporation efficiency into the InGaN/GaN MQWs at a high growth temperature [77, 84]. However, besides the growth temperature, it has also been reported that the InN incorporation depends both on the growth pressure [85, 86] and the chamber ambient [87]. A growth ambient of lower growth pressure and hydrogen free environment is helpful in enhancing the InN incorporation efficiency.

Additionally, the emission wavelength can also be modified by tuning the quantum well and/or quantum barrier thickness, which is illustrated in Figs. 3.3.5(a) and 3.3.5(b), respectively. Since the quantized energy levels for the bound carriers confined in the quantum well are elevated when the quantum well becomes thinner, the blue shift of the emission wavelength with decreased quantum well thickness is observed in Fig. 3.3.5(a) [24]. In addition, we can see that a thick quantum barrier red-shifts the emission wavelength due to the increased polarization effect in the quantum wells [88]. The blue shift of the emission wavelengths as a function of the increasing injection current levels in Figs. 3.3.5 (a) and 3.3.5 (b) is attributed to the screening effect to the polarizations in the quantum wells [28], which will be elucidated in the subsequent chapters.

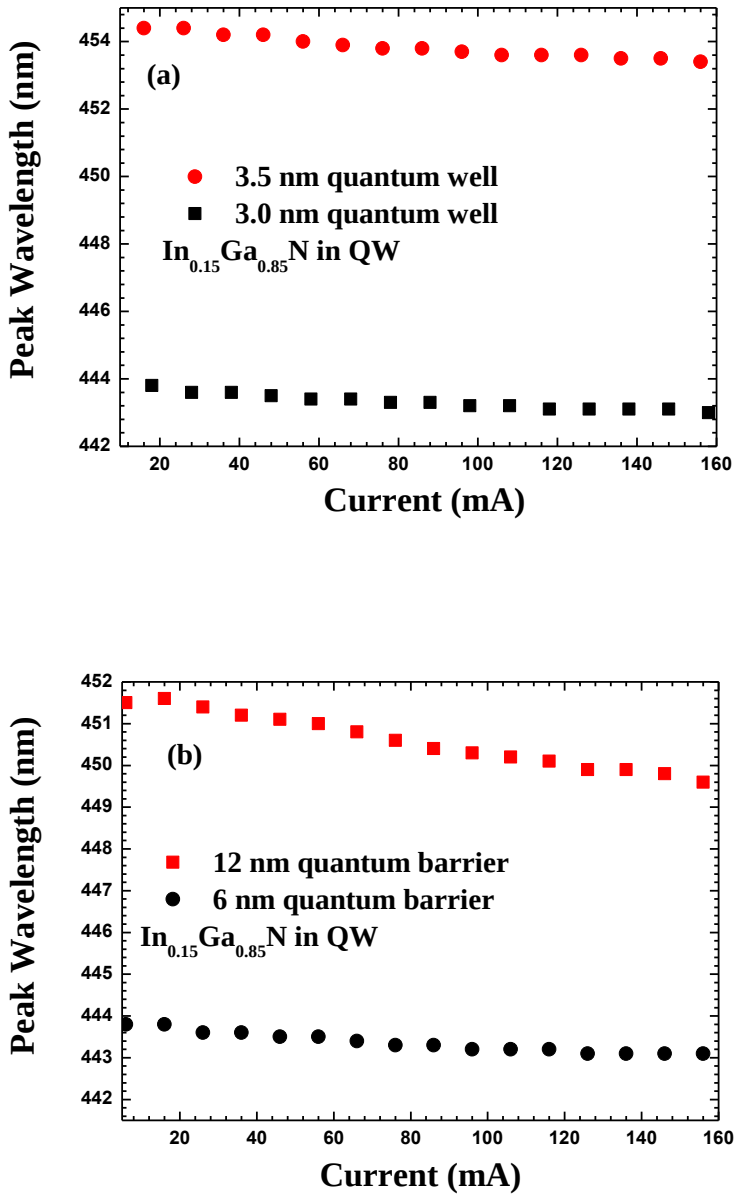

FIG. 3.3.5 Quantum well emission peak emission wavelength as a function of injection current under different (a) quantum well thicknesses and (b) quantum barrier thicknesses.

3.3.4 Growth and optimization for the p-GaN layer of InGaN/GaN light-emitting diodes

As previously reported, the activation efficiency of the Mg dopants in the p-type GaN layer is ~1% at room temperature due to the high activation energy

(~200 meV) and the hydrogen-passivation effect [63, 89]. Thus, InGaN/GaN LEDs have been prospered only after the issue of the p-type conductivity has been solved, which was first achieved by treating the p-GaN layers under low-energy electron-beam radiation (LEEBI) [6], producing a hole concentration of 2×10^{16} cm^{-3} with a resulting sheet resistivity of 35 Ω-cm. On the other hand, the p-type conductivity can also be conveniently realized through rapid thermal annealing the p-GaN films at 700 ^{o}C in the N_2 ambient or vacuum [7], by means of which the hydrogen-magnesium bonds can be broken and yield a hole concentration of 3×10^{17} cm^{-3} with the sheet resistivity of 2 Ω-cm. However, it was also reported that the p-GaN annealing is a reversible process such that the Mg acceptors can be passivated again once being annealed in NH_3 [7]. Nakamura concluded that the dissociated hydrogen from NH_3 at 400 ^{o}C diffuses into p-GaN film hence passivating the Mg acceptors. The realization of the conductive p-GaN films through rapid thermal annealing process has opened up the path to the mass production of InGaN/GaN LEDs.

It is found that the growth pressure and the Mg/Ga molar flow ratio for the p-GaN layer growth play an important role in producing a high hole concentration [90, 91]. The hole concentration in the p-GaN layer as a function of the growth pressure under various Mg/Ga molar flow ratios is presented in Fig. 3.3.6. It is shown that when the molar flow ratio between the Cp_2Mg and TMGa is 4.47% and 5.36%, the hole concentration in the p-GaN layer is around 2×10^{16} cm^{-3}. The reduced hole concentration under a high Cp_2Mg flow rate is due to the compensation effect of the ionized Mg acceptors by the Mg-related defects produced at a high Mg concentration [63]. However, when the Cp_2Mg/TMGa molar flow ratio is below 3%, it is found that a higher Cp_2Mg

flow rate is helpful in enhancing the hole concentration. In addition, we have also demonstrated the hole concentration changes with the growth pressure. The optimum growth press is 150 mbar, at which the highest hole concentration is 1.5×10^{17} cm^{-3}, indicating the compensation ratio increases with decreasing pressure. When the growth pressure is higher than 150 mbar, the hole concentration starts to decrease with increasing growth pressure, and this is due to the insufficient Mg incorporation efficiency or the compensation effect by the Mg-related defects [91].

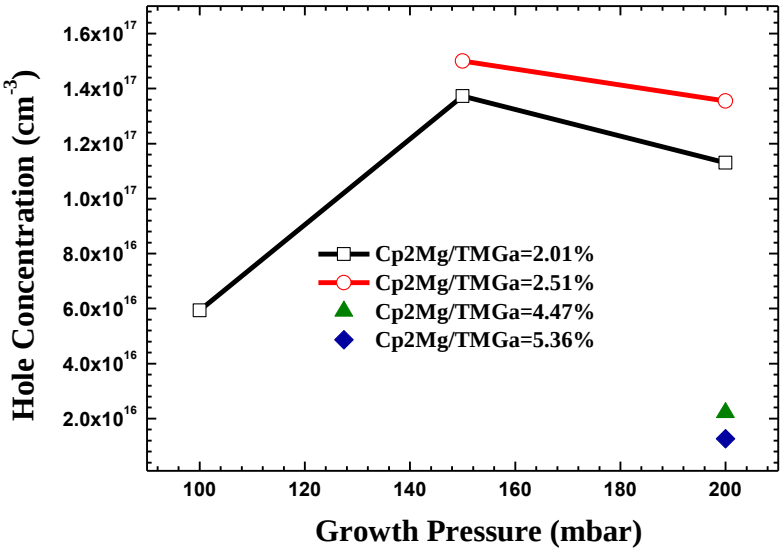

FIG. 3.3.6 Hole concentration for p-GaN layer in terms of the growth pressure under different Mg/Ga ratios.

3.4 Device fabrication for InGaN/GaN light-emitting diodes

After epitaxial growth for the InGaN/GaN LEDs, device fabrication is conducted to obtain the LED chips [92]. Fig. 3.4.1 shows the typical process flow for fabricating a standard InGaN/GaN LED chip, which starts from a bare InGaN/GaN LED wafer. Before the device fabrication starts, sample cleaning is

needed to remove the organic surface contaminations. The LED sample is cleaned by acetone and IPA, and then rinsed in DI water. The wafer can be dried through N_2 gun, then followed by the dehydration on the hot plate. The temperature of the hot plate is 110 ^oC and the dehydration lasts 5 min. Once the wafer has been sufficiently dried, then it is spin-coated with AZ5214 (2000 rpm for 60 sec in this work) photoresist (PR). Under these conditions, the coated PR thickness is around 1.4 μm. A PR dehydration after spin-coating is then performed on 110 ^oC hot plate for 105 s, and then the PR is patterned through exposure to UV light (at a light intensity of 15 mJ/cm^2) for 25 s. AZ400K developer is used to remove the UV illuminated PR, and the development process normally lasts 30 s in the mixture of DI water and AZ400K (DI water : AZ400K = 3 : 1).

Firstly, the AZ5214 PR to prepare a current spreading layer is spin-coated, patterned, and developed as shown in Fig. 3.4.1(a). Before we deposit the current spreading layer (CSL), the PR hard bake has to be conducted in an oven for 6 min at 110 ^oC. Then, the samples are ready for current spreading layer deposition. For the fabricated devices in this thesis, we use either a 200 nm thick sputtered indium tin oxide (ITO) or 5 nm/5 nm alloyed Ni/Au layers deposited by e-beam as the current spreading layer. After the current spreading layer is deposited, the AZ5214 PR will then be removed by acetone. To achieve Ohmic contact and an improved transparency, we anneal the ITO film in N_2 at 500 ^oC for 120 s [93, 94] while Ni/Au is annealed in the ambient of mixture of N_2 and O_2 at 550 ^oC for 5 min [95, 96].

After the current spreading layer is prepared, we pattern the mesa for InGaN/GaN LEDs by following the aforementioned cleaning and PR

preparation processes. The mesa formation is achieved through reactive ion etching (RIE) by flowing Cl_2 and BCl_3 gases within the RIE chamber [97-99]. We have investigated the etch rate of both PR and GaN materials, which is shown in Figs. 3.4.2(a) and 3.4.2(b), respectively. In our etching recipe, we set RF power to 200 mW, while the flow rate of Cl_2 and BCl_3 etchants is 20 and 40 sccm, respectively. The chamber pressure is 20 mTorr. According to Figs. 3.4.2(a) and 3.4.2 (b), we can see that the etch rate for PR and GaN is 0.07 and 0.06 μm/min, respectively. Hence, to obtain a 0.9 μm mesa depth, we need to etch the sample for 15 min. Fig. 3.4.1 (d) shows the mesa structure after RIE etching.

Finally, depositing of the P-contact and N-contact on the current spreading layer and the n-GaN layer is conducted after mesa process. We follow the same sample cleaning and PR preparation process as before to make the contact patterns. In our fabricated devices, we utilize Ti/Au (30 nm/150 nm) as the P-contact and N-contact for our LED chips. Fig. 3.4.1(f) shows the schematic diagram of a complete LED chip, along with which shows the microscopy images of the fabricated LED chips in Fig. 3.4.3(a). The illuminating InGaN/GaN LED chip is shown in Fig. 3.4.3(b).

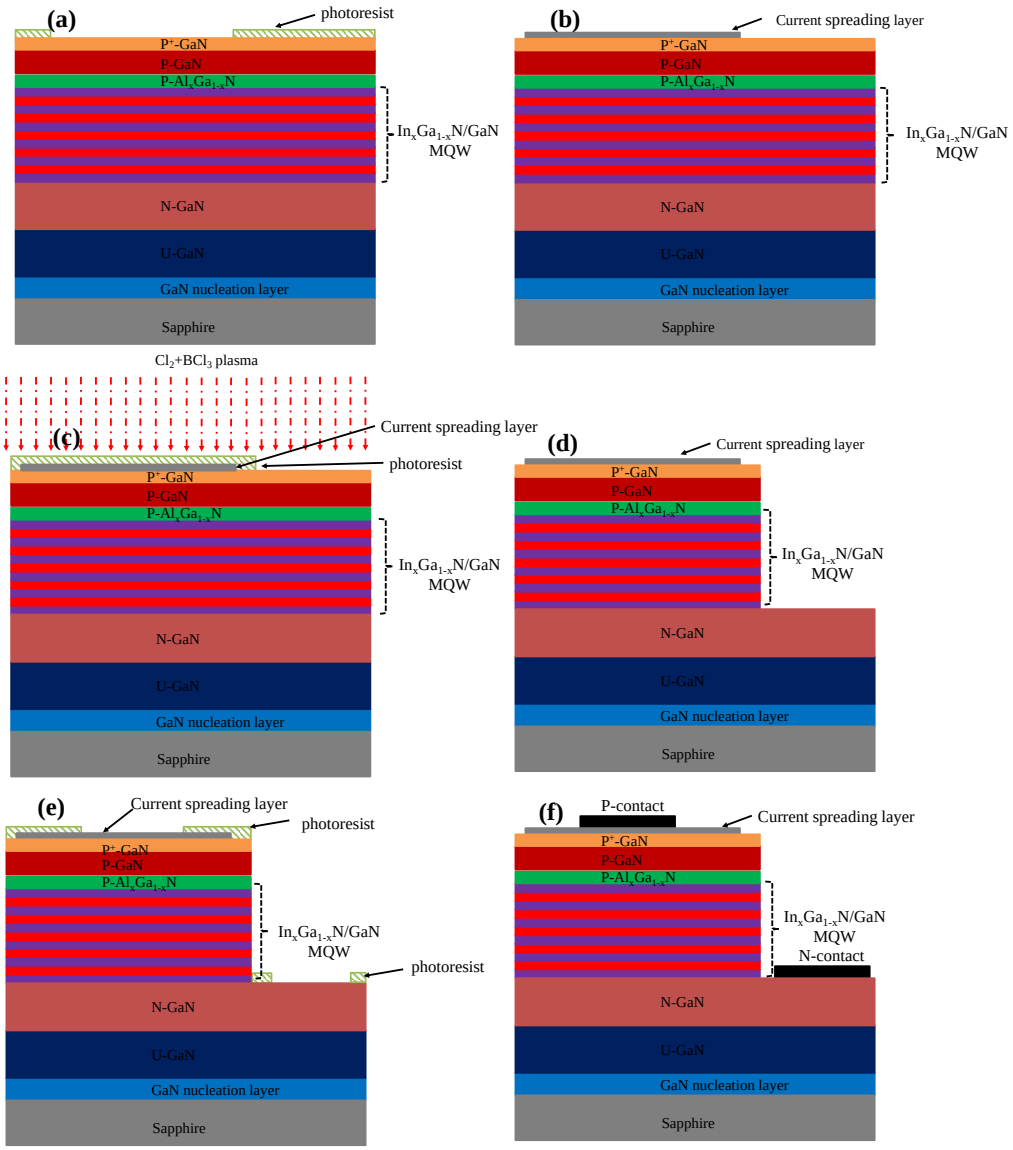

FIG. 3.4.1 Fabrication process for InGaN/GaN LED chips: (a) PR patterning for current spreading layer deposition, (b) patterned current spreading layer after liftoff, (c) PR patterning for reactive ion etch for exposing N-GaN layer, (d) mesa, (e) PR patterning for P-contact and N-contact, (f) a fabricated LED chip, (g) microscopy image of fabricated LED chips and (h) the lit LED chip.

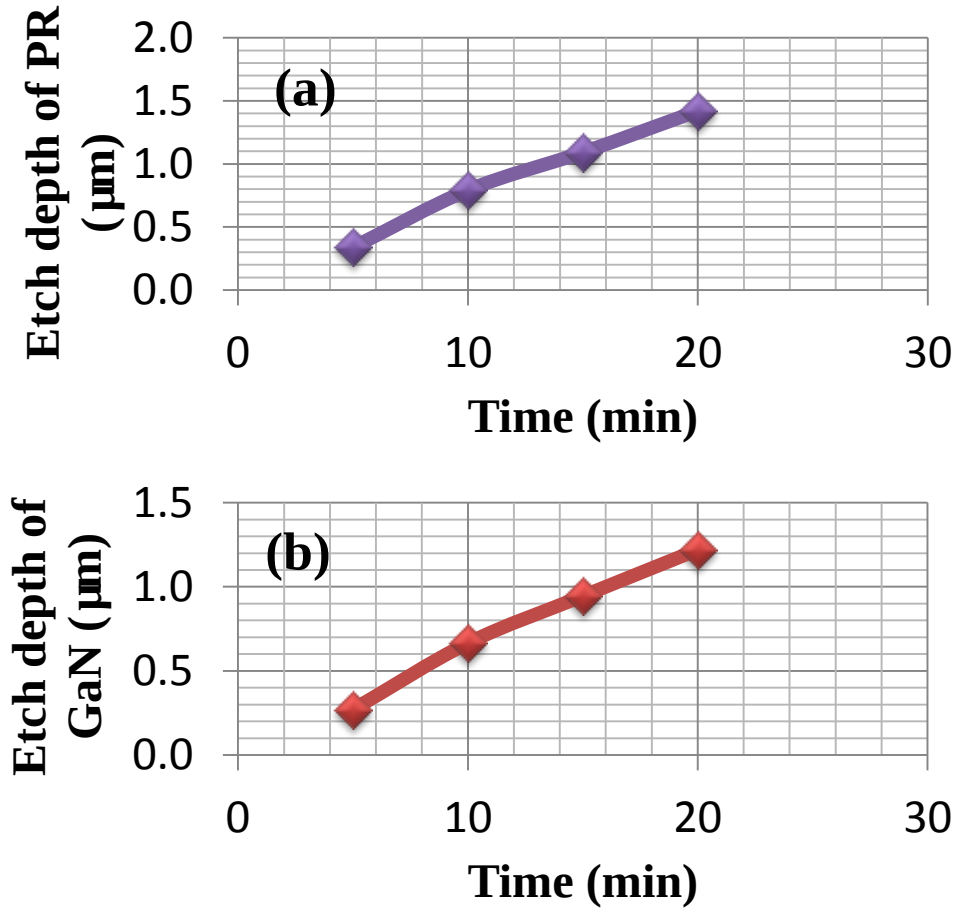

FIG. 3.4.2 Etch rate for (a) AZ5214 PR and (b) GaN material.

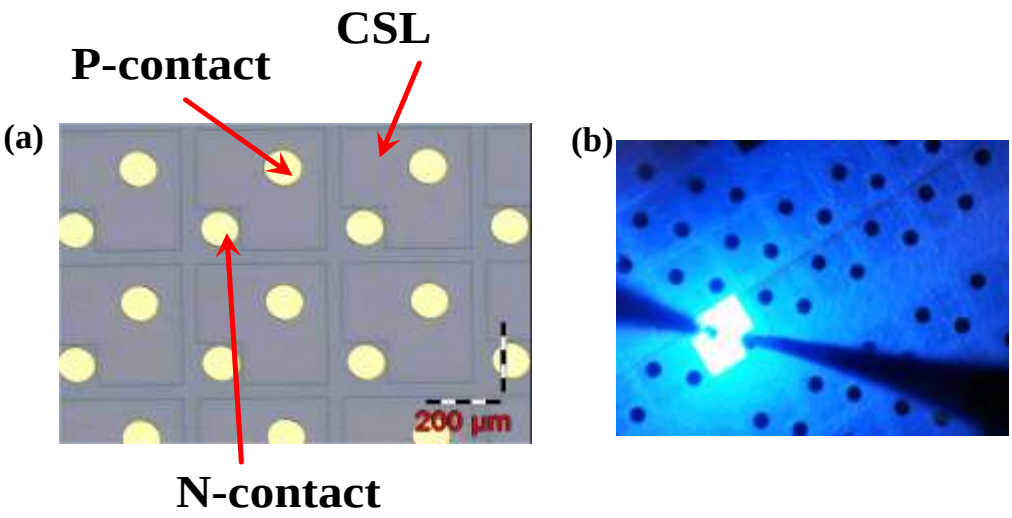

FIG. 3.4.3 (a) Microscopy image of fabricated LED chips and (b) the lit LED chip.

Chapter 4 Improved InGaN/GaN light-emitting diodes through engineering the quantum barriers

In this chapter, we have both theoretically and experimentally engineered the quantum barriers of the LED structure with Si step-doping and Mg-Si-doping (i.e., PN-type) features, respectively. Through Si-step doping the quantum barriers, we have observed the enhanced optical output power and external quantum efficiency (EQE), and we have attributed the improved device performance to the increased screening effect of the quantum confined Stark effect (QCSE). Moreover, compared to the conventional Si-fully doped quantum barriers, our device with Si-step doped quantum barriers exhibit an enhanced hole injection efficiency. However, though the device performance for InGaN/GaN light-emitting diode (LED) with Si-step doped quantum barriers has been significantly boosted, we still see somehow the hole blocking effect due to the incorporation of Si dopants in the quantum barriers. Thus, we have doped the Si-step doped quantum barriers with Mg dopants of proper dosage, such that a PN-type quantum barrier is formed of the InGaN/GaN LEDs. By doing so, the hole transport has been further increased and at the same time, the QCSE has also been screened. As a result, the device performance has been further enhanced.

4.1 The effect of step-doped quantum barriers in InGaN/GaN light-emitting diodes

4.1.1 Introduction

As is well-known, InGaN/GaN LEDs grown along c^+ orientation exhibit very strong polarization induced electric field [20, 29, 31, 42, 55], which

spatially reduces the electron-hole wave functions, thus suppressing the radiative recombination rates between electrons and holes within the InGaN/GaN multiple quantum wells (MQWs). In order to suppress the polarization induced electric field, staggered InGaN quantum wells have been proposed and investigated [29, 55, 100-102]. The spatial separation of the electron-hole wave functions can be reduced also by employing either the ternary InGaN substrate [31] or the electro-plated Ni metal substrate [103]. Recently, *c*-plane III-nitride quantum wells with embedded "delta" novel materials have proved to be effective in enhancing the electron-hole wave function overlap, therefore increasing the radiative recombination rates [104-108]. The polarization induced spatial separation of electron-hole wave functions can further be completely eliminated in the non-polar quantum wells and increased radiative recombination rates can thus be obtained [33, 34]. It has also been shown that the material quality and the device performance can be substantially improved by introducing Si doping in quantum barriers [109-111]. However, Si-doped barriers or even Si-delta-doped barriers usually have a setback from holes blocking [112, 113], which leads to a high local hole accumulation. Previously, Zhu *et al.* proposed the selective Si doped barriers to symmetrize the hole distribution and improve the device performance [114]. Nevertheless, selective Si doping could not effectively suppress the polarizations in those quantum wells due to the undoped quantum barriers. On the other hand, it has been reported that the free electrons (released by Si-doped quantum barriers) could screen the quantum confined Stark effect (QCSE), though the screening effect is not optimum due to the absence of ionized dopants [115]. In this section, we study both numerically and experimentally on

the step-doping of the quantum barriers with Si, which could effectively screen the QCSE through the ionized dopants by properly designing the doped thickness and position in the quantum barriers. This provides additional degree of freedom in designing thicker quantum wells to avoid carrier high energy state filling, relieving the efficiency droop in *c*-plane LEDs [116]. The proposed step-doped quantum barriers could reduce the hole blocking effect, promote electron injection, quench polarization fields and enhance electron-hole wave function overlap ($\Gamma_{e\text{-}hh}$) within the quantum wells. These improvements translate to the enhancement of optical output power and efficiency.

4.1.2 Experiment

To investigate the proposed step-doped barriers, InGaN/GaN LED epitaxial wafers were grown by AIXTRON close-coupled showerhead metal-organic chemical vapor deposition (MOCVD) reactor on *c*-plane sapphire substrates. The growth was initiated on a 30 nm thick low-temperature grown GaN buffer layer (at 560 ^{o}C with a growth pressure of 600 mbar and a V/III ratio between NH_3 and TMGa of 950). A 2 μm thick u-GaN layer was subsequently grown at 1050 ^{o}C with a growth pressure of 400 mbar and a V/III ratio of 2700. For the n-GaN growth (with $N_D = 8 \times 10^{18}$ cm^{-3}), the growth temperature, pressure and V/III ratio were set to 1060 ^{o}C, 250 mbar and 1140, respectively. A higher V/III ratio of 10064 was utilized for the growth of quantum barriers. The growth temperature was 820 ^{o}C and 737 ^{o}C for the quantum barriers and quantum wells, respectively, while the V/III ([NH3]/[TEGa]+[TMIn]) ratio during the quantum well growth was 10500. However, a constant growth pressure of 400 mbar was used during the growth of both the quantum barriers and quantum wells. The LED samples were finally covered with a 300 nm thick p-GaN grown at 950 ^{o}C

with the pressure of 150 mbar, and the hole concentration of the p-GaN is 1.0 × 10^{17} cm^{-3}. The structures were annealed in the N_2 ambient for 15 min at 687 ^{o}C. In our experiment, Cp_2Mg and diluted SiH_4 were used as p-type and n-type dopant sources, respectively.

In our study, we comparatively studied three structures of InGaN/GaN LED epi-wafers, which are called Devices I, II, and III. The schematic diagrams of the investigated devices are shown in Fig. 4.1.1. Among them, Device I is a standard LED with undoped barriers, while Device II is designed with 12 nm thick barriers each fully doped with Si (N_D = 2.6 × 10^{18} cm^{-3}), and Device III features step-doped barriers (6 nm undoped and followed by 6 nm doped with N_D = 2.6 × 10^{18} cm^{-3}). The three devices differ only in their quantum barriers. Note that at such high Si doping levels, the Si diffusion cannot be excluded, but such diffusion does not destroy the crystal, and instead it promotes smoother interfaces and improve the crystal quality [117].

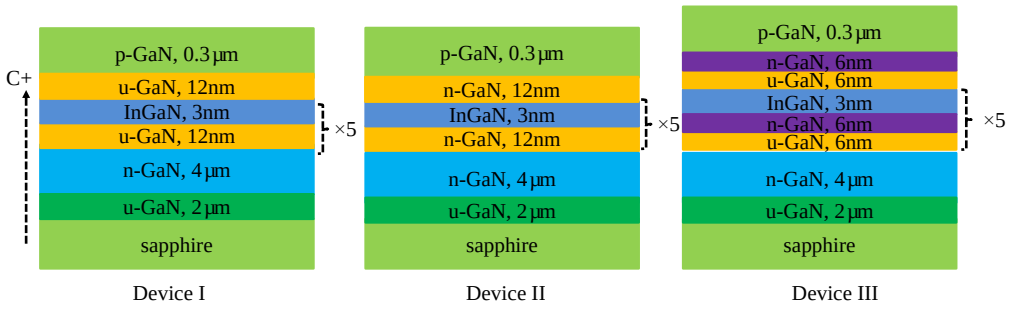

FIG. 4.1.1 Schematic diagrams of the studied LED structures. Device I has u-GaN as the quantum barriers, Device II uses Si-fully doped GaN as the quantum barriers, and Device III adopts Si-step doped GaN quantum barriers.

The studied LEDs all consist of 5-pair quantum well stack ($In_{0.15}Ga_{0.85}N$/GaN with 3 nm well and 12 nm barrier) as the active region. The devices were fabricated by using standard fabrication process. The LED mesa

was obtained through reactive ion etch with a size of 300 μm × 300 μm. Ni/Au (5 nm/150 nm) was deposited as the p-electrode, and then the thermal annealing was performed for the p-electrode in the mixture of N_2 and O_2 for 5 min. Finally Ti/Au (30 nm/150 nm) was deposited on the n-GaN layer as the n-electrode.

4.1.3 Results and discussions

Figure 4.1.2(a) shows the measured EQE and optical output power as a function of the current for all the devices [along with Fig. 4.1.2(b) depicting the numerical simulation results]. As demonstrated, Device II performs better than Device I when the current is increased beyond 26.5 mA, as the Si-doped barriers replenish electrons in the quantum wells. Furthermore, the screening effect on the QCSE improves the spatial overlap between the electron and hole wave functions [109], thus enhancing the radiative recombination rates. Nevertheless, in the low current regime (4.8 mA < I < 26.5 mA), Device II performs worse than Device I. On the other hand, across the whole current range tested, we see that Device III outperforms Devices I and II, and the power is experimentally enhanced by 90.79% between Devices I and III, while 27.90% between Devices I and II at 50 mA. According to the results in Fig. 4.1.2, the performance of Device III is the best even the current is further increased beyond 50 mA. Fig**.** 4.1.3 presents the electroluminescence (EL) for the studied devices, where the emission intensity is the strongest for Device III and the weakest for Device I. Meanwhile, Devices II and III show a shorter peak emission wavelength compared to Device I, which is attributed to the relieved QCSE by Si-doped quantum barriers [109]. However, the less pronounced blue-shift for all the three devices as the injection current increases

is caused by the junction heating effect [118].

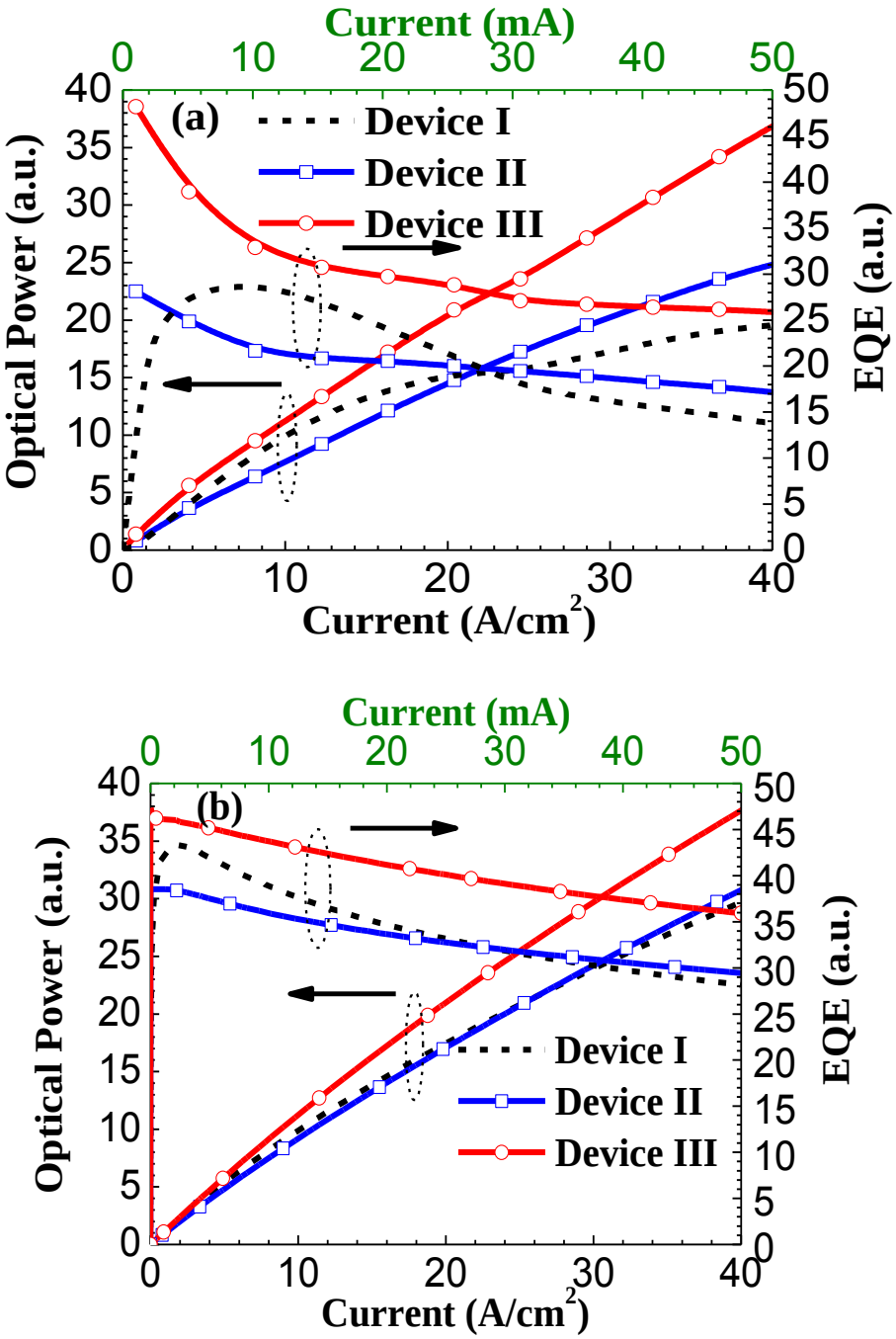

FIG. 4.1.2 (a) Experimentally measured and (b) numerically simulated optical output power and EQE as a function of current for Devices I, II and III.

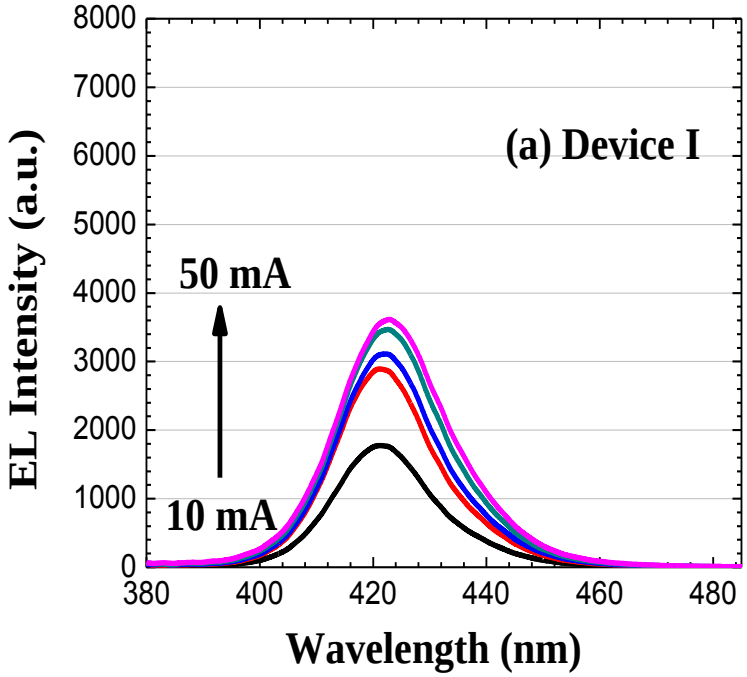
(a) Device I
50 mA
10 mA
EL Intensity (a.u.)
Wavelength (nm)
0
1000
2000
3000
4000
5000
6000
7000
8000
380
400
420
440
460
480

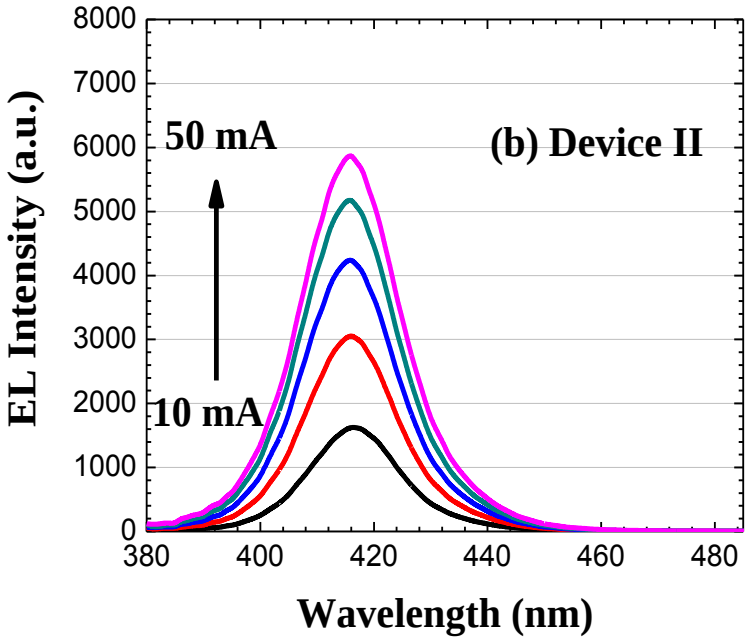
(b) Device II
50 mA
10 mA
EL Intensity (a.u.)
Wavelength (nm)
0
1000
2000
3000
4000
5000
6000
7000
8000
380
400
420
440
460
480

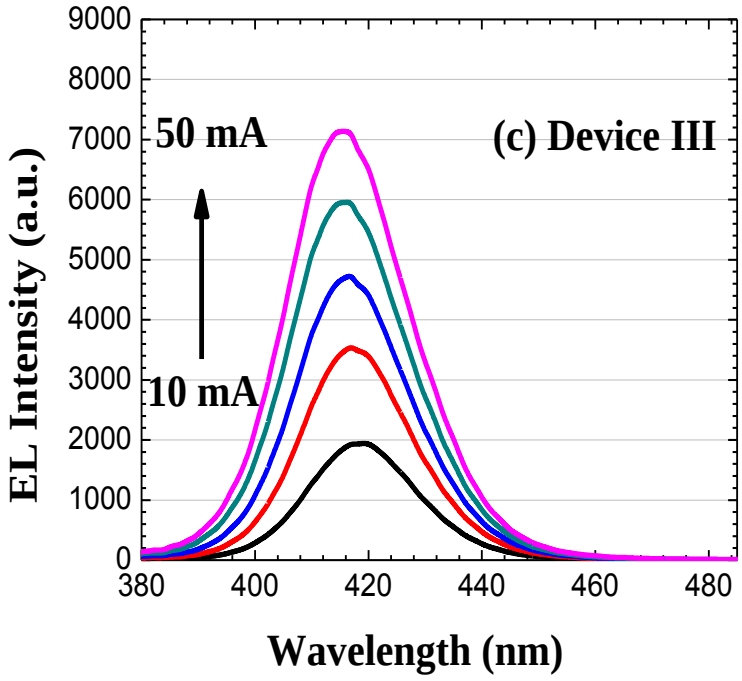

FIG. 4.1.3 EL spectra for (a) Device I, (b) Device II and (c) Device III.

In order to better understand the improvement of EQE and optical output power in Devices I, II and III, numerical simulations for the devices were performed by APSYS [119], which self-consistently solves the Poisson equation, continuity equation and Schrödinger equation with proper boundary conditions. The self-consistent six-band $k \cdot p$ theory is used to take account of the effect of carrier screening in InGaN quantum wells [25]. Here, the Auger recombination coefficient is taken to be 1×10^{-30} cm^6/s [18, 120]. The offset ratio between the conduction and valence bands for InGaN/GaN quantum well is assumed to be 70:30 [35]. Also, a 40% of the theoretical polarization charge is used due to the crystal relaxation through generating dislocations [20]. The other parameters used in the simulation can be found elsewhere [24, 83] and they are also illustrated in Table 4.1.1. Fig. 4.1.2(b) depicts the calculated EQE and optical output power, which demonstrates that similar trends of the

enhanced EQE and optical output power are observed after employing Si step-doped quantum barriers in Device III compared to Devices I and II. However, in the simulation, we did not consider the localized states caused by potential fluctuation of InGaN alloys [32], and the temperature/carrier concentration dependence of those nonradiative recombination factors (e.g. Auger recombination, Shockley-Read-Hall recombination), which caused the discrepancy between simulation and experiment [refer to Figs. 4.1.2(a) and 4.1.2(b)].

Table 4.1.1 Material parameters of the binary semiconductors GaN, AlN and InN at room temperature. After [24].

Parameter	**Symbol (unit)**	**GaN**	**AlN**	**InN**
Lattice constant	a_0 (nm)	0.3189	0.3112	0.3545
Spin–orbit split energy	Δ_{so} (eV)	0.017	0.019	0.005
Crystal-field split energy	Δ_{cr} (eV)	0.010	−0.169	0.040
Hole effective mass parameter	A_1	−7.21	−3.86	−8.21
	A_1	−0.44	−0.25	−0.68
	A_3	6.68	3.58	7.57
	A_4	−3.46	−1.32	−5.23
	A_5	−3.40	−1.47	−5.11
	A_6	−4.90	−1.64	−5.96
Hydrost. deform. potential (*c*-axis)	a_z (eV)	−4.9	−3.4	−3.5
Hydrost. deform. potential (transverse)	a_t (eV)	−11.3	−11.8	−3.5
Shear deform. potential	D_1 (eV)	−3.7	−17.1	−3.7
	D_2 (eV)	4.5	7.9	4.5
	D_3 (eV)	8.2	8.8	8.2
	D_4 (eV)	−4.1	−3.9	−4.1
Elastic stiffness constant	C_{33} (GPa)	398	373	224
Elastic stiffness constant	C_{13} (GPa)	106	108	92
Electron effective mass (*c*-axis)	$m_{e,z}/m_0$	0.2	0.32	0.07
Electron effective mass (transverse)	$m_{e,t}/m_0$	0.2	0.30	0.07

It is reported that the wholly-doped barrier increases the barrier height for holes, thus retarding the hole injection [112], which explains the worse

performance of Device II compared to Device I in low current regime (4.8 mA < I < 26.5 mA). Fortunately, hole-blocking effects in Device II can be suppressed by employing step-doped barriers. It is observed from Figs. 4.1.2(a) and 4.1.2(b) that Device III performs better than Device II due to an improved hole transport. Note that Device II performs better than Device I when the current is higher than 26.5 mA, which is attributed to the better screening effect of the polarizations in the quantum wells by the Si-doped quantum barriers.

To better probe the hole transport of Devices I, II and III, we further simulated the hole distribution and radiative recombination rates in their quantum wells at 50 mA [Figs. 4.1.4(a) and 4.1.4(b)]. As shown in Fig. 4.1.4(a), all devices possess the highest hole concentration in the fifth quantum well (the one closest to p-GaN) along [0001]-orientation. However, due to the highest valence-band barrier height in the wholly-doped Si barriers (Fig. 4.1.5 and Table 4.1.2), Device II cannot inject holes efficiently into the quantum wells that are close to n-GaN side (e.g. the first quantum well). On the other hand, Device III has half the thickness of doped barriers compared to Device II, which reduces the overall valence-band barrier height for the hole injection (Fig. 4.1.5 and Table 4.1.2). As a result, a much more homogeneous hole distribution can be obtained in Device III, which correspondingly leads to higher radiative recombination rates in the quantum wells close to the n-GaN side for Device III compared to Device II. Even though Device I shows the most homogeneous hole distribution among the three devices due to the smallest energy barrier height (Fig. 4.1.5 and Table 4.1.2), it suffers from the strongest QCSE and hence the low radiative recombination rates, as shown in Fig. 4.1.4(b).

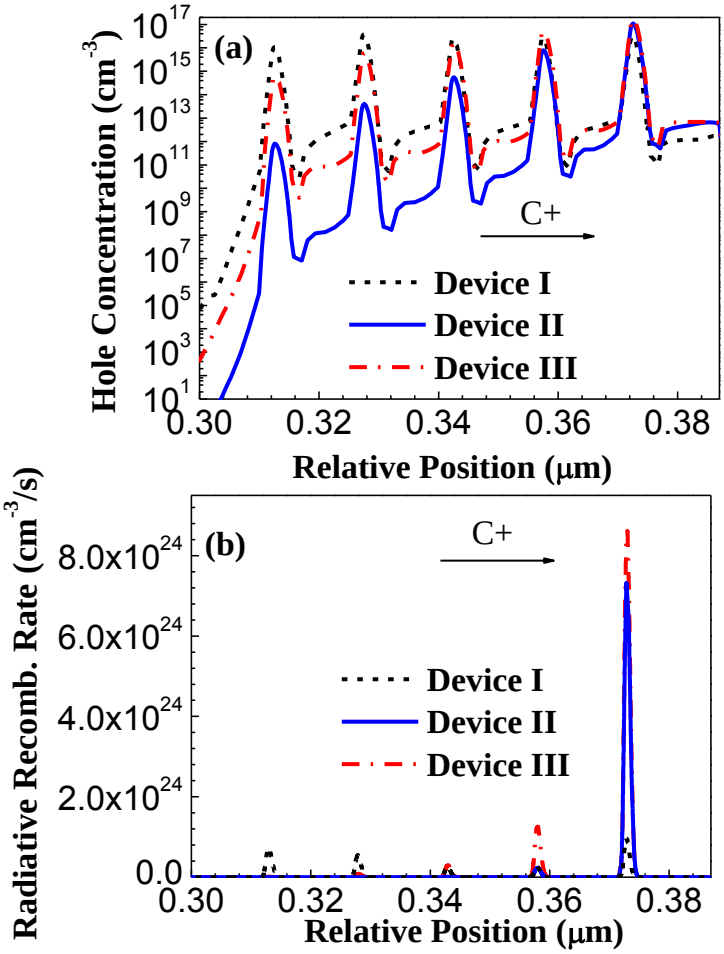

FIG. 4.1.4 (a) Simulated hole concentration and (b) simulated radiative recombination rates for Devices I, II and III at I = 50 mA.

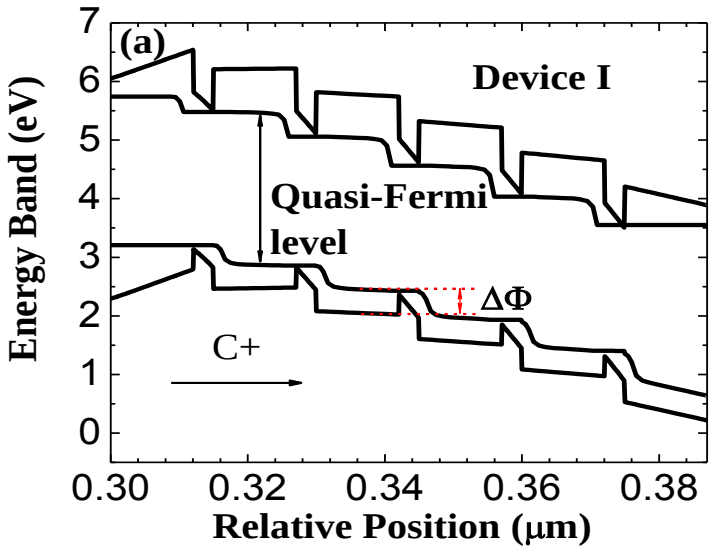

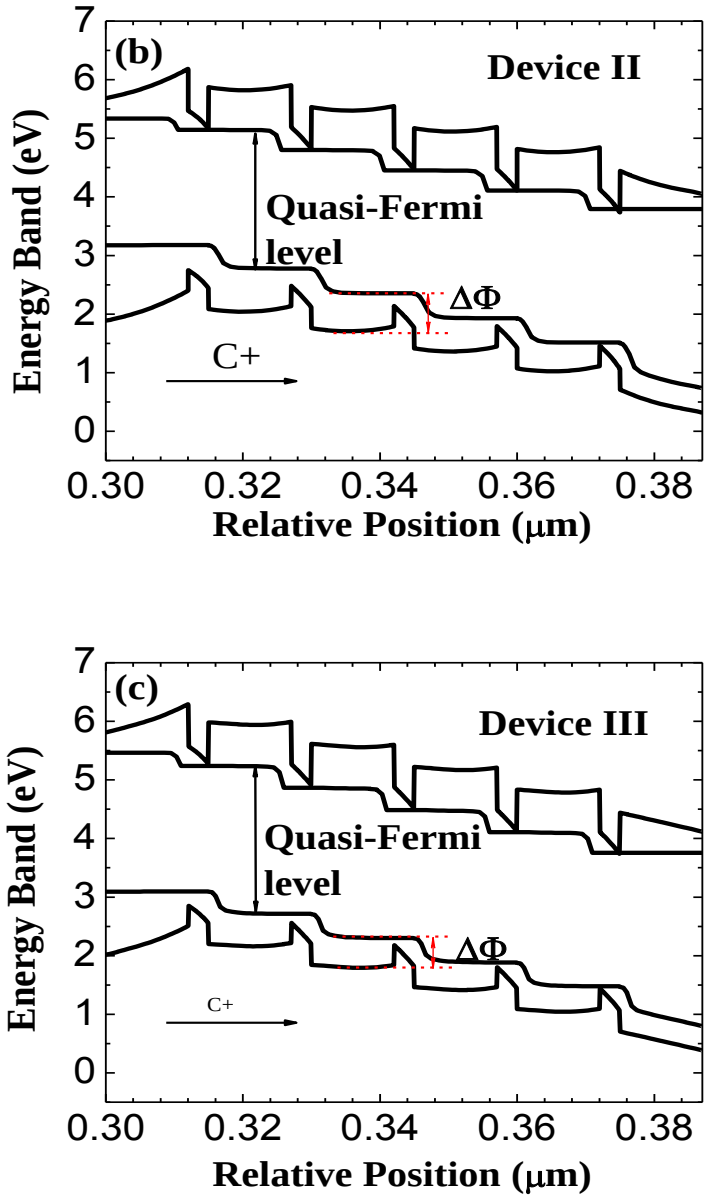

FIG. 4.1.5 (a) Simulated energy band for (a) Device I, (b) Device II, and (c) Device III. ΔΦ represents the energy barrier height for holes.

Table 4.1.2 The energy barrier height (ΔΦ) of holes for each quantum barrier in Devices I, II and III. Quantum barrier 1 refers to the barrier after the first quantum well while quantum barrier 5 refers to the barrier after the fifth quantum well.

	Device I (ΔΦ)	**Device II (ΔΦ)**	**Device III (ΔΦ)**
Quantum Barrier 1	402 meV	750 meV	563 meV
Quantum Barrier 2	402 meV	646 meV	510 meV
Quantum Barrier 3	410 meV	580 meV	479 meV
Quantum Barrier 4	410 meV	500 meV	455 meV
Quantum Barrier 5	406 meV	415 meV	413 meV

As is well recognized, the strong polarization induced field within the quantum wells spatially separates the electron and hole wave functions, thus reducing the interband transition probability of carriers. However, the internal electric field profile can be tuned by Si-doping the quantum barriers. On the other hand, it can be seen clearly from Fig. 4.1.4(b) that the fifth quantum well dominates the radiative recombination rates especially for Devices II and III. Thus analysing the electric field in the fifth quantum well (i.e., the quantum well closest to the p-GaN side) for these three devices comparatively is helpful for us to understand the mechanism for the QCSE suppression. Fig. 4.1.6(a) presents the electric field in the fifth quantum well for Devices I, II and III under equilibrium, where the positive direction is along [0001]. We can see a considerably flat electric field profile in Device I, whereas for devices with Si-doped quantum barriers (Devices II and III), the electric field is tilted as depicted in Fig. 4.1.6(a) and a reduction of the electric field in the well close to the n-GaN side ["B" site in Fig. 4.1.6(a)] is achieved, while an enhanced magnitude of electric field is simultaneously triggered at the interface close to p-GaN side ["A" site in Fig. 4.1.6(a)]. Figs. 4.1.6(b), 4.1.6(c) and 4.1.6(d) show the energy band diagrams and the charge profile for Devices I, II and III under equilibrium, respectively. In Device I, only polarization induced charges are

shown in Fig. 4.1.6(b), since there is no Si dopant in the quantum barriers and the simulated electron sheet charge density (n_S) in the fifth quantum well is around 1.4 $\times 10^2$ cm^{-2}, which is negligible compared to the polarization charge density that is in the order of 10^{13} cm^{-2} [109]. Thus we obtain the macroscopic electric field in Eqn. 4.1.1 at both "A" and "B" sites, respectively, which explains the field symmetry for Device I in Fig. 4.1.6(a).

$$\left|\vec{E}_{sp+pz}\right| = \frac{e \cdot \sigma_S}{\varepsilon_r \cdot \varepsilon_s} \tag{4.1.1}$$

where e is the elementary electronic charge, ε_r is the relative dielectric constant of InGaN, ε_s is the it electric permittivity in vacuum, and σ_S is denoted as the polarization induced charge density.

For Devices II and III, the Si dopants can be considered to be completely ionized [121], feeding electrons into the quantum well and leaving a depletion region in the barrier. The sheet charge density of the ionized Si atoms can be obtained from $\sigma_{Si} = N_D \cdot t_D$, where N_D is the Si dopant concentration (N_D = 2.6 $\times 10^{18}$ cm^{-3} for both Devices II and III) and t_D is the doped barrier thickness (t_D = 12 nm and 6 nm in for Devices II and III, respectively), and therefore we obtain the sheet charge density of Si (σ_{Si}), which is 3.12 $\times 10^{12}$ cm^{-2} and 1.56 $\times 10^{12}$ cm^{-2} for Device II and III, respectively. Besides, according to our simulation, the n_S in the fifth quantum well is about 3.0 $\times 10^{12}$ cm^{-2} and 1.5 $\times 10^{12}$ cm^{-2} in Devices II and III, respectively, which are slightly smaller than σ_{Si} by our simple calculation above. The smaller n_S compared to σ_{Si} is due to the loss of electron leaking into p-GaN region. Since we do not observe any holes diffusing into the quantum wells under the equilibrium state in the simulations, the effect of holes is not included here.

Accordingly, the electric field at "A" site in Device II can be given by Eqn. 4.1.2 [refer to Fig. 4.1.6(c)], while it can be expressed in Eqn. 4.1.3 for Device III if the diffused σ_{Si} from the doped part in the quantum barrier is negligible compared to σ_S as shown in Fig. 4.1.6(d). However, the electric field at "B" site for both Devices II and III can be represented in Eqn. 4.1.4 according to Figs. 4.1.6(c) and 4.1.6(d).

$$\left|\vec{E}_{sp+pz}+\vec{E}_{Si}+\vec{E}_{n_S}\right|=\frac{e\cdot\left|\left(\sigma_S+\sigma_{Si}-n_S\right)\right|}{\varepsilon_r\cdot\varepsilon_s} \tag{4.1.2}$$

$$\left|\vec{E}_{sp+pz}+\vec{E}_{n_S}\right|=\frac{e\cdot\left|\left(\sigma_S-n_S\right)\right|}{\varepsilon_r\cdot\varepsilon_s} \tag{4.1.3}$$

$$\left|\vec{E}_{sp+pz}+\vec{E}_{Si}\right|=\frac{e\cdot\left|\left(\sigma_S-\sigma_{Si}\right)\right|}{\varepsilon_r\cdot\varepsilon_s} \tag{4.1.4}$$

where $\vec{E}_{Si}$ and $\vec{E}_{n_S}$ represent the electric field caused by Si dopants and electrons, respectively.

It is well-known that the idea to screen the QCSE by introducing Si dopants in the quantum barriers is realized by releasing electrons [114] into the quantum wells (i.e., n_S in Eqns. 4.1.2 and 4.1.3), but, the effect of the ionized donors has never been properly recognized. As shown in Eqn. 4.1.4, a reduced electric field at "B" site [Fig. 4.1.6(a)] caused by the presence of ionized Si dopants [Figs. 4.1.6(c) and 4.1.6(d)] helps to make the valence band less titled for Devices II and III compared to Device I [Fig. 4.1.6(f), $\Delta\phi_h$ = 60 meV for Device II and 50 meV for Device III], which in turn pushes the hole wave function towards "A" site [Fig. 4.1.7(a)]. Thus, Device II and III enjoy a more overlapped electron-hole wave function than Device I. Device I has a $\Gamma_{e\text{-}hh}$ of 29.94%, while Device II and Device III feature a $\Gamma_{e\text{-}hh}$ of 34.81% and 37.76%,

respectively. The smallest $\Gamma_{e\text{-}hh}$ is responsible for the weakest emission intensity for Device I [Fig. 4.1.3(a)]. Moreover, the more increased $\Gamma_{e\text{-}hh}$ of Device III compared to Device II is attributed to the reduced electric field at "A" site compared to Device II, as a reduced field at "A" site that is caused by the absence of ionized Si dopants (refer to Eqns. 4.1.2 and 4.1.3) tilts the conduction band more [Fig. 4.1.6(e), $\Delta\phi_e$ = 26 meV for Device II and 50 meV for Device III] and pushes the electron wave function towards "B" site more [Fig. 4.1.7(a)]. Therefore, the largest $\Gamma_{e\text{-}hh}$ translates to the strongest emission intensity for Device III as shown in Fig. 4.1.3(c). Moreover, according to our simulation, Device III shows even better screening effect on the QCSE than Device II, and thus ideally a shorter wavelength is expected for Device III. However, as shown in Figs. 4.1.3(b) and 4.1.3(c), the peak emission wavelengths for Devices II and III are very close, the difference is ranged from 0.4 – 1.9 nm for various currents we used. As the devices were grown in different runs by MOCVD, it is possible, for example, we may have some slight difference in indium incorporation in the quantum wells. The peak wavelength difference between Device II and III is a combined result generated from different QCSE screening effect and possibly indium incorporation. Nevertheless, in order to verify the effect of step-doping feature, we have further investigated $\Gamma_{e\text{-}hh}$ for Devices II and III as a function of Si doping concentration in their quantum barriers as shown in Fig. 4.1.7(b), which indicates the advantage of the step-doped architecture in Device III over the wholly doped barriers in Device II.

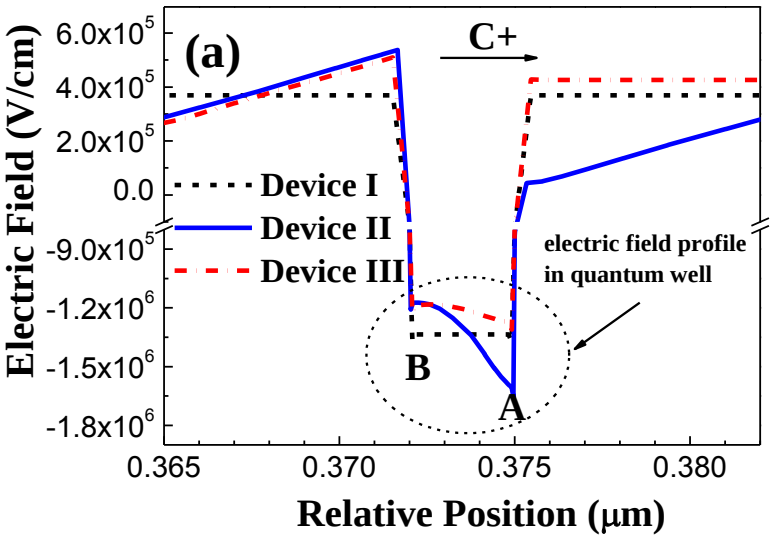
(a)
C+
Electric Field (V/cm)
6.0x10^5
4.0x10^5
2.0x10^5
0.0
-9.0x10^5
-1.2x10^6
-1.5x10^6
-1.8x10^6
Device I
Device II
Device III
electric field profile
in quantum well
B
A
0.365
0.370
0.375
0.380
Relative Position (μm)

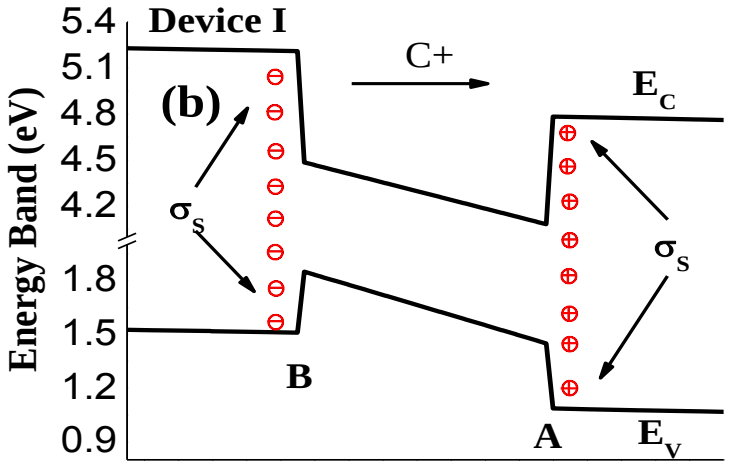
Device I
(b)
C+
Energy Band (eV)
5.4
5.1
4.8
4.5
4.2
1.8
1.5
1.2
0.9
E_C
E_V
σ_S
σ_S
B
A

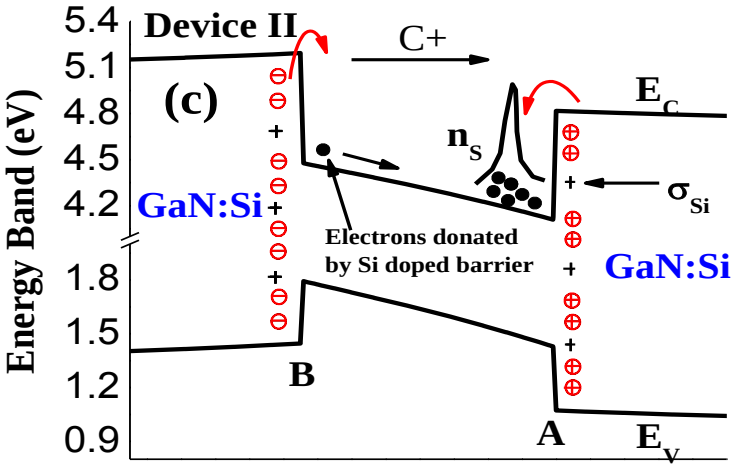
Device II
(c)
C+
E_C
n_S
σ_{Si}
GaN:Si
Electrons donated
by Si doped barrier
GaN:Si
B
A
E_V
Energy Band (eV)
5.4
5.1
4.8
4.5
4.2
1.8
1.5
1.2
0.9

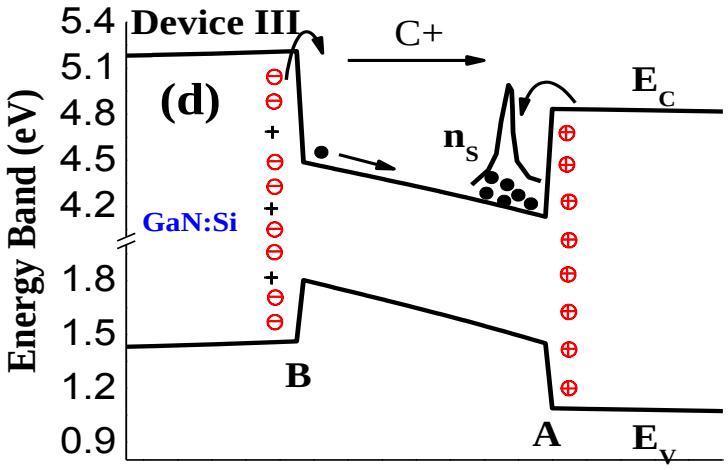
Device III
(d)
C+
E_C
n_S
GaN:Si
B
A
E_V
Energy Band (eV)
5.4
5.1
4.8
4.5
4.2
1.8
1.5
1.2
0.9

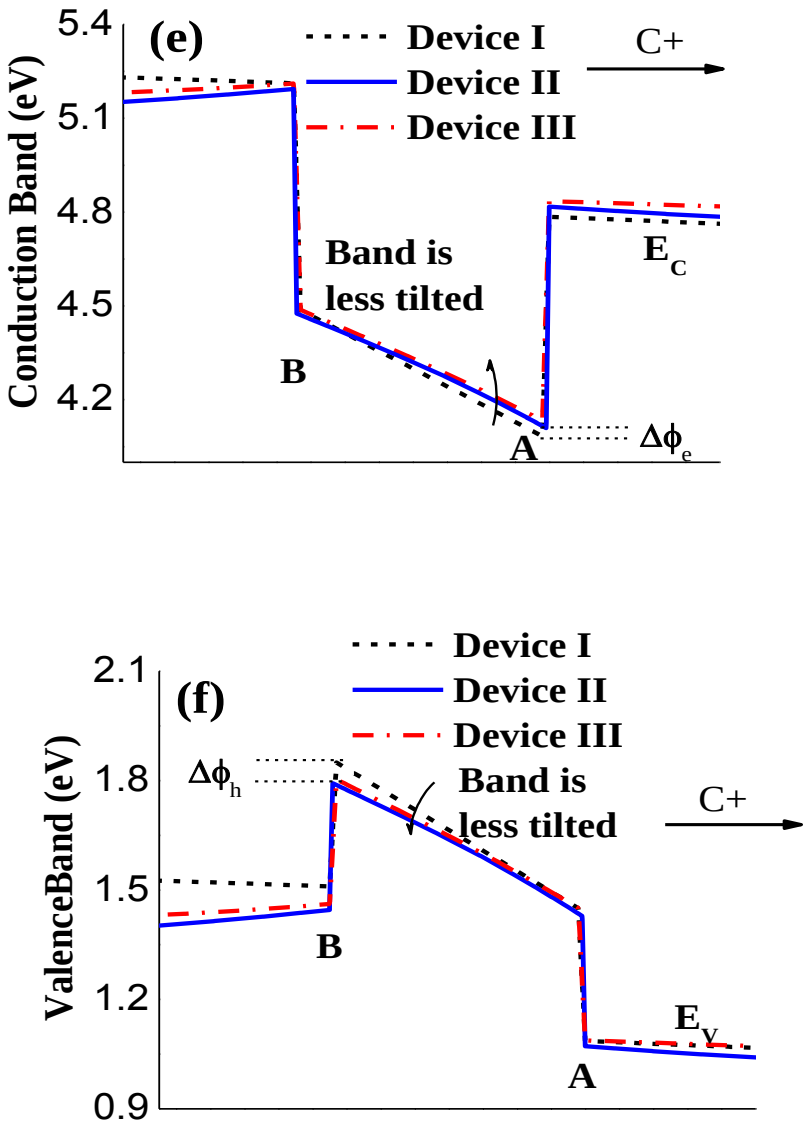

FIG. 4.1.6 (a) Simulated electric field profile in the fifth quantum well, where the positive direction is along the [0001], (b) energy band diagram and charge profile for (b) Device I, (c) Device II, (d) Device III, (e) combined conduction band diagrams and (f) combined valance band diagrams for Devices I, II and III. Data collected under equilibrium.

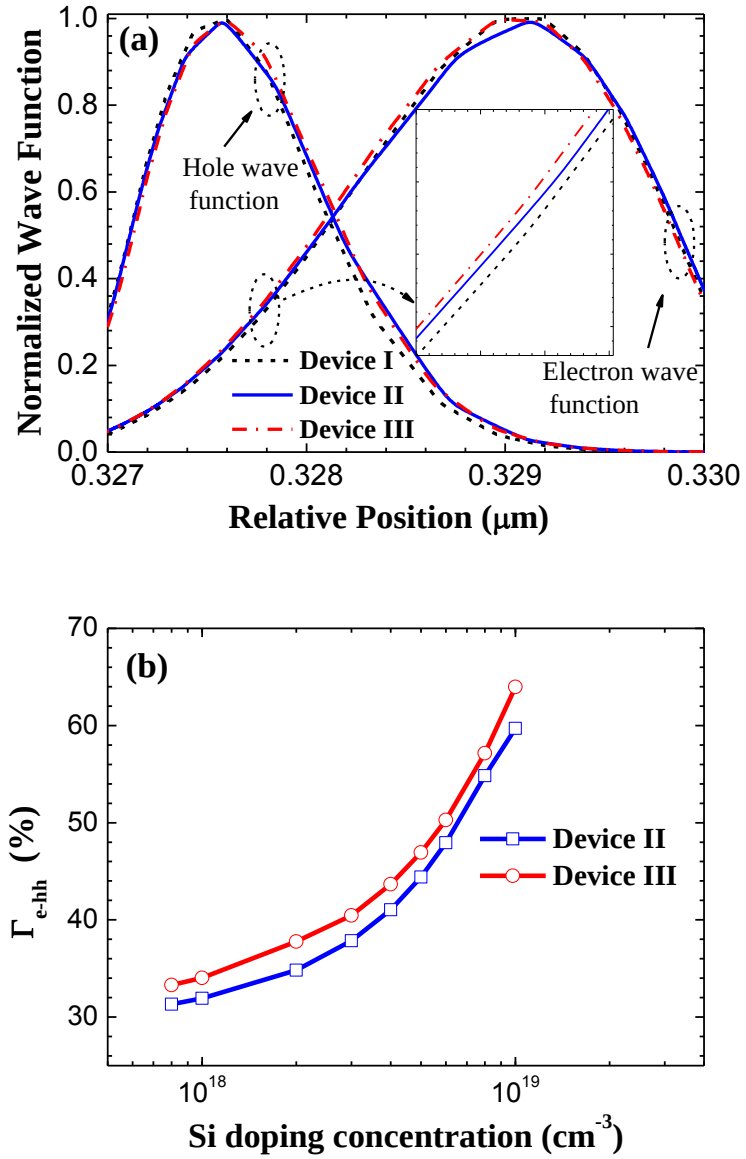

FIG. 4.1.7 (a) Normalized electron and hole wave functions for Devices I, II and III at 50 mA, and (b) $\Gamma_{e\text{-}hh}$ for Devices II and III as a function of Si doping concentration at 50 mA, while $\Gamma_{e\text{-}hh}$ for Device I is 29.94% as a reference.

4.1.4 Summary

In conclusion, the effect of Si step-doped quantum barriers on the optical power and EQE of the InGaN/GaN LEDs is studied. Improvements have been observed in the proposed LED with Si step-doped quantum barriers. This is mainly attributed to the reduced barrier height for the hole injection and the

excellent screening effect on QCSE. Furthermore, LEDs with Si step-doped quantum barriers shows better screening effect on the QCSE than LEDs with Si fully doped quantum barriers. The proposed approach of step-doped quantum barriers can be used to increase the efficiency and hence holds great promise for high-efficiency GaN-based LEDs.

4.2. A PN-type quantum barrier for InGaN/GaN light-emitting diodes

4.2.1 Introduction

P-type GaN is a milestone in the development of InGaN light-emitting diodes (LEDs), since the issues of low p-type conductivity have been solved [6, 7]. Tremendous progress has been made for InGaN/GaN LEDs in the past decades, and they are now regarded as the new-generation light-emitting sources to replace the traditional lamps [12-14]. However, due to the heavy effective mass and low mobility, a poor transport of holes is identified to be responsible for the undesired hole accumulation in the quantum well close to the p-GaN side, and thus significantly limits the device performance. In order to improve the hole transport in the active region, InGaN quantum barriers with a graded InN fraction was previously proposed to homogenize the hole distribution [64]. Besides, selectively Mg-doped quantum barriers were found to facilitate the hole transport in the active region both numerically [65] and experimentally [122]. A thinner quantum barrier proves effective in homogenizing the hole distribution [123], but the electrons may fly over the thin quantum barriers without recombining with the holes. Thus, in addition to enhancing the hole transport, it is also essential to enhance the electron

confinement by properly designing the electron blocking layer (EBL) and the quantum barriers, such as those based on the polarization matched AlGaInN used as EBL [66, 124] and thin AlGaN or InAlN used as the cap layer for the quantum barriers [44-46].

According to the discussions in Chapter 4.1, InGaN/GaN LEDs grown along *c*-orientation experience a strong polarization-induced electric field [42], which spatially separates the electron-hole wave functions (i.e., quantum confined Stark effect-QCSE), and thus reducing the radiative recombination rates of the active region [29, 30, 55]. Therefore, to improve the optical matrix element, as has also been demonstrated in Chapter 4.1, we designed and demonstrated high performance LEDs with Si step-doped quantum barriers, which effectively suppresses the QCSE in the active region [28]. Though the QCSE could be effectively suppressed through Si step-doped quantum barriers, the hole injection was still affected with the introduction of Si dopants in the quantum barriers compared to the case of undoped quantum barriers. To address this problem, we have numerically and experimentally investigated light-emitting diodes with the PN-type quantum barriers, which can effectively reduce the QCSE while keeping a better hole transport across the active region.

4.2.2 Experiment

Figures 4.2.1(a), 4.2.1(b), and 4.2.1(c) depict the schematic energy band diagrams of the InGaN/GaN active region for the devices with the undoped quantum barriers, Si step-doped quantum barriers, and PN-doped quantum barriers, respectively. The devices were grown on c-sapphire substrates by AIXTRON metal-organic chemical vapor deposition (MOCVD) system. The growth was initiated on c-sapphire substrates. A 30 nm low-temperature

nucleation layer was grown prior to a 2 μm u-GaN layer. The doping profile in the subsequent 4 μm thickness n-GaN layer ($N_D = 5 \times 10^{18}$ cm^{-3}) was achieved through the diluted SiH_4, while Cp_2Mg was used for the p-GaN layer (0.2 μm with the Mg dopant concentration of 3×10^{19} cm^{-3}). TMGa and NH_3 serve as the precursors for the bulk GaN layer. A 20 nm p-$Al_{0.20}Ga_{0.80}N$ layer was inserted between the five-period InGaN/GaN multiple quantum wells (MQWs) and the p-GaN layer as the electron blocking layer, which was grown under 100 mbar to prevent the parasitic reaction between TMAl and NH_3. The width of the $In_{0.15}Ga_{0.85}N$ quantum wells is 3 nm, for which TMIn and TEGa were used as the group-III reaction precursors. We used a growth temperature of 742 ^oC and 785 ^oC for the quantum well and quantum barrier growth, respectively. The three devices only differ from each other in their quantum barrier architecture. Device I is the reference device with the undoped GaN as the quantum barriers (12 nm), while N-type step-doped quantum barriers [4 nm doped thickness with $N_D = 5 \times 10^{17}$ cm^{-3} in Fig. 4.2.1(b)] were used in Device II according to our previous work [28]. Device III is the with PN-type quantum barriers. In order to suppress the Mg diffusion [125], the quantum barriers are selectively doped by Mg dopants as shown in Fig. 4.2.1(c). Specifically, the growth of each PN-type quantum barrier was divided into three steps under the same growth temperature of 742 ^oC, while the growth pressure was kept to be 305 mbar. We grew undoped GaN region for 4 nm first, then Cp_2Mg was supplied to grow the P-type region of 4 nm thickness. The molar ratio between Cp_2Mg and TEGa was 5.26×10^{-4}. Lastly, the remaining 4 nm N-type GaN region was grown by closing the Cp_2Mg supply and opening SiH_4 supply. The thermal annealing to activate Mg dopants for both PN-type quantum barriers and p-GaN layer was

conducted for 600 sec under 730 ^{o}C. However, because of the large ionization energy of Mg (~ 200 meV) and the hydrogen-passivation in the GaN layer, thus, we set the Mg ionization efficiency to 1% in our simulation [89]. Note that, although we have selectively doped the quantum barriers by Mg dopants, the Mg diffusion still cannot be avoided, and this inevitably increases the Shockley-Read-Hall recombination rates [126]. However, this negative aspect will be cancelled out by enhancing the hole transport and suppressing the polarizations in the quantum wells.

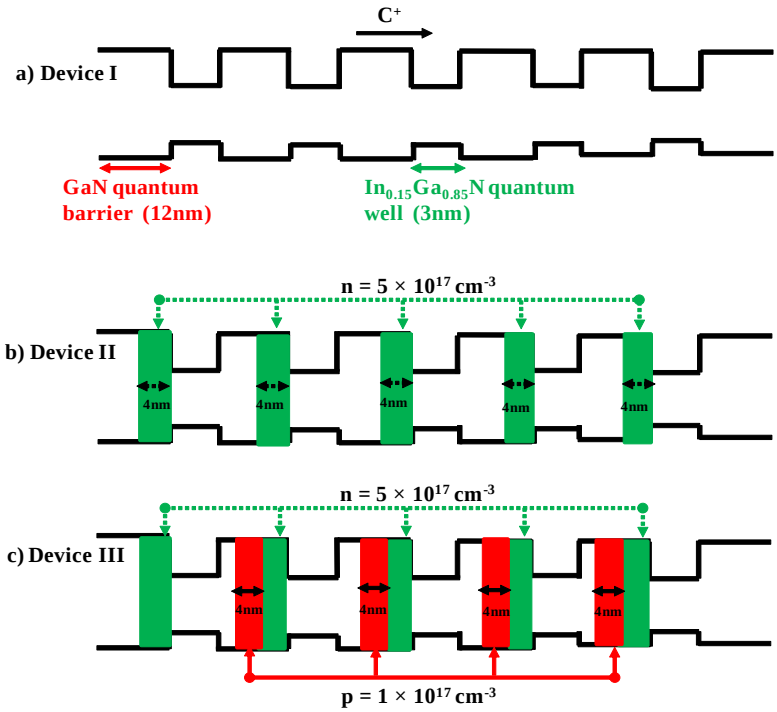

FIG. 4.2.1 Schematic energy band diagrams of the InGaN/GaN active region for (a) Device I with the undoped quantum barriers, (b) Device II with the Si step-doped quantum barriers and (c) Device III with the PN-type quantum barriers.

4.2.3 Results and discussions

The devices are modelled and systematically simulated using APSYS [119], which self-consistently solves the Poisson equations, Schrödinger equations and

the continuity equations with the proper boundary conditions. The six-band *k* p theory is performed to take account of the carrier screening effect in InGaN quantum wells [25]. The energy band offset ratio between the conduction band and the valence band in the InGaN/GaN quantum well region is set to be 70/30 [35]. In order to consider the crystal relaxation by generating misfit dislocations, only 40% of the theoretical polarization charge density is assumed [20]. We have set the Auger recombination coefficient to be 1×10^{-30} cm^6/s [18, 19]. The Shockley-Read-Hall (SRH) lifetime for electrons and holes is set to be 43 ns [19]. The other parameters used in the simulations can be found in the previous work [83].

To verify the theoretical results, InGaN/GaN LED chips were fabricated by a standard fabrication process. The mesa of the LED (with a chip size of 350 × 350 μm^2) was obtained by reactive ion etch (RIE). Ni/Au (5 nm/5 nm) was deposited by E-beam as the transparent current spreading layer (TCL) on the p-GaN layer. Ti/Au (30 nm/150 nm) was finally deposited on the n-GaN layer and TCL simultaneously for metal contacts.

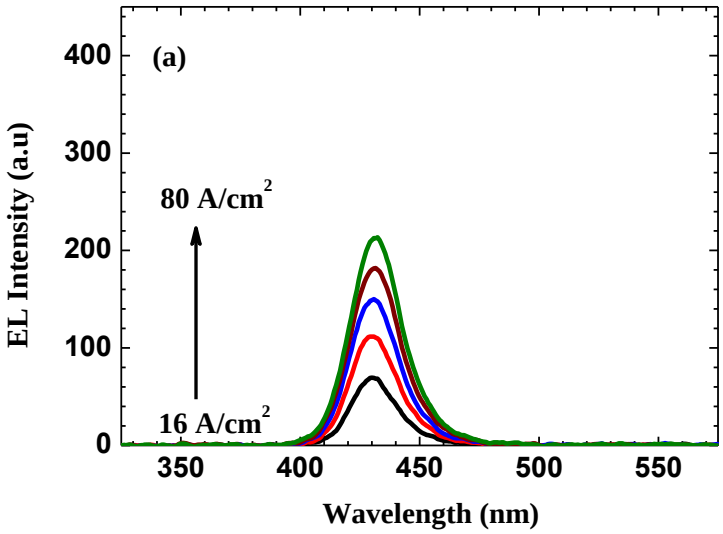

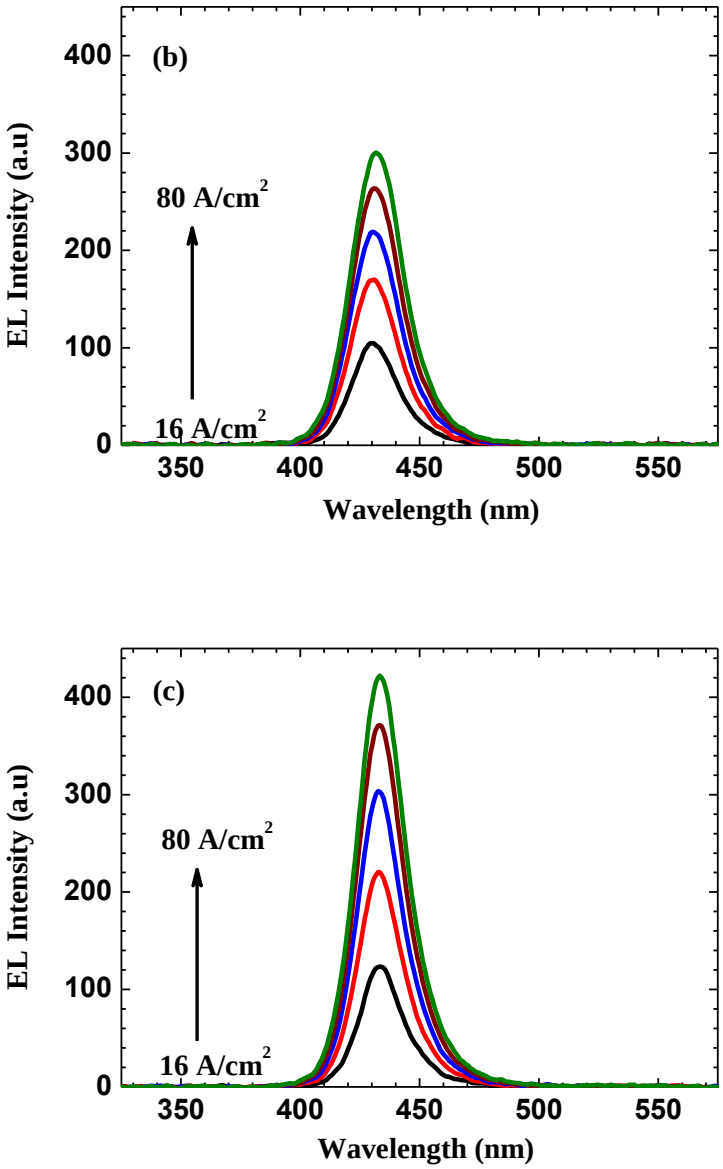

FIG. 4.2.2 Experimentally measured EL spectra for (a) Device I, (b) Device II and (c) Device III at 16, 32, 48, 64 and 80 A/cm^2, respectively.

Figures 4.2.2(a), 4.2.2(b) and 4.2.2(c) show the experimentally measured electroluminescence (EL) spectra at various current density levels for Devices I, II and III, respectively. Among the three devices, the strongest EL intensity is observed from Device III with the PN-type quantum barriers. The strong EL intensity is attributed to the improved hole transport across the active region with the introduction of Mg dopants. In addition, the screening of the QCSE by

Si step-doping the quantum barriers has also increased the radiative recombination rates in the quantum wells, resulting in a better device performance.

The experimentally measured optical output power and external quantum efficiency (EQE) for Devices I, II and III are shown in Fig. 4.2.3(a). Consistently with the EL results shown in Fig. 4.2.2 and the simulated results shown in Fig. 4.2.3(b), Device II and Device III emit more optical power than Device I with Device III being the strongest. The optical power measured for Devices I, II and III at 150 A/cm^2 is 18.29, 24.50, and 31.65 mW, respectively in Fig. 4.2.3(a). This translates to a power enhancement of 33.95% and 73.05% for Device II and Device III, respectively, compared to that of Device I. The simulated optical output power and EQE for Devices I, II and III are shown in Fig. 4.2.3(b) which are in excellent agreement with the experimental results shown in Fig. 4.2.3(a). The simulated results provide us an insightful understanding on the improvement of the optical power and EQE of the proposed device. It is found that the screening effect of the QCSE by the Si-doped quantum barriers is responsible for the improvement observed in Device II [28] and partially responsible for Device III. The further improvement in Device III comes from the hole transport promotion by Mg doping the quantum barriers. Through the application of the PN-type quantum barriers, the energy band structure, hole distribution across the active region, and the electric field profile have been modified and become favourable for the improvement of the optical output power and EQE, which will be shown in detail subsequently. It should be noted that although the experimental and simulated results are generally in excellent agreement, there still exist some discrepancies in the

absolute values and trending details at the low current density levels. These are due to the uncertainties in the temperature dependence of the parameters used in simulation such as the Auger recombination coefficient, the Shockley-Read-Hall recombination coefficient and the thermal conductivity of the compounds as well as the experimental error at the low current density levels.

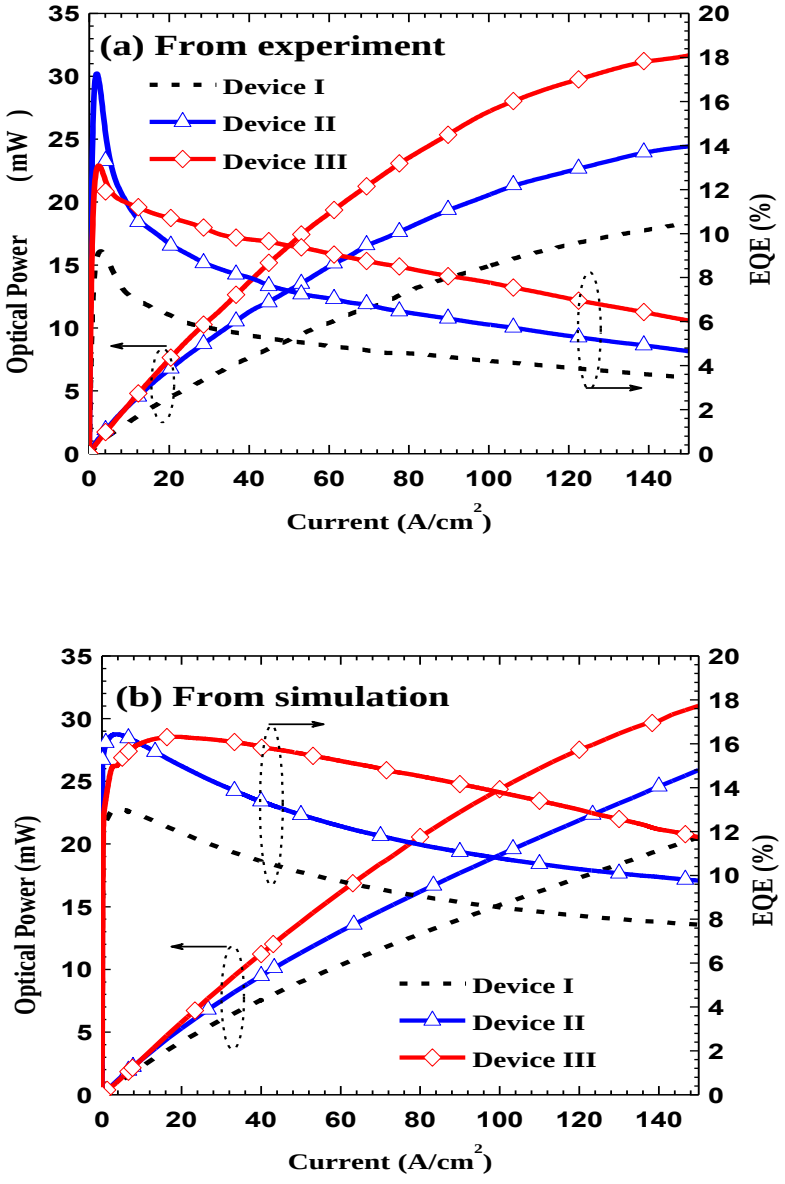

FIG. 4.2.3 (a) Experimental and (b) simulated optical output power and EQE as a function of the driving current for Devices I, II and III, respectively.

Figures 4.2.4(a), 4.2.4(b) and 4.2.4(c) show the calculated energy band diagrams for Devices I, II and III with the injection current of 40 A/cm^2, respectively. It is clearly shown that Device I has the smallest energy barrier height for holes [Fig. 4.2.4(a)]. The effective valance band barrier heights ($\Delta\Phi_h$) are 840, 716, 625 and 545 meV, respectively, as shown in Fig. 4.2.4(a). However, once the quantum barriers are step-doped with Si in Device II [see Fig. 4.2.4(b)], the effective valance band barrier heights are increased to 875, 755, 655 and 567 meV, respectively. Although the step-doped quantum barrier with Si dopants is effective in screening the QCSE [28], the increase in its valance band barrier height blocks the hole injection into the quantum wells away from the p-GaN layer, and this may limit the device performance. Fortunately, the hole blocking effect can be relieved in the PN-type quantum barriers through the introduction of Mg dopants [see Device III in Fig. 4.2.4(c)]. Therefore, the effective valence band barrier heights in the LED with PN-type quantum barriers are reduced to 845, 719, 627 and 550 meV, respectively.

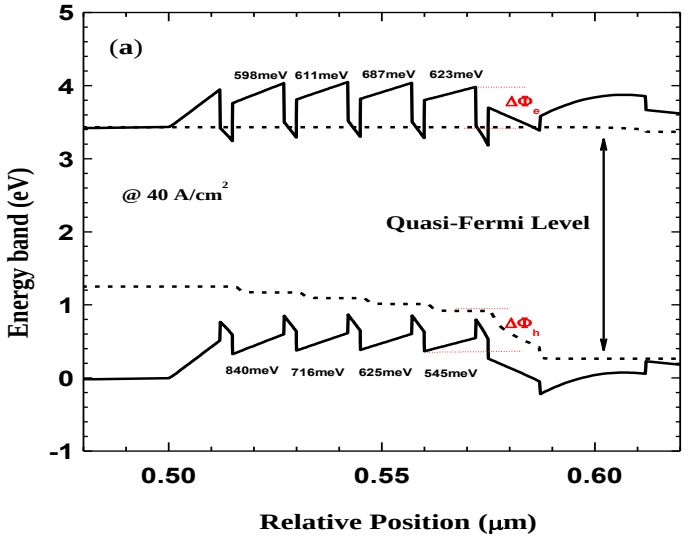

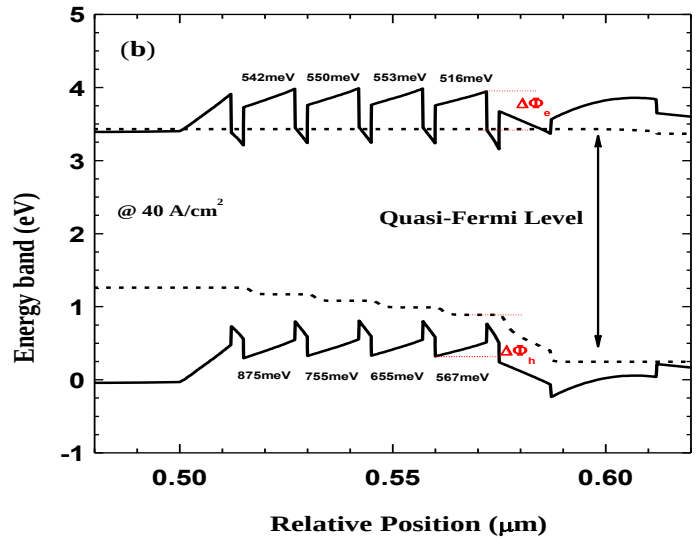

FIG. 4.2.4 Calculated energy band diagrams for (a) Device I, (b) Device II and (c) Device III at 40 A/cm^2, along with the effective conduction band barrier height ($\Delta\Phi_e$) and the effective valance band barrier height ($\Delta\Phi_h$).

In order to reveal the hole transport for Devices I, II and III with various quantum barrier schemes, we have further simulated the hole distribution across the quantum wells, as shown in Fig. 4.2.5(a). Comparatively, we can see that Device I shows the most homogenous hole distribution across the active region

because of the undoped GaN quantum barriers. On the other hand, for Device II, the holes have difficulty to penetrate deep into the active region due to its increased valence band barrier heights. As for Device III, since the valance band barrier heights are reduced through introducing Mg in the quantum barriers, holes are better distributed compared to Device II. However, according to the aforementioned molar ratio between Cp_2Mg and TEGa in the experiment, the ionized Mg in the quantum barriers is assumed to be 1×10^{17} cm^{-3} in our simulation, which is still smaller than the Si doping concentration, thus the valance band barrier height in Device III is still a bit larger than that in Device I, and we still observe a less homogenous hole distribution if compared to Device I. Nevertheless, one can also properly reduce the quantum barrier thickness of Device III for an even better hole transport. Separately, we have examined the radiative recombination rates in each quantum well for Devices I, II and III numerically, as shown in Fig. 4.2.5(b). Although Devices I, II and III have the identical hole concentration in the quantum well that is closest to the p-GaN layer, the excellent screening of the QCSE with the Si-doped quantum barriers facilitates the strongest radiative recombination rates in the last quantum well for both Devices II and III [28]. Therefore, the enhanced overall radiative recombination rates and optical output power have been obtained in Figs. 4.2.3(a) and 4.2.3(b), respectively. For the rest of the quantum wells that are away from the p-GaN layer, Device III has the better radiative recombination rates compared to Device II due to the reduced valance band barrier height by selectively doping Mg in the quantum barriers, and this translates to the strongest optical output power for Device III according to Figs. 4.2.3(a) and 4.2.3(b), respectively.

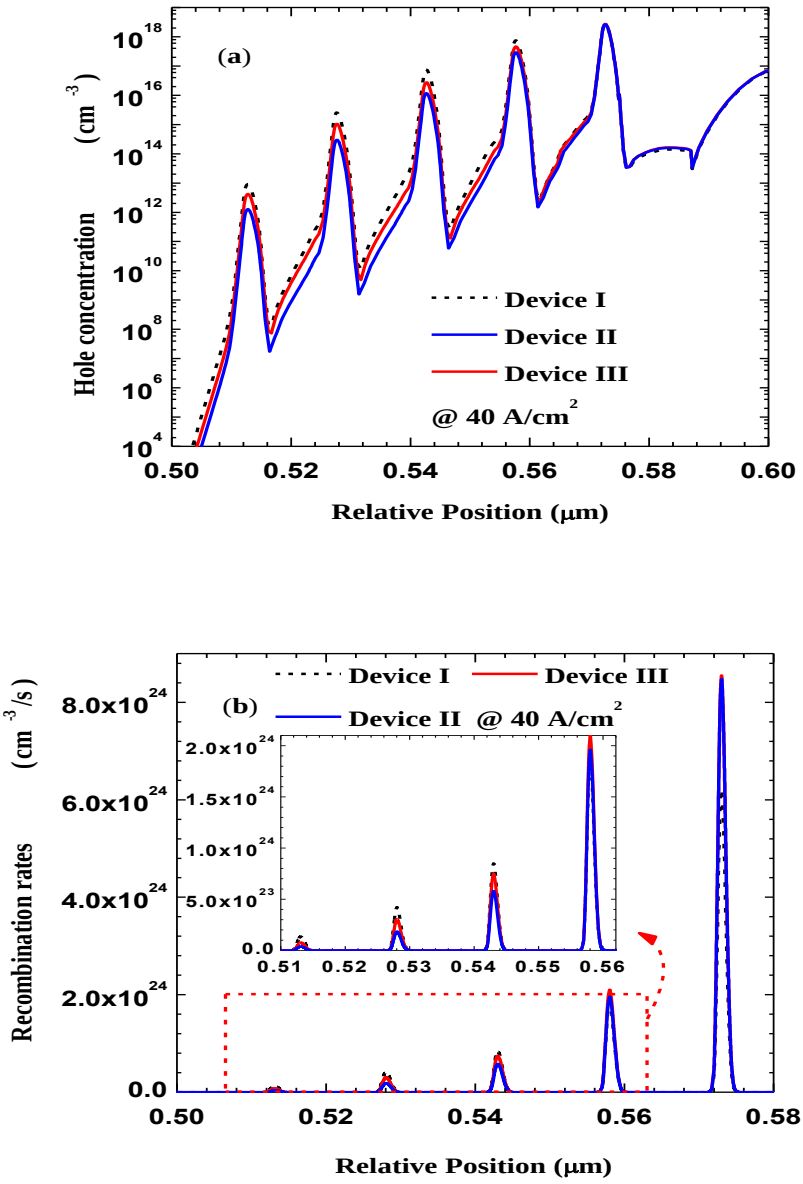

FIG. 4.2.5 Simulated (a) hole concentration and (b) the radiative recombination rates for Devices I, II and III, respectively.

The simulated leakage current is shown in Fig. 4.2.6. We have seen that the leakage current is 62.9%, 61.0% and 56.4% for Devices I, II and III, respectively. The suppressed leakage current in Devices II and III compared to Device I is attributed to the increased overall radiative recombination rates in the active region [see Fig. 4.2.5(b)] [35]. On the other hand, by introducing Mg dopants in the quantum barriers, the effective conduction band barrier height

($\Delta\Phi_e$) can be increased for Device III when compared to Device II [see $\Delta\Phi_e$ in Figs. 4.2.4(b) and 4.2.4(c)]. Thus, an even better electron confinement in Device III is obtained once the effective conduction band barrier height is increased [44, 66], and this can further reduce the electron leakage current according to Fig. 4.2.6.

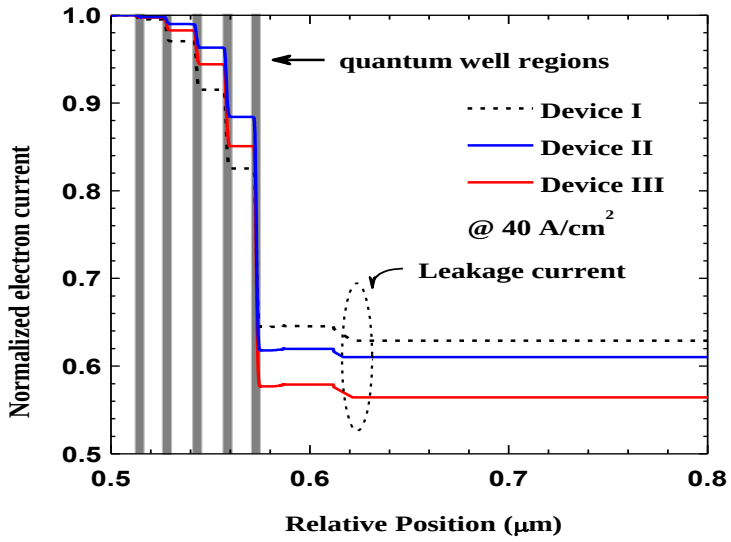

FIG. 4.2.6 Simulated leakage current for Devices I, II and III, respectively.

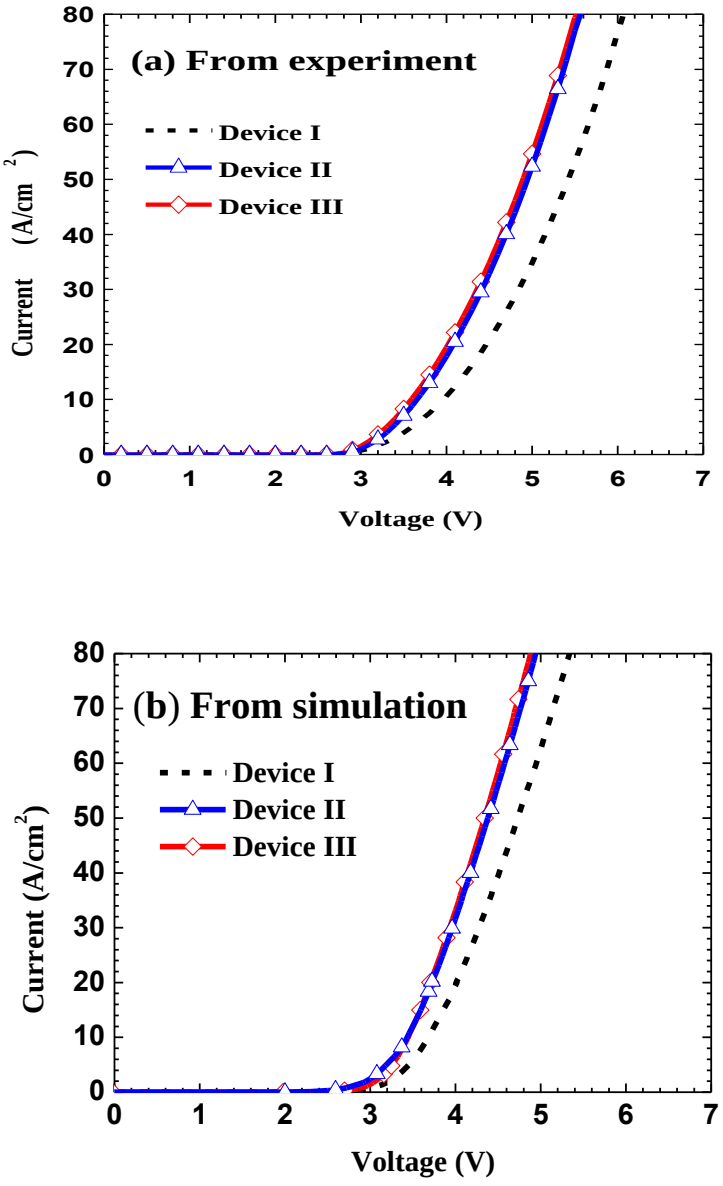

FIG. 4.2.7 (a) Experimentally measured and (b) simulated current as a function of the applied voltage for Devices I, II and III, respectively.

The measured and simulated current as a function of the applied bias for the LED chips are demonstrated in Figs. 4.2.7(a) and 4.2.7(b), respectively. It can be seen from Figs. 4.2.7(a) and 4.2.7(b) that Devices II and III exhibit a substantial improvement in their electrical performance compared to Device I. The enhanced on-state current is due to the improved electron transport in Devices II and III both with Si-doped quantum barriers. The Mg-doping in the

quantum barriers for Device III also helps to enhance the hole injection and thus Device III has a slightly better electrical performance than Device II both from experiment and simulation. Furthermore, the strong radiative recombination current helps for a better electrical conductivity.

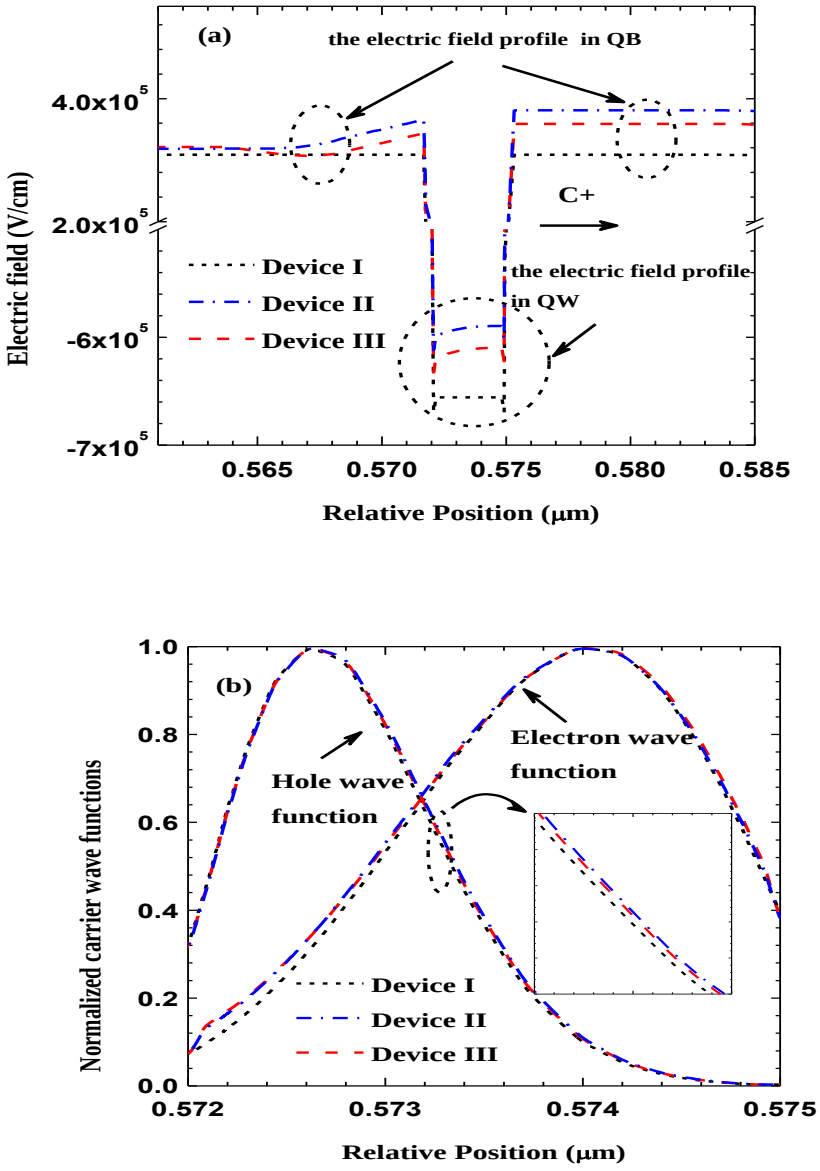

FIG. 4.2.8 (a) Electric field profile under equilibrium and (b) distribution of the electron and hole wave functions in the quantum well closest to the p-GaN layer for Devices I, II, and III, respectively. The positive direction of the electric field in (a) is along the growth orientation, i.e., c^{+}-orientation.

According to Fig. 4.2.5(b), the quantum well closest to the p-GaN layer contributes most to the radiative recombination, and thus it is worth studying the electric field within it through the theoretical simulation. We have shown the electric field profile for the last quantum barrier (QB)-quantum well (QW) pair under the equilibrium in Fig. 4.2.8(a). It can be seen that the electric field within the QW is reduced in both Devices II and III compared to Device I. The reduced electric field in the QW is due to the screening effect of the QCSE by the ionized Si dopants and the electrons diffusing into the QW, as has been reported by our previous work [28]. The QW electric field in Device III is slightly larger than that in Device II, which is due to the Mg compensation effect to the Si dopants in the quantum barrier. The carrier wave functions at 40 A/cm^2 are demonstrated in Fig. 4.2.8(b) for Devices I, II and III, respectively. As has been reported in our previous work [28], a reduced electric field in the quantum well enhances the electron-hole overlap level ($\Gamma_{e\text{-}hh}$). Hence, the calculated $\Gamma_{e\text{-}hh}$ is 30.83%, 33.13% and 32.87% in Fig. 4.2.8(b) for Devices I, II and III, respectively. It can be seen that PN-type quantum barrier is less effective in screening QCSE if compared to Si-step-doped quantum barrier. Nevertheless, the improved hole transport promotes the radiative recombination and thus the optical power and EQE have been significantly enhanced. It should be noted that the existence of the Mg-Si-doped quantum barrier as shown in Device III will gives rise to a built-in PN-junction which is reversely biased when the device is forwardly operated. However, this reversely biased PN-junction will not result in a large electrical resistance, since the ionized Mg dopants in the quantum barriers is 1×10^{17} cm^{-3} with a 4 nm thickness while the Si doping concentration is 5×10^{17} cm^{-3} with a 4 nm thickness, and hence the P-

doped region in the quantum barriers is fully depleted and the quantum barriers will be in a reach-through mode [21]. As a result, any increased bias can promote a high current flow.

Besides, it is noteworthy that we have utilized four PN-type quantum barriers in this work. However, the Mg doping concentration, the number of PN-type quantum barriers and the Mg-doped position in each quantum barrier can be further optimized. By doing so, the possible Mg diffusion from the PN-type quantum barriers into the quantum wells can be further suppressed. Meanwhile, considering the compensation effect to the Si-doped position by those diffused Mg dopants in each quantum barrier, the Si dosage and Si-doped thickness can also be properly increased.

4.2.3 Summary

In conclusion, the InGaN/GaN LED with PN-type quantum barriers is proposed and investigated both numerically and experimentally in this work. Substantial enhancement of the optical output power of the LED has been achieved, which is due to the screening of the QCSE by Si doping and the promoted hole transport across the multiple quantum wells of the LED structure. The PN-type quantum barrier is favourable for the more homogenous distribution of holes and radiative recombination rates across the whole active region in the proposed device, yielding a better device performance. In addition, the increased effective conduction band barrier height in the proposed PN-type quantum barriers further suppresses the electron overflow, which further improves the device performance. As a result, the proposed PN-type quantum barriers theoretically and experimentally prove to be very promising for high-performance LEDs.

4.3 Summary

In this chapter, we have investigated and demonstrated the effect of quantum barriers with Si-step-doping and Mg-Si-doping (i.e., PN-type) features on InGaN/GaN LEDs. Substantially improved screening effect of the QCSE has been obtained due to the optimized doped position in quantum barriers through Si dopants. The hole blocking effect by Si-step doped quantum barriers has been further suppressed through selectively doping the quantum barriers with Mg dopants of proper dosage. By doing so, we have received, on one hand, the improved hole transport, and on the other hand, the excellent screening effect to the polarizations in the quantum wells, thus reducing the spatial separation between electron-hole wave functions. Nevertheless, the dosage and the doped region for both Si and Mg dopants can be further optimized in the future work. In the meanwhile, the number for doped quantum barriers is also awaiting further optimizations.

Chapter 5 Improved InGaN/GaN light-emitting diodes through manipulating the current spreading effect

In addition to the quantum confined Stark effect and the insufficient hole injection, current crowding underneath the p-contact has also significantly limited the device performance of InGaN/GaN light-emitting diodes (LEDs) grown on insulating substrates (e.g., sapphire) with lateral current injection scheme [21, 28, 57-60]. The schematic diagram of current flow for InGaN/GaN LEDs grown on sapphire substrates and the corresponding equivalent electric circuit are shown in Figs. 5.1(a) and 5.1(b). According to Fig. 5.1(a), the InGaN/GaN LED comprises n-GaN layer, multiple quantum wells (MQWs), p-GaN layer and transparent current spreading layer (TCL). Meanwhile, we can see that the current both go vertically and laterally. As suggested by Fig. 5.1(b), we have the resistance of TCL (R_{TCL}) and n-GaN layer ($R_{n\text{-}GaN2}$ and $R_{n\text{-}GaN3}$). The total vertical resistance for each branch is denoted as R_x, which is the summation of the resistance of p-GaN ($R_{p\text{-}GaN}$), MQW (R_{MQW}) and n-GaN ($R_{n\text{-}GaN1}$) regions while the interfacial resistance between TCL and p-GaN is $R_{TCL/p\text{-}GaN}$. Thus, $R_x = R_{p\text{-}GaN} + R_{MQW} + R_{n\text{-}GaN1} + R_{TCL/p\text{-}GaN}$. We have also divided the total current into I_0, I_1 and I_2.

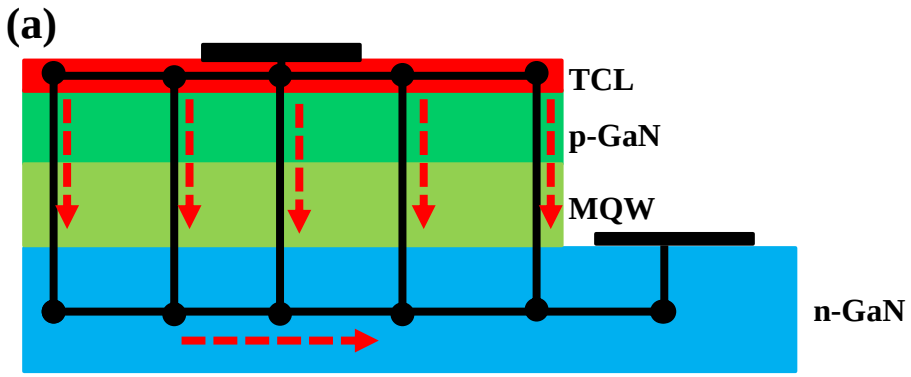

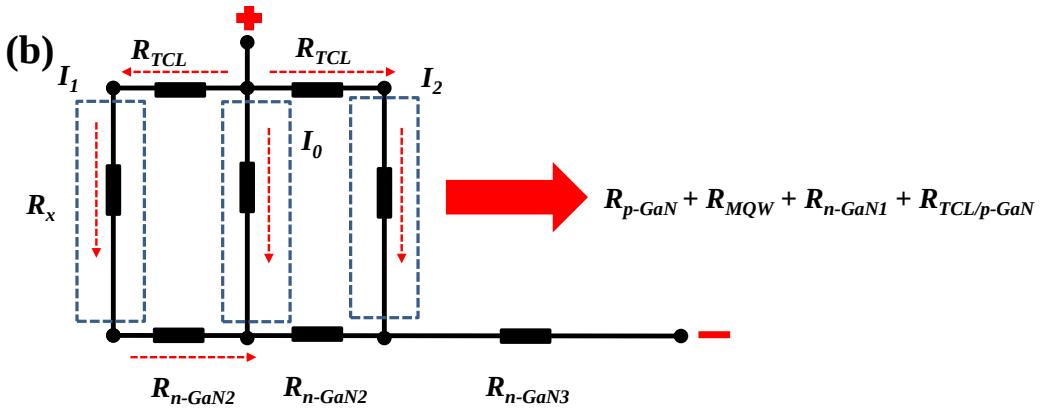

FIG. 5.1 (a) Schematic diagram for current flow and (b) simplified equivalent electric circuit for InGaN/GaN light-emitting didoes grown on insulating substrates.

According to Fig. 5.1(b), we can get the relationship among I_0, I_1 and I_2, as has been shown in Eqs. 5.1 and 5.2. Thus, in order to increase I_1, one can either increase R_x or reduce R_{TCL}. Moreover, a reduced R_{TCL} also benefits I_2. However, our TCL normally is 100 ~ 200 nm, while the n-GaN layer is of 2 ~ 4 μm, thus the area of the cross section through which the current flow of TCL is smaller than that of n-GaN layer, and hence it is believed $R_{n\text{-}GaN2} < R_{TCL}$. Hence, according to Eq. 5.2, an increase in R_x enhances I_2.

$$\frac{I_1}{I_0} = \frac{1}{1 + \dfrac{R_{TCL} + R_{n-GaN2}}{R_x}} \tag{5.1}$$

$$\frac{I_2}{I_0} = 1 + \frac{R_{n-GaN2} - R_{TCL}}{R_x + R_{TCL}} = \frac{R_{n-GaN2} + R_x}{R_x + R_{TCL}} \tag{5.2}$$

Thus, the objective of this chapter is to reduce the current crowding effect for InGaN/GaN LEDs through growing either a resistive layer or a conductive layer depending on the location of the layer along the current path. We have obtained the improved optical output power and external quantum efficiency from the proposed devices. We have attributed the enhanced device

performance to the improved current spreading effect by increasing R_x and decreasing R_{TCL}. The details are to be addressed in sections 5.1 and 5.2, respectively.

5.1 Improved current spreading for InGaN/GaN light-emitting diodes with a p-GaN/n-GaN/p-GaN/n-GaN/p-GaN electrically resistive layer

5.1.1 Introduction

Besides the charge separation in QWs [31, 55, 105, 127-129], the high dislocation density [130-132] that limits the internal quantum efficiency (IQE), and the carrier leakage process that leads to the efficiency-droop [44, 133, 134], the current crowding at the p-contact is also regarded as one of the main obstacles [57, 135, 136], especially for conventional devices grown on insulating substrates (e.g., sapphire) [58]. The driven current tends to flow through the path with smaller resistivity, resulting in current crowding at the p-contact of these InGaN/GaN LEDs. The current crowding effect generates highly localized carrier density and heat underneath the p-electrode and thus leads to a non-uniform light emission of the InGaN/GaN LEDs [137]. In order to improve the current spreading, a resistive layer is generally added into the LED architecture [1]. For example, Tsai *et. al*. has proposed a current blocking layer formed by silicon dioxide nanoparticles [138] and the patterned Al_2O_3 on p-GaN for a better current spreading [59], while n-type InGaN was also proposed and inserted underneath the InGaN/GaN active region to improve the current spreading [139]. On the other hand, tunneling junction has also been proposed as a current spreading layer [140]. Most recently, more efforts have

been invested to the single-crystal ZnO as the current spreading layer [141]. In addition, the use of vertical LEDs has also been investigated for suppressing the current crowding in nitride-based LEDs [59, 60, 142]. In this work, we propose and demonstrate a lattice-matched p-GaN/n-GaN/p-GaN/n-GaN/p-GaN (PNPNP-GaN) epitaxial current spreading layer in the p-type cap region of the InGaN/GaN LEDs. In these devices, with this PNPNP-GaN epi-structure, the electrical performance is improved. Further enhancement of the optical output power and external quantum efficiency (EQE) has also been achieved, which is attributed to the improved current spreading in the proposed epi-structure.

5.1.2 Experiment

In our study, two sets of InGaN/GaN LED wafers (i.e., Reference LED and PNPNP-GaN LED sketched in Fig. 5.1.1) were grown by an AIXTRON close-coupled showerhead metal-organic chemical vapor deposition (MOCVD) reactor on c-plane patterned-sapphire substrates. The growth was initiated from a 30 nm low-temperature GaN buffer layer, then followed by a 2 μm u-GaN layer and a 4 μm n-GaN layer ($N_d = 5 \times 10^{18}$ cm^{-3}), which were both grown at 1050 ^oC. In the grown LED epi-samples, the active layer consists of five-period $In_{0.15}Ga_{0.75}N$/GaN multiple quantum wells (MQWs), with well and barrier thickness of 3 nm and 12 nm, respectively. The wells and barriers were grown at the same temperature of 730 ^oC. The Reference LED has a 0.2 μm thick p-GaN layer with a hole concentration of 3×10^{17} cm^{-3}. By inserting two 20 nm n-GaN ($N_d = 2 \times 10^{17}$ cm^{-3}) layers into p-GaN layer evenly, we obtained the PNPNP-GaN structure (0.067 μm /20 nm /0.067 μm /20 nm /0.067 μm) with the same thickness of the p-GaN layer in the reference device (refer to Fig. 5.1.1). The PNPNP-GaN layers were all grown at 1020 ^oC, which was lower

than the temperature (1050 ^{o}C) used for the growth of u-GaN and n-GaN layers to suppress the out-diffusion of the InN from the InGaN quantum wells. Specifically, the growth pressure for the n-GaN and p-GaN in the PNPNP-GaN structure was set to 150 mbar. The V/III ratio (NH_3/TMGa) during PNPNP-GaN growth was kept to be 4100. After the epi-wafers were grown, we performed the thermal annealing to activate the Mg dopants for p-GaN layers. The annealing was conducted for 10 min in the ambient of N_2 at a temperature of 720 ^{o}C for both the Reference LED and PNPNP-GaN LED wafers.

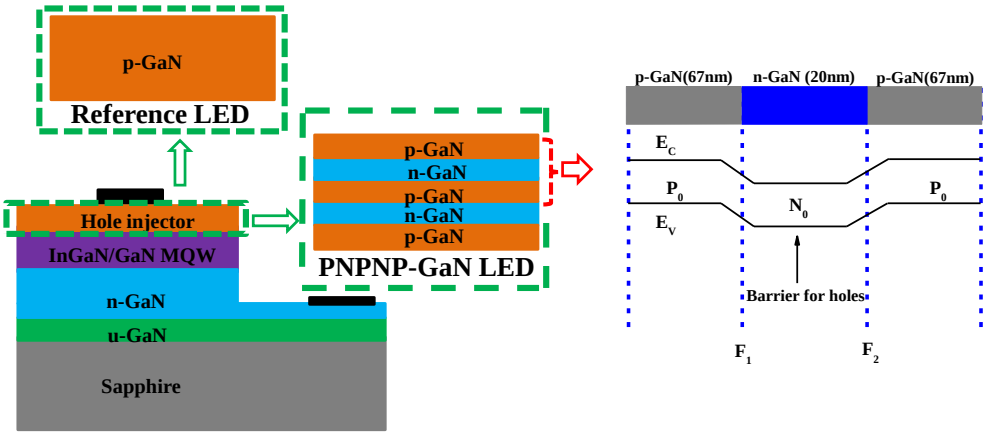

FIG. 5.1.1 Schematic diagrams of the studied devices (Reference LED without ITO coating and PNPNP-GaN LED without ITO coating), shown along with the band diagram of one PNP-GaN junction in the PNPNP-GaN LED.

After the LED wafers were grown, four sets of LED chips were fabricated using the standard fabrication process. The epi-wafers were patterned into mesas of size 350 μm × 350 μm through reactive ion etch (RIE). Ni/Au film (10 nm/150 nm) was first deposited as the p-electrode, and then the p-contact was annealed in the mixture of O_2 and N_2 at 515 ^{o}C for 5 min under the atmosphere pressure. Finally, Ti/Au (30 nm/150 nm) was deposited as the n-electrode. We have prepared two sets of devices without indium tin oxide (ITO)

coating (i.e., the Reference LED without ITO and PNPNP-GaN LED without ITO). The other two sets were prepared with ITO coating as the transparent current spreading layer (i.e., Reference LED with ITO and PNPNP-GaN LED with ITO, which are shown in the supplementary material). The transparent current spreading layer (i.e., ITO) was sputtered and annealed in the ambient of N_2 at 500 ^oC for 120 s before depositing electrodes. Also, we performed numerical simulations for the four sets of devices in APSYS [119], which solves the Poisson equation, continuity equation and Schrödinger equation with proper boundary conditions. The Auger recombination coefficient used in these simulations was 1×10^{-30} cm^6s^{-1} [19], and the energy band offset between the conduction band and the valence band was 70/30 [35]. Considering the crystal relaxation by generating dislocations, 40% of the theoretical polarization charge was assumed [20]. Other parameters can be found elsewhere [83].

5.1.3 Results and discussions

As indicated in Fig. 5.1.1, the PNPNP-GaN LEDs (i.e., PNPNP-GaN LED without ITO and PNPNP-GaN LED with ITO) own two layers of thin n-GaN (20 nm), sandwiched between 67 nm thick p-GaN layers. Each thin n-GaN forms two junctions at the interfaces (i.e., F_1 and F_2). When the InGaN/GaN LED is forward biased, F_1 is also forward biased, whereas F_2 is reversely biased. As the applied bias increases, the depletion region of F_1 shrinks, while F_2 extends its depletion region across the n-GaN. Thereby, the depletion region in the entire n-GaN layer can be retrieved, thus with the ionized Si donors here acting as the hole spreaders. With the doping concentration of n-GaN (2×10^{17} cm^{-3}) and p-GaN (3×10^{17} cm^{-3}), the built-in potential in the p-GaN/n-GaN is

3.23 V ($V_{bi} = \frac{kT}{e}\ln\left(\frac{N_A N_D}{n_i^2}\right)$, e is the elementary electronic charge, and n_i = 1.9 $\times 10^{-10}$ cm^{-3} for GaN). The total depletion region thickness is 162.83 nm ($W_T = \sqrt{\frac{2\varepsilon_r\varepsilon_0}{e}\left(\frac{N_A + N_D}{N_A N_D}\right)V_{bi}}$, ε_r = 8.9 for GaN, and ε_o is the absolute dielectric constant) [23], which consists of the depletion region in n-GaN and p-GaN of 97.70 and 65.13 nm, respectively, provided that n-GaN and p-GaN have infinite lengths. Therefore, the n-GaN layer, which has a thickness of only 20 nm, is fully depleted in PNPNP-GaN LEDs. Meanwhile, according to the principle of charge neutrality in the depletion region of a homojunction, the actual depletion width in p-GaN of the PNP-GaN junction is only about 13.33 nm. On the other hand, the diffusion length (L_D) of holes in the n-GaN can be obtained by using $L_D = \sqrt{D_p\tau_p} = \sqrt{kT\mu_p / e\tau_p}$ (where D_p is the diffusion constant of holes, correlated with μ_p by Einstein relationship, and k is the Boltzman constant). Here, the minority carrier (hole) lifetime in n-GaN with a doping concentration of 2 $\times 10^{17}$ cm^{-3} is assumed to be 0.8 ns, while the hole mobility is set to be 26 cm^2/Vs [22]. Thus, the diffusion length for holes is calculated to be ~231.9 nm, which is much larger than the thickness of n-GaN (20 nm) in each PNP-GaN junction of the PNPNP-GaN LED. As a result, there will be very few loss across the n-GaN region. Furthermore, there exists a reach-through breakdown voltage for the reversely biased junction (i.e., F_2), and the reach-through breakdown voltage is 0.08V in this case ($BV_{RT} = \frac{eN_D W_N^2}{2\varepsilon_r\varepsilon_0}$, and W_N is the width of n-GaN) [143]. It is worth mentioning that this BV_{RT} is smaller than the built-in potential within the p-GaN/n-GaN junctions, and this also manifests itself in

the full depletion of n-GaN by leaving behind ionized Si dopants as the hole spreaders. Therefore, after the depletion region extends through the whole n-GaN region, any increase in the applied bias will promote the injection of minority carriers (i.e., holes in our case) from the forward biased junction (i.e., F_1) to produce a high-current flow. For InGaN/GaN LEDs grown on insulating substrates with lateral current-injection scheme, the current travels both vertically and laterally as indicated in Fig. 5.1.2(a). As the sheet resistance of thick n-GaN layer is much smaller than the sheet resistance of the p-GaN layer, the current tends to flow through the low-resistivity n-GaN layer [Fig. 5.1.2(a)], giving a non-uniform current distribution in p-GaN (i.e., $I_1 > I_2 > I_3 > I_4 > ..... > I_n$), well known as the current crowding effect [1]. This current crowding effect can be suppressed if PNPNP-GaN is employed in the LED structure. A simplified equivalent circuit of the InGaN/GaN LEDs with the embedded PNPNP-GaN homojunctions is depicted in Fig. 5.1.2(b), in which the total current is divided into vertical current (J_1) and horizontal current (J_2). The total voltage drop consists of those in the p-contact, p-GaN, MQW region, n-GaN as well as n-contact. Based on the equivalent circuit in Fig. 5.1.2(b), Eq. 5.1.1 (for current path 1) and Eq. 5.1.2 (for current path 2) are obtained.

$$J_1 lw\frac{\rho_{p-GaN}t_p}{lw}+J_1 lw\frac{N\cdot\rho_{PNP}}{lw}+V_{pn}+V_{p-contact}+V_{n-contact}+J_1 lw\frac{\rho_{n-GaN}l}{wt_n}+\left(J_1 lw+J_2 wt_p\right)\frac{\rho_{n-GaN}l_0}{wt_n}=U \tag{5.1.1}$$

$$J_2 wt_p\frac{\rho_{p-GaN}l}{t_p w}+J_2 wt_p\frac{\rho_{p-GaN}t_p}{lw}+J_2 wt_p\frac{N\cdot\rho_{PNP}}{lw}+V_{pn}+V_{p-contact}+V_{n-contact}+\left(J_1 lw+J_2 wt_p\right)\frac{\rho_{n-GaN}l_0}{wt_n}=U \tag{5.1.2}$$

where l represents the length of the lateral current path, l_0 is the distance from the mesa edge to the center of the n-contact, and w is the length of the stripped

p-contact. The thickness of p-GaN and n-GaN is t_p and t_n, respectively; $\rho_{p\text{-}GaN}$ and $\rho_{n\text{-}GaN}$ are the resistivities for p-GaN and n-GaN, respectively. V_{pn} denotes the junction voltage drop of multiple quantum wells in InGaN/GaN LED; and $V_{p\text{-}contact}$ and $V_{n\text{-}contact}$ are the voltage drops across the p-contact and n-contact, respectively. ρ_{PNP} is the specific interfacial resistivity induced by the barrier height in each PNP-GaN junction. N is the total number of PNP-GaN junction, and in our device, there are two PNP-GaN junctions (i.e., PNPNP-GaN), and thus N is 2 (i.e., the total interfacial specific resistivity is $2 \times \rho_{PNP}$).

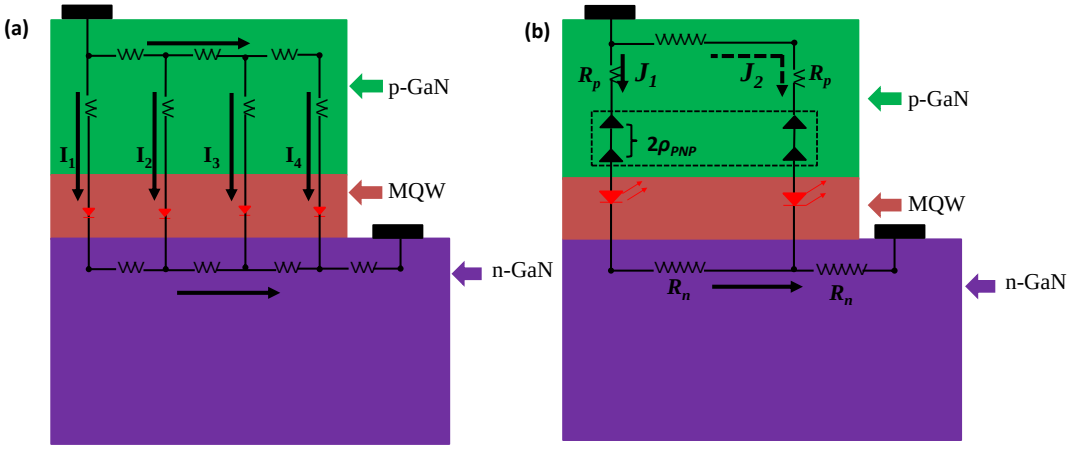

FIG. 5.1.2 (a) Equivalent circuit of an InGaN/GaN LED grown on an insulating substrate (e.g., sapphire) with lateral current-injection scheme ($I_1 > I_2 > I_3 > I_4 > ..... > I_n$), and (b) a simplified equivalent circuit of this InGaN/GaN LED with possible current paths (J_1 and J_2) when a PNPNP-GaN current spreading layer is embedded. ITO is not used in these two devices.

By equating Eq. 5.1.1 and Eq. 5.1.2, Eq. 5.1.3 is derived. However, l is in the order of device mesa size, which is 350 μm × 350 μm, while t_p is the scale of p-GaN thickness, which is ~ 200 nm. Since $t_p << l$, then Eq. 5.1.3 can be simplified into Eq. 5.1.4.

$$\frac{J_1}{J_2} = \frac{l}{t_p + \frac{N \cdot \rho_{PNP}}{\rho_{p-GaN}}} + \frac{t_p}{l} \tag{5.1.3}$$

$$\frac{J_1}{J_2} \cong \frac{l}{t_p + \frac{N \cdot \rho_{PNP}}{\rho_{p-GaN}}} \tag{5.1.4}$$

Equation 5.1.4 shows that a higher ratio of $N \cdot \rho_{PNP} / \rho_{p-GaN}$ is beneficial for enhancing the lateral current (i.e., J_2). To increase the ratio of $N \cdot \rho_{PNP} / \rho_{p-GaN}$, either $N \cdot \rho_{PNP}$ has to be increased or ρ_{p-GaN} has to be reduced. It is also feasible to increase the lateral current flow by increasing the p-GaN layer thickness (t_p).

Furthermore, the PNPNP-GaN will not have very abrupt interfaces because of the dopant diffusion, especially the Mg diffusion [144]. However, one still can maintain the PNPNP-GaN junctions by properly increasing the Si doping concentration and/or the n-GaN thickness. Through this, the junction barrier (i.e., ρ_{PNP}) in each PNP-GaN can be formed, and Eq. 5.1.3, Eq. 5.1.4, Eq. 5.1.S3 and Eq. 5.1.S4 are still valid to explain the current spreading. Meanwhile, the n-GaN doping and n-GaN thickness have to follow the design guidelines, which were addressed previously, such that n-GaN has to be completely depleted and the reversed junction F_2 will not block any current.

In order to probe the embedded PNPNP-GaN in terms of spreading current, we present the current as a function of voltage, as shown in Figs. 5.1.3(a) and 5.1.3(b). In the low forward voltage regime [0 ~ 3V in Figs. 5.1.3(a) and 5.1.3(b)], the PNPNP-GaN LED without ITO coating exhibits lower leakage current with respect to the Reference LED without ITO film in Fig. 5.1.3(a), while the same conclusion can be made for PNPNP-GaN LED with ITO

coating with respect to its Reference LED with ITO according to Fig. 5.1.3(b). The Reference LEDs (i.e., Reference LEDs without and with ITO) and PNPNP-GaN LEDs (i.e., PNPNP-GaN LEDs without and with ITO) have the similar crystal quality, as their full-width at half-maximum (FWHM) of (102) and (002) X-ray diffraction spectra are both about 213.5 and 216.0 arcsec, respectively. Thus the suppressed leakage current in PNPNP-GaN LEDs comes from the increased junction barrier height. As the PNPNP-GaN junctions are embedded in such InGaN/GaN LEDs with multiple heterojunctions, it is therefore difficult to extract the barrier height for PNPNP-GaN. Here, we calculate the effective overall barrier height by the following,

$$\phi_B = \frac{kT}{e}\ln\left(\frac{A \bullet T^2}{I_s}\right), \text{ with } I = I_s \bullet e^{\frac{eV}{nkT}} \qquad (5.1.5)$$

where $\varnothing_B$ is the overall barrier height within the LED device, and n is the ideality factor for the diodes [145, 146], which measures how close a diode follows the ideal diode equation. $\varnothing_B$ is calculated to be 1.10V for Reference LED without ITO and 1.31V for PNPNP-GaN LED without ITO, respectively. It is clearly revealed that a higher overall barrier height is obtained when PNPNP-GaN feature is integrated in the p-type layer. The ideality factor is 5.32 and 4.19 for Reference LED without ITO and PNPNP-GaN LED without ITO, respectively. An improved current spreading in PNPNP-GaN LED is responsible for the reduced ideality factor [147]. Furthermore, because of the improved current spreading effect in PNPNP-GaN LED without ITO, the electrical performance is improved compared to Reference LED without ITO when the applied bias is higher than 3V. Similarly, $\varnothing_B$ is determined to be 1.33V for Reference LED with ITO and 1.44V for PNPNP-GaN LED with ITO,

respectively. Moreover, the ideality factor is 6.52 and 4.51 for Reference LED with ITO and PNPNP-GaN LED with ITO, respectively. We also observed the increased overall energy barrier height in PNPNP-GaN LED with ITO, which in the meanwhile features the reduced ideality factor and the improved electrical properties compared to those in Reference LED with ITO. This is well attributed to the improved current spreading effect by the incorporation of PNPNP-GaN homojunctions. Note that, in order to improve the electrical property, the thickness of the n-GaN layer in the PNPNP-GaN junction has to be fully depleted under equilibrium.

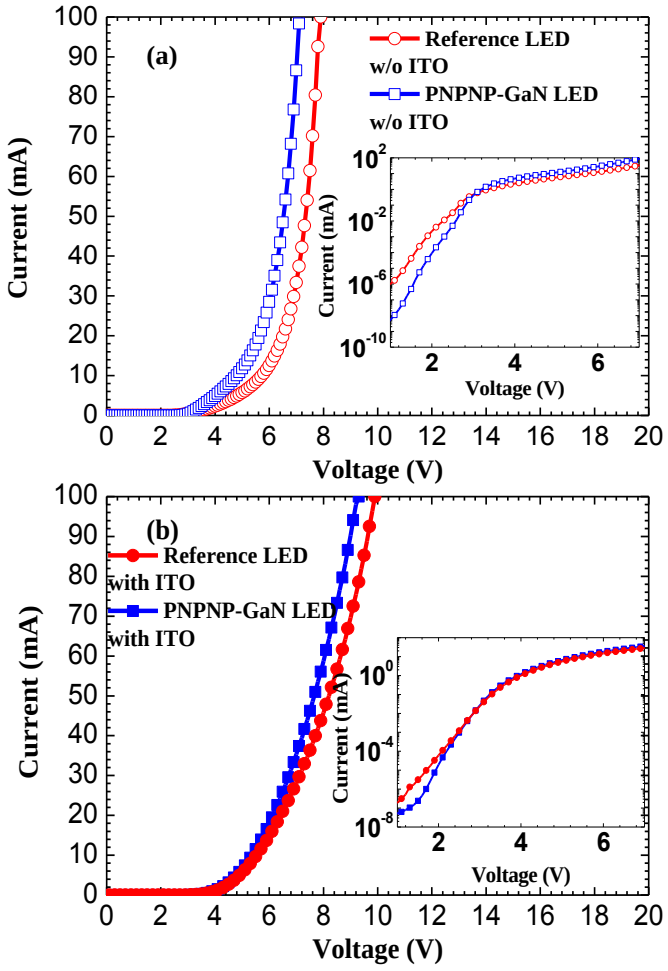

FIG. 5.1.3 Linear-plot of experimentally measured current as a function of the applied voltage for (a) Reference LED without ITO coating and PNPNP-GaN LED without

ITO coating (along with a semi-log plot inserted in the inset) and (b) Reference LED with ITO coating and PNPNP-GaN LED with ITO coating (again with a semi-log plot given in the inset).

The electroluminescence (EL) spectra [Figs. 5.1.4(a), 5.1.4(b), 5.1.4(c) and 5.1.4(d)] were collected under 10, 20, 30, 40 and 50 mA of the injection current for both Reference LEDs without and with ITO and PNPNP-GaN LEDs without and with ITO. Both the EL spectra of Reference LED without ITO and PNPNP-LED without ITO in Figs. 5.1.4(a) and 5.1.4(b) show a red shift as the injection current increases, which is due to a gradually increasing junction temperature during testing [118]. However, a less pronounced red shift observed in the EL spectra of Reference LED with ITO and PNPNP-LED with ITO in Fig. 5.1.4(c) and 5.1.4(d) is attributed to the significantly improved current spreading after ITO incorporation, which suppresses the high local heat caused by current crowding [137]. We can also see the EL intensity of PNPNP-GaN LEDs without and with ITO is enhanced compared to that of Reference LEDs without and with ITO, respectively. We also measured the integrated optical output power and EQE [Fig. 5.1.5(a)], which is compared with the simulated results for the four sets of studied devices [Fig. 5.1.5(b)]. We can see an improved optical output power and EQE for PNPNP-GaN LEDs without and with ITO in both experiments and simulations. Compared to Reference LED without ITO in Fig. 5.1.5(a), PNPNP-GaN LED without ITO shows a power enhancement of 10.19% and 12.16% at 20 mA and 100 mA, respectively, while PNPNP-GaN LED with ITO enhances the output power by 16.98% and 14.37% at 20 mA and 100 mA, respectively compared to Reference LED with ITO. The improved device performance in PNPNP-GaN LEDs without and with ITO is

attributed to the reduced current crowding effect. This in turn suppresses the high local carrier concentration, resulting in the reduced nonradiative Auger recombination in the multiple quantum wells [120]. Note that the slight discrepancies in the trending details for Figs. 5.1.5(a) and 5.1.5(b) are due to the uncertainties of the physcial parameters for III-nitride materials, such as the temperature/carrier dependance of the energy band offset, Auger recombination coefficient, etc. Especially, we have assumed a constant SRH recombination coefficient for each quantum well. However, in reality, the SRH recombination coefficient might vary in different quantum wells.

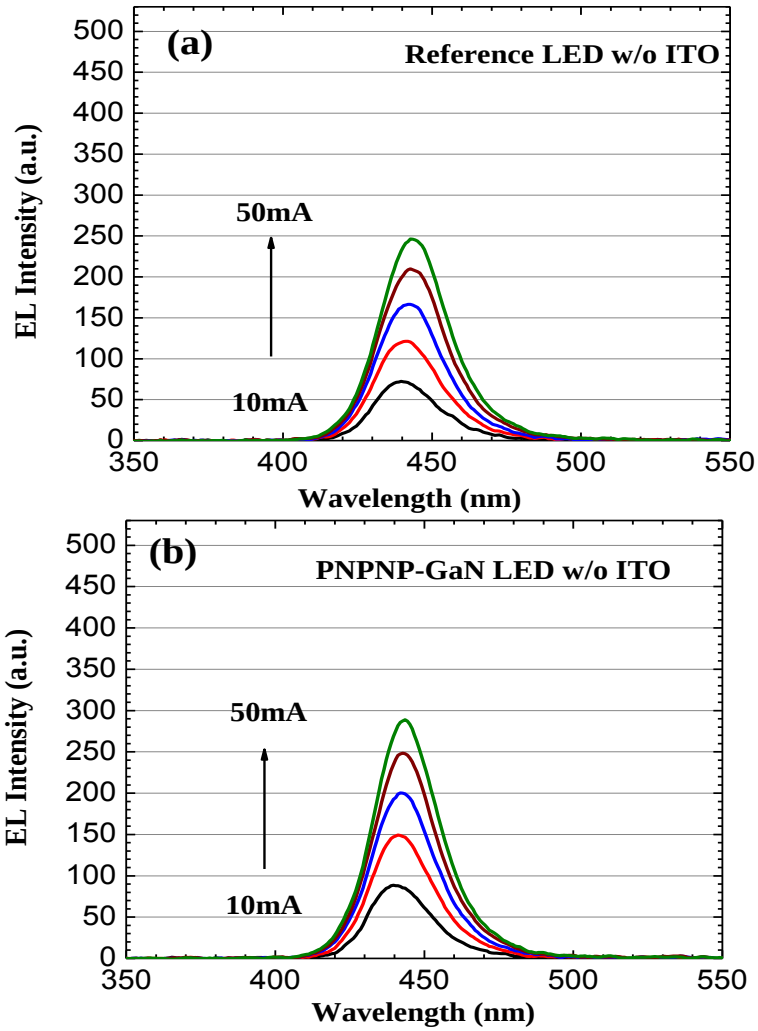

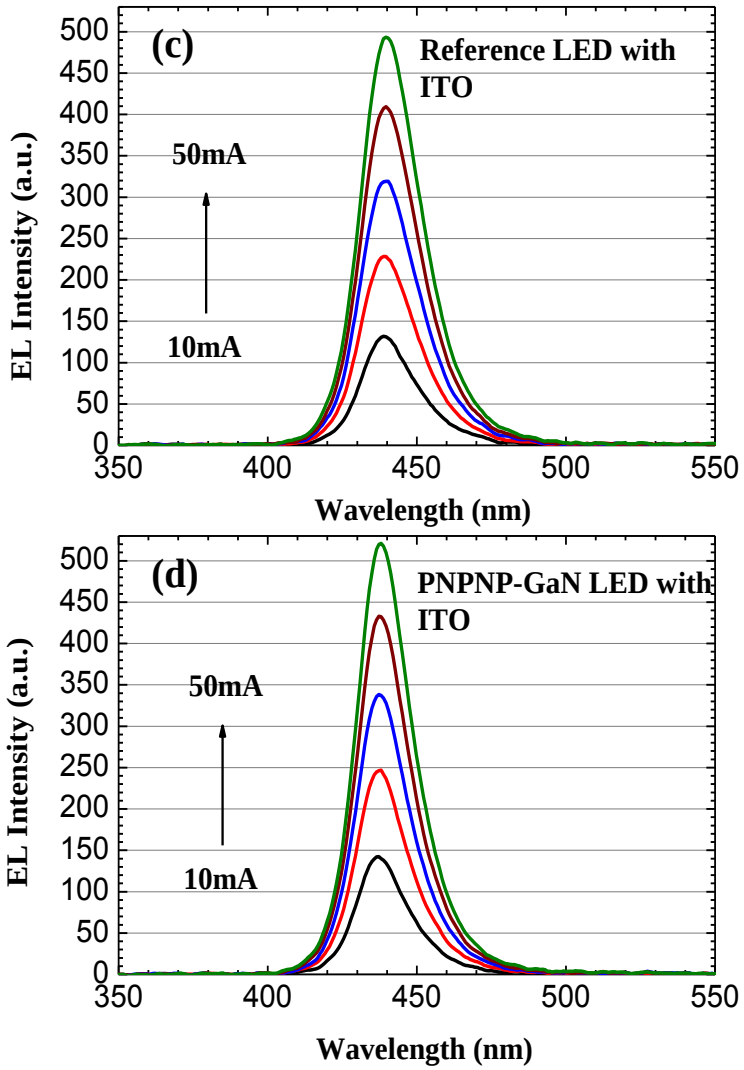

FIG. 5.1.4 Experimental EL intensity for (a) Reference LED without ITO coating, (b) PNPNP-GaN LED without ITO coating, (c) Reference LED with ITO coating, and (d) PNPNP-GaN LED with ITO coating.

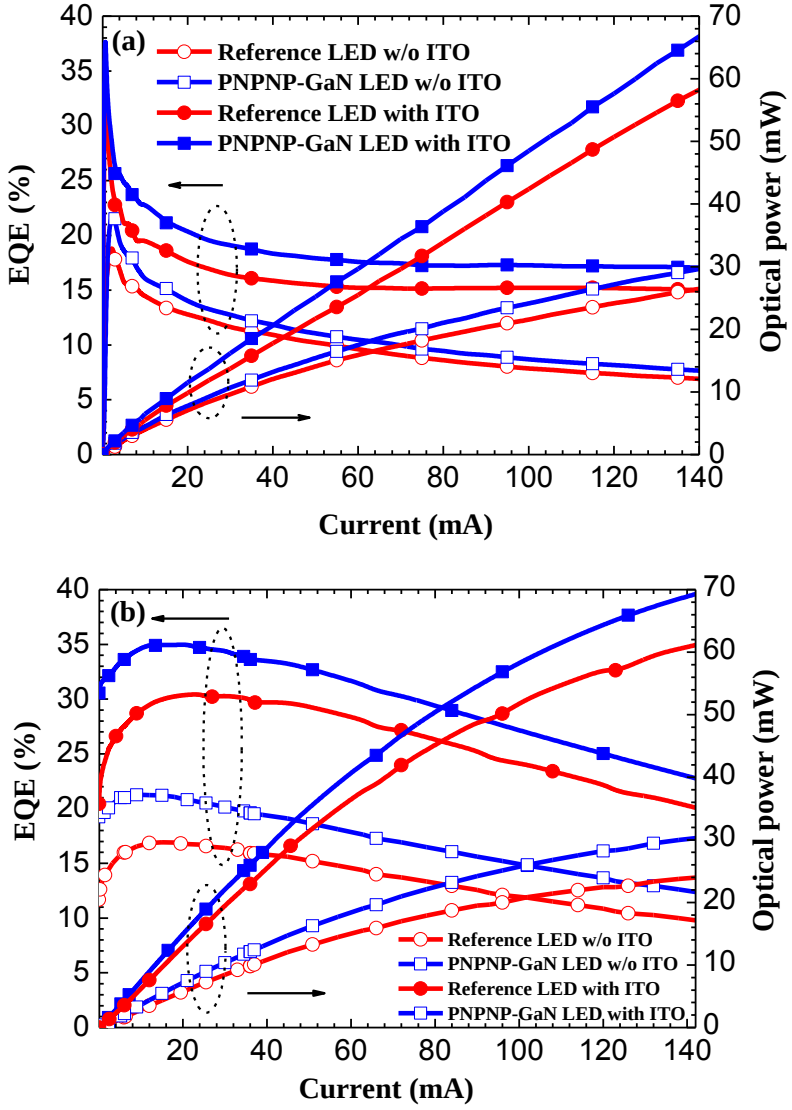

FIG. 5.1.5 (a) Experimentally measured optical output power and EQE as a function of the current injection, and (b) numerically simulated optical output power and EQE as a function of the current for Reference LEDs without and with ITO coatings and PNPNP-GaN LEDs without and with ITO coatings.

The energy band diagrams of the Reference LEDs (i.e., Reference LED without and with ITO) and PNPNP-GaN LEDs (i.e., PNPNP-GaN LED without and with ITO) are shown in Figs. 5.1.6(a) and 5.1.6(b), respectively. The holes in the Reference LEDs experience no barriers when transporting through p-GaN according to Fig. 5.1.6(a). In contrast, for the PNPNP-GaN LEDs, there

are two hole energy barriers, which are due to the ionized Si donors in the n-GaN layers. With the aid of the hole barriers, hole spreading is enhanced, and this alleviates the hole crowding effect in InGaN/GaN LEDs and leads to an improved lateral hole distribution.

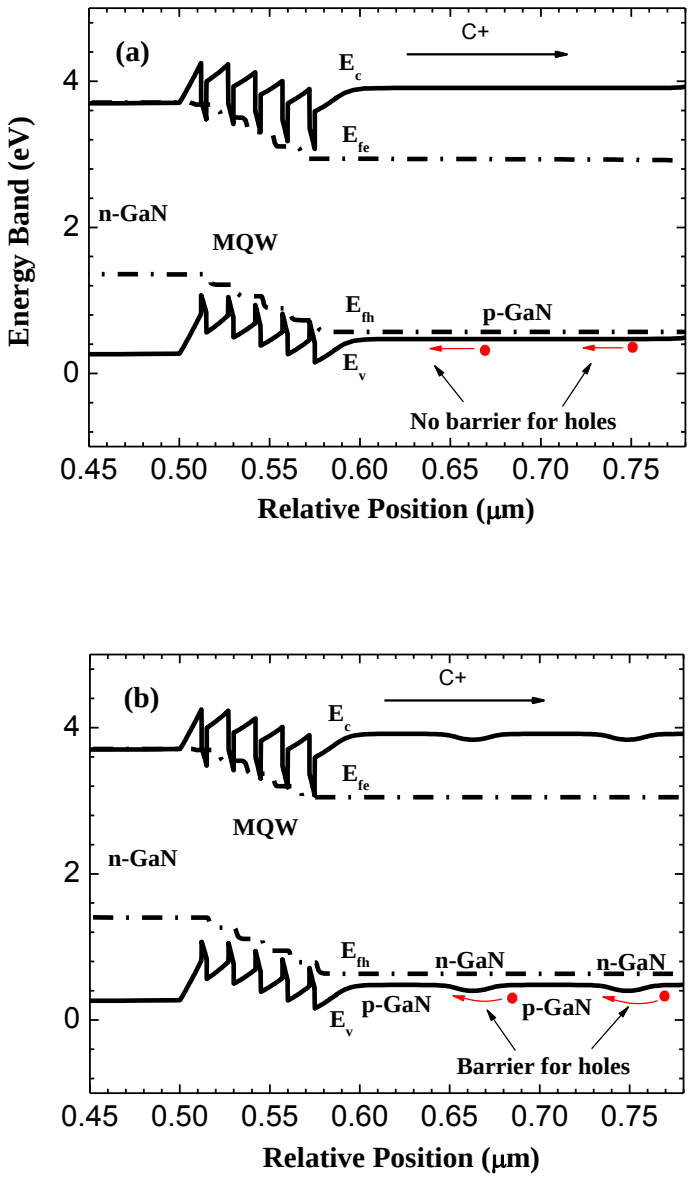

FIG. 5.1.6 (a) Energy band diagram for Reference LEDs and (b) energy band diagram for PNPNP-GaN LEDs. E_c, E_v, E_{fe} and E_{fh} denote the conduction band, valance band, and quasi-Fermi level for electrons and holes, respectively.

5.1.4 Supplementary material

We have also fabricated the InGaN/GaN LEDs coated with ITO films as the external transparent current spreading layers (i.e., Reference LEDs with ITO coatings and PNPNP-GaN LED with ITO coatings), which are shown in Figs. 5.1.7(a) and 5.1.7(b). A 200 nm thick ITO film was sputtered on each device and then annealed in the ambient environment of N_2 at 500 ^{o}C for 120 s. In these devices, the deposited Ti/Au (30 nm/150 nm) contacts were used as the p-electrode and n-electrode, respectively.

Figures 5.1.7(a) and 5.1.7(b) depict the simplified equivalent circuit of InGaN/GaN LEDs. In the case of PNPNP-GaN incorporated as the current spreading layer, we divide the total current into the vertical portion (J_1) and the horizontal portion (J_2). Similar to the devices without transparent current spreading layer, the total voltage drop consists of those between ITO and Ti/Au in the p-contact, p-GaN, MQW region, n-GaN as well as the n-contact. Based on the equivalent circuit in Fig. 5.1.7(b), Eq. 5.1.S1 (for current path 1) and Eq. 5.1.S2 (for current path 2) are obtained.

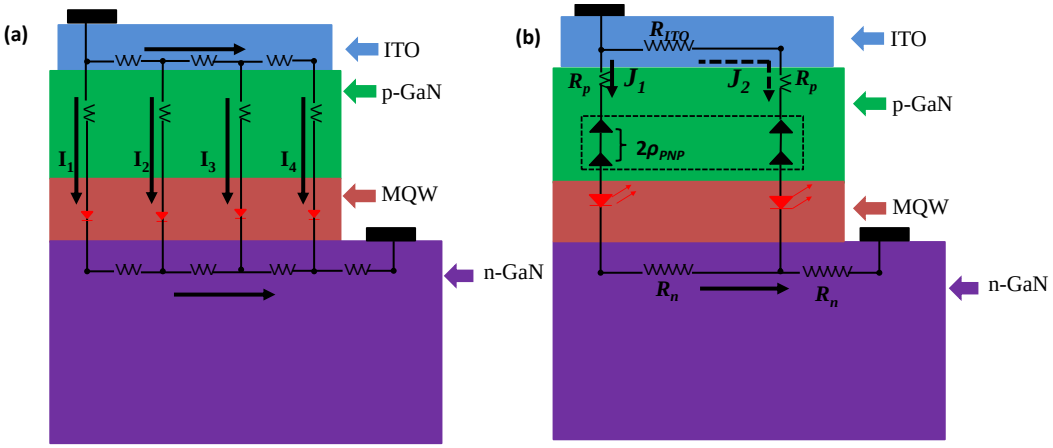

FIG. 5.1.7 (a) Equivalent circuit of an InGaN/GaN LED grown on an insulating substrate (e.g., sapphire) using ITO top coating with lateral current-injection scheme

($I_1 > I_2 > I_3 > I_4 > ..... > I_n$), and (b) a simplified equivalent circuit of this InGaN/GaN LED with possible current paths (J_1 and J_2) when a PNPNP-GaN current spreading layer is embedded, along with additional ITO film used as the transparent current spreading layer on the top.

$$J_1 lw\frac{\rho_{p-GaN}t_p}{lw} + J_1 lw\frac{N\cdot\rho_{PNP}}{lw} + V_{pn} + V_{p-contact} + V_{n-contact} + J_1 lw\frac{\rho_{n-GaN}l}{wt_n} + \left(J_1 lw + J_2 w_{ITO}t_{ITO}\right)\frac{\rho_{n-GaN}l_0}{wt_n} = U \quad (5.1.S1)$$

$$J_2 w_{ITO}t_{ITO}\frac{\rho_{ITO}l}{t_{ITO}w_{ITO}} + J_2 w_{ITO}t_{ITO}\frac{\rho_{p-GaN}t_p}{lw} + J_2 w_{ITO}t_{ITO}\frac{N\cdot\rho_{PNP}}{lw} + V_{pn} + V_{p-contact} + V_{n-contact} + \left(J_1 lw + J_2 w_{ITO}t_{ITO}\right)\frac{\rho_{n-GaN}l_0}{wt_n} = U \quad (5.1.S2)$$

where l represents the length of the lateral current path, l_0 is the distance from the mesa edge to the center of the n-contact, and w is the width of the device mesa. t_{ITO} and w_{ITO} is the thickness and width of the ITO film (in our case, w = 350 μm and w_{ITO} = 330 μm), respectively, and ρ_{ITO} is the ITO resistivity. The thickness of p-GaN and n-GaN is t_p and t_n, respectively; $\rho_{p\text{-}GaN}$ and $\rho_{n\text{-}GaN}$ are the resistivities for p-GaN and n-GaN, respectively. V_{pn} denotes the junction voltage drop of multiple quantum wells in InGaN/GaN LED; and $V_{p\text{-}contact}$ and $V_{n\text{-}contact}$ are the voltage drops across the p-contact (Ti/Au on ITO) and n-contact, respectively. ρ_{PNP} is the specific interfacial resistivity induced by the barrier height in each PNP-GaN junction. N is the total number of PNP-GaN junction, and in our device, we have two PNP-GaN junctions (i.e., PNPNP-GaN), and thus N is 2 (i.e., the total interfacial specific resistivity is $2 \times \rho_{PNP}$).

By equating Eq. 5.1.S1 and Eq. 5.1.S2, Eq. 5.1.S3 is derived. However, l, w and w_{ITO} are in the order of the device mesa size, which is 350 μm × 350 μm,

while t_{ITO} is 200 nm (t_{ITO} << l), then Eq. 5.1.S3 can be simplified into Eq. 5.1.S4.

$$\frac{J_1}{J_2} = \frac{w_{ITO} t_{ITO}}{lw} + \frac{l}{\frac{\rho_{P-GaN}}{\rho_{TCL}} t_p + \frac{N \cdot \rho_{PNP}}{\rho_{TCL}}} \quad (5.1.S3)$$

$$\frac{J_1}{J_2} \cong \frac{l}{\frac{\rho_{P-GaN}}{\rho_{TCL}} t_p + \frac{N \cdot \rho_{PNP}}{\rho_{TCL}}} \quad (5.1.S4)$$

Equation (5.1.S4) shows that a higher ratio of $N \cdot \rho_{PNP} / \rho_{TCL}$ helps to enhance the lateral current (i.e., J_2). Therefore, either $N \cdot \rho_{PNP}$ has to be increased or ρ_{TCL} has to be reduced for an increased ratio of $N \cdot \rho_{PNP} / \rho_{TCL}$. Meanwhile, the current spreading effect will also be improved by properly increasing the p-GaN thickness (t_p).

5.1.5 Summary

To summarize, a promising epitaxial current spreading technology based on a lattice-matched PNPNP-GaN current spreading layer was proposed and investigated both theoretically and experimentally for InGaN/GaN LEDs. The proposed PNPNP-GaN current spreading layer can be directly achieved in the MOCVD LED growth, avoiding the need for additional post-growth treatments, unlike those typically necessary for special current spreading layers (e.g., silicon dioxide nanoparticles used as the current spreading layer). Besides, n-GaN is lattice matched with p-GaN, which reduces the growth difficulty, as opposed to the growth of InGaN layers when used as a current spreading layer. In the proposed epitaxial current-spreading layer, the thin n-GaN layers between p-GaN layers are completely depleted, leaving behind positively ionized Si donors, which spread the injection current. This mitigates the current

crowding effect and resulting in 12.16% improvement in the optical output power and 10.95% enhancement in EQE for the InGaN/GaN LEDs without using ITO as the transparent current spreading layer. Besides, the reduced current crowding effect was also observed for PNPNP-GaN LEDs even when using ITO coating compared with Reference LEDs with ITO films. In this case, the enhancement factors of 14.37% in the optical output power and 13.54% in EQE have been obtained. Also, a theoretical model was proposed to illustrate and explain the mechanism of the enhanced lateral current through incorporating PNPNP-GaN into the p-type layer. The simulation results were in good agreement with the experimental measurements. The enhanced current spreading effect was found to improve the electrical property even if the overall barrier height is increased due to the PNPNP-GaN junctions. As a result, the luminous efficacy (in lm/W) can also be increased. These findings indicate that the proposed PNPNP-GaN current spreading layer improves the InGaN/GaN LED performance both electrically and optically in any case, when using or not using an ITO coating as the transparent current spreading layer. We believe that PNPNP-GaN homojunction current-spreading holds great promise for energy-saving LEDs.

5.2 InGaN/GaN light-emitting diodes with tunnel homo-junction and polarization tunnel junction to improve the current spreading effect

5.2.1 Introduction

Significant efforts have been devoted to boosting the optical output power and enhancing the external quantum efficiency (EQE) of InGaN/GaN light-emitting diodes (LEDs) [12-14]. These approaches include charge seperation

suppression via quantum well engineering [53, 55, 148], barrier engineering [28, 45, 46, 149, 150], electron blocking layer engineering [151-154], and novel epitaxy methods for dislocation density suppression [130, 132]. Recently, these efforts have also been extended to improving the current spreading and, thus, the EQE and output power of InGaN/GaN LEDs [21, 58, 135]. However, the improved current spreading can be achieved either by inserting a resistive layer into the p-GaN layer, such as the novel device demonstrated in section 5.1, or increasing the conductivity of the contact layer for p-electrode. For this purpose, the p^+/n^+ tunnel junction has previously been proposed to enhance the lateral current distribution in InGaN/GaN LEDs [140, 155-158]. In these devices, the heavy doping in GaN layers induces a strong built-in electric field, which aligns the conduction band of the n^+-GaN layer with the valence band of the p^+-GaN layer [23]. However, this tunnel region is a homojunction with no polarization induced electric fields and yields a low level of tunneling efficiency. Moreover, the additional voltage drop in the tunnel junction significantly increases the forward voltage of the resulting LED device. Here, different from the previous reports on homo-tunnel junction, to enhance the tunneling efficiency and reduce the voltage drop across the tunnel junction, we propose and demonstate the InGaN/GaN LED integrated with a polarization tunnel junction.

III-nitride epitaxial layers grown along c-orientation are well known to exhibit strong spontanous polarization and piezo-electric polarization [20], which induce positive and negative sheet charges with relatively high densities at the heterojunction interfaces. These charges are able to generate strong electric field resulting in the band bending, similar to the ionized dopants in the p^+/n^+ homojunctions. Hence, the tunneling probability can be significantly

affected by the strong polarization. The polarization tunneling has been investigated for both the metal-face (Ga/Al/In-face for c^+ growth orientation) and the nitrogen-face (N-face for c^- growth orientation) III-nitride heterojunctions [159-161], and excellent tunneling probability was obtained through those polarized junctions. However, to date, polarization tunneling phenomenon has not been investigated or demonstrated for InGaN/GaN LEDs. In this work, to understand the effect of the polarization tunnel junction on both the current spreading and the carrier tunneling, we integrated a p^+-GaN/InGaN/n^+-GaN polarization tunnel junction into the InGaN/GaN LED architecture. In the proposed device, enhanced optical output power and EQE are observed. This is explained by the improved current spreading and increased carrier tunneling enabled by the polarization tunneling.

5.2.2 Experiment

For our experiments, three types of InGaN/GaN LED samples were grown on c-sapphire substrates. The growth procedures of the epi-layers for the LED samples are identical to those in Chapter 5.1, except that on top of the MQWs, a 25 nm Mg-doped-$Al_{0.15}Ga_{0.85}N$ layer was grown as the electron blocking layer (EBL). After that, a 0.2 μm thick Mg-doped GaN (p-GaN) layer with a hole concentration of 3×10^{17} cm^{-3} was grown. For the Reference Device [see Fig. 5.2.1(a)], a 30 nm thick heavily Mg-doped GaN (p^+-GaN) layer was finally grown as the p-type contact layer. For our epitaxial wafers, the flow rates of Cp_2Mg and TMGa are 1.3 μmol/min and 22.0 μmol/min, respectively, and the ionization ratio of Mg dopants at room temperature is 1% in GaN [90]. Thus, the ionized Mg doping concentration in the p^+-GaN layer is estimated to be 3×10^{19} cm^{-3}. For Device A with the conventional tunnel junction [see Fig.

5.2.1(b)], another 30 nm n^+-GaN layer with the Si doping concentration of 1 × 10^{20} cm^{-3} was grown on the p^+-GaN layer, which is helpful to suppress the Mg compensation effect due to the Mg diffusion. In order to reduce the Mg diffusion, the following n^+-GaN layer was grown under the same condition as p^+-GaN, except that Cp_2Mg was replaced by SiH_4. Meanwhile, considering the compesation effect of Mg dopants, the n^+-GaN layer was intentionally doped at a higher level than the p^+-GaN layer. As for Device B with the polarization tunnel junction [see Fig. 5.2.1(c)], a 3 nm thick undoped $In_{0.15}Ga_{0.85}N$ layer was sandwiched between the p^+-GaN layer and n^+-GaN layer. The growth condition for $In_{0.15}Ga_{0.85}N$ is the same as that for the quantum well region.

After growing these described epi-layers in our MOCVD system, we further fabricated three sets of device-level samples. During fabrication, the LED mesa with a chip size of 350 × 350 μm^2 was patterned by using reactive ion etch (RIE). Indium tin oxide (ITO) of 200 nm was sputtered as the transparent current spreading layer. Finally, Ti/Au (30 nm/150 nm) was deposited by e-beam evaporation serving as the p-contact and n-contact.

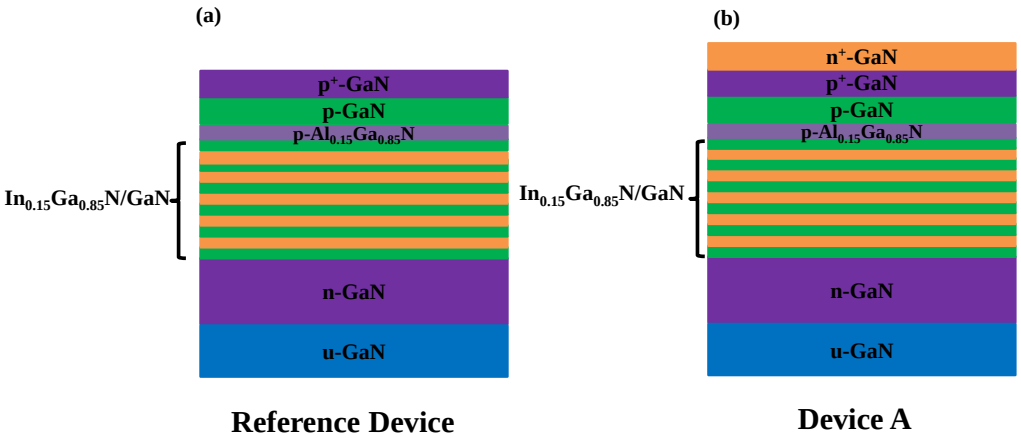

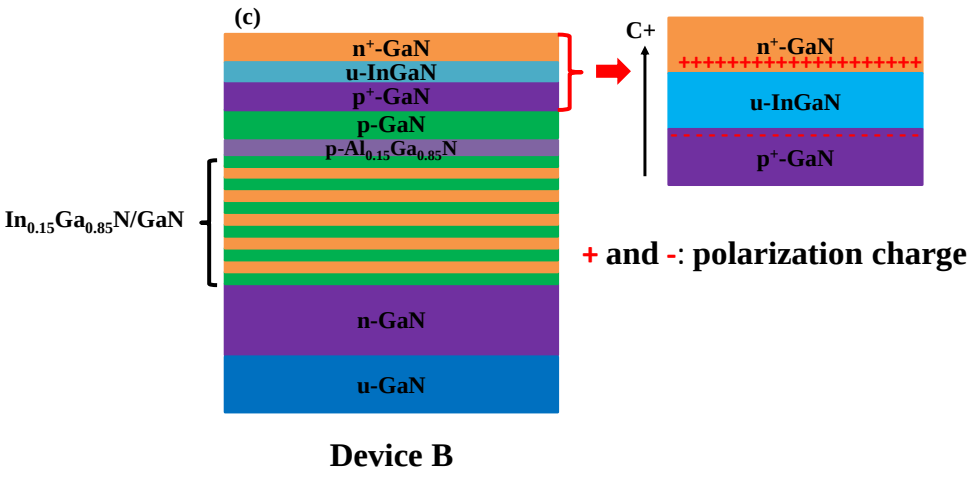

FIG. 5.2.1 Device architectures: (a) Reference Device, (b) Device A with the conventiaonal p^+/n^+ tunnel junction, and (c) Device B with the polarization tunnel junction.

We also performed the numerical simulations to understand the underlying device physics by using APSYS [119], which self-consistently solves the Poisson equation, continuity equation and Schrödinger equation with proper boundary conditions. The self-consistent six-band $k\,p$ theory is used to take account of the carrier screening effect in InGaN quantum wells [25]. In our simulations, the Auger recombination coefficient is taken to be $1 \times 10^{-30}\,cm^6s^{-1}$ [19]. The Shockley-Read-Hall (SRH) lifetime for electron and hole is set to be 43 ns [19]. Meanwhile, a 40% of the theoretical polarization induced sheet charge density is assumed due to the crystal relaxation through dislocation generation during the growth [20]. The energy band offset ratio of $\Delta E_c/\Delta E_v$ = 70/30 is set in the InGaN/GaN quantum well regions [35]. The other parameters used in the simulation can be found elsewhere [83].

5.2.3 Results and discussions

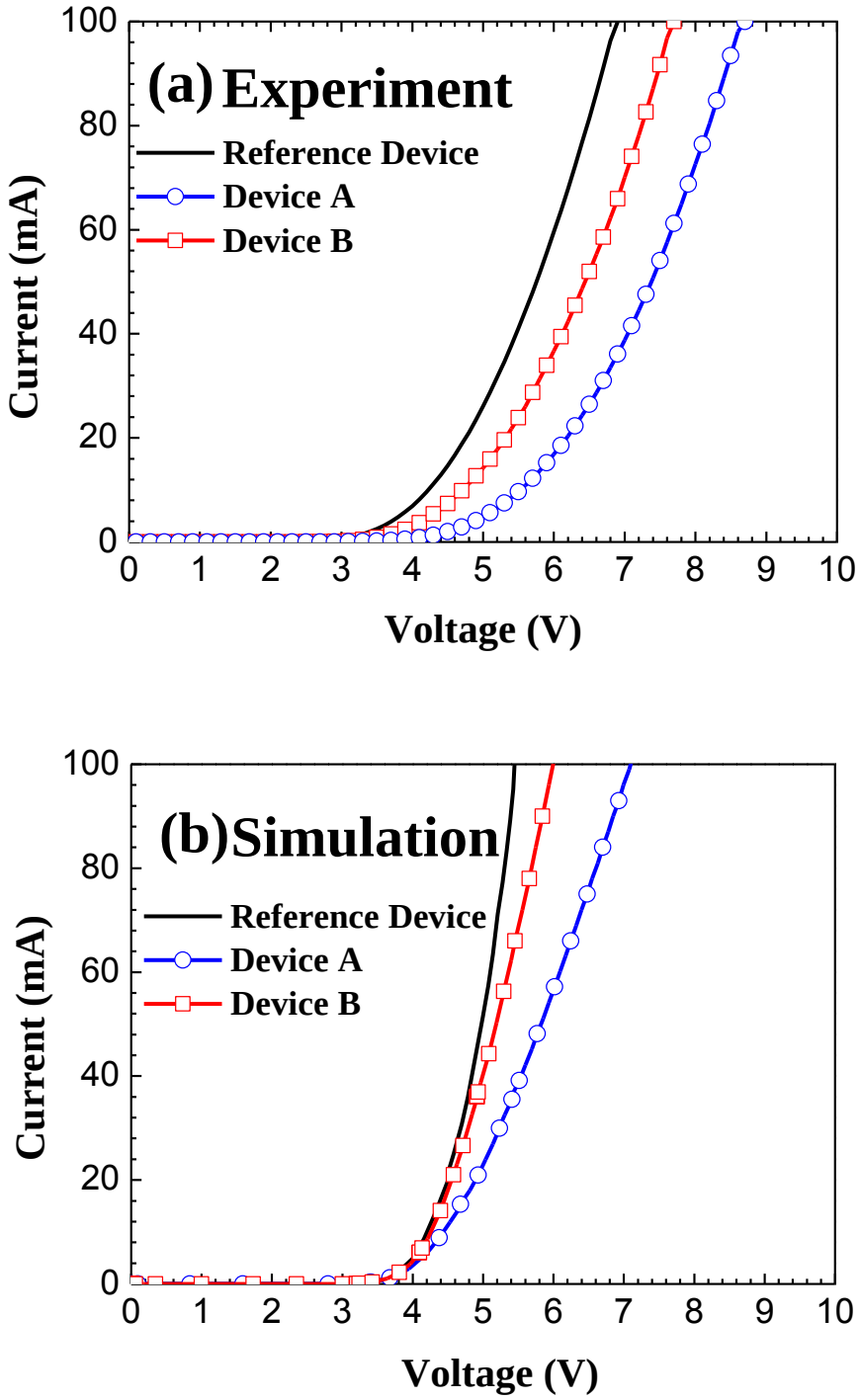

FIG. 5.2.2 Injection current *versus* applied bias: (a) experiment and (b) simulation.

Figs. 5.2.2(a) and 5.2.2(b) show the experimental and simulated injection current as a function of the applied bias for the devices. The simulated current-

voltage characteristics of the studied devices agree well with the experimental ones. It can be seen from Figs. 5.2.2(a) and 5.2.2(b) that the Reference Device and Device A (with the conventional p^+/n^+ tunnel junction) has the lowest and highest forward voltage, respectively. On the other hand, the forward voltage is reduced in Device B as compared to Device A when the polarization tunnel junction is used. The improved electrical performance in Device B compared to Device A is attributed to the enhanced tunneling probability (P_t as shown in Eqn. 1) of the carrers in the p^+-GaN/InGaN/n^+-GaN region:

$$P_t \sim \exp\left(-\frac{\pi \times m^{*1/2} \times E_g^{3/2}}{2\sqrt{2}e \times \hbar \times E}\right) \tag{5.2.1}$$

where m^* is the effective mass of the carriers in the tunnel layer and E_g is the energy bandgap of the tunnel region while E is the electric field, which assists the carrier tunneling [23]. Note that the simulated turn-on voltage of the Reference device is around 4.0 V while the experimentally measured turn-on voltage for the Reference device is around 3.2 V, and this slight discrepancy is due to the uncertainly of the physical parameters for the ITO coating, which are strongly affected by the deposition conditions.

According to Eqn. 5.2.1, the tunnel region with a small energy bandgap produces a large tunneling probability. Since the InGaN tunnel junction in Device B has a smaller energy band gap compared to the GaN tunnel junction in Device A, Device B leads to a higher tunneling probability than Device A [160]. Also, the additional polarization induced electric field in the p^+-GaN/InGaN/n^+-GaN junction further increases the carrier tunneling probability according to Eqn. 5.2.1. Fig. 5.2.3 shows the calculated electric fields within the tunnel junction for Device A and Device B. In the p^+-GaN/n^+-GaN junction

of Device A, besides the field produced by the external applied bias, the additional electric field is generated by the ionized Si donors in the n^+-GaN and and Mg acceptors in the p^+-GaN layers. Nevertheless, when the InGaN layer is sandwiched between the p^+-GaN/n^+-GaN junction in Device B, the polarization charges will be generated as indicated in Fig. 5.2.1(c). The polarization induced electric field in the compressive-strained InGaN layer is added as the third electric field component in the tunnel junction. For that, the magnitude of the total electric field in the tunnel junction for Device B is larger than that for Device A, as indicated in Fig. 5.2.3. The enhanced electric field, therefore, results in a better carrier tunneling probability and a reduced voltage drop in the tunnel region for Device B when compared to Device A.

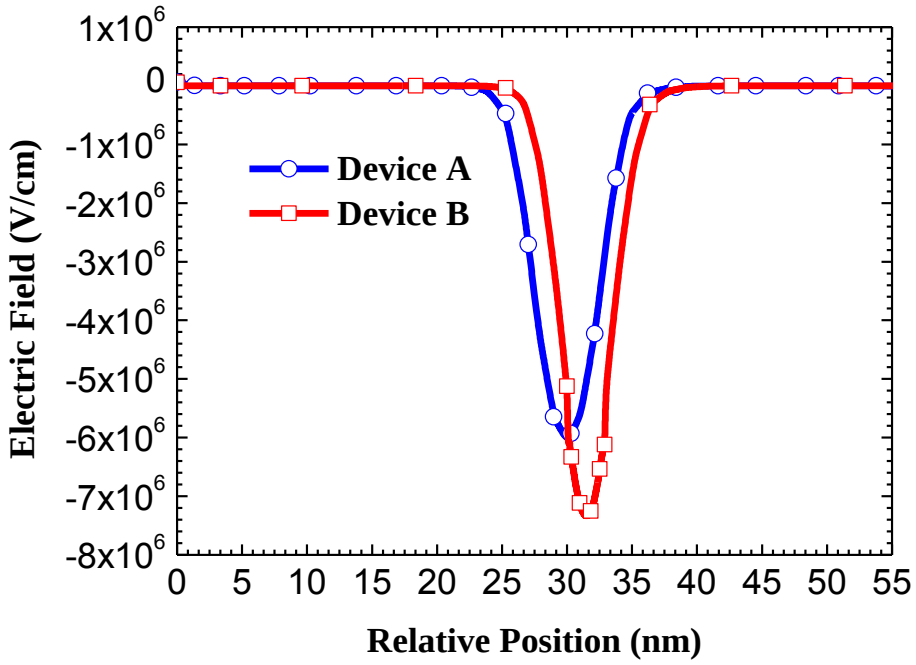

FIG. 5.2.3 Electric field profile computed across the tunnel junction at 4.5 V for Device A and Device B. The positive direction of the electric field is along the growth orientation (i.e., [0001]).

Figs. 5.2.4(a) and 5.2.4(b) present the energy band diagrams of the tunnel junctions for Devices A and B, respectively. We can see that, for both devices, the conduction band of the n^+-GaN layer is well aligned with the valance band of the p^+-GaN layer. Thus, those electrons in the valance band of the p^+-GaN layer are able to tunnel into the conduction band of the n^+-GaN layer through the forbidden band. Along with this process, holes will be generated in the valance band of the p^+-GaN layer and then injected into the quantum wells for the recombination under the electric field. However, as indicated in Fig. 5.2.4 for Device A, the tunnel region consists of two electric fields, i.e., the built-in electric field (E_{bi}) due to the ionized dopants and the electric field by the external applied bias (E_{ext}). On the other hand, in Device B, in addition to the E_{bi} and E_{ext}, the polarization induced electric field (E_{sp+pz}) increases further the overall magnitude of the total electric field. The stronger electrical field in Device B promotes the carrier tunneling probility and thus improves the electrical and optical performance.

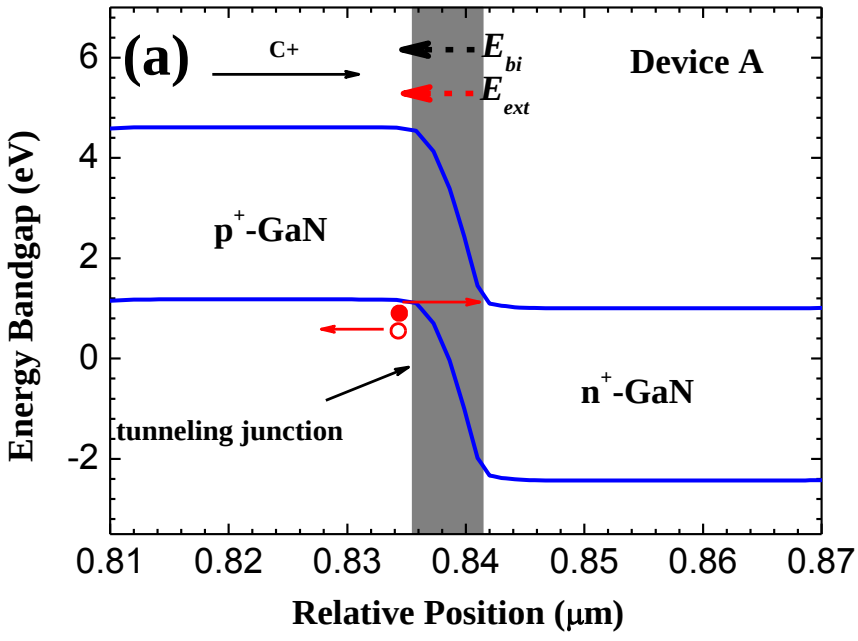

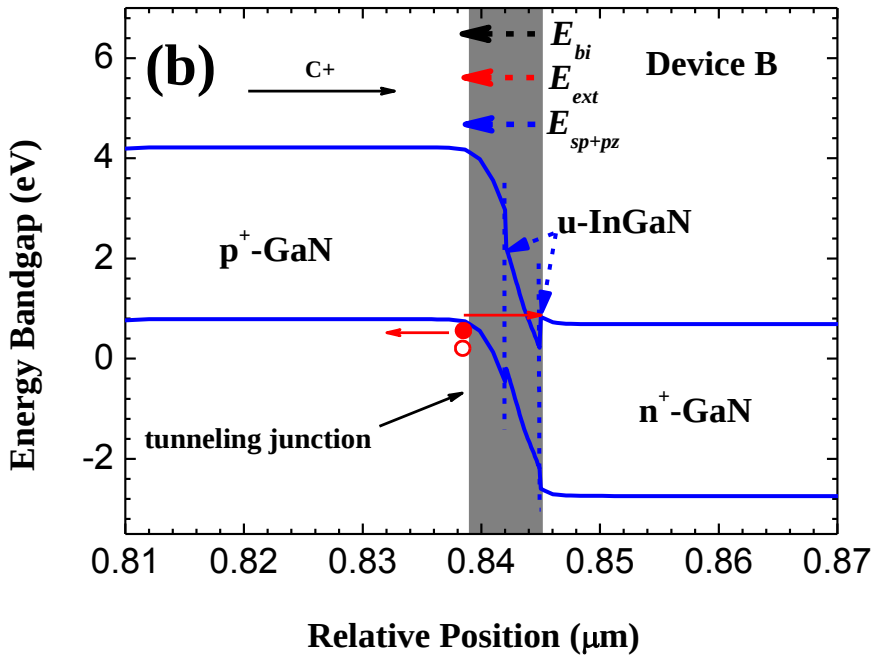

FIG. 5.2.4 Energy band diagrams of the tunnel junction for (a) Device A and (b) Device B.

It should be noted that Device B features a higher forward voltage compared to the Reference Device, as shown both in Figs. 5.2.2(a) and 5.2.2(b). This is mainly because of two reasons: First, it is difficult to grow high quality crystalline and thick InGaN layer with high indium content on the p-GaN layer. Second, the crystal relaxation may happen during the epitaxial process, and therefore, the actual polarization charge density in the InGaN/GaN hetero-interface could be smaller than the theoretical value. In our case, we assumed a 40% of the theoretical polarization induced sheet charge density in our simulation [20]. To assist the tunneling process, we intentionally heavily doped the GaN layers with Mg and Si in Device B. However, improvement in the electrical properties using the polarization tunneling without heavily doping is theoretically possible according to the report by Schubert *et al.* [159]. The

detailed discussion regarding the effect of InGaN thickness and InN fraction on improving the electrical property can further be found in the supplementary material in section 5.2.4.

Fig. 5.2.5 presents the hole concentration across the MQWs for the three devices. It shows that the Reference Device has the smallest hole concentration in each quantum well. In Device A with the p^+/n^+-tunnel junction, the hole concentration within the MQWs is increased compared to that in the Reference Device, which is due to the improved current spreading in the n^+-GaN layer of Device A [21]. Device B with the p^+-GaN/InGaN/n^+-GaN junction has the highest hole concentration in the MQWs, which stems from the improved current spreading effect and higher carrier tunneling probabiliy.

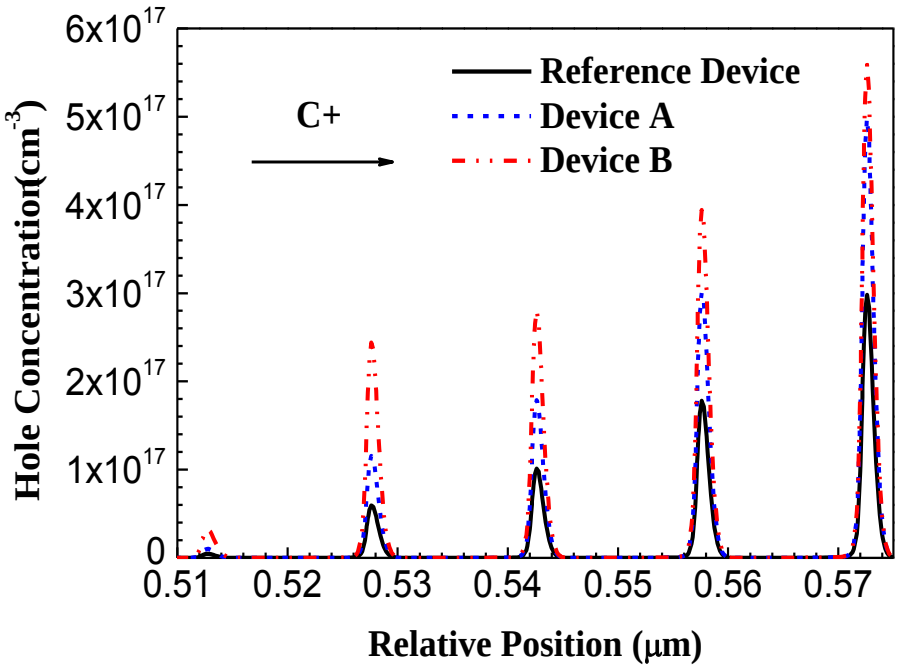

FIG. 5.2.5 Hole concentrations in InGaN/GaN MQWs for the Reference Device, Device A and Device B at 50 mA.

The electroluminescence (EL) spectra measured from the Reference Device, Device A and Device B are shown in Figs. 5.2.6(a), 5.2.6(b) and 5.2.6(c), respectively. We can see that the Reference Device has the lowest EL intensity. With the incorporation of the p^+/n^+-tunnel junction (Device A), the emission is improved due to the improved current spreading in the n^+-GaN layer [21]. Meanwhile, the strongest EL emission intensity is obtained from Device B, as shown in Fig. 5.2.6(c). The enhanced optical performance in Device B results from the improved current spreading effect [21] and the enhanced carrier tunneling probability in the polarization tunnel junction. We also observed a redshift of the emission wavelength as the injection current increases for all the three devices, and this is due to the increased junction temperature during the testing [118].

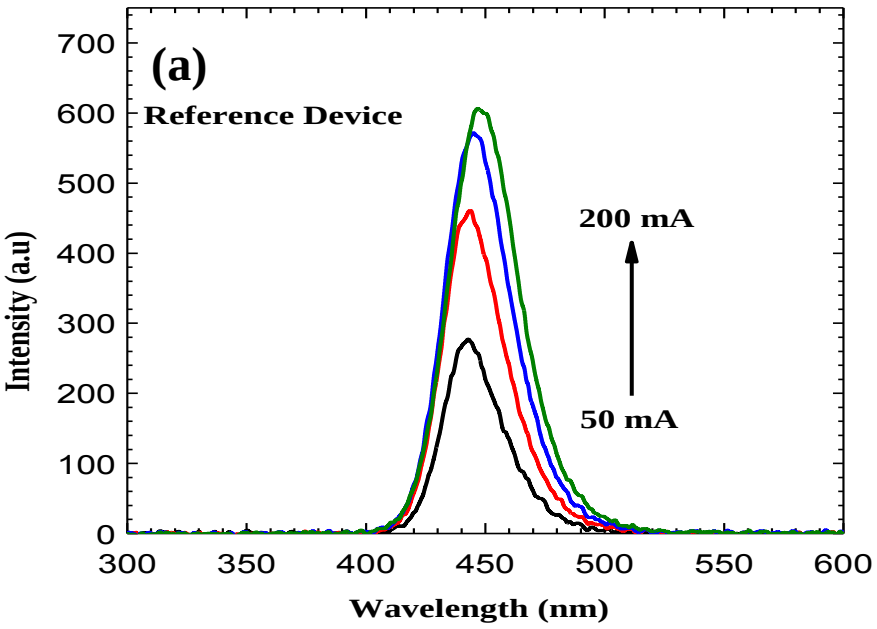

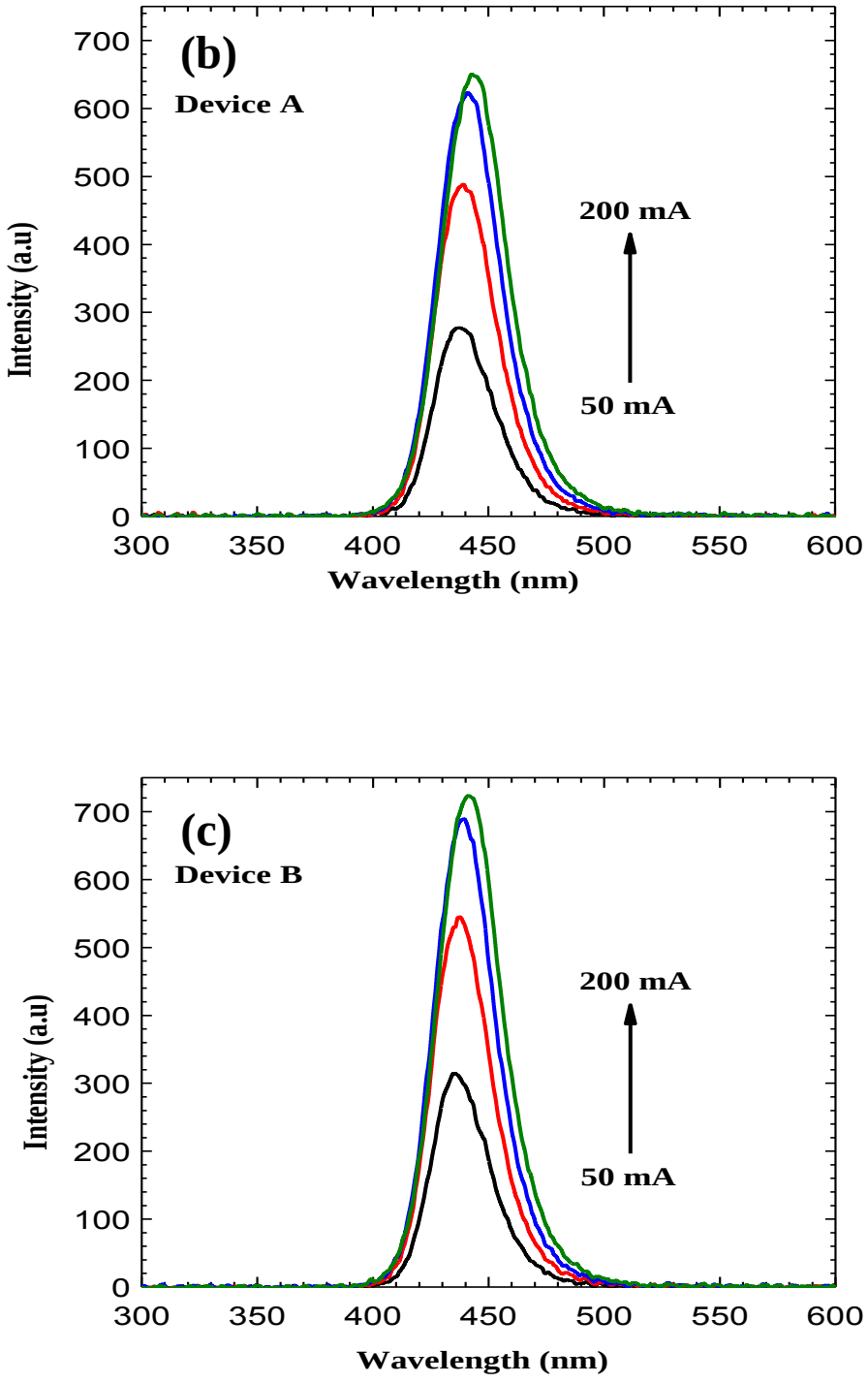

FIG. 5.2.6 Electroluminescence (EL) spectra measured from (a) Reference Device, (b) Device A and (c) Device B.

The optical output power and EQE were measured and are presented in Fig. 5.2.7. Correspondingly, we observed the lowest optical output power and EQE

from the Reference Device. Because of the improved current spreading effect, the optical output power in Device A is increased by 8.46% and 9.34% at 20 and 200 mA, respectively, as compared to the Reference Device. For Device B, an enhancement of 18.08% and 20.87% for the optical output power is realized at 20 and 200 mA, respectively.

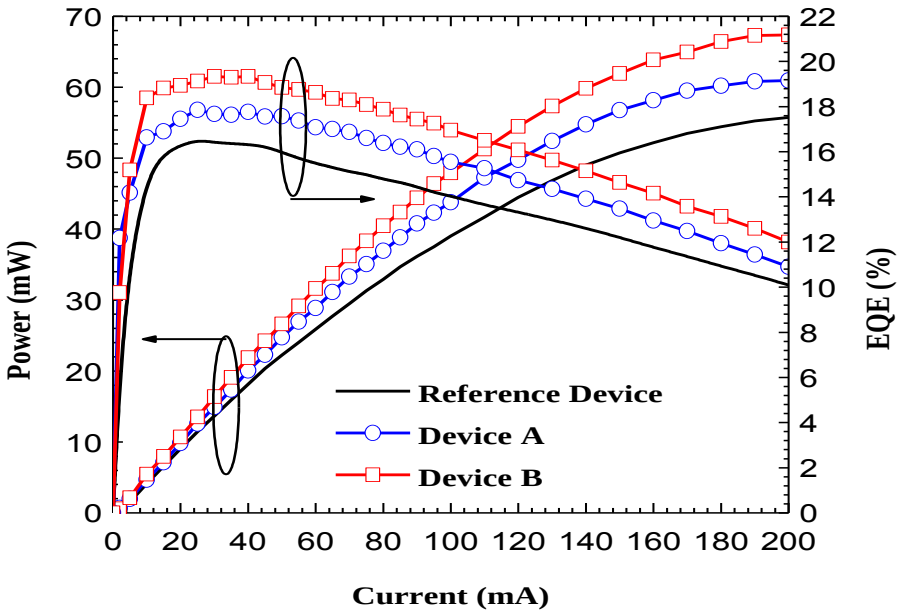

FIG. 5.2.7 Experimental optical output power and EQE as a function of the injection current for the Reference Device, Device A and Device B.

5.2.4 Supplementary material

To consistently interpret the experimental results, we have taken into account the partial strain relaxation effect in our numerical simulations. Due to the growth difficulty of thick InGaN layer with high InN fraction as well as the strain relaxation during growth process, the crystal quality of InGaN tunnel junction is far from perfection. However, it is still worth performing the numerical study assuming perfect crystalline quality in order to fully understand the potential advantages of InGaN tunnel junction for the improved

electrical properties of InGaN/GaN LEDs. Fig. 5.2.8 depicts the ideal case, for which the simulated current is shown as a function of the applied bias. Here we utilized 3 and 10 nm thick InGaN layers. Instead of the 40% polarization level used in the aforementioned simulations presented in the main text, here we assumed an ideal 100% polarization level in the InGaN tunnel junction and disregarded the dislocation generation. Meanwhile, we also considered the case of using InN as the tunnel layer in these simulations. Based on the simulation results shown in Fig. 5.2.8, we can see that the forward voltage can be reduced if the polarization level is increased to 100% (see Devices B1 and B2). The comparison between Device B2 and Device B3 indicates that a higher InN fraction in the InGaN tunnel layer can reduce the forward bias. Moreover, increasing the thickness of the InGaN tunnel layer is also helpful for further reducing the forward voltage of the device to a value even smaller than that of the Reference Device, as can be seen from the results of Device B3 and Device B4.

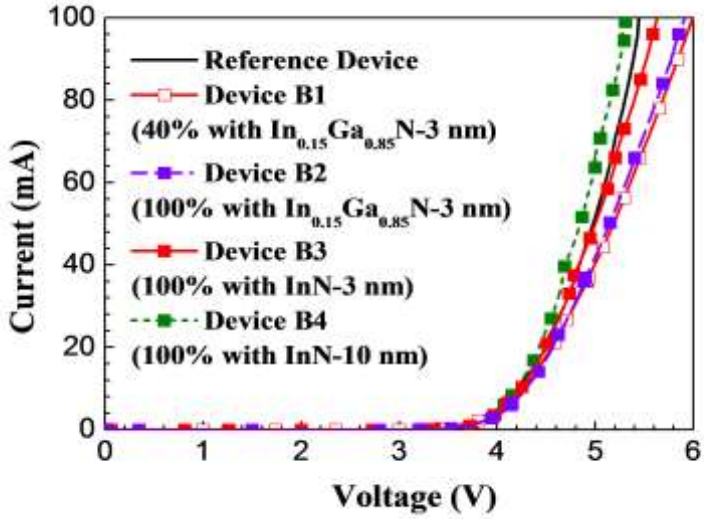

FIG. 5.2.8 Simulated current as a function of the applied bias for the Reference Device and Devices B (namely, B1, B2, B3 and B4) with various InN fractions (15% and

100%), InGaN layer thicknesses (3 and 10 nm) and polarization levels (40% and 100%), as indicated in the legend.

5.2.5 Summary

In conclusion, the InGaN/GaN LED with a p^+-GaN/InGaN/n^+-GaN polarization tunnel junction has been proposed and studied in this work. Our findings indicate that the polarization induced electric field in the p^+-GaN/InGaN/n^+-GaN polarization tunnel junction further increases the magnitude of the total electric field, and thus enhances the electrical performance for the proposed device when compared to the InGaN/GaN LED using the conventional p^+/n^+-GaN tunnel junction. Moreover, the increased magnitude of the electric field within the tunnel junction also increases the carrier tunneling probability, and promotes the carrier injection into the MQWs and therefore enhances the optical output power and EQE for the proposed device.

5.3 Summary

In this chapter, the current spreading effect on InGaN/GaN LEDs has been discussed. We have proposed and demonstrated two current spreading epitaxial structures to suppress the current crowding effect. On one hand, the current crowding can be relieved through incorporating a resistive layer in the hole injector region, i.e., p-GaN/n-GaN/p-GaN/n-GaN/p-GaN current spreading layer. On the other hand, the current can more uniformly spread by increasing the electrical conductivity of the contact layer for the p-electrode. We have demonstrated a current spreading architecture through a tunnel homojunction. However, such tunnel homojunction increases the forward voltage of the device, and meanwhile, the tunneling efficiency is low. Hence, in this chapter, we have

shown a novel polarization tunnel junction to increase the carrier tunneling probability and current spreading effect simultaneously. We have received an improved optical output power and external quantum efficiency from the proposed devices with enhanced current spreading.

Chapter 6 Electron overflow reduction through engineering the electron transport mechanism for InGaN/GaN light-emitting diodes

Unlike holes, electrons have a longer current spreading length due to the higher carrier mobility. However the incompatible carrier mobility between electrons and holes leads to the electron overflow, thus limiting the quantum efficiency of InGaN/GaN light-emitting diodes. InGaN electron cooler is inserted before growing InGaN/GaN multiple quantum wells (MQWs) to reduce electron overflow and improve the device efficiency. The detailed mechanisms of how the InGaN electron cooler contributes to the efficiency improvement remain unclear so far. In this work, we have theoretically proposed and experimentally demonstrated an electron mean-free-path model which reveals that the InGaN electron cooler actually reduces the electron mean free path in MQWs, increases the electron capture rate by the MQWs and reduces the valence band barrier heights of the MQWs which in turn promotes the transport of holes into MQWs. Our electron mean-free-path model is useful in optimizing the InGaN electron cooler to maximize the device efficiency. Further, based on the mean-free-path model, we have demonstrated the origin of electron blocking effect by *n*-type $Al_{0.25}Ga_{0.75}N$ electron blocking layer (EBL) for c^+ InGaN/GaN light-emitting diodes through dual-wavelength method. It is found that the strong polarization induced electric field within the *n*-EBL reduces the thermal velocity and thus the mean free path of the hot electrons. As a result, the electron capture efficiency by the multiple quantum wells has

been enhanced, which has significantly reduced the electron overflow from the active region and increased the radiative recombination with holes.

6.1 On the mechanisms of reduced electron overflow by InGaN electron cooler in InGaN/GaN light-emitting diodes

6.1.1 Introduction

As a clean and energy-saving solid-state lighting source, high-efficiency InGaN/GaN multiple quantum well (MQW) light-emitting diodes (LEDs) have been investigated with tremendous efforts in the past decades [13, 21, 28, 44, 56, 66, 150, 162]. However, the InGaN/GaN LED performance is still limited by efficiency droop, such that the quantum efficiency is reduced at an elevated injection current level. It is reported that the electron overflow from the InGaN/GaN MQW region is responsible for the efficiency droop [66]. One of the solutions proposed is to increase the electron confinement in the InGaN/GaN MQWs by using the polarization-matched AlGaInN electron blocking layer (EBL) [66] and the AlGaN or InAlN cap layer for the quantum barriers [44]. The increased energy barrier height in the novel EBL and the cap layers suppresses the electron escape from the MQW region. Another solution is to grow InGaN intermediate layer before MQWs which proves effective in improving the InGaN/GaN LED external quantum efficiency (EQE) and optical output power [67, 68, 163-165]. The reasons of the effectiveness of InGaN intermediate layer were tentatively attributed to either the improved current spreading effect promoted by the InGaN intermediate layer [164, 165], or the electron cooler (EC) effect [67, 68, 163], whereas the hot electrons are thermalized by interacting with longitudinal optical (LO) phonons [166]. The

exact mechanisms of the InGaN EC contributing to the reduction of electron overflow and the efficiency improvement still remain unclear so far. This inhibits the optimization of the InGaN EC and the maximization of its effectiveness. In addition, the n-InGaN EC has shown the effectiveness in reducing the electron overflow for double heterostructure (DH) active region [67, 68, 163]. However, it is not clear if electron cooler is still effective for a typical MQW stack with thick GaN barriers of 12 nm. Also different from the previous works [164, 165] where the improved current spreading effect is assigned as the reason of the efficiency improvement by using InGaN insertion layer, here it is found that the improved device performance is actually owing to the promoted hole transport into the MQWs by reducing the valance band barrier height of MQWs. Thus, in this work, we have studied InGaN/GaN MQW LEDs with the InGaN intermediate layer below the MQW region as the EC layer both experimentally and theoretically. An electron mean-free-path model is developed to understand the effect of the InGaN EC layer.

6.1.2 Experiment

Two InGaN/GaN LED wafers were grown by a metal-organic chemical vapor deposition (MOCVD) system. LED I is the reference sample, while LED II is the sample with InGaN as the EC layer. The growth of the two samples was initiated on *c*-sapphire substrates. A 30 nm low-temperature GaN nucleation layer was firstly grown. Then a 4 μm u-GaN layer was deposited as the template for the subsequent epitaxial growth. In LED I, a 2 μm n-GaN layer with Si doping concentration of 5×10^{18} cm^{-3} was grown before growing the five-period $In_{0.15}Ga_{0.85}N$ /GaN MQW region. The thicknesses of quantum wells and quantum barriers are 3 nm and 12 nm, respectively. For LED II, a 20 nm n-

type $In_{0.10}Ga_{0.90}N$ EC layer of 5×10^{18} cm^{-3} Si doping concentration was grown before growing the InGaN/GaN MQWs, for which the growth temperature was 748 ^{o}C while the quantum well growth temperature was 742 ^{o}C in our MOCVD chamber. Both LEDs I and II have a 20 nm p-$Al_{0.15}Ga_{0.85}N$ as the EBL layer. Finally, the LED samples were both covered with 0.2 μm p-GaN layer as the hole injector. The effective hole concentration in EBL and p-GaN layers for LEDs I and II is estimated to be $3 \times 10^{17} cm^{-3}$.

6.1.3 Results and discussions

The electroluminescence (EL) spectra and the optical output power were measured for the two LED samples using the calibrated integrating sphere attached to an Ocean Optics spectrometer (QE65000), respectively. The metal contacts were made by indium balls on LED dies with a diameter of 2.0 mm.

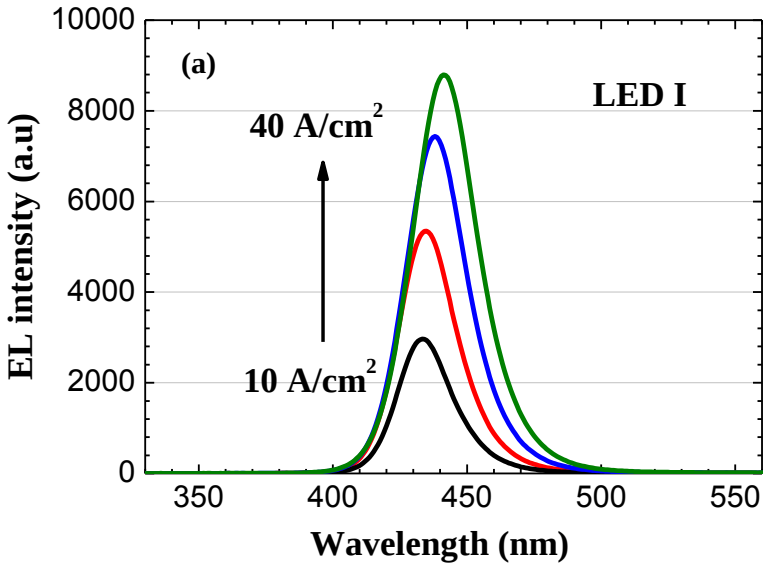

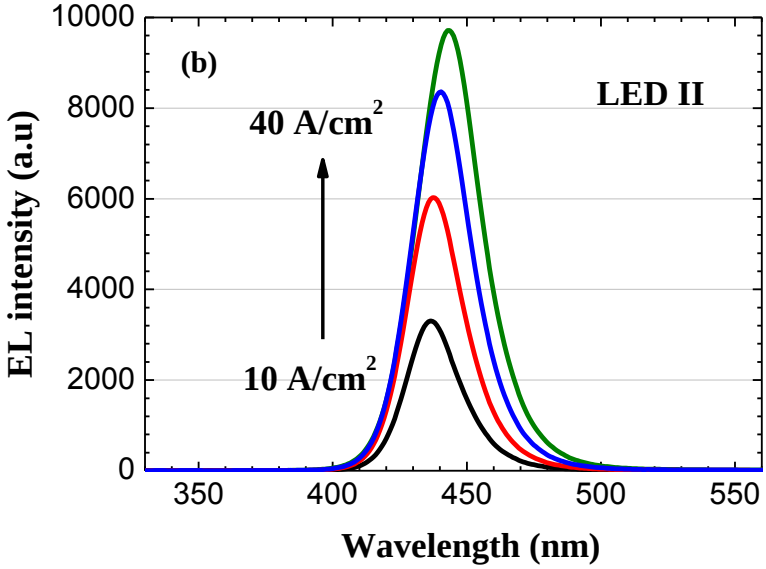

FIG. 6.1.1 EL spectra for (a) LED I, and (b) LED II under various injection current levels of 10, 20, 30 and 40 A/cm^2.

The EL spectra have been measured and shown in Figs. 6.1.1(a) and 6.1.1(b) for LEDs I and II, respectively. It can be seen that the EL intensity of LED II is stronger than that of LED I from lower injection current density of 10 A/cm^2 to higher injection current density of 40 A/cm^2. We have also observed a red shift of the emission wavelengths as a function of the increased injection current for both LED samples, and we have attributed the red shift of the emission wavelength to the increased junction temperature during testing [21, 28, 118].

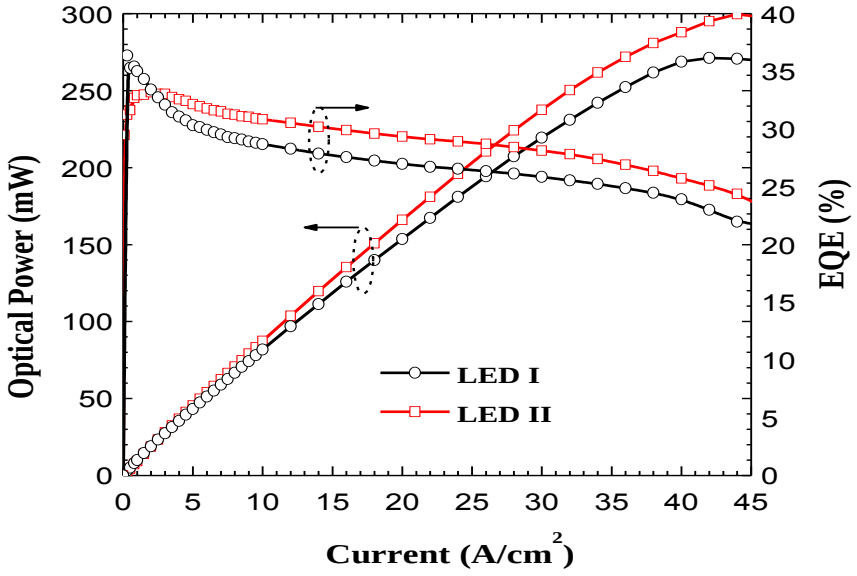

FIG. 6.1.2 Optical output power and EQE for LEDs I and II.

The integrated optical output power and the EQE are depicted in Fig. 6.1.2 for both LED samples. Being consistent with the EL spectra in Figs. 6.1.1(a) and 6.1.1(b), LED II emits stronger optical output power than LED I and the optical output power enhancement is 7.76% at 35 A/cm^2. Correspondingly the EQE of LED II is enhanced compared to that of LED I from low current density of 2 A/cm^2 to high current density of 45 A/cm^2. More importantly, the efficiency droop [$droop = (EQE_{\max} - EQE_{test}) / EQE_{\max}$] for LED II has been reduced significantly compared to LED I as shown in Fig. 6.1.2. For example, at 35 A/cm^2, the *droop* is 31.59% and 18.37% for LEDs I and II, respectively. The improved performance of LED II over LED I is attributed to the InGaN EC layer inserted before the InGaN/GaN MQW region. The detailed mechanisms of the InGaN EC Layer on the improvement of the LED performance are theoretically investigated through the mean-free-path model as follows.

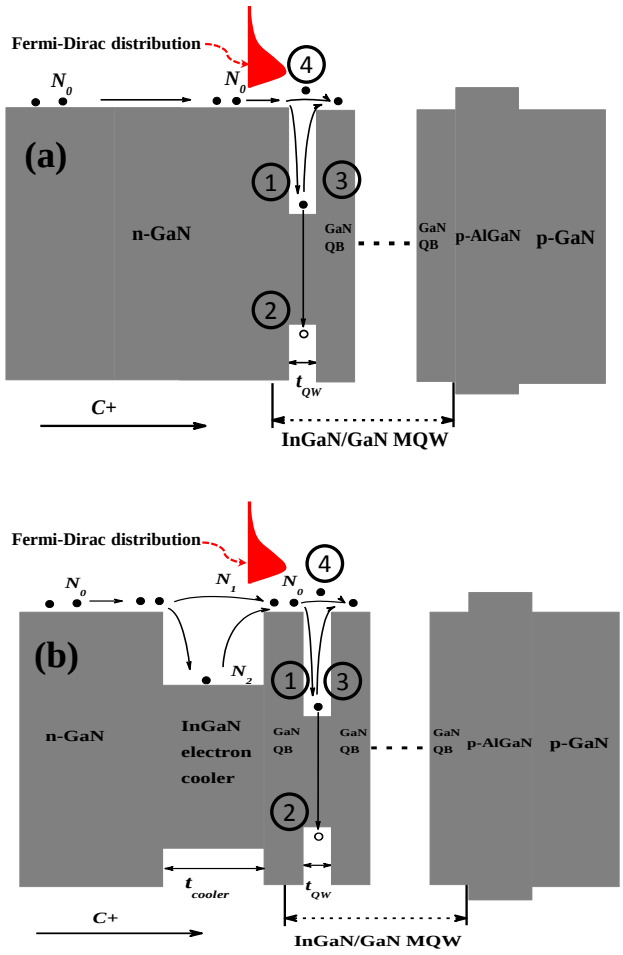

FIG. 6.1.3 Schematic energy diagrams for (a) LED I, and (b) LED II, along with which, four electron transport/transition processes are demonstrated in the InGaN/GaN MQWs. ① electron capture into the quantum well, ② recombination with holes and defects, ③ electron re-escape from the quantum well and ④ electrons direct fly over to a remote position without being captured by the quantum well.

The schematic drawings of energy band diagrams of LED I and LED II are depicted in Figs. 6.1.3(a) and 6.1.3(b), respectively, along with the four electron transport/transition processes in the InGaN/GaN MQWs. Note that the active region was grown directly after n-InGaN EC in the previous works [67, 68, 163]. Yet, the gained energy due to the conduction band offset between the n-GaN layer and n-InGaN EC (i.e., ΔE_c) may accelerate the electrons again. Hence, in this work, we have purposely grown a 12 nm thick GaN barrier of 5 ×

10^{17} cm^{-3} Si doping concentration between the n-InGaN EC and the first quantum well. Then the gained ΔE_c can be consumed by those electrons climbing over the next ΔE_c between the n-InGaN EC and the adjacent GaN barrier. Moreover, our design is different from the one reported by Rebane *et al*.[167]. In their design, they have grown a thin GaN barrier (0.5-5 nm) between the n-InGaN EC and the DH active region, hence transparent for electrons to tunnel through. However, as mentioned, the ΔE_c between the n-GaN layer and the n-InGaN EC may accelerate the electrons again. On the other hand, we grow our LED samples along [0001] orientation, and thus we have to consider the acceleration effect on electrons through the polarization induced electric field within the n-InGaN EC, which is sandwiched between two GaN layers.

According to Figs. 6.1.3(a) and 6.1.3(b), the incoming electrons are scattered and fall into the quantum wells (i.e., process ①) with τ_{cap} as the electron capture time, and a value of 4×10^{-12} s is used for electrons in the calculation [168]. Those fallen electrons thereafter on one hand are trapped onto the quantum energy levels and become bound electrons. Then, the recombination with holes and crystal defects takes place and it is depicted by process ②, and we define $1/\tau_{recomb}$ as the electron recombination rate which includes radiative recombination ($1/\tau_{rad}$) and nonradiative recombination ($1/\tau_{nonrad}$). However, there is also a thermionic electron re-escape process from the quantum wells and become free electrons again as illustrated by process ③ in Figs. 6.1.3(a) and 6.1.3(b). The re-escape process is modeled by the electron escape time, i.e., τ_{esc}, and it can be expressed by $\tau_{esc} = e \cdot t_{QW} \cdot n / J_e$ [46], where n presents the

electron concentration received by process ① while J_e is the electron current caused by thermionic emission in any heterojunction. Hence the relationship among electron capture, electron recombination and electron re-escape within the quantum wells can be illustrated by $1/\tau_{cap} = 1/\tau_{recomb} + 1/\tau_{esc}$. The radiative recombination rates within the quantum wells can be expressed by $R_{rad} = B \cdot n \cdot p \cdot \left[1 - e^{-(E_{fn} - E_{fp})/kT}\right]$ with $\tau_{rad} = 1/B\left(n_0 + p_0\right)$, where n and p is the electron and hole concentration while n_0 and p_0 is the thermal-equilibrium electron and hole concentration, B is the bimolecular recombination coefficient. E_{fn} and E_{fp} denote the quasi-Fermi levels for non-equilibrium electrons and hole, respectively. Therefore, an increased n favors the radiative recombination processes. Process ④ denotes those electrons of a longer mean free path traveling to a remote position without being captured by quantum wells, which has to be suppressed for an enhanced n.

We set the number of the electrons injected into the n-GaN region to N_0 for both LED samples. We neglect the electron loss through Shockley-Read-Hall (SRH) recombination in the n-GaN and n-$In_{0.10}Ga_{0.90}N$ EC layers to simplify our model since the crystal quality of the two samples is identical. Furthermore, the hole concentration in the n-$In_{0.10}Ga_{0.90}N$ EC is much lower than the electron concentration, so the electron loss through radiative recombination with holes is also negligible. For LED II with n-$In_{0.10}Ga_{0.90}N$ EC layer, we have assumed electrons of N_2 are captured by the n-$In_{0.10}Ga_{0.90}N$ EC layer with LO phonon emission, while the rest electrons of N_1 directly fly over the EC layer without undergoing thermalization. The electrons of N_2 are then injected to InGaN/GaN MQW region after undergoing thermalization. Here, we correlate the quantum

well captured electrons [i.e., process ① in Figs. 6.1.3(a) and 6.1.3(b)] with electron mean free path (MFP) by Eq. (6.1.1) and Eq. (6.1.2) for LEDs I and II, respectively [169]. Note, the electron loss due to processes ③ and ④ contribute to the electron overflow from the MQW region.

$$N_t = N_0 \times \left[1 - \exp(-t_{QW} / l_{MFP})\right] = \left(N_1 + N_2\right) \times \left[1 - \exp(-t_{QW} / l_{MFP})\right] \quad (6.1.1)$$

$$M_t = N_1 \times \left[1 - \exp(-t_{QW} / l_{MFP})\right] + N_2 \times \left[1 - \exp(-t_{QW} / l_{MFP}^{cooler})\right] \quad (6.1.2)$$

where t_{QW} is the thickness of the quantum well, l_{MFP} is the mean free path of electrons within the InGaN/GaN MQWs without electron thermalization and l_{MFP}^{cooler} is the mean free path of electrons in the InGaN/GaN MQWs with electron thermalization in the n-$In_{0.10}Ga_{0.90}N$ EC layer. Here, the relationship between N_0 and N_2 in Fig. 3(b) can be expressed in Eq. (6.1.3), in which, we assume the mean free path of electrons in the n-GaN layer before entering the n-$In_{0.10}Ga_{0.90}N$ EC layer is l_{MFP}. It is shown that, in order to have more electrons thermalized, it is useful to properly increase the thickness of the n-$In_{0.10}Ga_{0.90}N$ EC layer (t_{cooler}).

$$N_2 = N_0 \times \left[1 - \exp(-t_{cooler} / l_{MFP})\right] \quad (6.1.3)$$

The comparison between Eqs. (6.1.1) and (6.1.2) reveals that in order to increase the number of the quantum well captured electrons by inserting the InGaN EC layer, the electron mean free path within the InGaN/GaN MQW region with electron thermalization must be reduced, such that $l_{MFP}^{cooler} < l_{MFP}$. Nevertheless, the electron mean free path is a function of the thermal velocity (i.e., v_{th}-electron thermal velocity before undergoing thermalization and v_{th}^{cooler} -

electron thermal velocity after undergoing thermalization) and the scattering time (τ_{SC}), as shown in Eq. (6.1.4.1) and Eq. (6.1.4.2), respectively. Moreover, v_{th} and v_{th}^{cooler} can be expressed in Eq. (6.1.5.1) and Eq. (6.1.5.2), respectively.

$$l_{MFP} = v_{th} \times \tau_{SC} \tag{6.1.4.1}$$

$$l_{MFP}^{cooler} = v_{th}^{cooler} \times \tau_{SC} \tag{6.1.4.2}$$

$$v_{th} = \sqrt{2 \times [E + qV] / m_e} \tag{6.1.5.1}$$

$$\begin{aligned} v_{th}^{cooler} &= \sqrt{2 \times [E + \Delta E_c - \hbar\omega_{LO} + qV - \Delta E_c] / m_e} \\ &= \sqrt{2 \times [E + qV - \hbar\omega_{LO}] / m_e} \end{aligned} \tag{6.1.5.2}$$

where E is the excess kinetic energy in the n-GaN layer referenced to the conduction band of the n-GaN layer, and m_e is the effective mass of electrons. The first ΔE_c represents the kinetic energy received by the electrons when jumping over the conduction band offset between n-GaN and n-$In_{0.10}Ga_{0.90}N$ EC layer. $-\hbar\omega_{LO}$ means the energy loss by phonon emission. qV is the work done to the electrons by the polarization induced electric field in the in-plane compressive n-$In_{0.10}Ga_{0.90}N$ EC layer. The $-\Delta E_c$ in Eq. (6.1.5.2) depicts the energy loss for electrons when climbing over the conduction band offset between the n-$In_{0.10}Ga_{0.90}N$ EC layer and the first quantum barrier. In our calculation, in order to consider the crystal relaxation by generating misfit dislocations, we have only assumed 40% of the theoretical polarization induced charge density [20]. Meanwhile, we have assumed the energy band offset ratio between InGaN and GaN to be 70:30 [35], and thus ΔE_c between n-GaN and n-$In_{0.10}Ga_{0.90}N$ EC layer is 379.64 meV. Here we have also assumed the thermionic emission process dominates over the intra-band tunneling in the

process of the electrons transport into the first quantum well. Thus ΔE_c can be eliminated as shown in Eq. (6.1.5.2). The energy loss through LO phonon emission is 92 meV, i.e., $\hbar\omega_{LO}$ = 92 meV [170]. Since the electric field within the EC layer is not linear and varies with position, we use APSYS simulator to calculate it [119]. The calculated electric field is shown in Fig. 6.1.4. Since $qV = \int_0^{t_{cooler}} q \times E(y)dy$, thus qV equals to 27.82 meV in our case. When the carrier temperature is 500 K, l_{MFP} is 14.47 nm while l_{MFP}^{cooler} is 1.32 nm. Obviously the $In_{0.10}Ga_{0.90}N$ EC layer has a significant effect in reducing the electron mean free path in InGaN/GaN MQWs, and therefore increasing the quantum well capture efficiency of electrons, i.e., $M_t > N_t$. Here we only consider the constant mean free path in InGaN/GaN MQWs and did not consider its position dependence since it will not change the conclusion by doing so but only making the calculation more complex. Note, the electrons follow Fermi-Dirac distribution, and therefore Eq. [6.1.5.2] is valid when $E + qV - \hbar\omega_{LO} > 0$ for those hot electrons with a high carrier temperature, while for those with $E + qV - \hbar\omega_{LO} < 0$ (i.e., $E + \Delta E_c - \hbar\omega_{LO} + qV < \Delta E_c$) will be blocked by the conduction band offset between the EC layer and the first quantum barrier. However, the electrons will be accumulated in the EC layer until a high electron density is obtained. Thus according to $J_e = \frac{4 \cdot \pi \cdot e \cdot (k_B T)^2}{h^3} \cdot m_e^* \exp\left[-\Delta E_c / k_B T + \ln\left(n / N_c\right)\right]$ [23], where ΔE_c is the conduction band offset between GaN and the EC layer, and N_c is the effective density of state for electrons, while k_B is Boltzmann constant, m_e^* is the electron

effective mass, *h* is the Planck constant and *n* is the electron density, the electrons still can transport into the active region.

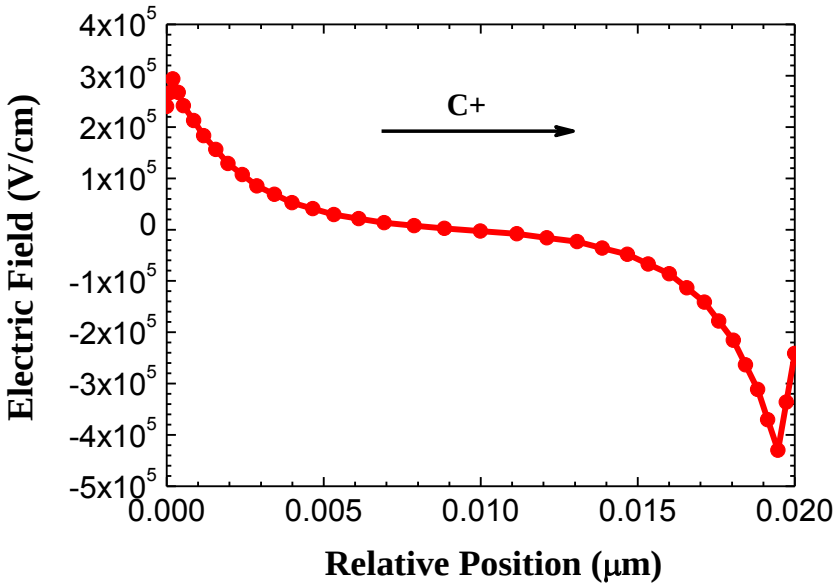

FIG. 6.1.4 Calculated electric field as a function of position within the EC layer at 20 A/cm^2. The positive direction of the electric field is along the growth orientation, i.e., c^+.

In order to more accurately investigate the studied InGaN/GaN LED samples, we have also performed theoretical simulations on the energy band diagrams, electron and hole distributions, electron currents and the radiative recombination rates for the two samples to confirm that the reduction of the electron mean free path by the $In_{0.10}Ga_{0.90}N$ EC layer can enhance the optical output power performance of LEDs. In our simulation, APSYS simulator is used, which can well model the carrier transport processes [i.e., processes ①, ②, ③, and ④ in Figs. 6.1.3(a) and 6.1.3(b)] within the InGaN/GaN MQW region. The model of electron tunneling through the GaN layer between the n-InGaN EC and the first quantum well has not been used purposely to study the thermionic process for electron transport within that region. Besides the

previously mentioned band offset ratio and polarization charge level, we have also assumed 1×10^{-30} cm^6/s as the Auger recombination coefficient [19]. The SRH recombination lifetime in the InGaN/GaN MQW region is set to be 43 ns [19]. Other parameters on nitrogen-contained compounds used in the simulation can be found somewhere else [83].

The simulated energy band diagrams at 20 A/cm^2 for LEDs I and II are shown in Figs. 6.1.5(a) and 6.1.5(b), respectively. We have defined the effective valance band barrier height ($\Delta\Phi_i$) for different quantum barriers (QB1, QB2, QB3 and QB4). The values of $\Delta\Phi_i$ are extracted and demonstrated in TABLE 6.1.1, from which we can see the effective valence band barrier heights of the quantum barriers for LED II are smaller than those for LED I. It has been reported that the effective valance band barrier height for the p-EBL can be reduced by employing GaN/InGaN as the last quantum barrier, hence promoting the hole injection into InGaN/GaN MQWs [171, 172]. However, as it is found in this work, the same physical principle can be applied to the case when the n-type $In_{0.10}Ga_{0.90}N$ layer is inserted between n-GaN layer and InGaN/GaN MQW region. As the polarization induced electric field within the n-type $In_{0.10}Ga_{0.90}N$ layer is opposed to the built-in electric field of the diode, thus the n-type $In_{0.10}Ga_{0.90}N$ layer "pulls up" the valance band of the MQWs for a better hole transport across the active region.

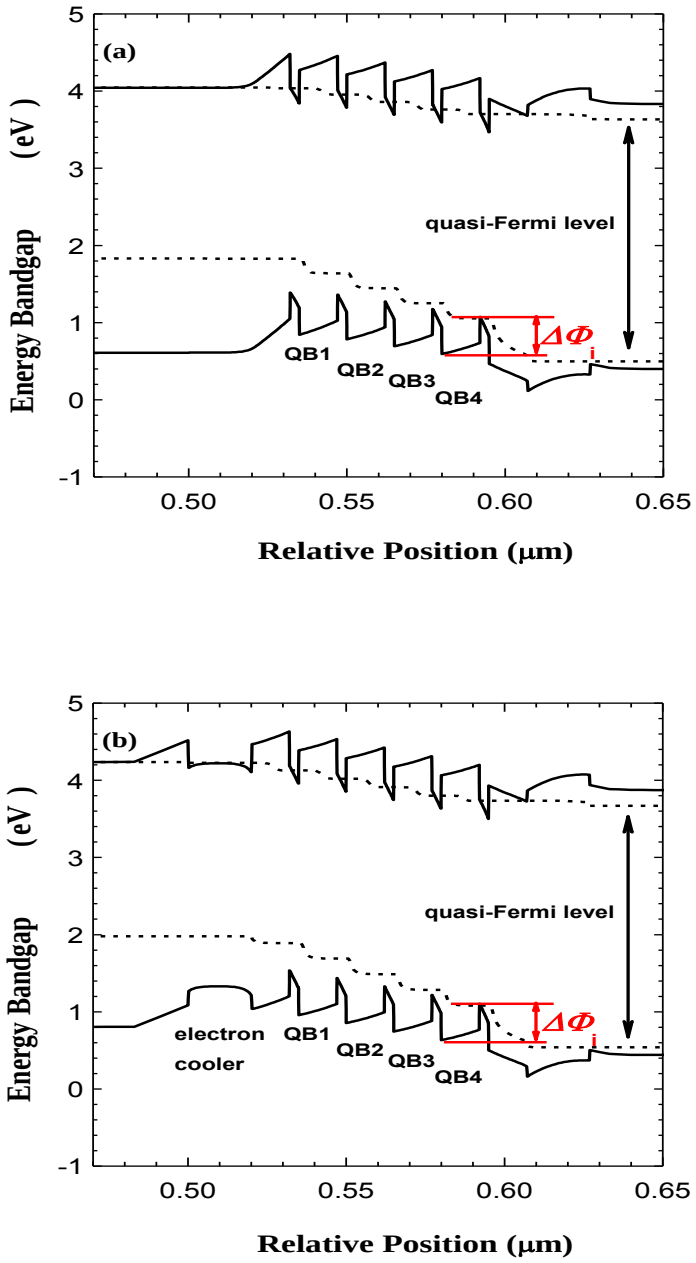

FIG. 6.1.5 Energy band diagrams for (a) LED I, and (b) LED II.

Table 6.1.1 The effective valence band barrier heights of InGaN/GaN MQWs for LEDs I and II.

	$\Delta\Phi_1$	$\Delta\Phi_2$	$\Delta\Phi_3$	$\Delta\Phi_4$
LED I	792.98 meV	666.84 meV	553.80 meV	489.90 meV
LED II	742.00 meV	638.99 meV	532.50 meV	447.29 meV

The simulated electron profiles of LEDs I and II are demonstrated in Fig. 6.1.6(a). We can see that the electron overflow is reduced in LED II with the n-type $In_{0.10}Ga_{0.90}N$ EC layer, compared to that in LED I. Meanwhile, the electron current distribution is also shown in Fig. 6.1.6(b). Being consistent with Fig. 6.1.6(a), the electron leakage current into the p-type region has been reduced from 26.56% to 18.86% at 20 A/cm^2, if we compare LED II to LED I. It should be noteworthy that the thermionic emission for process ③ in Figs. 6.1.3(a) and 6.1.3(b) can also be expressed by $J_e \propto \exp\left[-\Delta E_{c\_wb}/k_BT + \ln\left(n/N_c\right)\right]$ [23], where ΔE_{c_wb} is the conduction band offset of InGaN/GaN MQWs, N_c is the effective density of state for electrons, while k_B is Boltzmann constant. We can conclude that an increased electron concentration (i.e., *n*) within the InGaN/GaN MQWs enhances the electron re-escape process in Figs. 6.1.3(a) and 6.1.3(b) [173]. However, we have known that $M_t > N_t$, and thus LED II has a more severe electron re-escape process than LED I in Figs. 6.1.3(a) and 6.1.3(b). As a result, the reduced electron leakage in LED II is well attributed to the reduced electron mean free path by the n-type $In_{0.10}Ga_{0.90}N$ EC layer that suppresses those electrons directly flying over the quantum wells. In addition, we have also shown the hole profiles for LEDs I and II in Fig. 6.1.6(c), respectively. According to Fig. 6.1.6(c), we can see that LED II shows a more homogenous hole distribution across the InGaN/GaN MQWs than LED I which is due to the reduced valence band barrier heights of InGaN/GaN MQWs by the InGaN EC layer as shown in Fig. 6.1.5. The radiative recombination rates for LEDs I and II are shown in Fig. 6.1.6(d). The increased electron capture efficiency and the improved hole transport in the InGaN/GaN MQWs due to the

InGaN EC layer account for the enhanced radiative recombination rate for LED II, as indicated in Fig. 6.1.6(d).

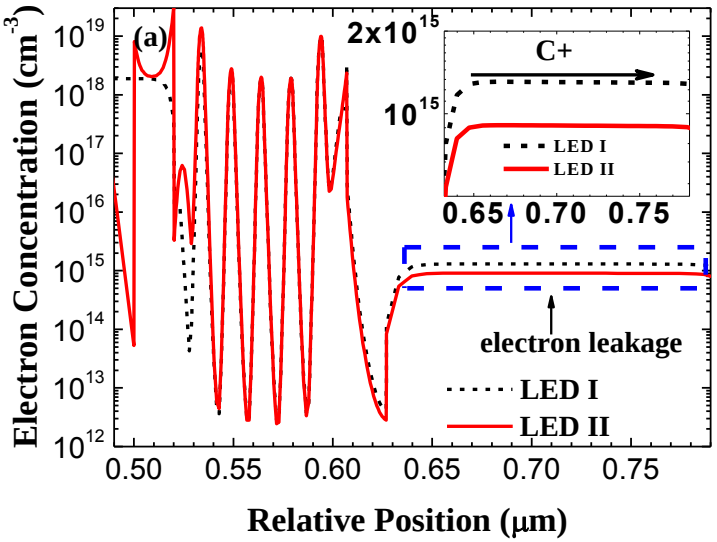

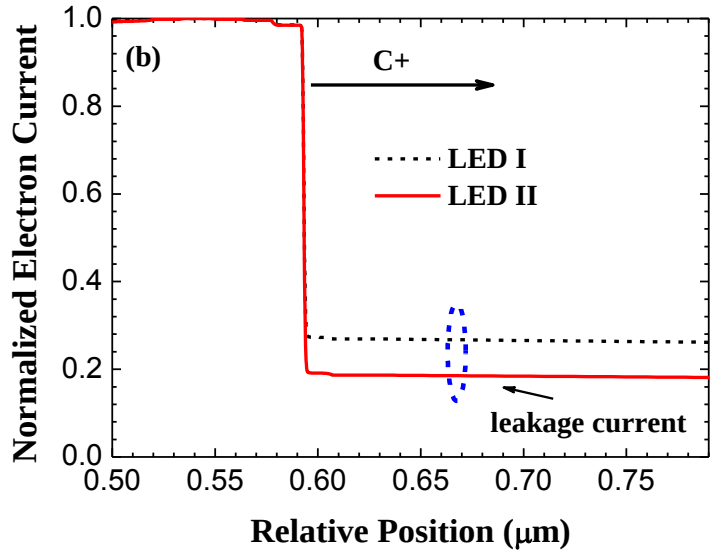

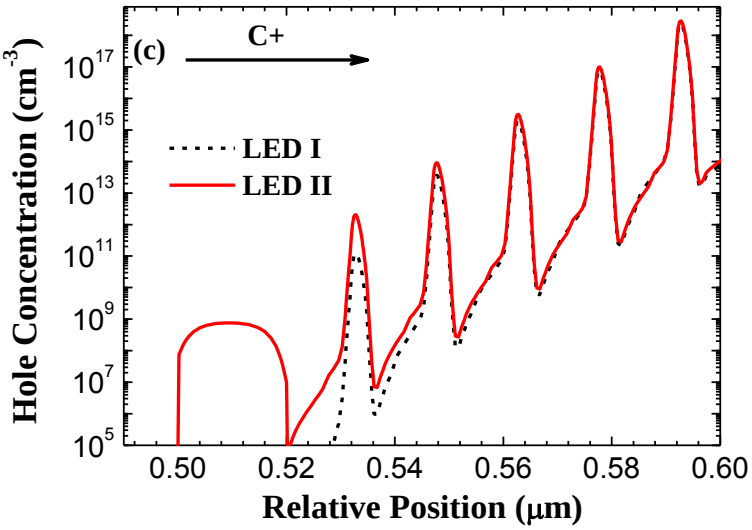

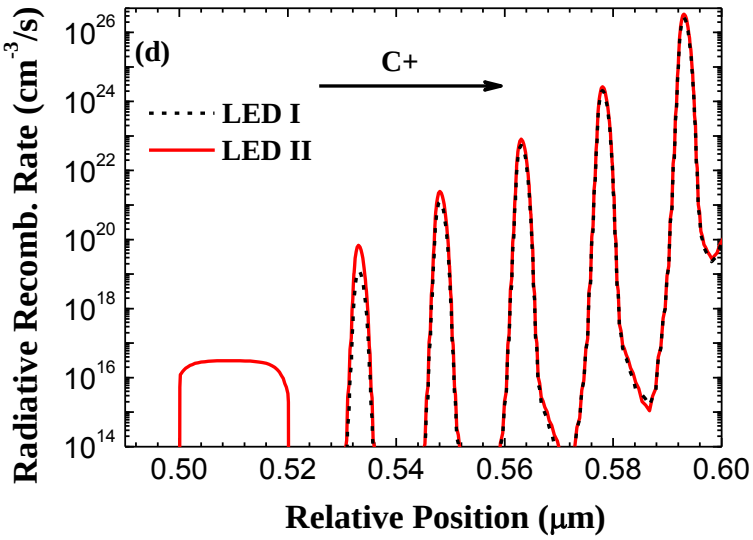

FIG. 6.1.6 Simulated (a) electron concentration with inset figure depicting the electron leakage out of the active region, (b) normalized electron current, (c) hole concentration, and (d) radiative recombination rates at 20 A/cm^2 across the InGaN/GaN MQW region for LEDs I and II, respectively.

6.1.4 Summary

In conclusion, the InGaN/GaN LED with an n-type $In_{0.10}Ga_{0.90}N$ electron cooler layer has been demonstrated and investigated. The enhanced electron

capture efficiency by the multiple quantum wells is attributed to a reduced mean free path after electrons undergo thermalization by phonon emission in the electron cooler layer. Moreover, we have found that the n-type $In_{0.10}Ga_{0.90}N$ electron cooler layer also promotes the hole transport by "pulling up" the valence band of the quantum barriers. Thus, the increased electron capture efficiency and the improved hole transport across the multiple quantum wells lead to the improvement of the radiative recombination rate, and thus the enhanced optical output power and the reduced efficiency droop. Therefore, InGaN electron cooler holds great promise for achieving better-performance InGaN/GaN LEDs.

6.2 On the origin of the electron blocking effect by an n-type AlGaN electron blocking layer

6.2.1 Introduction

As has been discussed in Chapter 6.1, the electron overflow from the MQW active region has significantly limited the InGaN/GaN LED performance [44, 45, 66, 68]. Therefore, substantial efforts have also been devoted to reducing the electron leakage from the InGaN/GaN MQW region, and hence polarization matched *p*-type electron blocking layer (EBL) and quantum barrier cap layers with large energy bandgap have been demonstrated [44, 45, 66]. The *p*-type electron blocking layer, on one hand can reduce the electron overflow, but on the other hand, it also retards the hole injection [174]. As a result, the *n*-type electron blocking layer has been demonstrated [82, 175]. Although the simulations in Refs. [82, 175] show the advantage of the *n*-type EBL over the *p*-type EBL, the physical mechanism of electron blocking effect by the *n*-type

EBL has never been clear until now. In this work, we have theoretically and experimentally investigated the origin of the electron overflow reduction through the *n*-type EBL by using the dual-wavelength method. We have found that the polarization-induced electric field in the *n*-EBL decelerates the thermal velocity of the hot electrons, and hence, the electron mean free path has been reduced, which increases the quantum well capture efficiency for electrons and accounts for the reduced electron leakage from the InGaN/GaN MQW region.

6.2.2 Experiment

In this work, two InGaN/GaN LED samples as shown schematically in Figs. 6.2.1(a) and 6.2.1(b) with targeted dual-wavelength emissions have been designed and grown using metal-organic chemical vapor deposition (MOCVD) system. The epitaxial growth was initiated from a c^+ plane sapphire substrate. A 30 nm low-temperature GaN nucleation layer was deposited and followed by a 4 μm high-temperature unintentionally doped GaN (*u*-GaN) template. Then, a 2 μm *n*-GaN layer with electron concentration of 5×10^{18} cm^{-3} was grown. For Reference sample, the MQW regions were grown subsequently. Nevertheless, for Sample with *n*-EBL, a 25 nm *n*-$Al_{0.25}Ga_{0.75}N$ EBL was grown before the MQW regions and the electron concentration was estimated to be 5×10^{18} cm^{-3}. The MQW regions include two sets of MQW stacks for both Reference sample and Sample with *n*-EBL with five $In_{0.18}Ga_{0.82}N$/GaN quantum wells as the first stack and three $In_{0.10}Ga_{0.90}N$/GaN quantum wells as the second stack. The InN fraction in the quantum wells was controlled by controlling the growth temperature, i.e., 742 ^oC and 758 ^oC for $In_{0.18}Ga_{0.82}N$/GaN MQWs and $In_{0.10}Ga_{0.90}N$/GaN MQWs, respectively. Moreover, in order to promote the hole transport across the active region, the quantum barrier thicknesses for both

samples have been graded into 12 nm, 11 nm, 10 nm, 9 nm, 8 nm, 7 nm and 6 nm along the growth orientation, respectively. The last quantum barrier is kept to be 12 nm to suppress the Mg diffusion [125]. Meanwhile, the quantum well thickness is 3 nm. Finally, a 0.2 μm *p*-GaN layer was grown, and the effective hole concentration is estimated to be 3×10^{17} cm^{-3}.

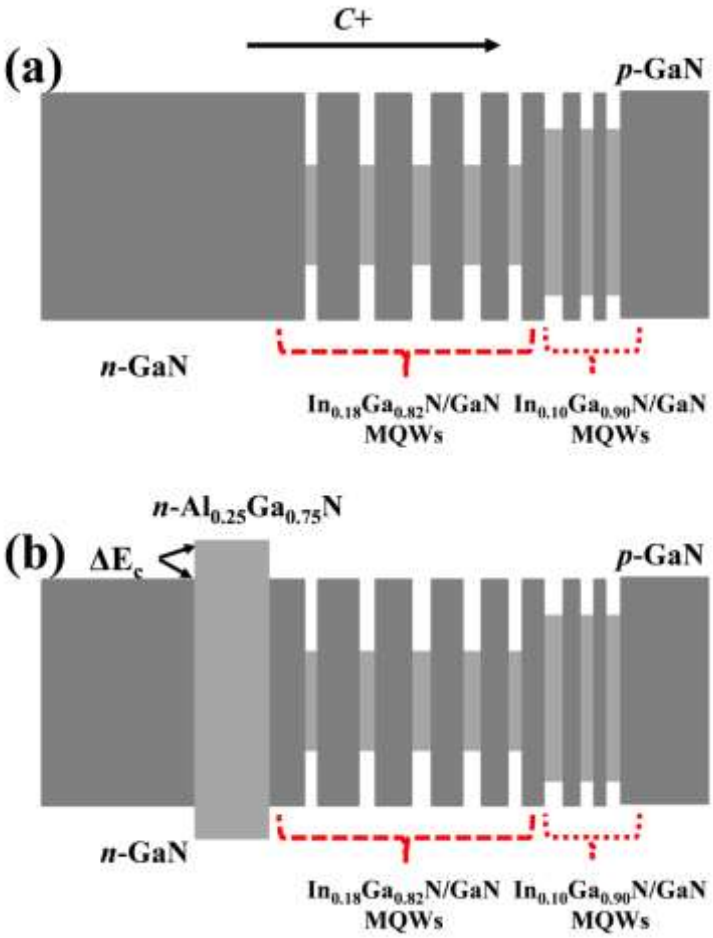

FIG. 6.2.1 Schematic energy band diagrams for (a) Reference sample, and (b) Sample with *n*-EBL.

6.2.3 Results and discussions

Photoluminescence (PL) measurement was conducted on the two samples using a PL mapper system (Nanometric RPM2000). The excitation wavelength of a 15 mW He-Cd laser source is 325 nm. The PL spectra for Reference

sample and Sample with *n*-EBL are shown in Fig. 6.2.2. It can be seen that both the samples show two emission peaks at around 427 nm and 467 nm, respectively. The emission spectrum with the shorter peak emission wavelength corresponds to $In_{0.10}Ga_{0.90}N$/GaN MQWs while the other corresponds to $In_{0.18}Ga_{0.82}N$/GaN MQWs. Since there are five $In_{0.18}Ga_{0.82}N$/GaN MQWs and three $In_{0.10}Ga_{0.90}N$/GaN MQWs, the PL signal for the longer emission wavelength is stronger than that for the shorter emission wavelength. In addition, the PL intensity for Sample with *n*-EBL is weaker than that for Reference sample, and this can be attributed to the increased QCSE within the MQWs caused by the underneath *n*-EBL. However we didn't see any significant difference in the emission peaks of the two LED samples, which is likely due to the slightly variation in the InN incorporation efficiency of different MOCVD growth runs for the two LED samples. Nevertheless, this will not affect the conclusions of this wok.

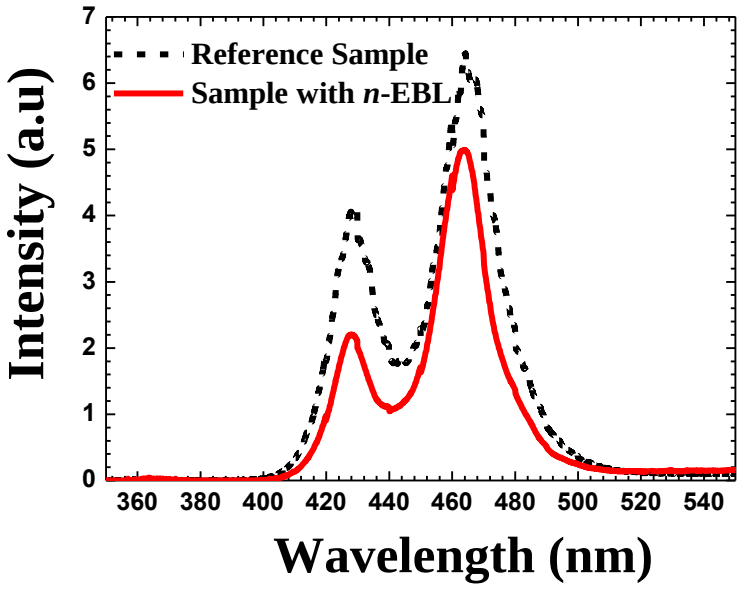

FIG. 6.2.2 PL spectra for Reference sample and Sample with *n*-EBL

The electroluminescence (EL) spectra and the optical output power for both the samples have been collected through an integrating sphere attached to an Ocean Optics spectrometer (QE65000). The metal contacts were made by indium balls on the LED dies with a diameter of 2.0 mm. The EL spectra under different injection current levels for both the samples are shown in Figs. 6.2.3(a)-(g). In addition, we have also shown the ratio of the external quantum efficiency (EQE) for $In_{0.10}Ga_{0.90}N$/GaN MQWs and $In_{0.18}Ga_{0.82}N$/GaN MQWs in Fig. 6.2.3(h). Two distinguished wavelength regimes have been observed at 5 A/cm^2 in Fig. 6.2.3(a) for both samples. As the injection current is increased, the emission intensity of the short wavelength regime for Sample with *n*-EBL is reduced relative to that for Reference sample, while the emission intensity of the longer wavelength regime for Sample with *n*-EBL becomes higher than that for Reference sample [see Figs. 6.2.3(b)-(f)]. When the current levels reach above 35 A/cm^2, the two distinct emission regimes for Reference sample can still be observed, while the short emission wavelength regime for Sample with *n*-EBL is immersed by the long wavelength emission regime according to Fig. 6.2.3(g). Fig. 6.2.3(h) demonstrates that the EQE ratio for $In_{0.10}Ga_{0.90}N$/GaN MQWs and $In_{0.18}Ga_{0.82}N$/GaN MQWs for Sample with *n*-EBL is always smaller than that for Reference sample within the measured current range. Since both the samples have identical MQW architectures and *p*-GaN layers, the different evolutional behavior of EL spectra for both the samples under various injection current levels should not be caused by the properties of holes. On the contrary, we attribute this to the different electron profiles within the MQW regions between Reference sample and Sample with *n*-EBL. The difference in the electron profiles is caused by the application of the *n*-EBL

which will be proved theoretically in the following discussion. The integrated optical output power for Reference sample and Sample with *n*-EBL has been shown in Fig. 6.2.4. Sample with *n*-EBL has demonstrated a substantial enhancement in the optical power compared to Reference sample. The reduced electron leakage for Sample with *n*-EBL is accountable to its power enhancement, as will be shown in the discussion next.

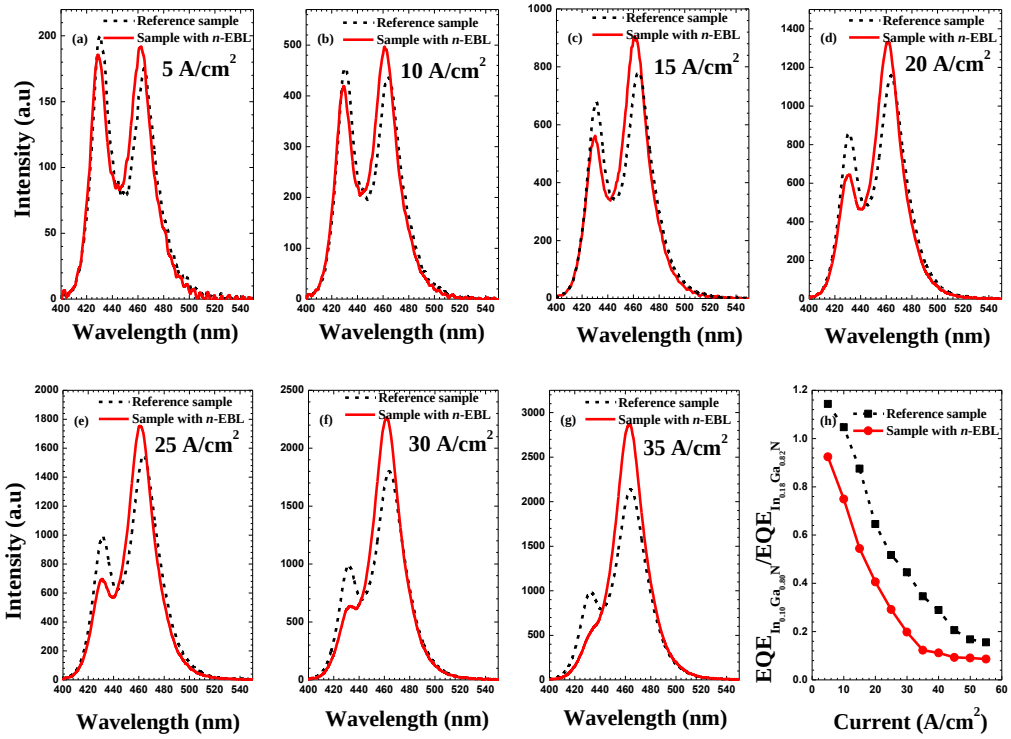

FIG. 6.2.3 EL spectra for Reference sample and Sample with *n*-EBL at the current density of (a) 5 A/cm^2, (b) 10 A/cm^2, (c) 15 A/cm^2, (d) 20 A/cm^2, (e) 25 A/cm^2, (f) 30 A/cm^2, (g) 35 A/cm^2, and (h) the ratio of the EQE for $In_{0.10}Ga_{0.90}N$/GaN MQWs and $In_{0.18}Ga_{0.82}N$/GaN MQWs, respectively.

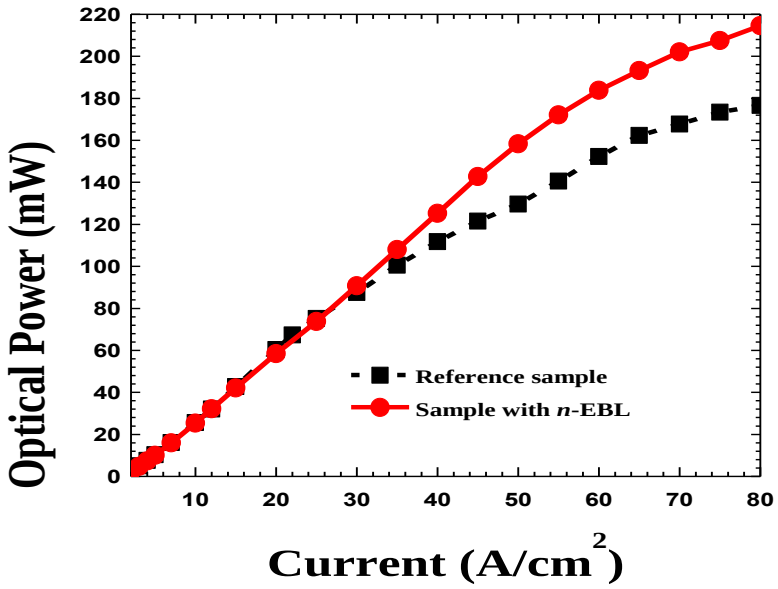

FIG. 6.2.4 Integrated optical output power for the Reference sample and the Sample with *n*-EBL.

In order to reveal the physical mechanism of the *n*-EBL on the electron distribution in MQWs, we have studied the two samples theoretically by using APSYS [119]. The simulation parameters regarding Auger recombination coefficient, Shockley-Read-Hall recombination lifetime and other nitrogen-contained simulation parameters have been reported in our previous works [21, 28, 56].

According to our previous study in Chapter 6.1, the relationship among the captured electrons by the quantum wells, mean free path and injected electrons can be expressed in Eqs. (6.2.1) and (6.2.2) as have been discussed in Chapter 6.1.

$$N_{capture} = N_0 \times \left[1 - \exp(-t_{QW} / l_{MFP})\right] \qquad (6.2.1)$$

$$l_{MFP} = v_{th} \times \tau_{SC} \qquad (6.2.2)$$

where, t_{QW} is the quantum well thickness, l_{MFP} is the electron mean free path and N_0 denotes the injected electrons, while $N_{capture}$ is the electrons captured by the quantum wells. v_{th} is the electron thermal velocity and τ_{SC} is the scattering time (i.e., the transport time for carriers before colliding with a particle to lose or obtain energy). Meanwhile, the schematic models of electron transport for InGaN/GaN LEDs with the *n*-EBL have been presented in Fig. 6.2.5. As illustrated in Fig. 6.2.5, process ① denotes the electrons crossing the *n*-EBL and entering the quantum wells for recombination, while process ② presents the electrons bounced back to the *n*-GaN layer by the conduction band offset between the *n*-GaN and the *n*-EBL layers, leading to a reduction of N_0 in Eq. (6.2.1). Here for simplicity, the tunneling electrons through the *n*-EBL are neglected, because the *n*-EBL thickness makes the electron tunneling negligible in this case. According to Eq. (6.2.1), the captured electrons are also a function of l_{MFP} which will be reduced by the *n*-EBL as shown next. Therefore, the captured electrons by the MQWs are determined by the competition of the reduction of N_0 due to the potential barrier of the *n*-EBL and the increase of the capture efficiency due to the reduction of l_{MFP}. The latter will be proved to be dominant and lead to the increase of the captured electron concentration as follows.

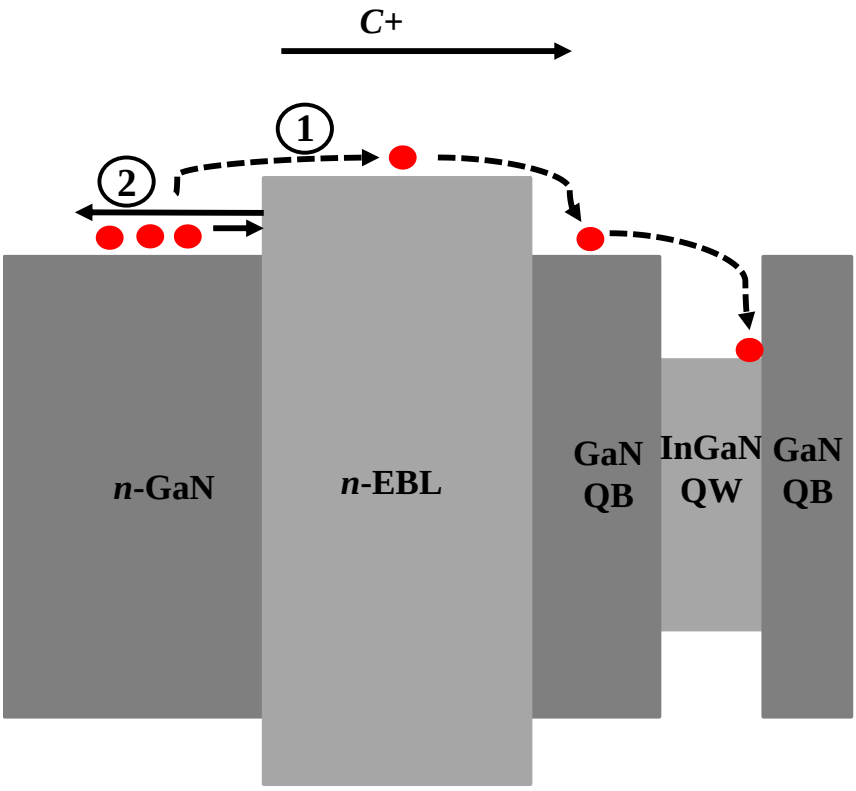

FIG. 6.2.5 Schematic electron transport processes for InGaN/GaN LEDs with the *n*-EBL, along with which shows the electron transport processes by ① crossing over the *n*-EBL and ② being bounced back by the *n*-EBL. Here, the tunneling process is not considered for simplicity.

As being well-known, III-nitride epitaxial films grown along c^+ orientation exhibit very strong polarization induced electric fields [28, 30, 55]. Moreover, for GaN/AlGaN/GaN heterostructure [refer to the inset of Fig. 6.2.6], the AlGaN layer is subject to tensile strain, and thus the piezoelectric field polarization and the spontaneous polarization are both oriented opposite to the growth orientation. Correspondingly, the polarization induced electric field is along the c^+ orientation. Since the electric field profile within the *n*-EBL varies with the different positions, APSYS is used to calculate the electric field as shown in Fig. 6.2.6. The electric field within GaN layer of this region has also

been shown for comparison. It is known that the work done to electron by the electric field is given by Eq. (6.2.3),

$$qV = \int_0^t q \times E(y) dy \tag{6.2.3}$$

If qV is positive, then the electrons are decelerated. The integration to the electric field profiles in Fig. 6.2.6 shows that qV equals 62.6 meV and 105.7 meV for the Reference sample and the Sample with *n*-EBL, respectively. Meanwhile, the thermal velocity can be expressed in Eq. (6.2.4),

$$v_{th} = \sqrt{2 \times [E - qV] / m_e} \tag{6.2.4}$$

where E is the excess kinetic energy in the *n*-GaN layer referenced to the conduction band of the *n*-GaN layer, and m_e is the effective mass of electrons. It should be noted that the electrons climb over the *n*-EBL by gaining the potential energy of $\Delta E_{c(GaN/AlGaN)}$ (conduction band offset between GaN and *n*-EBL) while falling down from the *n*-EBL by losing $\Delta E_{c(GaN/AlGaN)}$, and hence $\Delta E_{c(GaN/AlGaN)}$ does not appear in Eq. (6.2.4). As a result, more negative work is done to electrons, and thus the thermal velocity of electrons is reduced in the device with *n*-EBL. Based on Eq. (6.2.2), l_{MFP} is thus reduced by the *n*-EBL which will lead to the increase of the electron capture efficiency by MQWs and hence the captured electron concentration.

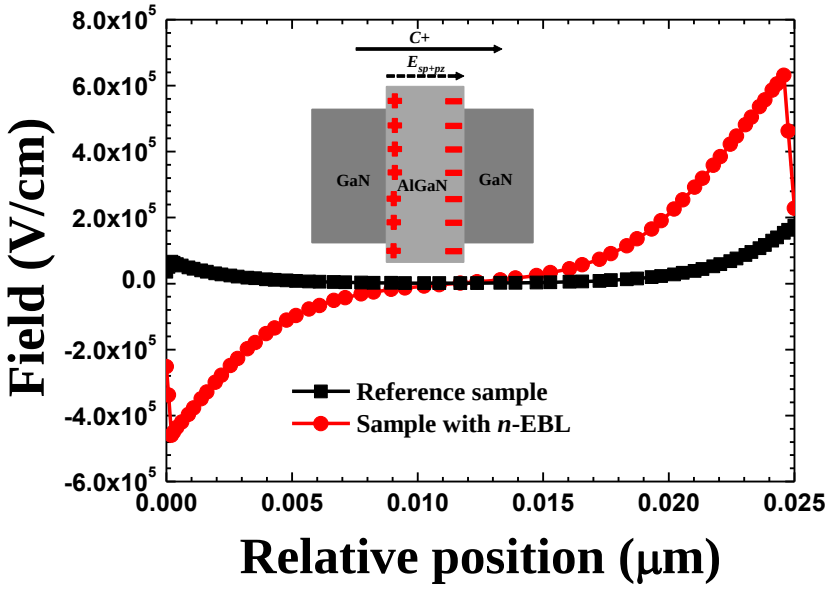

FIG. 6.2.6 Electric field profiles in the region of the *n*-EBL layer for Sample with *n*-EBL and GaN layer for Reference sample. Inset shows the polarized GaN/AlGaN/GaN heterostructure. The positive direction of the electric field is along the growth orientation, i.e., *c*+ orientation. The data are collected at current level of 25 A/cm^2.

Based on the model, we have numerically extracted the electron concentration profiles at 25 A/cm^2 for the Reference sample and the Sample with *n*-EBL, as are shown in Figs. 6.2.7(a), 6.2.7(b) and 6.2.7(c). Fig. 6.2.7(a) shows the electron distribution in the first five-pair $In_{0.18}Ga_{0.82}N$/GaN MQWs close to the *n*-GaN layer, and it can be seen that the electron concentration for the LED with *n*-EBL is higher than that for Reference sample. The increased electron concentration is due to the increased electron capture efficiency by the quantum wells after the electron deceleration by the *n*-EBL. Moreover, the electron profiles in the last three-pair $In_{0.10}Ga_{0.90}N$/GaN MQWs neighboring to the *p*-GaN layer for Reference sample and Sample with *n*-EBL are presented in Fig. 6.2.7(b), where the electron concentration for Sample with *n*-EBL has been reduced as compared to that of the Reference sample. This is reasonable since

the deceleration of electrons by the *n*-EBL causes the reduction of the mean free path and thus more electrons are captured by the $In_{0.18}Ga_{0.82}N$/GaN MQWs, and hence the electron injection efficiency of the $In_{0.10}Ga_{0.90}N$/GaN MQWs is lower. The characteristics of the electron distribution in the two MQW stacks explain the evolutional behavior of EL spectra under different current levels in Figs. 6.2.3(a)-(h). Note, according to Fig. 6.2.3(g), the short wavelength emission regime for the Sample with *n*-EBL is immersed by the long wavelength emission regime, and this is attributed to the improved transport of hot holes across the $In_{0.10}Ga_{0.90}N$/GaN MQWs with thin quantum barriers when the bias is increased. Furthermore, we have also demonstrated the electron leakage into the *p*-GaN layer for the two samples in Fig. 6.2.7(c). It can be clearly seen that the electron leakage of the InGaN/GaN LED with *n*-EBL is significantly reduced as compared to that of the Reference sample. The reduced electron leakage as a result of the electron blocking effect by the *n*-EBL, accounts for the improved optical output power for Sample with *n*-EBL as observed in Fig. 6.2.4.

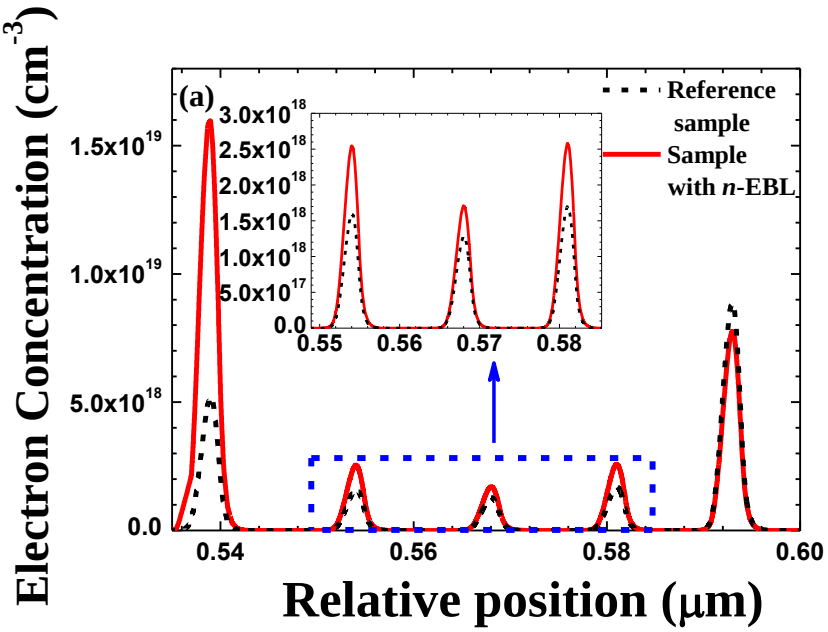

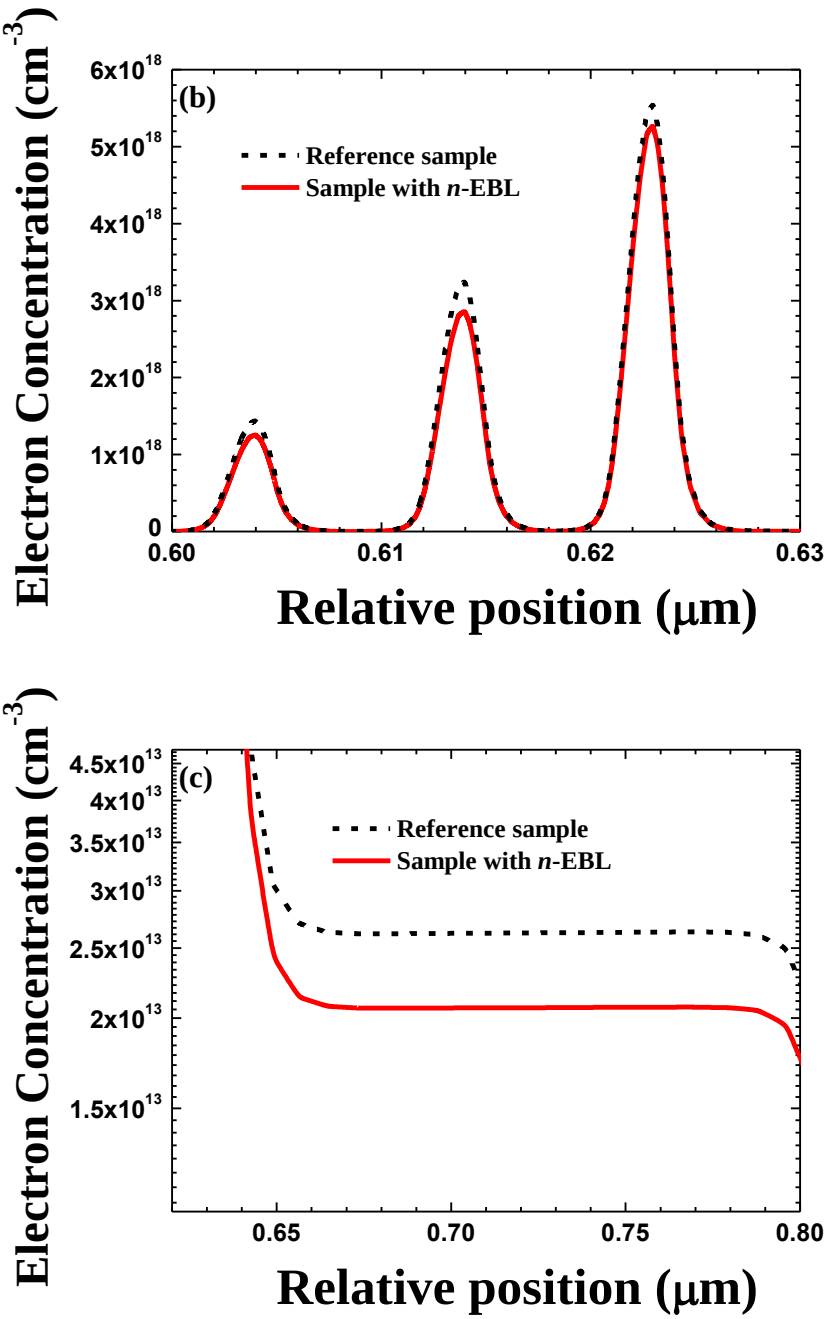

FIG. 6.2.7 Electron profiles for Reference sample and Sample with *n*-EBL (a) in linear scale for first five $In_{0.18}Ga_{0.72}N$/GaN MQWs, (b) in linear scale for last three $In_{0.10}Ga_{0.90}N$/GaN MQWs and (c) in semilog scale in p-GaN region. The data are collected at current level of 25 A/cm^2.

6.2.4 Summary

To summarize, the effect of the *n*-EBL on the electron blocking has been investigated both theoretically and experimentally. Through the analysis of the

evolutional behavior of the dual-wavelength EL spectra of the Reference sample and the Sample with *n*-EBL under different current injection levels, the origin of the *n*-EBL on the reduction of electron overflow has been revealed. The polarization induced electric field caused by the *n*-EBL decelerates the thermal velocity of electrons and thus the mean free path of electrons has been reduced and the electron capture efficiency by quantum wells has been enhanced. As a result, the electron overflow from the active region has been suppressed by the *n*-EBL. Therefore, AlGaN as the *n*-type electron blocking layer holds great promise for achieving better-performance InGaN/GaN LEDs.

6.3 Summary

In this chapter, we have proposed a mean-free-path model to explain the electron overflow suppression through an InGaN layer as the electron cooler and an AlGaN layer as the n-type electron blocking layer. The electron thermal transport velocity can be reduced by interacting with LO phonon, which takes place in the InGaN layer, while the thermal velocity can also be reduced by the polarization induced electric field in the *n*-type AlGaN electron blocking layer. As a result, our mean-free-path model is quite useful in helping understand the device physics and optimize the LED performance.

Chapter 7 P-doping-free InGaN/GaN light-emitting diodes driven by three-dimensional hole gas

As has been discussed in Chapter 6, electron overflow significantly deteriorates the efficiency of the InGaN/GaN light-emitting diodes (LEDs). However, the electron overflow can be suppressed once the p-GaN doping efficiency can be enhanced. Here, GaN/$Al_xGa_{1-x}N$ heterostructures with a graded AlN fraction, completely lacking *p*-doping, are designed and grown using metal-organic-chemical-vapor deposition (MOCVD) system to realize the three-dimensional hole gas (3DHG). The existence of the 3DHG is confirmed by capacitance-voltage measurements. Based on this design, a p-doping-free InGaN/GaN LED driven by the 3D-HG is proposed and grown using MOCVD. The electroluminescence, which is attributed to the radiative recombination of injected electrons and holes in InGaN/GaN quantum wells, is observed from the fabricated p-doping-free devices. These results suggest that the 3DHG can be an alternative hole source for InGaN/GaN LEDs besides common Mg dopants.

7.1 Introduction

For the purpose of energy-saving lighting, InGaN/GaN light-emitting diodes (LEDs) have been regarded as excellent candidates to replace incandescent and fluorescent lighting sources [13, 162]. To this end, tremendous efforts have been devoted to improving the LED performance through addressing various issues related to material quality, structure optimization, and device design and fabrication [21, 28, 56, 62, 63, 150, 154, 176-178]. Among these issues to date, a low p-type doping efficiency remains as a limiting factor, which adversely affects the LED performance. In a typical p-type Mg doped GaN, the resulting

hole concentration is low because only ~1% of Mg dopants are ionized at room temperature [63]. To increase the ionization efficiency of the Mg dopants, a p-type GaN/AlGaN supperlattice was previously employed as the electron blocking layer [176, 177]. Also, the Mg dopants were reported to be more efficiently ionized under the polarization-induced electric fields within the supperlattice, which is known as Pool-Frenkel effect [178]. Recently, it has been reported that the hole concentration can be increased through the polarization doping [62, 154]. The GaN/$Al_xGa_{1-x}N$ heterostructures grown along the polar orientations exhibit strong spontaneous and piezo-electric polarizations [20]. Such strong polarizations can induce electric fields causing significant band bending in the GaN/$Al_xGa_{1-x}N$ heterostructures. This in turn generates a thin channel in the GaN layer near the GaN/$Al_xGa_{1-x}N$ interface where the two-dimensional hole gas (2D-HG) can be formed [179-181]. The 2D-HG can be extended into the three-dimensional hole gas (3DHG) distributing within the $Al_xGa_{1-x}N$ layer where the AlN fraction is graded to GaN [62, 154]. In the previous works (Refs. 61 and 151), the $Al_xGa_{1-x}N$ layer with the graded AlN fraction was doped with Mg dopants, and the strong polarization induced electric fields in the $Al_xGa_{1-x}N$ layer with the graded AlN fraction could increase the ionization rate of the Mg dopants through Pool-Frenkel effect, which may also contribute to the enhancement of the hole concentration. Therefore, it remains unclear if the polarization doping induced 3D hole gas plays a significant role in the enhancement of the hole concentration. In this work, we designed and grown undoped GaN/$Al_xGa_{1-x}N$ heterostructures with a graded AlN fraction. We investigated and confirmed the generation of the 3DHG in this class of heterostructures. Furthermore, we

incorporated these GaN/$Al_xGa_{1-x}N$ heterostructures with the graded AlN fraction in the InGaN/GaN multiple-quantum-well (MQW) LED architecture, completely lacking *p*-doping. We observed the diode-rectifying characteristics in the current-voltage curve and the electroluminescence from such 3D hole gas driven LEDs. Being consistent with the experimental results, our simulations have theoretically shown that the 3DHG has been formed as a result of AlN composition grading in $Al_xGaN_{1-x}N$/GaN heterostructures, and more importantly, the 3DHG gas can be injected into the quantum wells for recombination with electrons.

7.2 Experiment

Four [0001] orientated epi-structures as shown in Fig. 7.1 were designed and grown by a metal-organic chemical vapor deposition (MOCVD) system,. The growth was initiated on c-plane sapphire substrates followed by a 30 nm GaN as the nucleation layer. Then, a 4 μm unintentionally doped GaN (u-GaN) was grown. For Sample *A*, a 100 nm $Al_xGa_{1-x}N$ layer with 10% AlN fraction was grown, which was followed by a 10 nm u-GaN layer. For Sample *B*, a 100 nm $Al_xGa_{1-x}N$ layer with the AlN fraction was linearly graded from 0.10 to 0.02 along the growth orientation, which was then covered by a 10 nm u-GaN layer. Furthermore, we also grew a full LED architecture (i.e., Sample *D*) by using Sample *B* as the template, on which a 10 nm n-GaN with a doping concentration of 5×10^{17} cm^{-3} was grown as the current spreading layer for holes [21]. Then, three-period $In_{0.12}Ga_{0.88}N$/GaN MQWs were grown, of which the well and barrier thickness are 3 and 8 nm, respectively. Finally, a 0.3 μm n-GaN layer with the doping concentration of 5×10^{18} cm^{-3} was grown. As a

reference, Sample *C* was grown with the InGaN/GaN MQWs and the n-GaN layer on top of the u-GaN template.

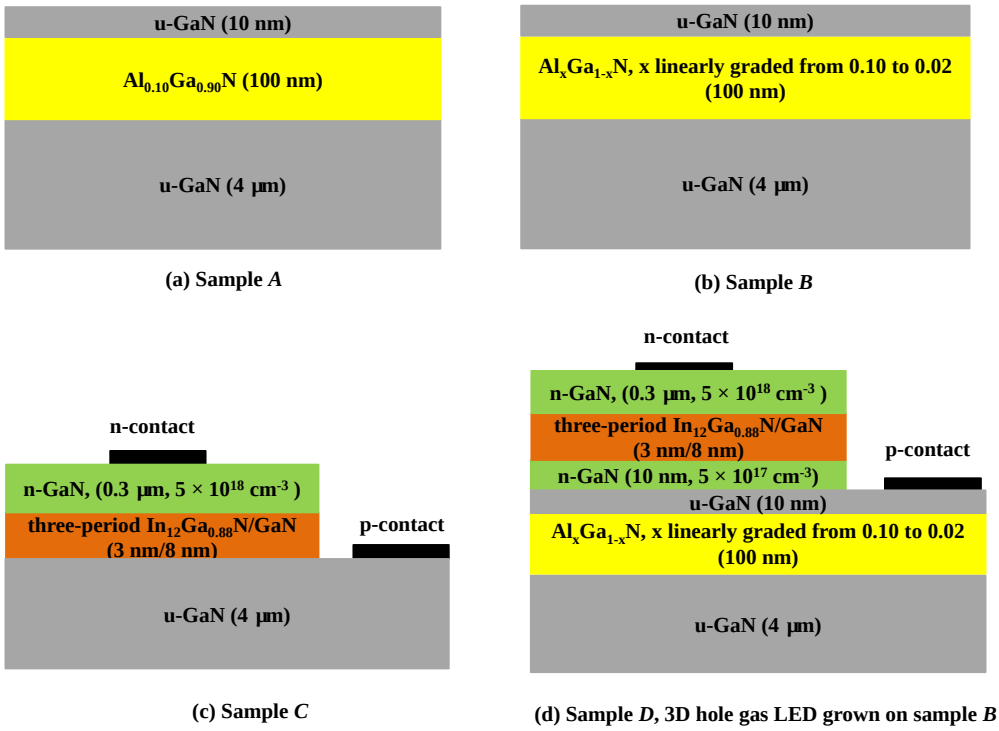

FIG. 7. 1 (a) Sample *A* with a GaN/$Al_{0.10}Ga_{0.90}N$ heterostructure, (b) Sample *B* with a graded AlN fraction in the $Al_xGa_{1-x}N$ layer, (c) Sample *C* with an InGaN/GaN LED directly grown on u-GaN template and (d) Sample *D* with an InGaN/GaN LED grown on Sample *B*.

Following the epitaxial growths, we have characterized the quality of the samples through XRD. The full-width at half-maximum (FWHM) of (102) and (002) X-ray diffraction spectra of the two samples are all around 213.5 and 216.0 arcsec. Hence excellent crystal quality has been obtained for our grown samples. Meanwhile the capacitance-voltage (CV) measurements were performed for Samples *A* and *B* at room temperature to probe the hole gas. The CV test system used in this work is a conventional mercury-based CV measurement system (802B MDC three function mercury probe) operating at

an AC frequency of 100 KHz. The area for the circular mercury probe to record the capacitance value of the tested samples is 4.582×10^{-3} cm^{-2}. The photoluminescence (PL) measurements were conducted on Samples *C* and *D* using a PL mapper system (Nanometric RPM2000) to characterize the quantum well emission. The excitation wavelength of the 15 mW He-Cd laser source is 325 nm.

The device fabrication was conducted for Samples *C* and *D*. Device mesas of 350×350 μm^2 were obtained by reactive ion etch (RIE) to expose the u-GaN layers for Samples *C* and *D*, respectively. Then Ni/Au (5 nm/5 nm) was deposited on the u-GaN layers as the p-contact for the two samples. The annealing was conducted for Ni/Au contact at 575 ^oC in the O_2 ambient for 5 minutes. Then, Ti/Au (30 nm/150 nm) was finally deposited as the contact pads both on the n-GaN layer and Ni/Au.

7.3 Results and discussions

The measured capacitance is depicted as a function of the applied bias as shown in Fig. 7.2(a) for both Samples *A* and *B*. The positive bias has been applied to deplete the holes on Samples *A* and *B*. Note that we have the u-GaN layer under the $Al_xGa_{1-x}N$ layer, and thus the electron gas generated below the $Al_xGa_{1-x}N$ layer will affect our measurement [179-181]. Since $C_t = C_p \times C_n / (C_p + C_n)$, in which C_t, C_p and C_n denote the total capacitance; the capacitance due to the hole depletion and the capacitance due to the electron accumulation, respectively. When $C_n >> C_p$, $C_t \approx C_p$. This condition can be realized when the applied bias exceeds 2V for Sample *A* and 3V for Sample *B*. According to Fig. 7.2(a), we can see that the capacitance decreases with the

increasing applied bias for both samples, which is due to the extension of the depletion region width. Meanwhile, we also calculated the hole concentration according to the CV curves obtained. The detailed hole concentration for Sample *B* is shown in Fig. 7.2(b). The inset figure shows the hole concentration extracted for both Samples *A* and *B* for comparison purposes. The inset figure in Fig. 7.2(b) shows that the 2D hole gas is generated and localized in the GaN/$Al_{0.10}Ga_{0.90}N$ interface for Sample *A*, and the highest hole concentration is measured to be ~10^{20} cm^{-3}. The hole concentration quickly drops to ~10^{16} cm^{-3} in the region away from the GaN/$Al_{0.10}Ga_{0.90}N$ interface. On the contrary, the hole gas distribution is larger even across the $Al_xGa_{1-x}N$ layer in Sample *B*. The hole concentration is ~10^{19} cm^{-3} near the GaN/$Al_{0.02}Ga_{0.98}N$ interface [Region I shown in Fig. 7.2(b)], and is flattened to ~5 × 10^{17} cm^{-3} across the $Al_xGa_{1-x}N$ layer [Region II shown in Fig. 7.2(b)], representing the 3D hole distribution. Since the volume density of the polarization charge is depicted as $N_D^{Pol}(z) = \nabla \cdot P(z) = \partial P(z)/\partial z$ [182], in which *P(z)* is the polarization charge profile along the growth orientation (i.e., *z*, with the unit of nm). In Sample *B*, we have linearly graded the AlN fraction in the $Al_xGa_{1-x}N$ layer from 0.10 to 0.02 within 100 nm, and thus the relationship between *x* and *z* is $z = (-1.25x + 0.125) \times 1000$. Note that the negative polarization induced charges pull the holes into the $Al_xGa_{1-x}N$ layer. Therefore, $N_D^{Pol}(z) = \nabla \cdot P(z) = (\partial P/\partial x) \times (\partial x/\partial z)$. It is known that an approximately linear relationship between the polarization charge (i.e., *P*) and the AlN fraction (i.e., *x*) can be obtained [20]. Thus, $N_D^{Pol}(z)$ can be treated as the "bulk dopants" to achieve the bulk carrier concentration, i.e., holes in this case as indicated in Region II of Fig. 7.2(b). Our finding shows that the 3D hole gas can be realized

through the polarization doping in the undoped GaN/$Al_xGa_{1-x}N$ heterostructures with the graded AlN fraction, just like the 2D hole gas formed in the previously reported abrupt GaN/$Al_xGa_{1-x}N$ heterostructure interface of polar-orientations [183-185]. It is believed that the native defects in the material such as Ga vacancies and the background intrinsic carriers are regarded as the hole sources. Nevertheless, we can only detect the hole concentration within the $Al_xGa_{1-x}N$ layer for 50 nm according to Fig. 7.2(b). The strong positive bias significantly accumulates the 2D electron gas mentioned previously, and thus the electron accumulation prevents the further extension of the depletion region.

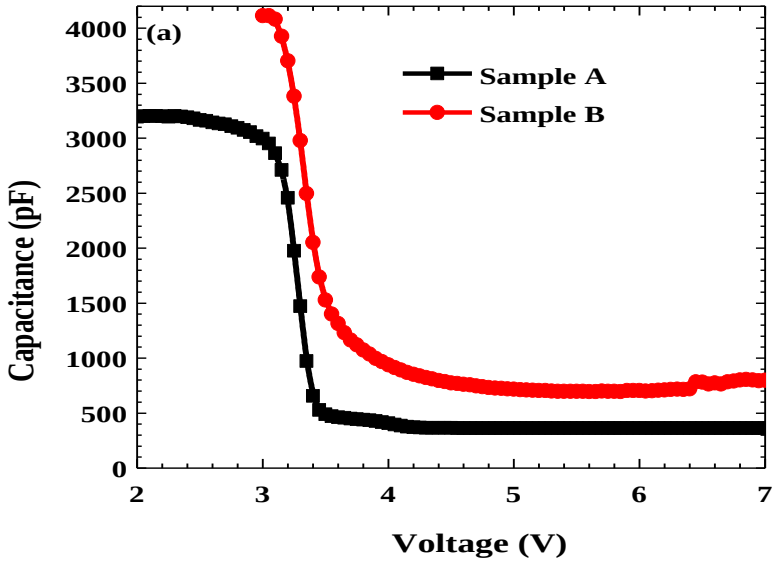

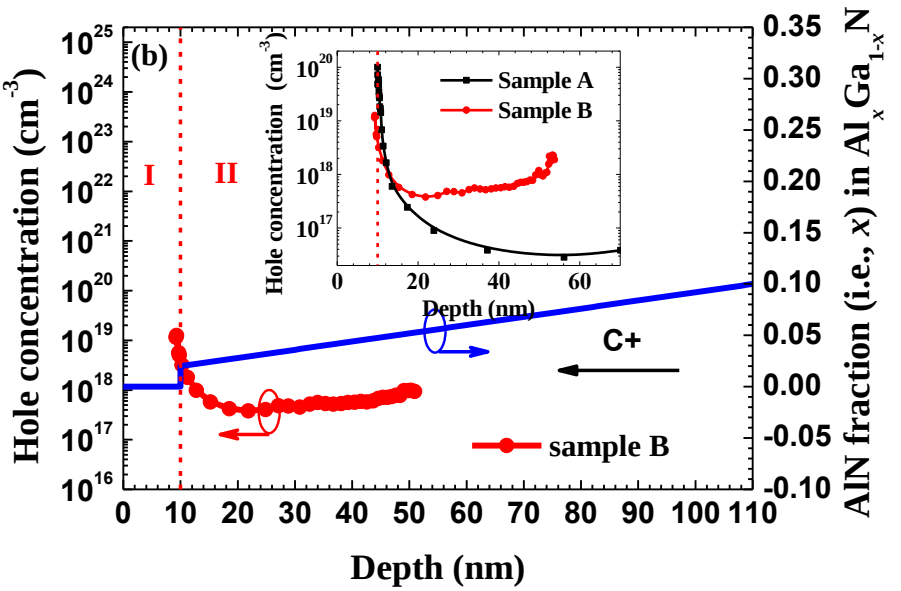
(b)
I
II
Hole concentration (cm^{-3})
AlN fraction (i.e., x) in Al$_x$Ga$_{1-x}$N
Depth (nm)
C+
sample B
Sample A
Sample B

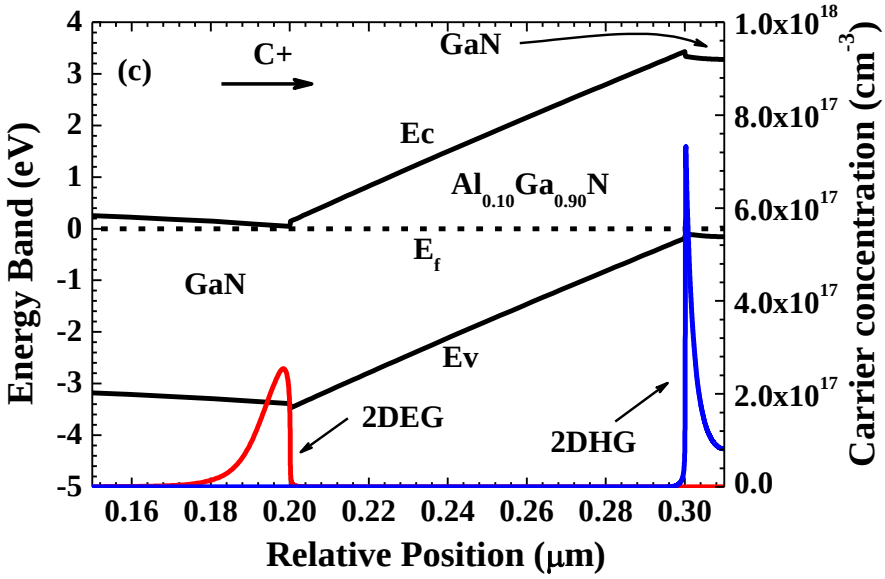
(c)
C+
GaN
Ec
Al$_{0.10}$Ga$_{0.90}$N
E$_f$
GaN
Ev
2DEG
2DHG
Energy Band (eV)
Carrier concentration (cm^{-3})
Relative Position (μm)

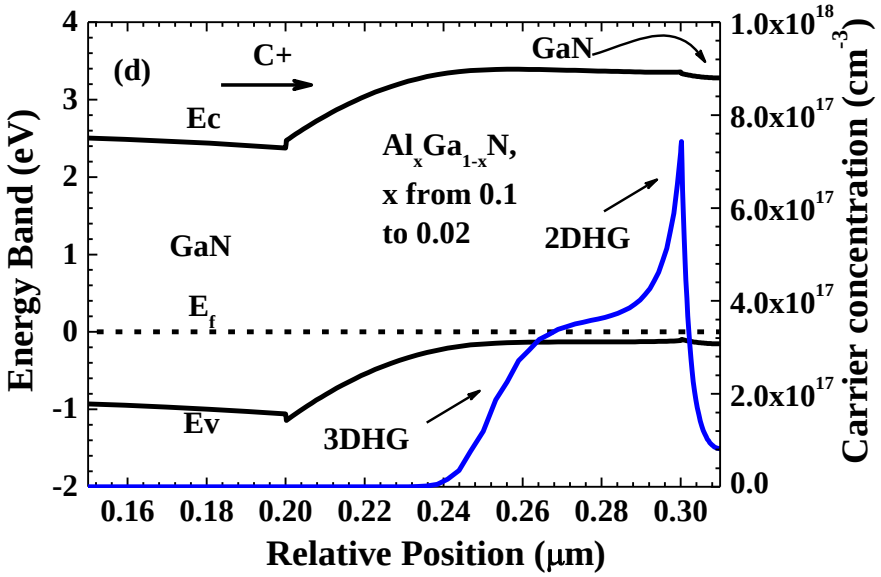

FIG. 7. 2 (a) Capacitance *versus* the applied bias for Samples *A* and *B*, (b) extracted hole concentration for Sample *B*, and the carrier concentration for both Samples *A* and *B* (inset) with the AlN fraction (i.e., *x*) along the growth orientation (c^+) in the $Al_xGa_{1-x}N$ layer being shown, (c) simulated equilibrium energy band, 2DEG, 2DHG for Sample *A* and (d) simulated equilibrium energy band and 3DHG for Sample *B*.

In order to better depict the physical mechanism, we have calculated the energy band diagrams and the hole gas distribution for Samples *A* and *B* by using APSYS [119], which self-consistently solves the Poisson and Schrödinger equations with proper boundary conditions. In our models, we have considered the polarization induced interface charges for any heterostructure. The polarization charge density is calculated based on the models developed by Fiorentini *et al*.[20] The polarization induced sheet charge density between the GaN and $Al_{0.10}Ga_{0.90}N$ layers is set to 2.43 $\times 10^{12}$ cm^{-2} while the polarization induced sheet charge density of 8.74 $\times$ 10^{11} cm^{-2} is assumed between the $Al_{0.02}Ga_{0.98}N$ layer and GaN cap layer for Sample *B*. Meanwhile, we have the $Al_xGa_{1-x}N$ layer with a graded AlN composition in Sample *B*, and hence

according to $N_D^{Pol}(z) = \nabla \cdot P(z) = (\partial P / \partial x) \times (\partial x / \partial z)$, a volume charge density of 3.58 $\times 10^{17}$ cm^{-3} has been assumed in the $Al_xGa_{1-x}N$ region. Such volume charges in the $Al_xGa_{1-x}N$ region with a linearly graded AlN composition are crucial, since no 3DHG is produced if the volume charges are lacked. In addition, the donor-type states with the energy level of Ec-0.5 eV have also been included in our models [185]. The density of those donor-type states has been assumed to be 7 $\times 10^{17}$ cm^{-3} [24]. In addition, the Ga-vacancy has been considered as a p-type dopant with the deep acceptor level of 0.86 eV above the valance band and we have set it to 0.2 $\times 10^{17}$ cm^{-3} in the undoped layers [186, 187].

The calculated energy band diagrams and carrier distribution for Samples *A* and *B* under the equilibrium state have been shown in Figs. 7.2(c) and 7.2(d), respectively. Both the 2DEG and 2DHG have been obtained at the $GaN/Al_{0.10}Ga_{0.90}N$ and $Al_{0.10}Ga_{0.90}N/GaN$ interfaces. Interestingly, we did not observe the 2DEG in Fig. 7.2(d) for Sample *B*, since the 2DEG has been depleted by the negative charges in the $Al_xGa_{1-x}N$ region with a graded AlN composition. Nevertheless, the hole gas has been obtained at the $Al_xGa_{1-x}N$ region and the cap GaN layer. Specifically, the 2DHG exists between the cap GaN layer and the $Al_{0.02}Ga_{0.98}N$ region, while the hole gas has been extended into three-dimensional within the $Al_xGa_{1-x}N$ region, i.e., 3DHG with the carrier density of ~3.5 $\times 10^{17}$ cm^{-3}. The 3DHG only distributes with the 50 nm range in the $Al_xGa_{1-x}N$ region, while the energy alignment in the remaining $Al_xGa_{1-x}N$ region has depleted the holes. A further insight into to Fig. 7.2(d) reveals that, unlike Fig. 7.2(c), there is less GaN band bending in the lower interface of $GaN/Al_{0.10}Ga_{0.90}N$, and this is due to the screening effects of the positive

polarization induced sheet charges at the GaN/$Al_{0.10}Ga_{0.90}N$ interface by the aforementioned negative volume charges in the $Al_xGa_{1-x}N$ region for Sample *B*.

Note that the generation of hole gas is closely related to the AlGaN layer thickness, GaN cap layer thickness and the AlN composition in the AlGaN layer [180, 181, 185]. The spontaneous polarization and piezoelectric polarization mismatches between the AlGaN layer and GaN cap layer will cause the generation of negative polarization charges which will subsequently draw the holes to form the hole gas. The density of the hole gas is determined by the polarization charge density which is determined by the AlGaN thickness, AlN composition and the GaN cap layer thickness. Based on these considerations, we have chosen AlGaN with 10% AlN composition and 100 nm thickness and GaN cap layer with 10 nm thickness for Samples *A*. On the other hand, we purposely design an $Al_xGa_{1-x}N$ layer of 100 nm with AlN composition linearly grading from 0.1 to 0.02 and a GaN cap layer of 10 nm for Sample *B* and Sample *D* to facilitate the formation of 3DHG. In addition, the calculated 2DHG and the 3DHG density in Fig. 7.2(c) and 7.2(d) is lower than the measured values in Fig. 7.2(c). This is due to the reduced polarization charge density in each heterostructure surface by considering the crystal relaxation [20].

The injection current has been measured as a function of the applied bias for the fabricated devices of Samples *C* and *D*, as shown in Fig. 7.3. Sample *C* grown on u-GaN template shows no electrical rectifying behaviour that means no pn-junction has been formed. while the diode behaviour is observed from Sample *D*. The diode behaviour for Sample *D* indicates the formation of the pn-junction between the n-GaN layer and the 3D hole gas in the $Al_xGa_{1-x}N$ layer

with the graded AlN fraction. The turn-on voltage of Sample *D* is about 30V, which is much higher than the conventional InGaN/GaN LED with the Mg doped GaN layer on the top. In Sample *D*, the turn-on voltage mainly consists of three components: the pn-junction voltage drop, the voltage drop on the contacts, and the voltage drop across the conduction layer underlying the active region. However, in the conventional InGaN/GaN LED, the underlying conduction layer is the n-GaN layer with the thickness ranging from 2 to 4 μm [21, 150]. The mobility of electrons in the n-GaN layer is as high as 200 cm^2/Vs and the electron concentration is typically 1×10^{19} cm^{-3}. Therefore, the voltage drop across the underlying n-GaN layer is negligible. Nevertheless, in Sample *D*, the underlying conduction layer is the 3D hole gas layer with the thickness of only ~50 nm, which significantly reduces the cross-sectional area for the current in the device with a lateral current injection scheme. Moreover, the hole mobility is typically less than 10 cm^2/Vs, which is much lower than that of the electrons [188], while the hole concentration is also lower (8×10^{17} cm^{-3}). Therefore, the voltage drop across the 3D hole gas layer is quite large, mainly accountable for the large turn-on voltage observed in Fig. 7.3. Meanwhile, the poor electrical conductance in the 3DHG $Al_xGa_{1-x}N$ layer causes the significant current crowding effects, which is also accountable for the high turn-on voltage [21]. However, the 3D hole gas generated in the $Al_xGa_{1-x}N$ layer with a graded AlN fraction can be integrated in the InGaN/GaN LED with the p-type GaN layer on top. On one hand, the cross-sectional area for the hole current will be increased, and on the other hand, the overall hole concentration (holes donated by ionized Mg dopants and 3D hole gas) can be significantly enhanced, and hence the device performance can be substantially improved [62, 189].

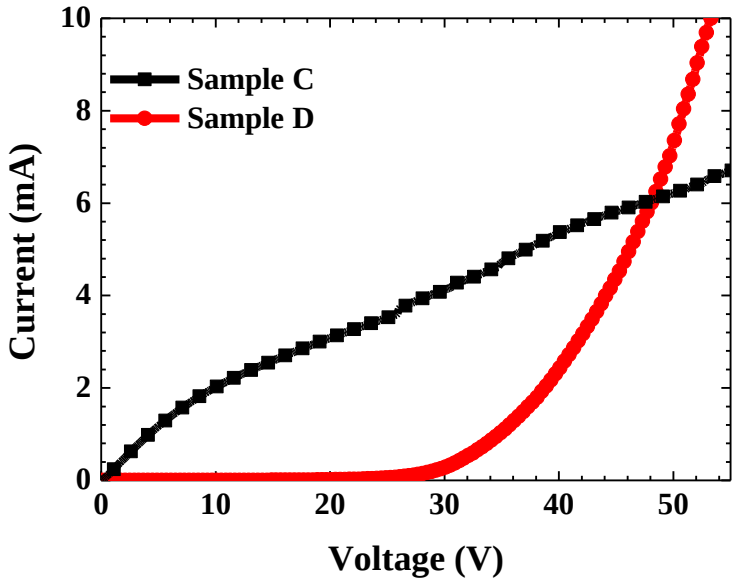

FIG. 7. 3 Experimentally measured current as a function of the applied voltage for InGaN/GaN LED grown on u-GaN (i.e., Sample *C*), and InGaN/GaN LED grown on 3D hole gas structure (i.e., Sample *D*).

In Fig. 7.4(a), the PL spectra for both Samples *C* and *D* were shown. The full width at half maximum (FWHM) of the PL spectra for Samples *C* and *D* is both around 15 nm, which means the excellent crystal quality of the grown InGaN/GaN quantum wells for Samples *C* and *D*. The peak emission wavelength is about ~ 417 nm and ~ 420 nm for Samples *C* and *D* at room temperature, respectively. The slightly longer emission wavelength for Sample *D* is due to the stronger compressive strain from the $Al_xGa_{1-x}N$ layer underneath the MQWs [80]. In addition, we have also measured the electroluminescence (EL) from the fabricated devices of Sample *D*, which is shown in Fig. 7.4(b). The emission wavelength at the low current level peaked at 420 nm, which matches well the PL emission in Fig. 7.4(a). Besides, we have also measured the EL spectra at various current levels as presented in Fig. 7.4(b). A red shift of the emission wavelength with increasing injection current levels has been

observed and is attributed to the increasing junction temperature during testing [21]. Meanwhile, the integrated optical output power in terms of the injection current for Sample *D* is shown in Fig. 7.4(c). The optical output power increases linearly at a lower current regime and starts to saturate above 10 mA. The saturation of optical power could be due to the significant Joule heating caused by the high device resistance mentioned previously. On the other hand, the EL of Sample *C* is extremely weak (not detectable in our measurement system) though the PL is observed at room temperature, suggesting Sample *C* has a low hole concentration in the u-GaN template.

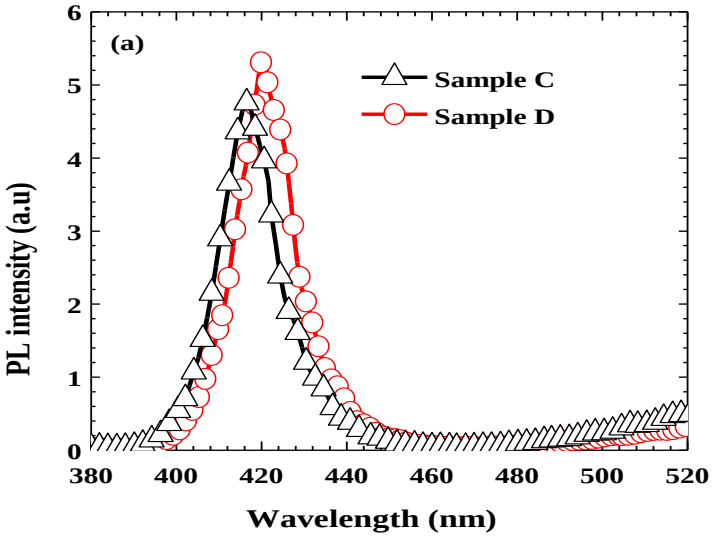

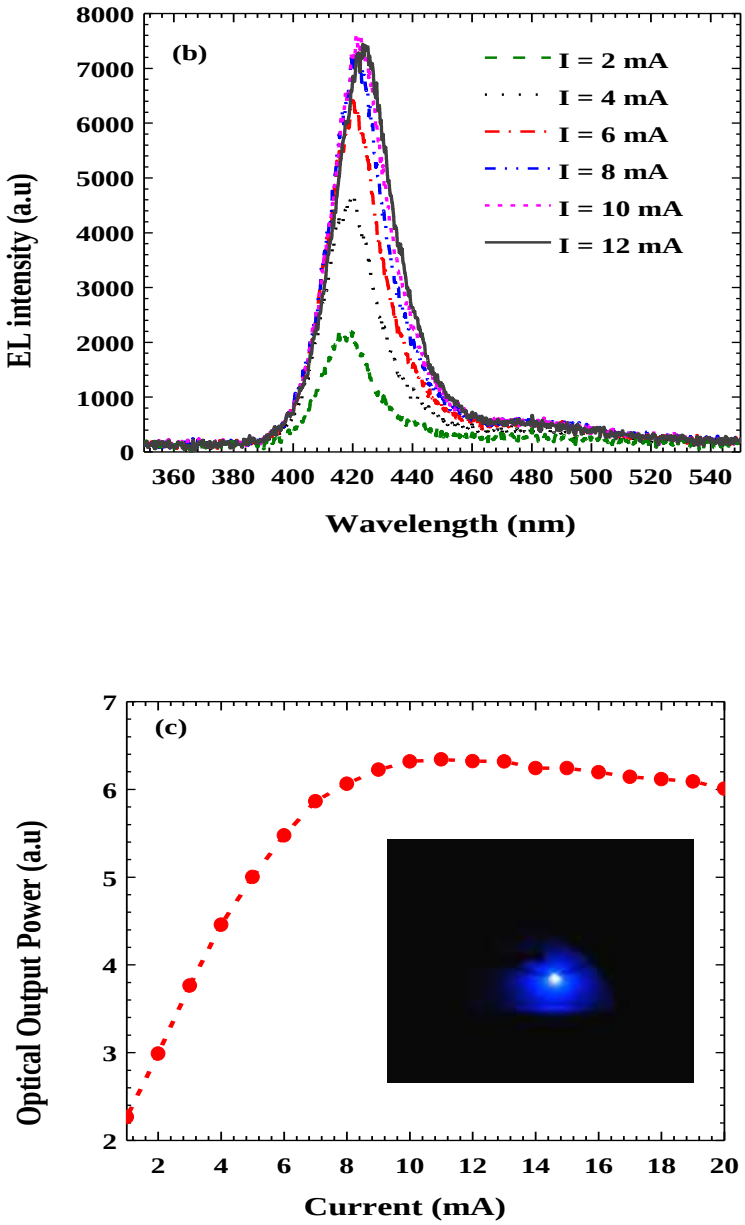

FIG. 7. 4 (a) PL spectra for Samples *C* and *D* and (b) EL spectra at various injection current levels for Sample *D* and (c) optical output power for Sample *D*.

The non-equilibrium band structure, carrier concentration and radiative recombination rate have also been simulated and demonstrated for Sample *D*. The calculated energy band diagrams for Sample *D* is presented in Fig. 7.5. A continuous energy band has been obtained in the $Al_xGa_{1-x}N$ layer with the AlN fraction linearly graded from 0.10 to 0.02 along the growth orientation. The

polarization effects strongly bend the energy bands for the underlying u-GaN layer and the $Al_xGa_{1-x}N$ layer. When the relative position is smaller than 0.16 μm in Fig. 7.5, the quasi-Fermi level for holes (E_{fh}) deviates away from the valance band (E_v) of the $Al_xGa_{1-x}N$ layer in the region close to the underlying u-GaN layer, while the quasi-Fermi level for electrons (E_{fe}) approaches the conduction band (E_c) of the underlying u-GaN layer. The alignment of E_{fh}, E_{fe}, E_v and E_c predicts a 2D electron formation at the interface between the underlying u-GaN and the $Al_xGa_{1-x}N$ layer and the depletion of holes in the region between 0.1 and 0.16 μm [179-181], which can be seen in Fig. 7.6(a) and 7.6(b). Unlike Figs. 7.2(c) and 7.2(d), the electrons formed 2DEG here are provided by the injected non-equilibrium electrons, which are attracted by the positive polarization induced charges in the $GaN/Al_{0.10}GaN_{0.90}N$ interface. Meanwhile, a nearly constant distribution of 3D hole gas in the region between 0.16 and 0.20 μm is also achieved. Furthermore, the carriers are also injected into the quantum wells and the radiative recombination has been calculated in the quantum wells as shown in Fig. 7.6(b).

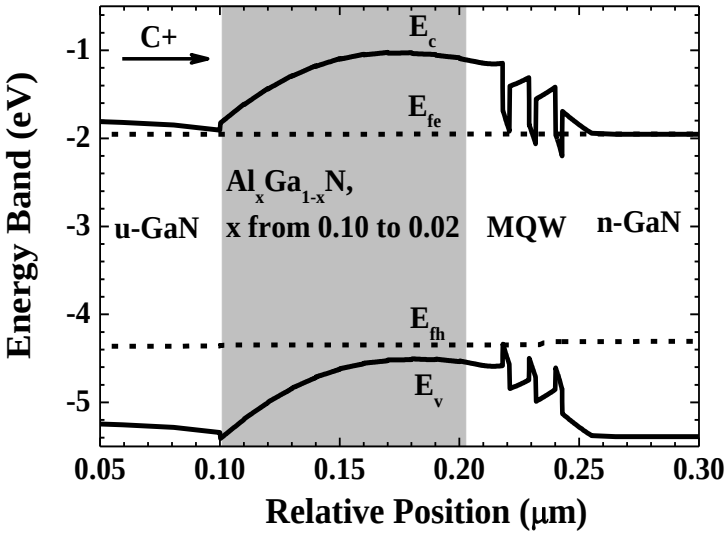

FIG. 7. 5 Calculated energy band diagram for Sample *D*.

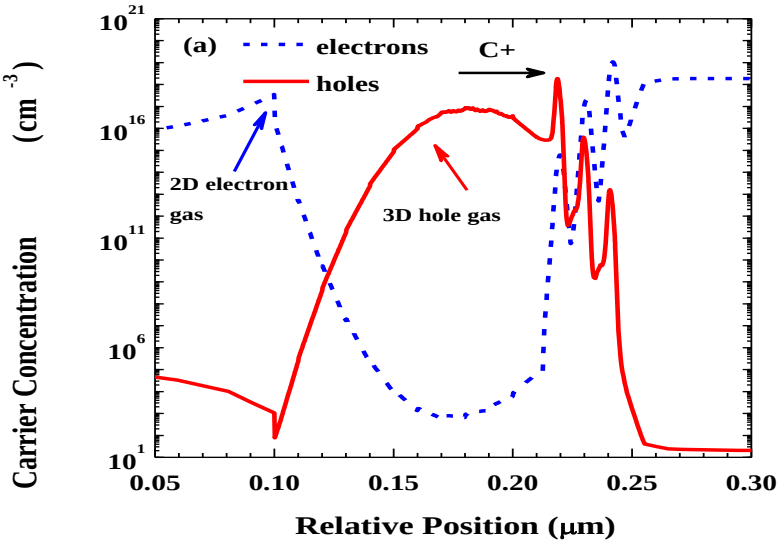

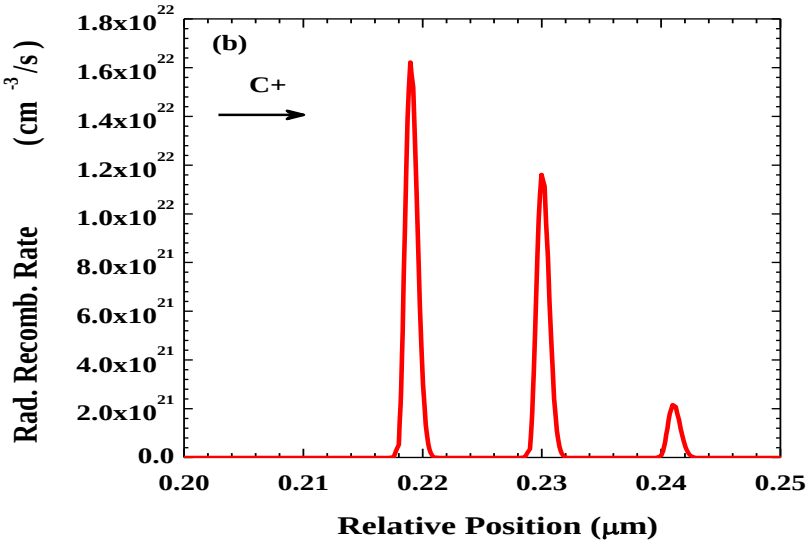

FIG. 7. 6 (a) Calculated electron and hole concentration and (b) radiative recombination rates in the MQW for Sample *D*.

7.4 Summary

In conclusion, 3D hole gas has been generated in the undoped $Al_xGa_{1-x}N$ layer with the AlN fraction linearly graded from 0.10 to 0.02 along the [0001] growth orientation. The designed structure was further employed as the p-conduction layer to replace the Mg-doped GaN layer in the InGaN/GaN LED. The fabricated device with the 3DHG structure shows an obvious rectifying diode characteristic in IV measurement. More importantly, EL has been observed and detected from the 3D hole gas driven InGaN/GaN LED, which is attributed to the radiative recombination between the electrons injected by the n-GaN layer and holes provided by the 3D hole gas in the $Al_xGa_{1-x}N$ layer. On the other hand, the 3D hole gas density can be increased by further enhancing the AlN composition in the $Al_xGa_{1-x}N$ layer while keeping a low dislocation density to suppress the crystal relaxation. Also, the $Al_xGa_{1-x}N$ layer can be properly doped by any p-type dopants, such as Mg and Be. This work

demonstrates that, besides conventional Mg-doped p-type GaN, 3D hole gas generated through polarization doping can also be an alternative hole source for the InGaN/GaN LEDs. Therefore, such 3D hole gas design can be adopted into the p-type electron blocking layer and is promising to achieve better performance in InGaN/GaN LEDs.

Chapter 8 Conclusions, summaries and recommendations for future work

8.1 Conclusions and summaries

In this thesis, the epitaxial growth and device design of the InGaN/GaN light-emitting diodes have been studied and demonstrated. In order to improve the quantum efficiency for the InGaN/GaN multiple quantum well light-emitting diodes, several approaches have been proposed and demonstrated. Furthermore, we have also shown a proposed model to explain the physics mechanism of electron overflow and the approaches to avoid it. The major achievements can be summarized below:

(1) We have demonstrated the carrier recombination and light generation processes for InGaN/GaN light-emitting diodes. Specifically, we have studied the spontaneous and piezoelectric polarization effects for wurtzite III-nitride compounds. As have been discussed, the polarization induced electric field within the InGaN/GaN multiple quantum wells can be suppressed in those semi-polar epitaxial films and the films completely lacking polarization induced electric field can be achieved along those non-polar growth orientations.

(2) We have discussed the approaches for growing high-quality InGaN/GaN light-emitting diode epitaxial films. In addition, the methods for achieving InGaN/GaN light-emitting diodes with desired emission wavelength have been demonstrated. The processes for fabricating InGaN/GaN light-emitting diodes into chips have been discussed in this thesis.

(3) Currently, the market for InGaN/GaN light-emitting didoes is still dominated by those grown along [0001] orientation. There exists a strong polarization induced electric field within the InGaN/GaN multiple quantum wells, which has significantly spatially separated the carrier wave functions, and therefore reduced the radiative recombination rates and quantum efficiency for the devices. We have proposed and demonstrated InGaN/GaN light-emitting diodes with Si-step-doped quantum barriers. When compared to the light-emitting diodes with Si-fully-doped quantum barriers, we proposed the Si-step-doped device substantially enhanced the spatial overlap between carrier wave functions that is due to the optimized Si-doped position in the quantum barriers. Our proposed device has also reduced the hole blocking effect. However, the hole retardation can be further reduced by employing Mg-Si-doped quantum barriers, i.e., PN-type quantum barriers, which are proposed and applied by us in our LED devices. We have demonstrated the effectiveness of the PN-type quantum barriers in the suppression of the QCSE and the enhancement of hole transport, and thus the improvement of the device performance.

(4) Due to the low hole mobility in the p-type GaN layer, InGaN/GaN light-emitting diodes suffered from serious current crowding effect. Tremendous efforts have been devoted to improving the current spreading effect. In this thesis, we have increased the current spreading length either by embedding a resistive layer within the p-GaN layer or/and making the p-type contact layer more conductive. To address these issues, we have proposed and demonstrated an InGaN/GaN light-

emitting diode with an *in-situ* p-GaN/n-GaN/p-GaN/n-GaN/p-GaN (PNPNP-GaN) layer. Increased optical output power and quantum efficiency have been obtained from the device, which is attributed to the increased current spreading. In addition, an increased current spreading can also be obtained by making the p-type contact layer more conductive. Therefore, a p^+-GaN/n^+-GaN tunnel homojunction has been proposed. However, the additional voltage is consumed in the tunnel homojunction, and hence, we have also proposed and presented a p^+-GaN/u-InGaN/n^+-GaN tunnel heterojunction. The polarization induced electric field and a smaller band gap in the strained u-InGaN layer promote the tunneling efficiency. As a result, the optical power and quantum efficiency of the device have been improved while the forward voltage for the device can be reduced.

(5) Electron overflow is regarded as one of the causes for the InGaN/GaN LEDs' efficiency droop, and therefore numerous methods have been reported to reduce the electron overflow. Among those, n-type InGaN electron cooler proves to be effective in reducing the electron overflow, and the reduced electron escape from the quantum wells is identified to be responsible for the electron overflow suppression in the literatures. However, in this thesis, we have proposed that the reduced electron overflow by the n-type InGaN electron cooler is actually attributed to the reduced electron mean free path through interacting with longitudinal optical phonons, which has prevented the electrons from directly flying over the quantum wells to a remote position. With the electron mean-free-path model, we have also explained the origin of the electron

overflow reduction by introducing the n-type AlGaN electron blocking layer in the device structure through dual-emission-wavelength method. The polarization induced electric field in the strained n-type AlGaN electron blocking layer reduces the electron thermal velocity and the mean free path. As a result, the electrons which directly fly over the quantum wells to a remote position have been significantly decreased. Therefore, a reduced electron overflow has increased the electron capture rate by the multiple quantum wells and thus the radiative recombination rates between electrons and holes, which in turn increase the device performance.

(6) The performance for InGaN/GaN light-emitting diodes is limited by the low hole concentration in the p-type AlGaN and GaN layers. Thus, in this thesis, we have proposed and demonstrated a p-doping free InGaN/GaN light-emitting diode driven by three-dimensional hole gas (3DHG). The 3DHG is confirmed through the room-temperature capacitance-voltage measurement. The radiative recombination rates between electrons provided by the n-GaN layer and the 3DHG contribute to the spontaneous emission spectra. Therefore, besides the holes supplied by the common Mg acceptors, the 3DHG can be the additional hole source for InGaN/GaN light-emitting diodes.

8.2 Recommendations for future work

In this thesis, we have improved the performance of InGaN/GaN light-emitting diodes from multiple aspects including optimizing the crystal quality, suppressing the polarization effects in the quantum wells, improving the current

spreading, enhancing the electron injection efficiency and finding novel ways to increase the doping efficiency of the p-type material.

However, the efficiency of InGaN/GaN light-emitting didoes is also affected by the low hole injection efficiency. Therefore it is quite advisable to make holes more energetic so that holes can obtain sufficient energy to climb over the valance band discontinuity between the p-type electron blocking layer and the p-type GaN layer. In addition, the hole injection efficiency can be improved by manipulating the hole transport mechanisms, such that we can combine the thermionic emission and tunneling processes for holes.

As being realized, the serious Auger recombination also hinders the device performance especially when the device is biased at a high current level. One approach to suppress the Auger recombination is to make the carriers more evenly distributed across the multiple quantum wells. Therefore, the quantum well thickness, the quantum well number and the quantum barrier thickness shall be optimized so that the carriers can be more homogeneously transported.

In addition, because of the big contrast of the refractive index for the device material and the air, we have a very low light extraction efficiency of less than 20%. Therefore, most of the photons are trapped and re-absorbed by the crystal to generate the electron-hole pairs. Such electron-hole pairs tend to recombine non-radiatively and produce heat. Hence, in the future proposals, the light extraction efficiency can be improved by surface roughing, photonic crystal and surface plasmonics. Enhanced light extraction efficiency can also be realized by growing the light-emitting diode wafers on the nano-patterned substrates.

The last but not the least concern is to better thermally manage the devices so that there is a reduced thermal droop. One promising method to reduce the heat accumulation is to transfer the light-emitting diodes from the sapphire substrates to any other temporary supporting layers such as the copper, nickel, and Si substrates with better thermal conductivity. In this way, we can make a vertical light-emitting diode chip so that the current can more uniformly spread across the device. A reduced current crowding also helps to suppress the thermal droop of the devices.

PUBLICATIONS

1. **Z. -H. Zhang,** S. T. Tan, Z. Ju, W. Liu, Y. Ji, Z. Kyaw, Y. Dikme, X. W. Sun, and H. V. Demir, "On the Effect of Step-Doped Quantum Barriers in InGaN/GaN Light Emitting Diodes," **IEEE/OSA J. Disp. Technol.** 9(4), 226-233 (2013).

2. **Z. -H. Zhang,** S. T. Tan, W. Liu, Z. Ju, K. Zheng, Z. Kyaw, Y. Ji, N. Hasanov, X. W. Sun, and H. V. Demir, "Improved InGaN/GaN light-emitting diodes with a p-GaN/n-GaN/p-GaN/n-GaN/p-GaN current-spreading layer," **Opt. Express** 21(4), 4958-4969 (2013).

3. **Z. -H. Zhang,** S. T. Tan, Y. Ji, W. Liu, Z. G. Ju, Z. Kyaw, X. W. Sun and H. V. Demir, "A PN-type quantum barrier for InGaN/GaN light emitting diodes", **Opt. Express** 21(13), 15676–15685 (2013).

4. **Z. -H. Zhang**, S. T. Tan, Z. Kyaw, Y. Ji, W. Liu, Z. G. Ju, N. Hasanov, X. W. Sun and H. V. Demir, "InGaN/GaN light-emitting diode with a polarization tunnel junction", **Appl. Phys. Lett.** 102(19), 193508-5 (2013).

5. **Z. -H. Zhang,** S. T. Tan, Z. Kyaw, Y. Ji, W. Liu, Z. G. Ju, X. Zhang, X. W. Sun, and H. V. Demir, "*p-doping-free* InGaN/GaN light emitting diodes driven by three-dimensional hole gas", **Appl. Phys. Lett.** 103(26), 263501-5 (2013).

6. **Z. -H. Zhang,** W. Liu**,** S. T. Tan, Z. G. Ju, Y. Ji, Z. Kyaw, X. Zhang, N. Hasanov, B. Zhu, S. Lu, Y. Zhang, X. W. Sun, and H. V. Demir, "On the mechanisms of InGaN electron cooler in InGaN/GaN light emitting diodes", **Opt. Express,** 22 (S3), A779-A789 (2014).

7. **Z. -H. Zhang,** Y. Ji, Z. Kyaw, S. T. Tan, Z. G. Ju, W. Liu, X. Zhang, N. Hasanov, S. Lu, Y. Zhang, B. Zhu, X. W. Sun and H. V. Demir, "On the origin of the electron blocking effect by an *n*-type AlGaN electron blocking layer", **Appl. Phys. Lett.** 104(07), 073511-5 (2014).

8. Z. -H. Zhang, Z. G. Ju, S. T. Tan, Z. Kyaw, W. Liu, Y. Ji, X. L. Zhang, N. Hasanov, X. W. Sun and H. V. Demir, "Improving hole injection efficiency by manipulating its transport mechanism through the p-type electron blocking layer", **Opt. Lett.** 39(8), 2483-2486 (2014).

9. Z. Kyaw*, **Z. -H. Zhang*,** S. T. Tan, Z. G. Ju, X. Zhang, W. Liu, Y. Ji, N. Hasanov, X. W. Sun and H. V. Demir, "On the effect of n-GaN/p-GaN/n-GaN/p-GaN/n-GaN built-in junction in the n-GaN layer for InGaN/GaN light emitting didoes", **Opt. Express,** 22(1), 809-816 (2014), **(*authors of equal contribution).**

10**. Z. -H. Zhang**, W. Liu, Z. G. Ju, S. T. Tan, Y. Ji, Z. Kyaw, X. L. Zhang, L. Wang, X. W. Sun and H. V. Demir, "Self-screening of the quantum confined Stark effect by the polarization induced bulk charges in the quantum barriers", **Appl. Phys. Lett.**, 104(24), 243501 (2014).

11**.** **Z. -H. Zhang***, W. Liu*, Z. G. Ju, S. T. Tan, Y. Ji, Z. Kyaw, X. L. Zhang, L. Wang, X. W. Sun and H. V. Demir, "InGaN/GaN multiple-quantum-well light-emitting diodes with a gradient InN composition suppressing the Auger recombination", **Appl. Phys. Lett.**, 105(3), 033506(2014), **(*authors of equal contribution)**.

12**.** **Z. -H. Zhang**, W. Liu, Z. G. Ju, S. T. Tan, Y. Ji, Z. Kyaw, X. L. Zhang, L. Wang, X. W. Sun and H. V. Demir, "Polarization self-screening in [0001] oriented InGaN/GaN light-emitting diodes for improving the electron injection efficiency", **Appl. Phys. Lett.** 104(25), 251108 (2014).

13**.** Y. Ji, **Z. -H. Zhang,** S. T. Tan, Z. G. Ju, Z. Kyaw, N. Hasanov, W. Liu, X. W. Sun, and H. V. Demir, "Enhanced hole transport in InGaN/GaN multiple quantum well light-emitting diodes with a p-type doped quantum barrier," **Opt. Lett.** 38(2), 202-204 (2013).

14**.** Y. Ji, **Z. -H. Zhang,** Z. Kyaw, S. T. Tan, Z. G. Ju, X. L. Zhang, W. Liu, X. W. Sun, and H. V. Demir, "Influence of n-type versus p-type AlGaN electron-blocking layer on InGaN/GaN multiple quantum wells light-emitting diodes", **Appl. Phys. Lett.** 103(5), 053512-5 (2013).

15**.** Z. G. Ju, S. T. Tan, **Z. -H. Zhang,** Y. Ji, Z. Kyaw, Y. Dikme, X. W. Sun, and H. V. Demir, "On the origin of the redshift in the emission wavelength of InGaN/GaN blue light emitting diodes grown with a higher temperature interlayer," **Appl. Phys. Lett.** 100(12), 123503-4 (2012).

16**.** Z. G. Ju, W. Liu, **Z. -H. Zhang,** S. T. Tan, Y. Ji, Z. Kyaw, X. Zhang, S. Lu, Y. Zhang, B. Zhu, N. Hasanov, X. W. Sun and H.V. Demir, "Improved hole distribution in InGaN/GaN light-emitting diodes with graded thickness quantum barriers", **Appl. Phys. Lett.** 102(24), 243504-3(2013),

17**.** Y. Ji, W. Liu, T. Erdem, R. Chen, S. T. Tan, **Z. -H. Zhang**, Z. G. Ju, X. Zhang, H. Sun, X. W. Sun, S. P. DenBaars and H. V. Demir, "Comparative study on carrier dynamic of InGaN/GaN light emitting diodes grown on (0001) polar plane and (11-22) semipolar plane", **Appl. Phys. Lett.** 104(14), 143506 (2014).

18**.** Z. Kyaw, J. Wang, K. Dev, S. T. Tan, Z. G. Ju, **Z. -H. Zhang**, Y. Ji, N. Hasanov, W. Liu, X. W. Sun, and H. V. Demir, "Room-temperature larger-scale highly ordered nanorod imprints of ZnO film", **Opt. Express**, 21(22), 26846-26853 (2013).

19**.** Z. Kyaw, **Z. -H. Zhang**, W. Liu, S. T. Tan, Z. G. Ju, X. L. Zhang, Y. Ji, N. Hasanov, B. Zhu, S. Lu, Y. Zhang, J. H. Teng, X. W. Sun and H. V. Demir, "Simultaneous enhancement of electron overflow reduction and hole injection promotion by tailoring the last quantum barrier in InGaN/GaN light-emitting diodes", **Appl. Phys. Lett.** 104(16), 161113 (2014).

20. Z. G. Ju, W. Liu, **Z. -H. Zhang**, S. T. Tan, Y. Ji, Z. Kyaw, X. L. Zhang, S. P. Lu, Y. P. Zhang, B. B. Zhu, N. Hasanov, X. W. Sun and H. V. Demir, "Advantages of the blue InGaN/GaN light-emitting diodes with a AlGaN/GaN/AlGaN quantum well structured electron blocking layer", **ACS Photon.** 1 (4), 377–381 (2014).

PATENTS AND DISCLOSURES

1. **ZHANG Zi-Hui,** TAN Swee Tiam, SUN Xiaowei, Hilmi Volkan DEMIR, "A light-emitting device", **US provisional patent application No. 61/662,174**, **PCT application No. PCT/SG2013/000224**.

2. LIU Wei， **ZHANG Zi-Hui,** JU Zhen Gang， ZHANG Xueliang, TAN Swee Tiam, SUN Xiaowei and Hilmi Volkan DEMIR, "A Novel Method to Fabricate Dicing-Free Vertical LEDs", **US provisional patent application No. 61/847,295**, **PCT application No. PCT/SG2013/000542**.

3. ZHANG Xueliang, **ZHANG Zi-Hui**, JI Yun, JU Zhengang, LIU Wei, TAN Swee Tiam, SUN Xiaowei, and Hilmi Volkan DEMIR, "Designs and Methods for Fabricating a Diode with Double-sided Current Guiding Structures", **US provisional patent application No. 61/910,609.**

4. LIU Wei, Zabu KYAW, **ZHANG Zi-Hui**, ZHU Binbin, JU Zhengang, TAN Swee Tiam, ZHANG Xueliang, Hilmi Volkan DEMIR, "Polarity-Engineered High-Efficiency LEDs", **US Provisional application No. 61/996,661**.

5. JU Zhengang, LIU Wei, ZHANG Xueliang, TAN Swee Tiam, JI Yun, **ZHANG Zi-Hui,** Hilmi Volkan DEMIR, "Network Island Metal Support For Inverted LEDs", **US Provisional application 61/996,662.**

BIBLIOGRAPHY

[1] E. F. Schubert, *Light-Emitting Diodes*, 2nd ed. (Cambridge University Press, 2006).

[2] H. P. Maruska and J. J. Tietjen, "The preparation and properties of vapor-deposited single-crystal-line GaN," Appl. Phys. Lett., vol. 15, pp. 327-329, 1969.

[3] J. I. Pankove, E. A. Miller, D. Richman, and J. E. Berkeyheiser, "Electroluminescence in GaN," J. Lumin., vol. 4, pp. 63-66, 1971.

[4] J. I. Pankove, E. A. Miller, and J. E. Berkeyheiser, "GaN blue light-emitting diodes," J. Lumin., vol. 5, pp. 84-86, 1972.

[5] J. I. Pankove, E. A. Miller, and J. E. Berkeyheiser, "GaN electroluminescent diodes," International Electron Devices Meeting, pp. 78-78, 1971.

[6] H. Amano, M. Kito, K. Hiramatsu, and I. Akasaki, "P-type conduction in Mg-doped GaN treated with low-energy electron-beam irradiation (LEEBI)," Jpn. J. Appl. Phys., vol. 28, pp. L2112-L2114, 1989.

[7] S. Nakamura, T. Mukai, M. Senoh, and N. Iwasa, "Thermal annealing effects on p-type Mg-doped GaN films," Jpn. J. Appl. Phys., vol. 31, pp. L139-L142, 1992.

[8] H. Amano, N. Sawaki, I. Akasaki, and Y. Toyoda, "Metalorganic vapor phase epitaxial growth of a high quality GaN film using an AlN buffer layer," Appl. Phys.Lett., vol. 48, pp. 353-355, 1986.

[9] S. Nakamura, "GaN growth using GaN buffer layer," Jpn. J. Appl. Phys., vol. 30, pp. L1705-L1707, 1991.

[10] A. Isamu, A. Hiroshi, K. Masahiro, and H. Kazumasa, "Photoluminescence of Mg-doped p-type GaN and electroluminescence of GaN p-n junction LED," J. Lumin., vol. 48–49, pp. 666-670, 1991.

[11] S. Nakamura, M. Senoh, S. Nagahama, N. Iwasa, T. Yamada, T. Matsushita, H. Kiyoku, and Y. Sugimoto, "InGaN-based multi-quantum-well-structure laser diodes," Jpn. J. Appl. Phys., vol. 35, pp. L74-L76, 1996.

[12] N. Tansu, H. Zhao, G. Liu, X. H. Li, J. Zhang, H. Tong, and Y. K. Ee, "III-nitride photonics," IEEE Photon. J., vol. 2, pp. 241-248, 2010.

[13] S. T. Tan, X. W. Sun, H. V. Demir, and S. P. DenBaars, "Advances in the LED materials and architectures for energy-saving solid-state lighting toward "lighting revolution"," IEEE Photon. J., vol. 4, pp. 613-619, 2012.

[14] M. H. Crawford, "LEDs for solid-state lighting: performance challenges and recent advances," IEEE J. Sel. Top. Quantum Electron., vol. 15, pp. 1028-1040, 2009.

[15] K. D. Langer, J. Vucic, C. Kottke, L. F. del Rosal, S. Nerreter, and J. Walewski, “Advances and prospects in high-speed information broadcast using phosphorescent white-light LEDs,” 11th International Conference on Transparent Optical Networks, pp. 1-6, 2009.

[16] D. O'Brien, L. Zeng, L.-M. Hoa, G. Faulkner, J. W. Walewski, and S. Randel, “Visible light communications: challenges and possibilities,” IEEE 19th International Symposium on Personal, Indoor and Mobile Radio Communications, pp. 1-5, 2008.

[17] Y. Zheng and M. Zhang, “Visible light communications-recent progresses and future outlooks,” Symposium on Photonics and Optoelectronic (SOPO), pp. 1-6, 2010.

[18] K. T. Delaney, P. Rinke, and C. G. Van de Walle, “Auger recombination rates in nitrides from first principles,” Appl. Phys. Lett., vol. 94, pp. 191109-3, 2009.

[19] M. Meneghini, N. Trivellin, G. Meneghesso, E. Zanoni, U. Zehnder, and B. Hahn, “A combined electro-optical method for the determination of the recombination parameters in InGaN-based light-emitting diodes,” J. Appl. Phys., vol. 106, pp. 114508-4, 2009.

[20] V. Fiorentini, F. Bernardini, and O. Ambacher, “Evidence for nonlinear macroscopic polarization in III--V nitride alloy heterostructures,” Appl. Phys. Lett., vol. 80, pp. 1204-1206, 2002.

[21] Z. -H. Zhang, S. T. Tan, W. Liu, Z. Ju, K. Zheng, Z. Kyaw, Y. Ji, N. Hasanov, X. W. Sun, and H. V. Demir, “Improved InGaN/GaN light-emitting diodes with a p-GaN/n-GaN/p-GaN/n-GaN/p-GaN current-spreading layer,” Opt. Express, vol. 21, pp. 4958-4969, 2013.

[22] K. Kumakura, T. Makimoto, N. Kobayashi, T. Hashizume, T. Fukui, and H. Hasegawa, “Minority carrier diffusion length in GaN: Dislocation density and doping concentration dependence,” Appl. Phys. Lett., vol. 86, pp. 052105-3, 2005.

[23] S. M. Sze, *Physics of Semiconductor Devices*, 2nd ed. (John Wiley & Sons, 1981).

[24] J. Piprek, *Nitride Semiconductor Devices Principles and Simulation*, (WILEY-VCH Verlag GmbH & Co. KGaA, 2007).

[25] H. Zhao, R. A. Arif, Y. K. Ee, and N. Tansu, “Self-consistent analysis of strain-compensated InGaN-AlGaN quantum wells for lasers and light-emitting diodes,” IEEE J. Quantum Electron., vol. 45, pp. 66-78, 2009.

[26] S. L. Chuang and C. S. Chang, “kp method for strained wurtzite semiconductors,” Phys. Rev. B, vol. 54, pp. 2491-2504, 1996.

[27] S. L. Chuang and C. S. Chang, “Effective-mass Hamiltonian for strained wurtzite GaN and analytical solutions,” Appl. Phys. Lett., vol. 68, pp. 1657-1659, 1996.

[28] Z. H. Zhang, S. T. Tan, Z. G. Ju, W. Liu, Y. Ji, Z. Kyaw, Y. Dikme, X. W. Sun, and H. V. Demir, "On the effect of step-doped quantum barriers in InGaN/GaN light emitting diodes," J. Display Technol., vol. 9, pp. 226-233, 2013.

[29] R. A. Arif, Y.-K. Ee, and N. Tansu, "Polarization engineering via staggered InGaN quantum wells for radiative efficiency enhancement of light emitting diodes," Appl. Phys. Lett., vol. 91, pp. 091110-3, 2007.

[30] J.-H. Ryou, P. D. Yoder, J. Liu, Z. Lochner, K. Hyunsoo, S. Choi, H.-J. Kim, and R. D. Dupuis, "Control of quantum-confined Stark effect in InGaN-based quantum wells," IEEE J. Sel. Top. Quantum Electron., vol. 15, pp. 1080-1091, 2009.

[31] J. Zhang and N. Tansu, "Improvement in spontaneous emission rates for InGaN quantum wells on ternary InGaN substrate for light-emitting diodes," J. Appl. Phys., vol. 110, pp. 113110-5, 2011.

[32] T. Deguchi, A. Shikanai, K. Torii, T. Sota, S. Chichibu, and S. Nakamura, "Luminescence spectra from InGaN multiquantum wells heavily doped with Si," Appl. Phys. Lett., vol. 72, pp. 3329-3331, 1998.

[33] R. M. Farrell, P. S. Hsu, D. A. Haeger, K. Fujito, S. P. DenBaars, J. S. Speck, and S. Nakamura, "Low-threshold-current-density AlGaN-cladding-free m-plane InGaN/GaN laser diodes," Appl. Phys. Lett., vol. 96, pp. 231113-3, 2010.

[34] R. M. Farrell, D. A. Haeger, P. S. Hsu, K. Fujito, D. F. Feezell, S. P. DenBaars, J. S. Speck, and S. Nakamura, "Determination of internal parameters for AlGaN-cladding-free m-plane InGaN/GaN laser diodes," Appl. Phys. Lett., vol. 99, pp. 171115-3, 2011.

[35] J. Piprek, "Efficiency droop in nitride-based light-emitting diodes," Phys. Status Solidi A Appl. Mater. Sci., vol. 207, pp. 2217-2225, 2010.

[36] E. Kioupakis, P. Rinke, K. T. Delaney, and C. G. Van de Walle, "Indirect Auger recombination as a cause of efficiency droop in nitride light-emitting diodes," Appl. Phys. Lett., vol. 98, pp. 161107-161107-3, 2011.

[37] M. F. Schubert, S. Chhajed, J. K. Kim, E. F. Schubert, D. D. Koleske, M. H. Crawford, S. R. Lee, A. J. Fischer, G. Thaler, and M. A. Banas, "Effect of dislocation density on efficiency droop in GaInN/GaN light-emitting diodes," Appl. Phys. Lett., vol. 91, pp. 231114-3, 2007.

[38] M. Zhang, P. Bhattacharya, J. Singh, and J. Hinckley, "Direct measurement of auger recombination in In0.1Ga0.9N/GaN quantum wells and its impact on the efficiency of In0.1Ga0.9N/GaN multiple quantum well light emitting diodes," Appl. Phys. Lett., vol. 95, pp. 201108-3, 2009.

[39] A. Laubsch, M. Sabathil, J. Baur, M. Peter, and B. Hahn, "High-power and high-efficiency InGaN-based light emitters," IEEE Trans. Electron Dev., vol. 57, pp. 79-87, 2010.

[40] J. Hader, J. V. Moloney, B. Pasenow, S. W. Koch, M. Sabathil, N. Linder, and S. Lutgen, "On the importance of radiative and Auger losses in GaN-based quantum wells," Appl. Phys. Lett., vol. 92, pp. 261103-3, 2008.

[41] A. Armstrong, T. A. Henry, D. D. Koleske, M. H. Crawford, K. R. Westlake, and S. R. Lee, "Dependence of radiative efficiency and deep level defect incorporation on threading dislocation density for InGaN/GaN light emitting diodes," Appl. Phys. Lett., vol. 101, pp. 162102-4, 2012.

[42] S.-H. Park and S.-L. Chuang, "Comparison of zinc-blende and wurtzite GaN semiconductors with spontaneous polarization and piezoelectric field effects," J. Appl. Phys., vol. 87, pp. 353-364, 2000.

[43] E. Cho, "GaN based heterostructure grown and application to electronic devices and gas sensors," PHD thesis, Department of Electrical engineering, The University of Michigan, 2009.

[44] H. Zhao, G. Liu, R. A. Arif, and N. Tansu, "Current injection efficiency induced efficiency-droop in InGaN quantum well light-emitting diodes," Solid-State Electron., vol. 54, pp. 1119-1124, 2010.

[45] G. Liu, J. Zhang, C. K. Tan, and N. Tansu, "Efficiency-droop suppression by using large-bandgap AlGaInN thin barrier layers in InGaN quantum-well light-emitting fiodes," IEEE Photon. J., vol. 5, pp. 2201011-2201011, 2013.

[46] H. Zhao, G. Liu, J. Zhang, R. A. Arif, and N. Tansu, "Analysis of internal quantum efficiency and current injection efficiency in III-nitride light-emitting diodes," J. Display Technol., vol. 9, pp. 212-225, 2013.

[47] T. Takeuchi, H. Amano, and I. Akasaki, "Theoretical study of orientation dependence of piezoelectric effects in wurtzite strained GaInN/GaN heterostructures and quantum wells," Jpn. J. Appl. Phys., vol. 39, pp. 413-416, 2000.

[48] T. Detchprohm, M. W. Zhu, Y. F. Li, L. Zhao, S. You, C. Wetzel, E. A. Preble, T. Paskova, and D. Hanser, "Wavelength-stable cyan and green light emitting diodes on nonpolar m-plane GaN bulk substrates," Appl. Phys. Lett., vol. 96, pp. 051101-3, 2010.

[49] F. Wu, M. D. Craven, S. H. Lim, and J. S. Speck, "Polarity determination of a-plane GaN on r-plane sapphire and its effects on lateral overgrowth and heteroepitaxy," J. Appl. Phys., vol. 94, pp. 942-947, 2003.

[50] T. Detchprohm, M. W. Zhu, Y. F. Li, Y. Xia, C. Wetzel, E. A. Preble, L. H. Liu, T. Paskova, and D. Hanser, "Green light emitting diodes on a-plane GaN bulk substrates," Appl. Phys. Lett., vol. 92, 241109-3, 2008.

[51] C. Wetzel, M. Zhu, J. Senawiratne, T. Detchprohm, P. D. Persans, L. Liu, E. A. Preble, and D. Hanser, "Light-emitting diode development on polar and non-polar GaN substrates," J. Cryst. Growth, vol. 310, pp. 3987-3991, 2008.

[52] Y. Enya, Y. Yoshizumi, T. Kyono, K. Akita, M. Ueno, M. Adachi, T. Sumitomo, S. Tokuyama, T. Ikegami, K. Katayama, and T. Nakamura, "531 nm green lasing of InGaN based laser diodes on semi-polar {20-21} free-standing GaN substrates," Appl. Phys. Express, vol. 2, pp. 082101, 2009.

[53] D. F. Feezell, J. S. Speck, S. P. DenBaars, and S. Nakamura, "Semipolar (20-2-1) InGaN/GaN light-emitting diodes for high-efficiency solid-state lighting," J. Display Technol., vol. 9, pp. 190-198, 2013.

[54] A. E. Romanov, T. J. Baker, S. Nakamura, J. S. Speck, and E. J. U. Group, "Strain-induced polarization in wurtzite III-nitride semipolar layers," J. Appl. Phys., vol. 100, pp. 023522-10, 2006.

[55] H. Zhao, G. Liu, J. Zhang, J. D. Poplawsky, V. Dierolf, and N. Tansu, "Approaches for high internal quantum efficiency green InGaN light-emitting diodes with large overlap quantum wells," Opt. Express, vol. 19, pp. A991-A1007, 2011.

[56] Z. -H. Zhang, S. T. Tan, Y. Ji, W. Liu, Z. Ju, Z. Kyaw, X. W. Sun, and H. V. Demir, "A PN-type quantum barrier for InGaN/GaN light emitting diodes," Opt. Express, vol. 21, pp. 15676-15685, 2013.

[57] R.-M. Lin, Y.-C. Lu, Y.-L. Chou, G.-H. Chen, Y.-H. Lin, and M.-C. Wu, "Enhanced characteristics of blue InGaN/GaN light-emitting diodes by using selective activation to modulate the lateral current spreading length," Appl. Phys. Lett., vol. 92, pp. 261105-3, 2008.

[58] H.-Y. Ryu and J.-I. Shim, "Effect of current spreading on the efficiency droop of InGaN light-emitting diodes," Opt. Express, vol. 19, pp. 2886-2894, 2011.

[59] J. H. Son, B. J. Kim, C. J. Ryu, Y. H. Song, H. K. Lee, J. W. Choi, and J.-L. Lee, "Enhancement of wall-plug efficiency in vertical InGaN/GaN LEDs by improved current spreading," Opt. Express, vol. 20, pp. A287-A292, 2012.

[60] C. -K. Li and Y. -R. Wu, "Study on the current spreading effect and light extraction enhancement of vertical GaN/InGaN LEDs," IEEE Trans. Electron Dev., vol. 59, pp. 400-407, 2012.

[61] Z. -H. Zhang, S. T. Tan, Z. Kyaw, Y. Ji, W. Liu, Z. Ju, N. Hasanov, X. W. Sun, and H. V. Demir, "InGaN/GaN light-emitting diode with a polarization tunnel junction," Appl. Phys. Lett., vol. 102, pp. 193508-5, 2013.

[62] J. Simon, V. Protasenko, C. X. Lian, H. L. Xing, and D. Jena, "Polarization-induced hole doping in wide-band-gap uniaxial semiconductor heterostructures," Science, vol. 327, pp. 60-64, 2010.

[63] M. Lachab, D. H. Youn, R. S. Qhalid Fareed, T. Wang, and S. Sakai, "Characterization of Mg-doped GaN grown by metalorganic chemical vapor deposition," Solid-State Electron., vol. 44, pp. 1669-1677, 2000.

[64] C. H. Wang, S. P. Chang, P. H. Ku, J. C. Li, Y. P. Lan, C. C. Lin, H. C. Yang, H. C. Kuo, T. C. Lu, S. C. Wang, and C. Y. Chang, "Hole transport improvement in InGaN/GaN light-emitting diodes by graded-composition multiple quantum barriers," Appl. Phys. Lett., vol. 99, pp. 171106-3, 2011.

[65] M. -C. Tsai, S. -H. Yen, and Y. -K. Kuo, "Carrier transportation and internal quantum efficiency of blue InGaN light-emitting diodes with p-doped barriers," IEEE Photon. Technol. Lett., vol. 22, pp. 374-376, 2010.

[66] M.-H. Kim, M. F. Schubert, Q. Dai, J. K. Kim, E. F. Schubert, J. Piprek, and Y. Park, "Origin of efficiency droop in GaN-based light-emitting diodes," Appl. Phys. Lett., vol. 91, pp. 183507-3, 2007.

[67] X. Ni, X. Li, J. Lee, S. Liu, V. Avrutin, U. Ozgur, H. Morkoc, and A. Matulionis, "Hot electron effects on efficiency degradation in InGaN light emitting diodes and designs to mitigate them," J. Appl. Phys., vol. 108, pp. 033112-13, 2010.

[68] X. Ni, X. Li, J. Lee, S. Liu, V. Avrutin, U. Ozgur, H. Morkoc, A. Matulionis, T. Paskova, G. Mulholland, and K. R. Evans, "InGaN staircase electron injector for reduction of electron overflow in InGaN light emitting diodes," Appl. Phys. Lett., vol. 97, pp. 031110-3, 2010.

[69] AIXTRON LTD., "System Manual, 3 × 2FT system," MOCVD manual, 2010.

[70] J. I. Pankove and T. D. Moustakes, *Gallium nitride (GaN) I*, (Academic Press, 1998).

[71] AIXTRON LTD., "Multi-wafer interferometer, real-time interferometer analysis of GaN MOCVD growth," MOCVD manual, 2010.

[72] K. Uchida, A. Watanabe, F. Yano, M. Kouguchi, T. Tanaka, and S. Minagawa, "Nitridation process of sapphire substrate surface and its effect on the growth of GaN," J. Appl. Phys., vol. 79, pp. 3487-3491, 1996.

[73] N. Grandjean, J. Massies, and M. Leroux, "Nitridation of sapphire. Effect on the optical properties of GaN epitaxial overlayers," Appl. Phys. Lett., vol. 69, pp. 2071-2073, 1996.

[74] S. Keller, B. P. Keller, Y. F. Wu, B. Heying, D. Kapolnek, J. S. Speck, U. K. Mishra, and S. P. Denbaars, "Influence of sapphire nitridation on properties of gallium nitride grown by metalorganic chemical vapor deposition," Appl. Phys. Lett., vol. 68, pp. 1525-1527, 1996.

[75] O. Briot, J. P. Alexis, M. Tchounkeu, and R. L. Aulombard, "Optimization of the MOVPE growth of GaN on sapphire," Mater. Sci. Eng. B, vol. 43, pp. 147-153, 1997.

[76] S. Figge, T. Böttcher, S. Einfeldt, and D. Hommel, "In situ and ex situ evaluation of the film coalescence for GaN growth on GaN nucleation layers," J. Cryst. Growth, vol. 221, pp. 262-266, 2000.

[77] Y. Guo, X. L. Liu, H. P. Song, A. L. Yang, X. Q. Xu, G. L. Zheng, H. Y. Wei, S. Y. Yang, Q. S. Zhu, and Z. G. Wang, "A study of indium incorporation in In-rich InGaN grown by MOVPE," Appl. Surf. Sci., vol. 256, pp. 3352-3356, 2010.

[78] N. Fujimoto, T. Kitano, G. Narita, N. Okada, K. Balakrishnan, M. Iwaya, S. Kamiyama, H. Amano, I. Akasaki, K. Shimono, T. Noro, T. Takagi, and A. Bandoh, "Growth of high-quality AlN at high growth rate by high-temperature MOVPE," Phys. Status Solidi C, vol. 3, pp. 1617-1619, 2006.

[79] D. G. Zhao, J. J. Zhu, D. S. Jiang, H. Yang, J. W. Liang, X. Y. Li, and H. M. Gong, "Parasitic reaction and its effect on the growth rate of AlN by metalorganic chemical vapor deposition," J. Cryst. Growth, vol. 289, pp. 72-75, 2006.

[80] Z. G. Ju, S. T. Tan, Z. H. Zhang, Y. Ji, Z. Kyaw, Y. Dikme, X. W. Sun, and H. V. Demir, "On the origin of the redshift in the emission wavelength of InGaN/GaN blue light emitting diodes grown with a higher temperature interlayer," Appl. Phys. Lett., vol. 100, pp. 123503-4, 2012.

[81] S. Kim, J. Oh, J. Kang, D. Kim, J. Won, J. W. Kim, and H.-K. Cho, "Two-step growth of high quality GaN using V/III ratio variation in the initial growth stage," J. Cryst. Growth, vol. 262, pp. 7-13, 2004.

[82] S. -H. Yen, M. -C. Tsai, M. -L. Tsai, Y. -J. Shen, T.-C. Hsu, and Y. -K. Kuo, "Effect of n-Type AlGaN layer on carrier transportation and efficiency droop of blue InGaN light-emitting diodes," IEEE Photon. Technol. Lett., vol. 21, pp. 975-977, 2009.

[83] I. Vurgaftman and J. R. Meyer, "Band parameters for nitrogen-containing semiconductors," J. Appl. Phys., vol. 94, pp. 3675-3696, 2003.

[84] M. Bosi and R. Fornari, "A study of Indium incorporation efficiency in InGaN grown by MOVPE," J. Cryst. Growth, vol. 265, pp. 434-439, 2004.

[85] D. J. Kim, Y. T. Moon, K. M. Song, I. W. Lee, and S. J. Park, "Effect of growth pressure on indium incorporation during the growth of InGaN by MOCVD," J. Electron. Mater., vol. 30, pp. 99-102, 2001.

[86] C. G. Park, G. H. Gu, B. H. Lee, and D. H. Jang, "Effects of growth pressure on the structural and optical properties of multi quantum wells (MQWs) in blue LED," Ultramicroscopy, vol. 127, pp. 114-118, 2013.

[87] E. L. Piner, M. K. Behbehani, N. A. ElMasry, F. G. McIntosh, J. C. Roberts, K. S. Boutros, and S. M. Bedair, "Effect of hydrogen on the indium incorporation in InGaN epitaxial films," Appl. Phys.Lett., vol. 70, pp. 461-463, 1997.

[88] C. K. Wang, T. H. Chiang, K. Y. Chen, Y. Z. Chiou, T. K. Lin, S. P. Chang, and S. J. Chang, "Investigating the effect of piezoelectric polarization on GaN-based LEDs with different quantum barrier thickness," J. Display Technol., vol. 9, pp. 207-211, 2013.

[89] L. Lahourcade, J. Pernot, A. Wirthmuller, M. P. Chauvat, P. Ruterana, A. Laufer, M. Eickhoff, and E. Monroy, "Mg doping and its effect on the semipolar GaN(11-22) growth kinetics," Appl. Phys. Lett., vol. 95, pp. 171908-3, 2009.

[90] H. Tokunaga, A. Ubukata, Y. Yano, A. Yamaguchi, N. Akutsu, T. Yamasaki, and K. Matsumoto, "Effects of growth pressure on AlGaN and Mg-doped GaN grown using multiwafer metal organic vapor phase epitaxy system," J. Cryst. Growth, vol. 272, pp. 348-352, 2004.

[91] Y. Xian, S. Huang, Z. Zheng, B. Fan, Z. Wu, H. Jiang, and G. Wang, "Effects of growth pressure on the properties of p-GaN layers," J. Cryst. Growth, vol. 325, pp. 32-35, 2011.

[92] Samco., LED manufacturing Process, http://www.samcointl.com/app/01_led.phphttp://www.samcointl.com/app/01_led.php.

[93] S. J. Chang, C. H. Lan, J. D. Hwang, Y. C. Cheng, W. J. Lin, J. C. Lin, and H. Z. Chen, "Sputtered indium-tin-oxide on p-GaN," J. Electrochem. Soc., vol. 155, pp. H140-H143, 2008.

[94] Y. Han, L. Zhongtao, Y. Luo, M. Hongxia, z. Xianpeng, and L. Wang, "The effect of p-InGaN layer on ITO based ohmic contacts to p-GaN," International Nano-Optoelectronics Workshop, pp. 90-91, 2007.

[95] Z. Z. Chen, Z. X. Qin, Y. Z. Tong, X. D. Hu, T. J. Yu, Z. J. Yang, X. M. Ding, Z. H. Li, and G. Y. Zhang, "Thermal annealing effects on Ni/Au contacts to p-type GaN in different ambient," Mater. Sci. Eng. B, vol. 100, pp. 199-203, 2003.

[96] D. Qiao, L. S. Yu, S. S. Lau, J. Y. Lin, H. X. Jiang, and T. E. Haynes, "A study of the Au/Ni ohmic contact on p-GaN," J. Appl. Phys., vol. 88, pp. 4196-4200, 2000.

[97] S. Zhou, B. Cao, and S. Liu, "Dry etching characteristics of GaN using Cl2/BCl3 inductively coupled plasmas," Appl. Surf. Sci., vol. 257, pp. 905-910, 2010.

[98] Y. H. Lee, T. I. Kim, G. Y. Yeom, J. W. Lee, and M. C. Yoo, "Etch characteristics of GaN using inductively coupled Cl2/Ar and Cl2/BCl3 plasmas," J. Vac. Sci. Technol., A, vol. 16, pp. 1478-1482, 1998.

[99] K. Remashan, S. J. Chua, A. Ramam, S. Prakash, and W. Liu, "Inductively coupled plasma etching of GaN using BCl3/Cl2 chemistry and photoluminescence studies of the etched samples," Semicond. Sci. Technol., vol. 15, pp. 386-389, 2000.

[100] R. A. Arif, H. P. Zhao, Y. K. Ee, and N. Tansu, "Spontaneous emission and characteristics of staggered InGaN quantum-well light-emitting diodes," IEEE J. Quantum Electron., vol. 44, pp. 573-580, 2008.

[101] H. P. Zhao, G. Y. Liu, X. H. Li, G. S. Huang, J. D. Poplawsky, S. T. Penn, V. Dierolf, and N. Tansu, "Growths of staggered InGaN quantum wells light-emitting diodes emitting at 520-525 nm employing graded growth-temperature profile," Appl. Phys. Lett., vol. 95, pp. 061104-3, 2009.

[102] H. P. Zhao and N. Tansu, "Optical gain characteristics of staggered InGaN quantum wells lasers," J. Appl. Phys., vol. 107, pp. 113110-12, 2010.

[103] J. H. Son and J. L. Lee, "Strain engineering for the solution of efficiency droop in InGaN/GaN light-emitting diodes," Opt. Express, vol. 18, pp. 5466-5471, 2010.

[104] H. Zhao, R. A. Arif, and N. Tansu, "Self-consistent gain analysis of type-II `W' InGaN--GaNAs quantum well lasers," J. Appl. Phys., vol. 104, pp. 043104-7, 2008.

[105] H. Zhao, G. Liu, and N. Tansu, "Analysis of InGaN-delta-InN quantum wells for light-emitting diodes," Appl. Phys.Lett., vol. 97, pp. 131114-3, 2010.

[106] S.-H. Park, D. Ahn, B.-H. Koo, and J.-E. Oh, "Optical gain improvement in type-II InGaN/GaNSb/GaN quantum well structures composed of InGaN and GaNSb layers," Appl. Phys. Lett., vol. 96, pp. 051106-3, 2010.

[107] J. Zhang, H. Zhao, and N. Tansu, "Large optical gain AlGaN-delta-GaN quantum wells laser active regions in mid- and deep-ultraviolet spectral regimes," Appl. Phys. Lett., vol. 98, pp. 171111-3, 2011.

[108] R. A. Arif, H. Zhao, and N. Tansu, "Type-II InGaN-GaNAs quantum wells for lasers applications," Appl. Phys. Lett., vol. 92, pp. 011104-3, 2008.

[109] L. W. Wu, S. J. Chang, T. C. Wen, Y. K. Su, J. F. Chen, W. C. Lai, C. H. Kuo, C. H. Chen, and J. K. Sheu, "Influence of Si-doping on the characteristics of InGaN-GaN multiple quantum-well blue light emitting diodes," IEEE J. Quantum Electron., vol. 38, pp. 446-450, 2002.

[110]Z. Y. Zheng, Z. M. Chen, Y. L. Xian, B. F. Fan, S. J. Huang, W. Q. Jia, Z. S. Wu, G. Wang, and H. Jiang, "Enhanced electrostatic discharge properties of nitride-based light-emitting diodes with inserting Si-delta-doped layers," Appl. Phys. Lett., vol. 99, pp. 111109 -3, 2011.

[111] H. P. D. Schenk, A. Bavard, E. Frayssinet, X. Song, F. Cayrel, H. Ghouli, M. Lijadi, L. Naim, M. Kennard, Y. Cordier, D. Rondi, and D. Alquier, "Delta-doping of epitaxial GaN layers on large diameter Si(111) substrates," Appl. Phys. Express, vol. 5, pp. 025504-3, 2012.

[112] J.-H. Ryou, L. Jae, L. Wonseok, J. Liu, Z. Lochner, Y. Dongwon, and R. D. Dupuis, “Effect of silicon doping in the quantum-well barriers on the electrical and optical properties of visible green light-emitting diodes,” IEEE Photon. Technol. Lett., vol. 20, pp. 1769-1771, 2008.

[113] M.-K. Kwon, I.-K. Park, S.-H. Baek, J.-Y. Kim, and S.-J. Park, “Si delta doping in a GaN barrier layer of InGaN/GaN multiquantum well for an efficient ultraviolet light-emitting diode,” J. Appl. Phys, vol. 97, pp. 106109-3, 2005.

[114] D. Zhu, A. N. Noemaun, M. F. Schubert, J. Cho, E. F. Schubert, M. H. Crawford, and D. D. Koleske, “Enhanced electron capture and symmetrized carrier distribution in GaInN light-emitting diodes having tailored barrier doping,” Appl. Phys. Lett., vol. 96, pp. 121110-3, 2010.

[115] V. Fiorentini, F. Bernardini, F. Della Sala, A. Di Carlo, and P. Lugli, “Effects of macroscopic polarization in III-V nitride multiple quantum wells,” Phys. Rev. B, vol. 60, pp. 8849-8858, 1999.

[116] L. Wang, C. Lu, J. Lu, L. Liu, N. Liu, Y. Chen, Y. Zhang, E. Gu, and X. Hu, “Influence of carrier screening and band filling effects on efficiency droop of InGaN light emitting diodes,” Opt. Express, vol. 19, pp. 14182-14187, 2011.

[117] S. Keller, S. F. Chichibu, M. S. Minsky, E. Hu, U. K. Mishra, and S. P. DenBaars, "Effect of the growth rate and the barrier doping on the morphology and the properties of InGaN/GaN quantum wells," J. Cryst. Growth, vol. 195, pp. 258-264, 1998.

[118] Z. Gong, S. Jin, Y. Chen, J. McKendry, D. Massoubre, I. M. Watson, E. Gu, and M. D. Dawson, “Size-dependent light output, spectral shift, and self-heating of 400 nm InGaN light-emitting diodes,” J. Appl. Phys., vol. 107, pp. 013103-6, 2010.

[119] APSYS by Crosslight Software Inc., Canada, http://www.crosslight.com.

[120] Y. C. Shen, G. O. Mueller, S. Watanabe, N. F. Gardner, A. Munkholm, and M. R. Krames, “Auger recombination in InGaN measured by photoluminescence,” Appl. Phys. Lett., vol. 91, pp. 141101-3, 2007.

[121] L. T. Romano, C. G. Van de Walle, J. W. Ager Iii, W. Gotz, and R. S. Kern, “Effect of Si doping on strain, cracking, and microstructure in GaN thin films grown by metalorganic chemical vapor deposition,” J. Appl. Phys., vol. 87, pp. 7745-7752, 2000.

[122] S.-H. Han, C.-Y. Cho, S.-J. Lee, T.-Y. Park, T.-H. Kim, S. H. Park, S. W. Kang, J. W. Kim, Y. C. Kim, and S.-J. Park, “Effect of Mg doping in the barrier of InGaN/GaN multiple quantum well on optical power of light-emitting diodes,” Appl. Phys. Lett., vol. 96, pp. 051113-3, 2010.

[123] M. -C. Tsai, S. -H. Yen, Y. -C.Lu, and K. Y. -K. Kuo, “Numerical study of bue InGaN light-emitting diodes with varied barrier thicknesses,” IEEE Photon. Technol. Lett., vol. 23, pp. 76-78, 2011.

[124] S. Choi, M.-H. Ji, J. Kim, H. J. Kim, M. M. Satter, P. D. Yoder, J.-H. Ryou, R. D. Dupuis, A. M. Fischer, and F. A. Ponce, "Efficiency droop due to electron spill-over and limited hole injection in III-nitride visible light-emitting diodes employing lattice-matched InAlN electron blocking layers," Appl. Phys. Lett., vol. 101, pp. 161110-5, 2012.

[125] H. Xing, D. S. Green, H. Yu, T. Mates, P. Kozodoy, S. Keller, S. P. Denbaars, and U. K. Mishra, "Memory effect and redistribution of Mg into sequentially regrown GaN layer by metalorganic chemical vapor deposition," Jpn. J. Appl. Phys, vol. 42, pp. 50-53, 2003.

[126] E. H. Park and J. Jang, "The effect of Mg and Si impurities on the optical property of InGaN-light emitting diode," in Proceedings of SPIE - The International Society for Optical Engineering, 2009.

[127] R. M. Farrell, E. C. Young, F. Wu, S. P. DenBaars, and J. S. Speck, "Materials and growth issues for high-performance nonpolar and semipolar light-emitting devices," Semicond. Sci. Technol., vol. 27, pp. 024001, 2012.

[128] D. A. Browne, E. C. Young, J. R. Lang, C. A. Hurni, and J. S. Speck, "Indium and impurity incorporation in InGaN films on polar, nonpolar, and semipolar GaN orientations grown by ammonia molecular beam epitaxy," J. Vac. Sci. Technol., A, vol. 30, pp. 041513-8, 2012.

[129]H. P. Zhao, G. Y. Liu, X. H. Li, R. A. Arif, G. S. Huang, J. D. Poplawsky, S. Tafon Penn, V. Dierolf, and N. Tansu, "Design and characteristics of staggered InGaN quantum-well light-emitting diodes in the green spectral regime," IET Optoelectron., vol. 3, pp. 283-295, 2009.

[130] Y. K. Ee, J. M. Biser, W. Cao, H. M. Chan, R. P. Vinci, and N. Tansu, "Metalorganic vapor phase epitaxy of III-nitride light-emitting diodes on nanopatterned AGOG sapphire substrate by abbreviated growth mode," IEEE J. Sel. Top. Quantum Electron., vol. 15, pp. 1066-1072, 2009.

[131] Y.-K. Ee, X.-H. Li, J. Biser, W. Cao, H. M. Chan, R. P. Vinci, and N. Tansu, "Abbreviated MOVPE nucleation of III-nitride light-emitting diodes on nano-patterned sapphire," J. Cryst. Growth, vol. 312, pp. 1311-1315, 2010.

[132] Y. Li, S. You, M. Zhu, L. Zhao, W. Hou, T. Detchprohm, Y. Taniguchi, N. Tamura, S. Tanaka, and C. Wetzel, "Defect-reduced green GaInN/GaN light-emitting diode on nanopatterned sapphire," Appl. Phys. Lett., vol. 98, pp. 151102-3, 2011.

[133] J. Wang, L. Wang, L. Wang, Z. Hao, Y. Luo, A. Dempewolf, M. Muller, F. Bertram, and J. Christen, "An improved carrier rate model to evaluate internal quantum efficiency and analyze efficiency droop origin of InGaN based light-emitting diodes," J. Appl. Phys., vol. 112, pp. 023107-6, 2012.

[134] H. J. Kim, S. Choi, S.-S. Kim, J.-H. Ryou, P. D. Yoder, R. D. Dupuis, A. M. Fischer, K. Sun, and F. A. Ponce, "Improvement of quantum efficiency by employing active-layer-friendly lattice-matched InAlN

electron blocking layer in green light-emitting diodes," Appl. Phys. Lett., vol. 96, pp. 101102-3, 2010.

[135] H. Kim, S.-J. Park, and H. Hyunsang, "Effects of current spreading on the performance of GaN-based light-emitting diodes," IEEE Trans. Electron Dev., vol. 48, pp. 1065-1069, 2001.

[136] T. W. Kuo, S. X. Lin, P. K. Hung, K. K. Chong, C. I. Hung, and M. P. Houng, "Formation of selective high barrier region by inductively coupled plasma treatment on GaN-based light-emitting diodes," Jpn J. Appl. Phys., vol. 49, pp. 116504, 2010.

[137] D. Han, J. Shim, D.-S. Shin, E. Nam, and H. Park, "Effect of temperature distribution and current crowding on the performance of lateral GaN-based light-emitting diodes," Phys. Status Solidi C, vol. 7, pp. 2133-2135, 2010.

[138] C. -F. Tsai, Y. -K. Su, and C. -L. Lin, "Improvement in the light output power of GaN-based light-emitting diodes by natural-cluster silicon dioxide nanoparticles as the current-blocking layer," IEEE Photon. Technol. Lett., vol. 21, pp. 996-998, 2009.

[139] H. -H. Liu, P. -R. Chen, G. -Y. Lee, and J. -I. Chyi, "Efficiency enhancement of InGaN LEDs with an n-Type AlGaN/GaN/InGaN current spreading layer," IEEE Electr. Device Lett., vol. 32, pp. 1409-1411, 2011.

[140] S.-R. Jeon, Y.-H. Song, H.-J. Jang, G. M. Yang, S. W. Hwang, and S. J. Son, "Lateral current spreading in GaN-based light-emitting diodes utilizing tunnel contact junctions," Appl. Phys. Lett., vol. 78, pp. 3265-3267, 2001.

[141] A. H. Reading, J. J. Richardson, C.-C. Pan, S. Nakamura, and S. P. DenBaars, "High efficiency white LEDs with single-crystal ZnO current spreading layers deposited by aqueous solution epitaxy," Opt. Express, vol. 20, pp. A13-A19, 2012.

[142] V. K. Malyutenko, S. S. Bolgov, and A. N. Tykhonov, "Research on electrical efficiency degradation influenced by current crowding in vertical blue InGaN-on-SiC light-emitting diodes," IEEE Photon. Technol. Lett., vol. 24, pp. 1124-1126, 2012.

[143] B. J. Baliga, *Fundamentals of Power Semiconductor Devices*, (Springer Science + Business Media, LLC, 2008).

[144]M.-K. Kwon, I.-K. Park, J.-Y. Kim, J.-O. Kim, K. Bongjin, and S.-J. Park, "Gradient doping of Mg in p-type GaN for high efficiency InGaN/GaN ultraviolet light-emitting diode," IEEE Photon. Technol. Lett., vol. 19, pp. 1880-1882, 2007.

[145] D. K. Schroder, *Semiconductor Material and Device Characterization*, 2nd ed. (John Wiley & Sons, Inc., 1998).

[146] Y. -J. Liu, C. -C. Huang, T. -Y. Chen, C. S. Hsu, J. -K. Liou, and W. -C. Liu, "Improved performance of an InGaN-based light-emitting diode with a p-GaN/n-GaN barrier junction," IEEE J. Quantum Electron., vol. 47, pp. 755-761, 2011.

[147] V. K. Malyutenko and S. S. Bolgov, "Effect of current crowding on the ideality factor in MQW InGaN/GaN LEDs on sapphire substrates," Proc. SPIE vol. 7617, pp. 76171K-9, 2010.

[148] J. Zhang and N. Tansu, "Optical gain and laser characteristics of InGaN quantum wells on ternary InGaN substrates," IEEE Photon. J., vol. 5, pp. 2600111-2600111, 2013.

[149] X. Ni, Q. Fan, R. Shimada, U. Ozgur, and H. Morkoc, "Reduction of efficiency droop in InGaN light emitting diodes by coupled quantum wells," Appl. Phys. Lett., vol. 93, pp. 171113-3, 2008.

[150] Y. Ji, Z.-H. Zhang, S. T. Tan, Z. G. Ju, Z. Kyaw, N. Hasanov, W. Liu, X. W. Sun, and H. V. Demir, "Enhanced hole transport in InGaN/GaN multiple quantum well light-emitting diodes with a p-type doped quantum barrier," Opt. Lett., vol. 38, pp. 202-204, 2013.

[151] Y.-K. Kuo, J.-Y. Chang, and M.-C. Tsai, "Enhancement in hole-injection efficiency of blue InGaN light-emitting diodes from reduced polarization by some specific designs for the electron blocking layer," Opt. Lett., vol. 35, pp. 3285-3287, 2010.

[152] Y. -A. Chang, J. -Y. Chang, Y. -T. Kuo, and Y. -K. Kuo, "Investigation of green InGaN light-emitting diodes with asymmetric AlGaN composition-graded barriers and without an electron blocking layer," Appl. Phys. Lett., vol. 100, pp. 251102-4, 2012.

[153] J. -H. Lee and J. -H, Lee, "Enhanced output power of InGaN-based light-emitting diodes with AlGaN/GaN two-dimensional electron gas structure," IEEE Electr. Device Lett., vol. 31, pp. 455-457, 2010.

[154] L. Zhang, K. Ding, J. C. Yan, J. X. Wang, Y. P. Zeng, T. B. Wei, Y. Y. Li, B. J. Sun, R. F. Duan, and J. M. Li, "Three-dimensional hole gas induced by polarization in (0001)-oriented metal-face III-nitride structure," Appl. Phys. Lett., vol. 97, pp. 062103-3, 2010.

[155] S. -R. Jeon, M. S. Cho, A. Y. Min, and G.-M. Yang, "GaN-based light-emitting diodes using tunnel junctions," IEEE Sel. Top. Quantum Electron., vol. 8, pp. 739-743, 2002.

[156] S. R. Jeon, Y. H. Song, H. J. Jang, K. S. Kim, G. M. Yang, S. W. Hwang, and S. J. Son, "Buried tunnel contact junctions in GaN-based light-emitting diodes," Phys. Status Solidi A, vol. 188, pp. 167-170, 2001.

[157] C. -M. Lee, C. -C. Chuo, I. L. Chen, J. -C. Chang, and J. -I. Chyi, "High-brightness inverted InGaN-GaN multiple-quantum-well light-emitting diodes without a transparent conductive layer," IEEE Electr. Device Lett., vol. 24, pp. 156-158, 2003.

[158] T. Takeuchi, G. Hasnain, S. Corzine, M. Hueschen, R. P. Schneider, C. Kocot, M. Blomqvist, Y. L. Chang, D. Lefforge, M. R. Krames, L. W. Cook, and S. A. Stockman, "GaN-based light emitting diodes with tunnel junctions," Jpn J. Appl. Phys. vol. 40, pp. L861-L863, 2001.

[159] M. F. Schubert, "Interband tunnel junctions for wurtzite III-nitride semiconductors based on heterointerface polarization charges," Phys. Rev. B, vol. 81, pp. 035303, 2010.

[160] S. Krishnamoorthy, D. N. Nath, F. Akyol, P. S. Park, M. Esposto, and S. Rajan, "Polarization-engineered GaN/InGaN/GaN tunnel diodes," Appl. Phys. Lett., vol. 97, pp. 203502-3, 2010.

[161] J. Simon, Z. Zhang, K. Goodman, H. Xing, T. Kosel, P. Fay, and D. Jena, "Polarization-induced Zener tunnel junctions in wide-band-gap heterostructures," Phys. Rev. Lett., vol. 103, pp. 026801, 2009.

[162] S. Pimputkar, J. S. Speck, S. P. Denbaars, and S. Nakamura, "Prospects for LED lighting," Nature Photon., vol. 3, pp. 180-182, 2009.

[163] S. H. Park, Y. T. Moon, D. S. Han, J. S. Park, M. S. Oh, and D. Ahn, "High-efficiency InGaN/GaN light-emitting diodes with electron injector," Semicond. Sci. Technol., vol. 27, pp. 115003 2012.

[164] C. -H. Jang, J. -K. Sheu, C. M. Tsai, S. -J. Chang, W.-C. Lai, M. -L. Lee, T. K. Ko, C. F. Shen, and S. C. Shei, "Improved performance of GaN-based blue LEDs with the InGaN insertion layer between the MQW active layer and the n-GaN cladding layer," IEEE J. Quantum Electron., vol. 46, pp. 513-517, 2010.

[165] J. K. Sheu, G. C. Chi, and M. J. Jou, "Enhanced output power in an InGaN-GaN multiquantum-well light-emitting diode with an InGaN current-spreading layer," IEEE Photon. Technol. Lett, vol. 13, pp. 1164-1166, 2001.

[166] K. T. Tsen, R. P. Joshi, D. K. Ferry, A. Botchkarev, B. Sverdlov, A. Salvador, and H. Morkoc, "Nonequilibrium electron distributions and phonon dynamics in wurtzite GaN," Appl. Phys. Lett., vol. 68, pp. 2990-2992, 1996.

[167] Y. T. Rebane, Y. G. Shreter, B. S. Yavich, V. E. Bougrov, S. I. Stepanov, and W. N. Wang, "Light emitting diode with charge asymmetric resonance tunneling," Phys. Status Solidi A, vol. 180, pp. 121-126, 2000.

[168] D. Saguatti, L. Bidinelli, G. Verzellesi, M. Meneghini, G. Meneghesso, E. Zanoni, R. Butendeich, and B. Hahn, "Investigation of efficiency-droop mechanisms in multi-quantum-well InGaN/GaN blue light-emitting diodes," IEEE Trans. Electron Dev., vol. 59, pp. 1402-1409, 2012.

[169] C. S. Xia, Z. Q. Li, S. Yang, L. W. Cheng, W. D. Hu, and W. Lu, "Simulation of InGaN/GaN light-emitting diodes with a non-local quantum well transport model," 12th International Conference on

Numerical Simulation of Optoelectronic Devices (NUSOD), pp. 21-22, 2012.

[170] M. F. Schubert and E. F. Schubert, "Effect of heterointerface polarization charges and well width upon capture and dwell time for electrons and holes above GaInN/GaN quantum wells," Appl. Phys. Lett., vol. 96, pp. 131102-3, 2010.

[171] Y. -K. Kuo, Y. -H. Shih, M. -C. Tsai, and J. -Y. Chang, "Improvement in electron overflow of near-ultraviolet InGaN LEDs by specific design on last barrier," IEEE Photon. Technol. Lett., vol. 23, pp. 1630-1632, 2011.

[172]T. Lu, S. Li, C. Liu, K. Zhang, Y. Xu, J. Tong, L. Wu, H. Wang, X. Yang, Y. Yin, G. Xiao, and Y. Zhou, "Advantages of GaN based light-emitting diodes with a p-InGaN hole reservoir layer," Appl. Phys. Lett., vol. 100, pp. 141106-3, 2012.

[173] B. Romero, J. Arias, I. Esquivias, and M. Cada, "Simple model for calculating the ratio of the carrier capture and escape times in quantum-well lasers," Appl. Phys. Lett., vol. 76, pp. 1504-1506, 2000.

[174] S.-H. Han, D.-Y. Lee, S.-J. Lee, C.-Y. Cho, M.-K. Kwon, S. P. Lee, D. Y. Noh, D.-J. Kim, Y. C. Kim, and S.-J. Park, "Effect of electron blocking layer on efficiency droop in InGaN/GaN multiple quantum well light-emitting diodes," Appl. Phys. Lett., vol. 94, pp. 231123-3, 2009.

[175] Y. Li, Y. Gao, M. He, J. Zhou, Y. Lei, L. Zhang, K. Zhu, and Y. Chen, "Effect of polarization-Matched n-Type AlGaInN electron-blocking Layer on the optoelectronic properties of blue InGaN light-emitting diodes," J. Display Technol., vol. 9, pp. 244-248, 2013.

[176] Y. Y. Zhang and Y. A. Yin, "Performance enhancement of blue light-emitting diodes with a special designed AlGaN/GaN superlattice electron-blocking layer," Appl. Phys. Lett., vol. 99, pp. 221103-3, 2011.

[177] S. J. Lee, S. H. Han, C. Y. Cho, S. P. Lee, D. Y. Noh, H. W. Shim, Y. C. Kim, and S. J. Park, "Improvement of GaN-based light-emitting diodes using p-type AlGaN/GaN superlattices with a graded Al composition," J. Phys. D: Appl. Phys., vol. 44, pp. 105101 2011.

[178] J. Piprek, "AlGaN polarization doping effects on the efficiency of blue LEDs," Proc. SPIE, 8262, pp. 82620E, 2012.

[179] C. Buchheim, R. Goldhahn, G. Gobsch, K. Tonisch, V. Cimalla, F. Niebelschutz, and O. Ambacher, "Electric field distribution in GaN/AlGaN/GaN heterostructures with two-dimensional electron and hole gas," Appl. Phys. Lett., vol. 92, pp. 013510-3, 2008.

[180] K. Tonisch, C. Buchheim, F. Niebelschutz, A. Schober, G. Gobsch, V. Cimalla, O. Ambacher, and R. Goldhahn, "Piezoelectric actuation of (GaN/)AlGaN/GaN heterostructures," J. Appl. Phys., vol. 104, pp. 084516-8, 2008.

[181] S. Heikman, S. Keller, Y. Wu, J. S. Speck, S. P. DenBaars, and U. K. Mishra, "Polarization effects in AlGaN/GaN and GaN/AlGaN/GaN heterostructures," J. Appl. Phys., vol. 93, pp. 10114-10118, 2003.

[182] D. Jena, S. Heikman, D. Green, D. Buttari, R. Coffie, H. Xing, S. Keller, S. DenBaars, J. S. Speck, U. K. Mishra, and I. Smorchkova, "Realization of wide electron slabs by polarization bulk doping in graded III--V nitride semiconductor alloys," Appl. Phys. Lett., vol. 81, pp. 4395-4397, 2002.

[183] S. Acar, S. B. Lisesivdin, M. Kasap, S. Özçelik, and E. Özbay, "Determination of two-dimensional electron and hole gas carriers in AlGaN/GaN/AlN heterostructures grown by metal organic chemical vapor deposition," Thin Solid Films, vol. 516, pp. 2041-2044, 2008.

[184] T. Zimmermann, M. Neuburger, M. Kunze, I. Daumiller, A. Denisenko, A. Dadgar, A. Krost, and E. Kohn, "P-channel InGaN-HFET structure based on polarization doping," IEEE Electr. Device Lett., vol. 25, pp. 450-452, 2004.

[185] A. Nakajima, Y. Sumida, M. H. Dhyani, H. Kawai, and E. M. S. Narayanan, "High density two-dimensional hole gas induced by negative polarization at GaN/AlGaN heterointerface," Appl. Phys. Express, vol. 3, pp. 121004-3, 2010.

[186] C. G. Van de Walle and J. Neugebauer, "First-principles calculations for defects and impurities: applications to III-nitrides," J. Appl. Phys., vol. 95, pp. 3851-3879, 2004.

[187] D. G. Zhao, S. Zhang, W. B. Liu, X. P. Hao, D. S. Jiang, J. J. Zhu, Z. S. Liu, H. Wang, S. M. Zhang, H. Yang, and L. Wei, "Role of Ga vacancies in enhancing the leakage current of GaN Schottky barrier ultraviolet photodetectors," Chin. Phys. B, vol. 19, pp. 0578021-0578024, 2010.

[188]J. Hertkorn, S. B. Thapa, T. Wunderer, F. Scholz, Z. H. Wu, Q. Y. Wei, F. A. Ponce, M. A. Moram, C. J. Humphreys, C. Vierheilig, and U. T. Schwarz, "Highly conductive modulation doped composition graded p-AlGaN/(AlN)/GaN multiheterostructures grown by metalorganic vapor phase epitaxy," J. Appl. Phys., vol. 106, pp. 013720-6, 2009.

[189] L. Zhang, X. C. Wei, N. X. Liu, H. X. Lu, J. P. Zeng, J. X. Wang, Y. P. Zeng, and J. M. Li, "Improvement of efficiency of GaN-based polarization-doped light-emitting diodes grown by metalorganic chemical vapor deposition," Appl. Phys. Lett., vol. 98, pp. 241111-3, 2011.